frontiers | Research Topics

Neural signals acquisition and intelligent analysis

Edited by
Xiaomin Yang, Yin Tian, Gwanggil Jeon and
Yu Pang

Published in
Frontiers in Neuroscience

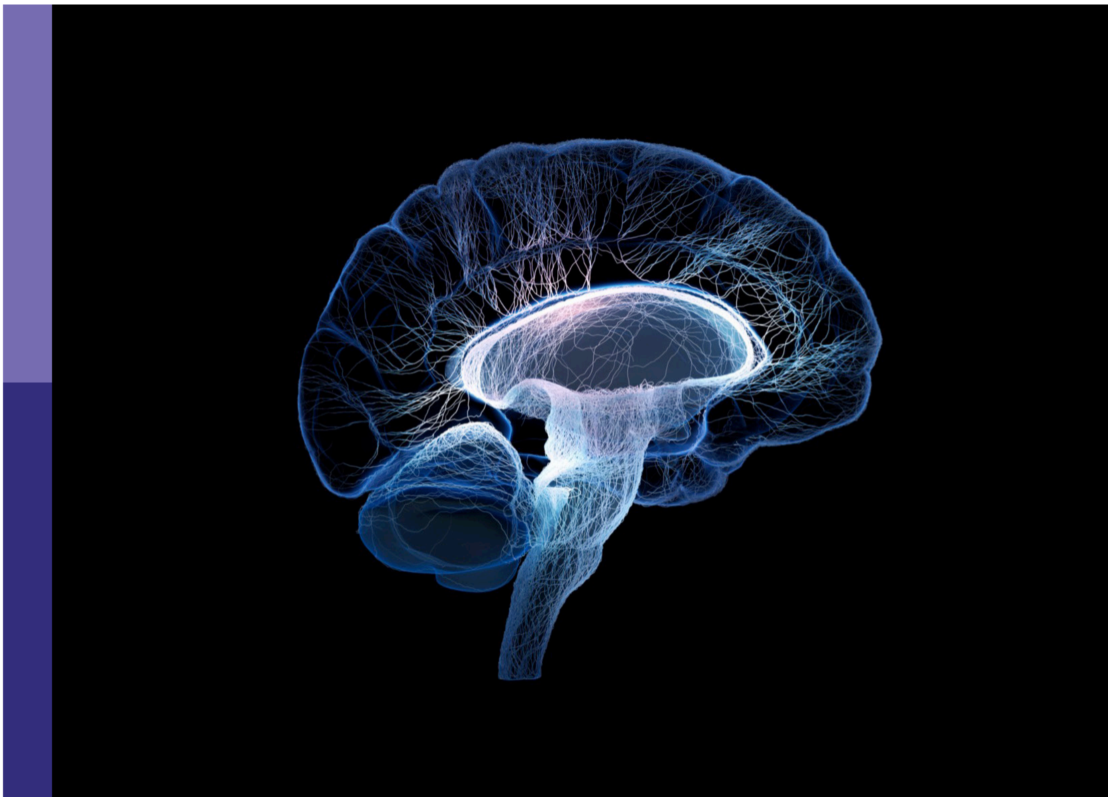

ISSN 1664-8714
ISBN 978-2-8325-3156-3
DOI 10.3389/978-2-8325-3156-3

About Frontiers

Frontiers is more than just an open access publisher of scholarly articles: it is a pioneering approach to the world of academia, radically improving the way scholarly research is managed. The grand vision of Frontiers is a world where all people have an equal opportunity to seek, share and generate knowledge. Frontiers provides immediate and permanent online open access to all its publications, but this alone is not enough to realize our grand goals.

Frontiers journal series

The Frontiers journal series is a multi-tier and interdisciplinary set of open-access, online journals, promising a paradigm shift from the current review, selection and dissemination processes in academic publishing. All Frontiers journals are driven by researchers for researchers; therefore, they constitute a service to the scholarly community. At the same time, the *Frontiers journal series* operates on a revolutionary invention, the tiered publishing system, initially addressing specific communities of scholars, and gradually climbing up to broader public understanding, thus serving the interests of the lay society, too.

Dedication to quality

Each Frontiers article is a landmark of the highest quality, thanks to genuinely collaborative interactions between authors and review editors, who include some of the world's best academicians. Research must be certified by peers before entering a stream of knowledge that may eventually reach the public - and shape society; therefore, Frontiers only applies the most rigorous and unbiased reviews. Frontiers revolutionizes research publishing by freely delivering the most outstanding research, evaluated with no bias from both the academic and social point of view. By applying the most advanced information technologies, Frontiers is catapulting scholarly publishing into a new generation.

What are Frontiers Research Topics?

Frontiers Research Topics are very popular trademarks of the *Frontiers journals series*: they are collections of at least ten articles, all centered on a particular subject. With their unique mix of varied contributions from Original Research to Review Articles, Frontiers Research Topics unify the most influential researchers, the latest key findings and historical advances in a hot research area.

Find out more on how to host your own Frontiers Research Topic or contribute to one as an author by contacting the Frontiers editorial office: frontiersin.org/about/contact

Neural signals acquisition and intelligent analysis

Topic editors
Xiaomin Yang — Sichuan University, China
Yin Tian — Chongqing University of Posts and Telecommunications, China
Gwanggil Jeon — Incheon National University, Republic of Korea
Yu Pang — Chongqing University of Posts and Telecommunications, China

Citation
Yang, X., Tian, Y., Jeon, G., Pang, Y., eds. (2023). *Neural signals acquisition and intelligent analysis*. Lausanne: Frontiers Media SA. doi: 10.3389/978-2-8325-3156-3

Table of contents

04 **Editorial: Neural signals acquisition and intelligent analysis**
Gwanggil Jeon, Xiaomin Yang, Yin Tian and Yu Pang

06 **Frequency set selection for multi-frequency steady-state visual evoked potential-based brain-computer interfaces**
Jing Mu, David B. Grayden, Ying Tan and Denny Oetomo

19 **A multimodal fusion method for Alzheimer's disease based on DCT convolutional sparse representation**
Guo Zhang, Xixi Nie, Bangtao Liu, Hong Yuan, Jin Li, Weiwei Sun and Shixin Huang

33 **Detection of astrocytic slow oscillatory activity and response to seizurogenic compounds using planar microelectrode array**
Taeko Kuroda, Naoki Matsuda, Yuto Ishibashi and Ikuro Suzuki

50 **Empirical comparison of deep learning methods for EEG decoding**
Iago Henrique de Oliveira and Abner Cardoso Rodrigues

62 **Abnormal structural and functional network topological properties associated with left prefrontal, parietal, and occipital cortices significantly predict childhood TBI-related attention deficits: A semi-supervised deep learning study**
Meng Cao, Kai Wu, Jeffery M. Halperin and Xiaobo Li

74 **Epileptic prediction using spatiotemporal information combined with optimal features strategy on EEG**
Lisha Zhong, Jiangzhong Wan, Fangji Yi, Shuling He, Jia Wu, Zhiwei Huang, Yi Lu, Jiazhang Yang and Zhangyong Li

87 **Energy minimization segmentation model based on MRI images**
Xiuxin Wang, Yuling Yang, Ting Wu, Hao Zhu, Jisheng Yu, Jian Tian and Hongzhong Li

98 **Study on characteristic of epileptic multi-electroencephalograph base on Hilbert-Huang transform and brain network dynamics**
Xiaojie Lu, Tingting Wang, Mingquan Ye, Shoufang Huang, Maosheng Wang and Jiqian Zhang

107 **A data security scheme based on EEG characteristics for body area networks**
Tong Bai, Yuhao Jiang, Jiazhang Yang, Jiasai Luo and Ya Du

frontiers | Frontiers in Neuroscience

TYPE Editorial
PUBLISHED 20 July 2023
DOI 10.3389/fnins.2023.1251280

OPEN ACCESS

EDITED AND REVIEWED BY
Michele Giugliano,
International School for Advanced Studies (SISSA), Italy

*CORRESPONDENCE
Gwanggil Jeon
✉ gjeon@inu.ac.kr

RECEIVED 01 July 2023
ACCEPTED 04 July 2023
PUBLISHED 20 July 2023

CITATION
Jeon G, Yang X, Tian Y and Pang Y (2023) Editorial: Neural signals acquisition and intelligent analysis.
Front. Neurosci. 17:1251280.
doi: 10.3389/fnins.2023.1251280

Editorial: Neural signals acquisition and intelligent analysis

Gwanggil Jeon[1]*, Xiaomin Yang[2], Yin Tian[3] and Yu Pang[4]

[1]Department of Embedded Systems Engineering, College of Information Technology, Incheon National University, Incheon, Republic of Korea, [2]College of Electronics and Information Engineering, Sichuan University, Chengdu, China, [3]Department of Biomedical Engineering, Chongqing University of Posts and Telecommunications, Chongqing, China, [4]School of Communication and Information Engineering, Chongqing University of Posts and Telecommunications, Chongqing, China

KEYWORDS

signal, neural network, intelligent system, EEG, medical information

Editorial on the Research Topic
Neural signals acquisition and intelligent analysis

Neural signals include physiological and pathological information, which requires psychological, biological, cognitive neuroscience, and clinical medicine information to efficiently analyze them. So far, it has been possible to record and analyze neural signals using EEG, brain magnetometer, functional magnetic resonance imaging, and computed tomography. On the other hand, artificial intelligence technology is becoming increasingly popular, and a neuroscience technology based on deep learning has recently been announced. This Research Topic aims to apply research on AI-based pattern recognition and signal processing to neuroscience. Interactions between these signal processing fields and the medical field will aid in the diagnosis, monitoring and treatment of neurological disorders. A total of 9 papers were published in this Research Topic.

EEG is used to measure the brain's electrical activity in a non-invasive brain-machine interface. Since the EEG signal is a non-linear and non-static signal, interpretation is difficult, but improved results have been obtained with the development of deep learning technology. In the contribution by de Oliveira and Rodrigues "*Empirical comparison of deep learning methods for EEG decoding*," the authors present two deep learning-based decoder implementations and compare their results with other state-of-the-art deep learning methods. The first method uses LSTM recurrent neural networks, and the second method combines EEGNet with LSTM. The results of this work could be important for new research and development as well as EEG-based BMI systems that can exploit the high precision of neural decoders.

In the contribution by Kuroda et al. "*Detection of astrocytic slow oscillatory activity and response to seizurogenic compounds using planar microelectrode array*," the authors studied the measurement of the spontaneous electrical activity of astrocytes alone using MEA. It was revealed that MEA measurement focused on the low frequency band could be used as one of the methods to evaluate drug response *in vitro*. The authors established nine parameters to evaluate astrocyte activity and evaluated five paroxysmal drug responses in human primary astrocytes and human iPSC-derived astrocytes. Astrocytes showed the most significant dose-dependent changes with pilocarpine. Principal component analysis using these parameter sets isolated the drug response to each seizure-inducing compound.

A multi-frequency steady-state visual evoked potential stimulation and decoding method enables the representation of various visual objects in a brain-computer interface. However, unlike single-frequency SSVEP, multi-frequency SSVEP is difficult to use. One of the main reasons is that it is difficult to define an effective set of frequencies for an interface due to duplication of input options. In the contribution by Mu et al. "*Frequency set selection for multi-frequency steady-state visual evoked potential-based brain-computer* *interfaces*" provides guidelines for frequency set selection in multi-frequency SSVEP. The proposed method showed a significant improvement in BCI performance (decoding accuracy) compared to the existing method. Both hypotheses were verified experimentally.

Medical information represented by MRI and PET has contributed to the development of intelligent diagnosis of Alzheimer's disease and multimodal medical imaging. This improves the existing multi-medical image fusion method based on sparse expression in terms of energy and contrast. In the contribution by Zhang et al. "*A multimodal fusion method for Alzheimer's disease based on DCT convolutional sparse representation*," the authors propose a multimodal convergence algorithm for Alzheimer's disease based on DCT convolutional sparse representation. Extensive experimental results demonstrate that the proposed method has excellent performance in enhancing contrast and maintaining texture and contour information.

Although many studies have been conducted on the characteristics of epileptic electroencephalograms, many studies are still needed. In the contribution by Lu et al. "*Study on characteristic of epileptic multi-electroencephalograph base on Hilbert-Huang transform and brain network dynamics*," a combination method of multi-channel characteristics in time-frequency and spatial domains was studied to study the characteristics of epileptic EEG signals from the perspective of the whole brain. The two contributions of the proposed study are: First, the signal was converted into a 2D Hilbert Spectrum image reflecting time-frequency characteristics through the Hilbert-Huang Transform. Second, multi-channel signals were converted into brain networks reflecting spatial characteristics by Symbolic Transfer Entropy between different EEG channels. When looking at the experimental results, it was found that it is effective in identifying and predicting epileptic seizures.

Traumatic brain injury, one of the major public health problems in children, leads to the development of attention deficit. Existing studies have shown that structural and functional changes in several brain regions are associated with TBI-related attention deficits in children. In the contribution by Cao et al. "*Abnormal structural and functional network topological properties associated with left prefrontal, parietal, and occipital cortices significantly predict childhood TBI-related attention deficits: a semi-supervised deep learning study*," the authors developed a method to provide accurate diagnosis by applying deep learning technology to multidimensional and non-linear information. In addition, a semi-supervised autoencoder, a deep learning model, was constructed to investigate the phase change of both structural and functional brain networks in children with TBI and their predictive power for attention deficit after TBI. As a result of the experiment, the proposed model was able to discriminate children with TBI and control groups with an average accuracy of 82.86%.

Epilepsy is the second most common cranial nerve disease after stroke. Seizure prediction is critical to improving patients' quality of life. In the contribution by Zhong et al. "*Epileptic prediction using spatiotemporal information combined with optimal features strategy on EEG*," the authors constructed an optimal spatiotemporal feature set to predict seizures from multidimensional perspectives including time-frequency, entropy, and brain networks. The proposed method shows strong independence and capacity for large-capacity information, and a two-dimensional feature screening algorithm was performed to remove unnecessary redundant features. As a result of the experiment, the proposed method was able to effectively extract spatiotemporal information of epileptic EEG signals to predict epileptic seizures with high performance.

BAN is a body-oriented network of wireless wearable devices and is a basic technology for telemedicine service. However, when strengthening BAN security, there is an aspect that makes it difficult to improve performance. In the contribution by Bai et al. "*A data security scheme based on EEG characteristics for body area networks*," a data encryption method based on EEG feature values and LFSR is proposed to solve the data security problem in BAN. To this end, first, based on the wavelet packet conversion method, the characteristics of the human brain wave signal are extracted as MD5 input data to ensure randomness, and then the LFSR stream key generator is adopted. The effectiveness of the proposed security technique was verified through various experimental evaluations.

Segmentation technology in medical imaging is a key technology that helps doctors accurately analyze the volume of brain tissue and lesions, and is important for accurate diagnosis of brain diseases. Existing manual methods are time-consuming, subjective, and difficult to reproduce in segmentation. In the contribution by Wang et al. "*Energy minimization segmentation model based on MRI images*," the authors present a method for detecting, characterizing, and quantifying brain tissue and lesions using non-invasive imaging techniques. We also address the effect of multiple sclerosis lesions on the segmentation accuracy of MRI. Experimental verification showed that the proposed AR-FCM algorithm better overcomes the problem of low segmentation accuracy of the RFCM algorithm for tissue border voxels.

Author contributions

GJ, XY, YT, and YP contributed to conception and design of the study. GJ wrote the first draft of the manuscript. All authors contributed to manuscript, read, and approved the submitted version.

Conflict of interest

The authors declare that the research was conducted in the absence of any commercial or financial relationships that could be construed as a potential conflict of interest.

Publisher's note

frontiers | Frontiers in Neuroscience

TYPE Original Research
PUBLISHED 21 December 2022
DOI 10.3389/fnins.2022.1057010

OPEN ACCESS

EDITED BY
Yin Tian,
Chongqing University of Posts and Telecommunications, China

REVIEWED BY
Minpeng Xu,
Tianjin University, China
Ilya Kuzovkin,
OffWorld, Inc., United States

*CORRESPONDENCE
Jing Mu
✉ j.mu@student.unimelb.edu.au

SPECIALTY SECTION
This article was submitted to Neural Technology, a section of the journal Frontiers in Neuroscience

RECEIVED 29 September 2022
ACCEPTED 30 November 2022
PUBLISHED 21 December 2022

CITATION
Mu J, Grayden DB, Tan Y and Oetomo D (2022) Frequency set selection for multi-frequency steady-state visual evoked potential-based brain-computer interfaces.
Front. Neurosci. 16:1057010.
doi: 10.3389/fnins.2022.1057010

Frequency set selection for multi-frequency steady-state visual evoked potential-based brain-computer interfaces

Jing Mu[1]*, David B. Grayden[2,3], Ying Tan[1,3] and Denny Oetomo[1,3]

[1]Department of Mechanical Engineering, The University of Melbourne, Parkville, VIC, Australia,
[2]Department of Biomedical Engineering, The University of Melbourne, Parkville, VIC, Australia,
[3]Graeme Clark Institute for Biomedical Engineering, The University of Melbourne, Parkville, VIC, Australia

Objective: Multi-frequency steady-state visual evoked potential (SSVEP) stimulation and decoding methods enable the representation of a large number of visual targets in brain-computer interfaces (BCIs). However, unlike traditional single-frequency SSVEP, multi-frequency SSVEP is not yet widely used. One of the key reasons is that the redundancy in the input options requires an additional selection process to define an effective set of frequencies for the interface. This study investigates systematic frequency set selection methods.

Methods: An optimization strategy based on the analysis of the frequency components in the resulting multi-frequency SSVEP is proposed, investigated and compared to existing methods, which are constructed based on the analysis of the stimulation (input) signals. We hypothesized that minimizing the occurrence of common sums in the multi-frequency SSVEP improves the performance of the interface, and that selection by pairs further increases the accuracy compared to selection by frequencies. An experiment with 12 participants was conducted to validate the hypotheses.

Results: Our results demonstrated a statistically significant improvement in decoding accuracy with the proposed optimization strategy based on multi-frequency SSVEP features compared to conventional techniques. Both hypotheses were validated by the experiments.

Conclusion: Performing selection by pairs and minimizing the number of common sums in selection by pairs are effective ways to select suitable frequency sets that improve multi-frequency SSVEP-based BCI accuracies.

Significance: This study provides guidance on frequency set selection in multi-frequency SSVEP. The proposed method in this study shows significant improvement in BCI performance (decoding accuracy) compared to existing methods in the literature.

KEYWORDS

brain-computer interface (BCI), brain-machine interface (BMI), electroencephalography (EEG), dual-frequency, multi-frequency, optimization, steady-state visual evoked potential (SSVEP)

1. Introduction

A steady-state visual evoked potential (SSVEP) is brain activity that frequency-locks to periodic visual stimulation (Zander et al., 2009). SSVEP is widely used in brain-computer interfaces (BCIs) due to its relatively high accuracy and information transfer rate as well as minimal training required of users compared to other modalities, such as motor imagery (Nicolas-Alonso and Gomez-Gil, 2012).

A standard SSVEP-based BCI includes multiple stimuli in the workspace that each flashes at a different frequency while electroencephalography (EEG) is measured primarily from the occipital lobe. The measured EEG reflects the frequency of the stimulus the user is focusing upon visually, as well as the harmonics of that frequency. The presence of the harmonics provides more reference points in the decoding process, but also presents additional complexities and challenges in the design of SSVEP-based BCIs. For example, if a frequency and its harmonic are both used in the same BCI for two different stimuli, there will be common frequencies in the recorded EEG from the two stimuli, which may confound the decoding algorithm. Therefore, in the literature, some studies intentionally avoided the use of frequencies with common harmonics in the stimulation (Volosyak et al., 2009; Chen et al., 2015). This harmonic issue, together with the limited responsive frequency range of the human brain to periodic visual stimulation (Regan, 1989), constrains the number of unique frequencies that can be used in standard SSVEP-based BCIs; i.e., low signal-to-noise ratio EEG recordings and small frequency separation impairs decoding performance. Therefore, it is challenging to use standard SSVEP-based BCIs in scenarios that require large numbers of unique frequencies to label all the targets.

To address this problem, multi-frequency stimulation methods utilizing more than one frequency in each stimulus have been introduced, with two frequencies (dual-frequency) being the most widely used modality (Shyu et al., 2010; Zhang et al., 2012; Chen et al., 2013; Hwang et al., 2013; Kimura et al., 2013; Chang et al., 2014; Mu et al., 2021a). However, these studies focused primarily on introducing multi-frequency stimulation methods, and did not explore frequency selection methods. The use of multiple frequencies on each stimulus or targets can exponentially increase the number of targets that can be represented in the work space as the number of frequencies used to label each target increases. Multi-frequency stimulation generates a complex periodic stimulation signal that triggers a more complex SSVEP response. In Mu et al. (2021a), it was demonstrated that multi-frequency SSVEP response contained not only the input frequencies and their harmonics, but also the integer linear combinations of the input frequencies with low order interactions more likely to be observed in the recorded SSVEP. Note that the order of interaction was defined as the sum of absolute values of the coefficients in the linear combination (Mu et al., 2021a). A dedicated decoding algorithm, multi-frequency canonical correlation analysis (MFCCA), was also introduced to decode complex multi-frequency SSVEP, leveraging the linear combinations produced by the frequency interactions (Mu et al., 2021b). A 20% increase in accuracy was observed when linear combinations of frequencies were utilized to capture the interactions between the input frequencies in the decoding algorithm; however, the study did not investigate whether this information could be used in frequency selection to further improve the performance of the multi-frequency SSVEP-based BCI.

While multi-frequency SSVEP can provide a large number of inputs for the interface, there is a need to select the most effective set of input frequencies to construct a high-performing BCI. In traditional single-frequency SSVEP, frequency selection is usually done following very simple rules: avoid harmonics in the same set (Volosyak et al., 2009), as mentioned above, and avoid small frequency intervals. In studies with a relatively large number of targets (40 targets) by Chen et al. (2015), Wang et al. (2016), and Liu et al. (2020), stimulation frequencies were equidistantly selected in a range (8–15.8 Hz with 0.2 Hz intervals) that avoided the existence of harmonics in the same range. Another common way to select frequencies in constructing an SSVEP-based BCI is based on the refresh rate of the screen (refresh rate divided by integer numbers; Bakardjian et al., 2010; Zhu et al., 2010; Hwang et al., 2013). In dual-frequency SSVEP, this problem was explored by minimizing the maximum input (stimulation) signal correlation (Liang et al., 2020). Although this optimization method demonstrated its advantage in improving the accuracy of the interface, only the optimization of input signals was investigated. Since multi-frequency SSVEP response shows more complex frequency interactions between the multiple frequencies used in the stimulation, optimization that takes into account such frequency interactions at the output signals may outperform techniques that only take into account the stimulation signals.

This work built upon Liang et al. (2020) and investigated whether optimizing on a known multi-frequency SSVEP feature would result in different performance in the multi-frequency SSVEP-based BCI. In this paper, the dual-frequency SSVEP is considered as a special case of multi-frequency SSVEP. Under such a setting, an optimization strategy based on not only the input frequencies, but also their harmonics and the integer linear combinations of the input frequencies, is proposed and tested. The number of frequencies used in constructing the targets, i.e., whether to select frequencies to make all the pairs or to select pairs directly from the range without any constraint, is also considered along with the output-based optimization. This work contributes toward the framework of increasing the number of commands in "BCI as a processor," where command processing capacity is a key (Xu et al., 2021).

2. Materials and methods

2.1. Definitions

To avoid confusion, some terms used in this paper are defined below.

Selection by frequencies

A frequency selection approach where the minimum number of frequencies in the given range are selected to construct the required number of targets.

Selection by pairs

Select the required number of pairs directly from the given frequency range (from all the possible pairs made by the frequencies within the range). Selection by pairs provides more freedom in frequency selection as opposed to selection by frequencies. Selection by pairs ignores additional constraints the system may have, for example, limited number of frequencies that can be produced by the hardware, in which case selection by frequencies would be preferred.

Frequency pair

In a dual-frequency application, the frequency pair refers to the two stimulation frequencies used to represent one target.

Frequency set

The set of all frequency pairs used in the interface.

Common sums

The common frequencies resulted from the integer linear combinations of different pairs of frequencies, where at least one of the coefficients is not zero. The number of common sums refers to the counted number of common sums between the frequency pairs in the frequency set [bounded by order, where order is the sum of absolute values of the coefficients in the linear combination (Mu et al., 2021b)].

Optimization strategy

In this paper, optimization strategy refers to the optimization problem formulations, which includes the cost function and the parameters to tune.

The following example is provided to help illustrate use of the terms. Given a 6-target setup and five frequencies to select from, selection by frequencies selects four frequencies out of the five because it needs at least four frequencies to make six targets with dual-frequency stimulation ($C_2^4 = 6$). For example, the five frequencies are 5, 6, 7, 8, and 9 Hz. The frequencies 5, 6, 7, and 9 Hz are selected from selection by frequencies, so the resulting frequency set will be {(5, 6), (5, 7), (5, 9), (6, 7), (6, 9), (7, 9)}, where each parenthesis includes one frequency pair; for example, (5, 6). On the other hand, selection by pairs selects 6 pairs from the $C_2^5 = 10$ total pairs of frequencies available. An example of the selected frequency set from selection by pairs could be {(5, 6), (5, 8), (5, 9), (6, 7), (6, 8), (8, 9)}.

TABLE 1 Integer linear combinations up to order 2 in frequency set {(5, 7), (7, 9)}.

Operation		f_1	f_2	$2 \times f_1$	$2 \times f_1$	$f_1 + f_2$	$\|f_1 - f_2$
Frequency pairs	(5, 7)	5	7	10	14	12	2
(f_1, f_2)	(7, 9)	7	9	14	18	16	2

Common sums can be found among the frequency pairs, for example between {(5, 7), (7, 9)}. Table 1 lists all the linear combinations (up to order 2) from the 2 frequency pairs. We can see from the table that there are three frequencies that are common to the two pairs (the common sums): 7, 14, and 2. Therefore, the number of common sums in the frequency set {(5, 7), (7, 9)} is 3. Note: the term "order" refers to the sum of the absolute values of the coefficients in the linear combination.

2.2. Hypotheses on frequency set selections

In multi-frequency SSVEP, the resulting brain response shows not only the input frequencies and their harmonics, but also the interactions between the input frequencies, in the form of the integer linear combinations of the input frequencies (Mu et al., 2021a). These peak occurrences in the SSVEP response increase the chances of the common sums as described above. Common sums are significant as they introduce ambiguity as to which frequency pair produces an identified SSVEP peak during decoding. Hence, we expect to see an increase in decoding accuracy when the number of common sums in the multi-frequency SSVEP is reduced. It is also worth noting that, in some SSVEP-based BCI setups, there are additional constraints, such as a limited number of frequencies that can be produced by the hardware. Therefore, we also consider the case where only the minimum number of frequencies needed for constructing all the targets can be selected (selection by frequencies). Selection by frequencies has more constraints compared to selection by pairs, so a less optimal result was expected, whereas the result from selection by pairs is anticipated to be closer to optimal. Therefore, in this work, two hypotheses on frequency set selection in dual-frequency SSVEP are tested:

Hypothesis 1. The performance (accuracy) of the multi-frequency SSVEP-based BCI will be improved when the number of

TABLE 2 Frequency set selection methods and the hypotheses.

	Not minimizing the number of common sums	Minimize the number of common sums	Maximize the number of common sums
Selection by frequencies	Method 1	Method 2	
Selection by pairs	Method 5	Method 3	Method 4

common sums is minimized in the selected frequency set.

Hypothesis 2. In frequency set selection in multi-frequency SSVEP-based BCIs, selection by pairs results in better performance than selection by frequencies.

In order to test the two hypotheses, four cases are considered:

1. Selection by frequencies without minimizing the number of common sums;
2. Selection by frequencies by minimizing the number of common sums;
3. Selection by pairs without minimizing the number of common sums;
4. Selection by pairs by minimizing the number of common sums.

We have added a fifth case to the list — selection by pairs by maximizing the number of common sums — to examine the efficiency of optimizing on the number of common sums.

2.3. Frequency set selection methods

In this work, a frequency range of 11–16 Hz and a 15-target arrangement were used. Single-frequency SSVEP was tested as a benchmark.

The test range 11–16 Hz was selected because it is within the most responsive range of SSVEP (5–25 Hz; Regan, 1989), large enough to test a couple of scenarios but keeping the experiment duration manageable and optimization not too computationally heavy.

2.3.1. Single-frequency

The frequencies selected was evenly spaced within the range with a varying 0.3 or 0.4 Hz interval between the frequencies: [11.3, 11.7, 12.0, 12.3, 12.7, 13.0, . . . , 15.7, 16.0].

2.3.2. Dual-frequency

The entire dual-frequency set selection is based heavily on the two hypotheses, which made the five cases for us to consider. Therefore, we decided upon five methods in frequency set selection. Table 2 illustrates the relationship between these five methods and the two hypotheses. Details about the five methods will be provided later in this section.

The decision tree method was selected for optimization because it produces a similar result to the global search method and is fast to calculate (Liang et al., 2020). In the decision tree method, two matrices are first constructed. A matrix **A** is constructed of size $N \times N$, where N is the total number of pairs available, and the value in each cell is the optimization parameter between the two pairs whose indices are the row and column indices. In our case, this is the number of common sums between the two pairs. The other matrix is **B** that is initialized to be a zero matrix of the same size as **A**. In each optimization iteration, the minimum (or maximum, if maximizing) value in **A** is first identified, then the value in this cell is updated to a large (or small) value to avoid being selected in the following iterations, and the value in the corresponding location in **B** is set to 1 (or any non-zero value). The **B** matrix then goes through a check to see if there exists a reduced **B** matrix, $\mathbf{B}'$, of size N_T that has all elements non-zero. If there exists a $\mathbf{B}'$ matrix that does not contain any zero elements, then the optimization is done and the resultant frequency set is made up of the frequency pairs whose indices are the selected rows and columns in the **B** to $\mathbf{B}'$ reduction. Otherwise, continue to the next iteration.

The number of common sums is calculated as the number of times the linear combination frequencies are repeated in the frequency set between the pairs up to a given order. In other words, the number of common sums is the number of times a frequency is repeated in the list of integer linear combinations of all the pairs in the frequency set up to a given order, and only the between-pairs repetitions are counted, any repetitions within a pair is ignored.

Since we are using a 15-target setup, six frequencies should be selected when selecting frequencies ($C_2^6 = 15$) and 15 pairs of frequencies should be selected when selecting pairs. To ensure there are sufficient numbers of frequencies to select from and not to over-complicate this problem, the frequency candidates were designed to be 0.5 Hz apart within the range 11–16 Hz; i.e., [11.0, 11.5, 12.0, 12.5, 13.0, 13.5, 14.0, 14.5, 15.0, 15.5, 16.0].

The methods used in this study are listed below:

Method 1: Selection by frequencies with evenly spaced frequency interval. Thus no effort was made to

minimize the number of common sum.
Frequencies are selected from the full range with even intervals (on the six integers).

Method 2: Selection by frequencies with unevenly spaced frequency interval, which was designed to enable the minimization of the number of common sum.
Frequencies are selected from the range with minimized number of common sums. The number of common sums is first checked at order 2, the pairs with the smallest number of common sums are then checked at order 3, etc. We bounded this process to check up to order 5.

Method 3: Selection by pairs with decision tree method (Liang et al., 2020) optimizing (minimizing) the number of common sums between the pairs.
Frequency pairs are selected from all possible pairs made by the frequency candidates with minimized number of common sums using decision tree. The common sums are calculated up to order 5.

Method 4: Selection by pairs with decision tree method maximizing the number of common sums between the pairs.
Frequency pairs are selected from all possible pairs made by the frequency candidates to maximize the occurrences of common sums using decision tree. The common sums are calculated up to order 5.

Method 5: Selection by pairs with decision tree method minimizing the maximum correlation between the input signals constructed with the pairs (Liang et al., 2020).
Frequency pairs are selected from all possible pairs made by the frequency candidates with minimized maximum correlations between the input signals using decision tree.

The resulting frequency sets and the their numbers of common sums are listed in Table 3.

2.4. Experimental setup

In the experiments, participants sat 70 cm away from a computer screen where the stimuli were shown. Participants were positioned to be centered to the screen and height adjusted to a comfortable level. All experiments were done in a dim, quiet room.

2.4.1. Stimulation methods

Visual stimulation was delivered through an Alienware monitor AW2518HF (24.5 inch, 1920 × 1080) running Unity programmed interface at 120 Hz. White color was used for all stimuli. The size of each stimulus was 108 × 108 pixels; the distance between adjacent stimuli was 108 pixels both horizontally and vertically. The 15 targets followed a 3 by 5 layout on the screen as shown in Figure 1.

Single-frequency stimulation was performed by presenting 50% duty cycle square waves on the screen at full brightness. All signals commenced with zero phase shift.

In this work, we have chosen frequency superposition (Mu et al., 2021a) as the multi-frequency stimulation method for its simplicity. Multi-frequency SSVEP stimulated with frequency superposition contains not only the input frequencies and their harmonics, but also the integer linear combinations of the input frequencies, with lower order interactions are more likely to be observed (Mu et al., 2021a,b). Considering the use of input frequencies with narrow frequency gaps (0.5 Hz), ADD logic with equal brightness distribution was selected for superimposing the input frequencies; i.e., in the dual-frequency case, the two input frequencies each correspond to half of the full brightness and the superimposed signal becomes the stimulation signal. Square waves at 50% duty cycle and zero phase shift were used in frequency superposition in this work.

2.4.2. Data acquisition

EEG data was recorded with g.USBamp EEG system and g.SAHARA dry electrodes (g.tec medical engineering GmbH, Austria). The recorded EEG signals were sampled at 512 Hz, with 50 Hz notch and $0.5 - 100$ Hz band pass filters on all channels. A 16-channel measurement was taken (P3, Pz, P4, PO3, POz, PO4, O1, Oz, O2, Fz, FCz, FC1, FC2, Cz, C1, and C2); however, only the first nine channels were used for SSVEP processing as these are closest to the visual cortex. Reference and ground electrodes were placed at the left and right mastoids, respectively.

2.4.3. Participants

Fifteen participants participated in the frequency selection experiment; however, three of them did not complete the experiment due to extremely low accuracy experienced in the experiment (on average below three out of 15 trials correct, which makes chance a factor that heavily affected the results). Therefore, data from 12 participants (nine males, three females) aged 22–34 years (28.08 ± 3.70) were included in the analysis.

The experiments were approved by the University of Melbourne Human Research Ethics Committee (Ethics ID: 1851283). Written consent was collected from all participants prior to the experiment.

TABLE 3 Frequency sets obtained from optimization and their corresponding number of common sums.

Method	Frequencies/frequency pairs						Number of common sums
Selection by frequencies							
1	11.0	12.0	13.0	14.0	15.0	16.0	355
2	11.0	12.0	12.5	14.5	15.5	16.0	282
Selection by pairs							
3	(11.0, 14.5)	(11.5, 14.0)	(11.5, 15.0)	(12.0, 14.5)	(12.0, 15.5)		285
	(12.5, 15.0)	(12.5, 16.0)	(13.0, 15.5)	(11.5, 15.5)	(12.0, 16.0)		
	(13.5, 16.0)	(11.0, 11.5)	(11.0, 15.5)	(11.5, 16.0)	(15.5, 16.0)		
4	(11.0, 11.5)	(11.0, 12.5)	(11.0, 13.0)	(11.0, 13.5)	(11.5, 13.0)		311
	(12.0, 12.5)	(12.0, 13.0)	(12.5, 15.0)	(13.5, 16.0)	(14.0, 15.5)		
	(14.0, 16.0)	(14.5, 15.0)	(14.5, 16.0)	(15.0, 15.5)	(15.5, 16.0)		
5	(11.5, 13.5)	(11.5, 15.5)	(11.5, 12.0)	(11.5, 14.5)	(13.5, 14.5)		301
	(14.5, 15.0)	(14.5, 16.0)	(15.5, 16.0)	(11.5, 15.0)	(12.5, 14.5)		
	(12.5, 13.5)	(12.5, 16.0)	(13.5, 16.0)	(11.0, 11.5)	(13.5, 14.0)		

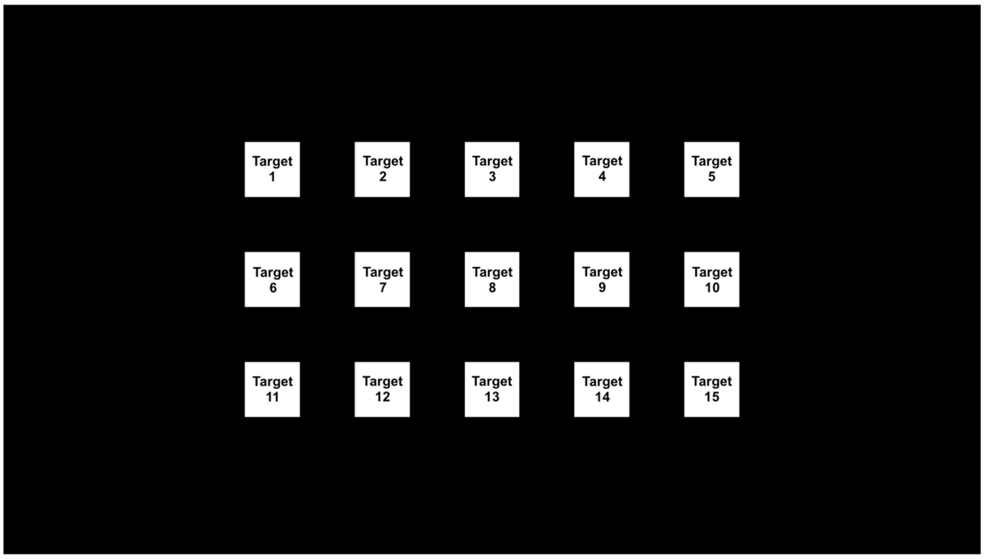

FIGURE 1
Stimuli layout on the screen.

2.5. Experimental protocols

The experiment contained four sessions with each session having six tests that evaluated the six stimulation frequency setups (five dual-frequency and one single-frequency) once each. Each test had 15 trials (15 targets, one trial per target). Each trial started with a 1 s cue (green outline at intended target, Figure 2A), followed by 5 s stimulation (with a fixation cross at the center of the intended target, Figure 2B, all targets are flashing during this stimulation period), then 1 s feedback (solid green or red square for successful or erroneous identification, respectively, Figures 2C, D), and 1 s rest. A score was shown to the participant after each completed test indicating the number of correct trials for the test (Figure 2E) with 0 indicating none of the 15 trials was identified correctly and 15 indicating all trials were correctly identified. 1 min breaks were provided after each test, 5–10 min breaks were placed between the sessions. The length of breaks were adjusted to the participant's need.

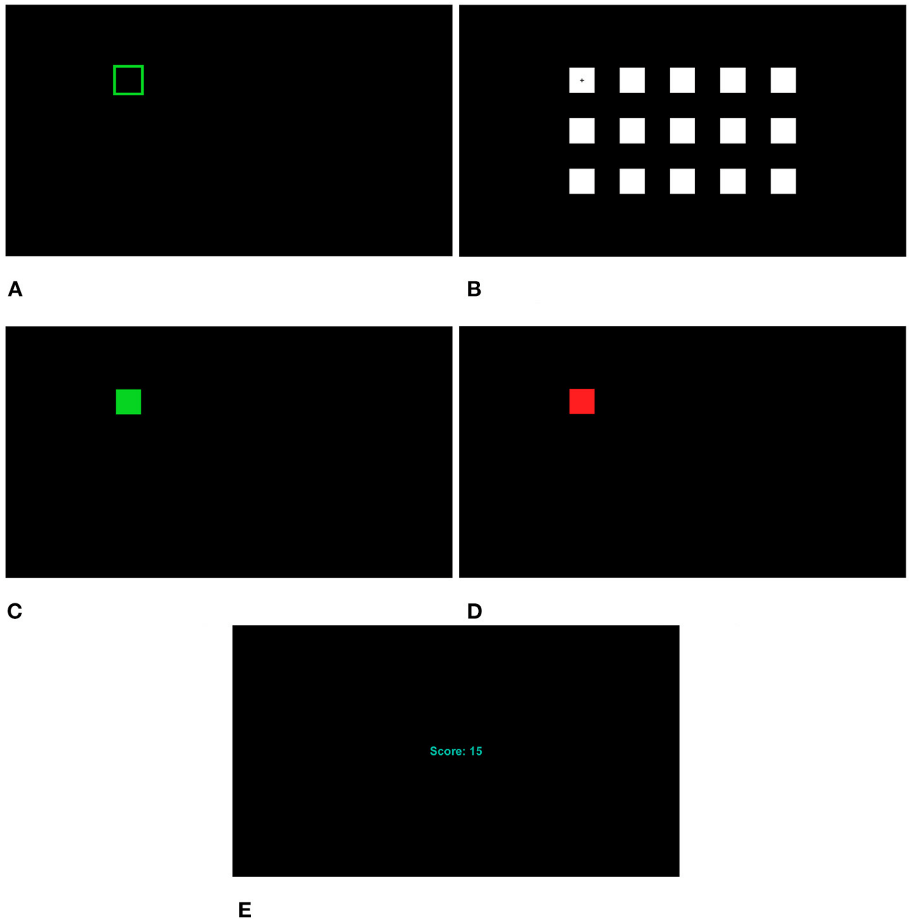

FIGURE 2
Interface at different stages. **(A)** Cue. **(B)** Fixation cross. All targets are flashing during stimulation. **(C)** Feedback (correct). **(D)** Feedback (incorrect). **(E)** Score.

In each test, the participant was asked to go through each of the 15 targets one-by-one following the cue. To simplify the participant's task, in each test, the trial sequence was always from left-to-right, top-to-bottom, going through the targets in target index ascending order (Figure 1). However, the stimulation frequencies or frequency pairs were randomly shuffled among the 15 targets.

To ensure the experimental results were not affected by user fatigue, Sudokus were used to generate randomized yet balanced test sequences. With six setups to test in this experiment, 6-by-6 Sudokus in brickwall style, as shown in Figure 3, were used. Numbers 1–5 in the Sudoku match to methods 1–5 in dual-frequency selections, and 6 matches to the single-frequency setup. These six different setups will be henceforth referred to as test 1, 2, . . . , 6.

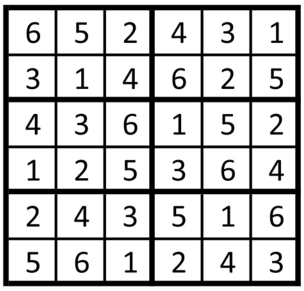

6	5	2	4	3	1
3	1	4	6	2	5
4	3	6	1	5	2
1	2	5	3	6	4
2	4	3	5	1	6
5	6	1	2	4	3

FIGURE 3
Example of a 6-by-6 Sudoku in brickwall style.

The experiments were arranged so that each participant used one row in each Sudoku and each session had a different Sudoku. Therefore, with four sessions in the experiment, at least four Sudokus were needed. In order to accommodate 12 participants, eight Sudokus were used in total in this experiment to make 12 rows for the 12 participants.

Participants were trained with up to two sessions with six tests (one test per setup) in each session in a random sequence before the experiment.

2.6. Data processing

During the experiments, 5 s of data was used for decoding to produce feedback to the participants. Canonical correlation analysis (CCA; Lin et al., 2006) with number of harmonics set to 3 was used in single-frequency SSVEP decoding. Multi-frequency canonical correlation analysis (MFCCA; Mu et al., 2021b) with order set to 1 was used in dual-frequency SSVEP decoding. The frequency candidate that gave the highest correlation was taken as the decoder output.

Information Transfer Rate (ITR) is often reported in SSVEP experiment results, defined as

$$ITR = \frac{60}{T}\left[\log_2 N + p\log_2 p + (1-p)\log_2\left(\frac{1-p}{N-1}\right)\right](bits/min), \tag{1}$$

where T is the time window (seconds) for a trial or time needed to produce one result, N is the number of targets or possible choices ($N \in \mathbb{Z}, N \geq 2$), p is the mean accuracy ($p \in (0,1)$); (Wolpaw et al., 2000). In this work, since a consistent setting (15 targets; trials consisted of 1 s cue, 5 s stimulation, 1 s feedback, and 1 s break) was used throughout both experiments, ITR is a static conversion from accuracy and so conveys equivalent information. Therefore, results are mainly shown in terms of accuracy.

3. Results

The average dual-frequency SSVEPs recorded in test 1 were plotted in both time domain and frequency-domain as shown in Figures 4, 5. The plots shown in the figures are averaged across all participants and all sessions. Figure 4 shows the first second (starting from stimulation onset) of the averaged filtered SSVEP (blue) in comparison to the waveform of the stimulation signal (orange). The SSVEPs recorded from channel Oz were bandpass filtered between 9 and 18 Hz using MATLAB function “bandpass” with “ImpulseResponse” set to “auto,” 0.85 “Steepness,” and 60 dB “StopbandAttenuation,” then averaged across all participants and all sessions. Figure 5 plots the averaged SSVEP recorded from channel Oz in frequency domain. The crosses label the two stimulation frequencies and their harmonics, circles label the linear interactions (integer linear combinations) of the two frequencies. The harmonics and linear interactions at different orders N_O (sum of absolute values of the coefficients in the integer linear combination Mu et al., 2021b) are labeled with different colors as explained in the figure caption.

Figure 6 plots the average accuracies and standard errors for the frequency set selection experiment. The yellow dots in the figure give the average accuracies for each subject. Tests 1–5 are dual-frequency methods with tests 1 and 2 implementing selection by frequencies and tests 3–5 implementing selection by pairs, and test 6 is single-frequency. Figure 6 shows that dual-frequency setups have similar accuracies, except test 3, where the number of common sums is minimized in selection by pairs. All dual-frequency tests (tests 1–5) showed a lower average accuracy compared to the single-frequency test (test 6).

Three-factor analyses of variance (ANOVAs) were performed using data from tests 1–5 with factors subject, test, and session, and the data was fitted using a linear mixed model. The normality of data was confirmed with box plots. Tukey correction was applied to correct for multiple comparisons in the family of five estimates (tests 1–5). Significant differences (adjusted p-value $p_{adj} < 0.05$) were found between tests 2 and 3 ($p_{adj} = 0.02$), and between tests 3 and 5 ($p_{adj} = 0.019$), as labeled in the figure with *.

Table 4 lists the ITR from the six tests calculated based on 8s trial duration and 15 targets. Note that the focus of this work is not to increase ITR, but rather to explore and compare different frequency set selection methods in multi-frequency SSVEP.

3.1. Effectiveness of minimizing the number of common sums

Our first hypothesis was that minimizing the number of common sums in the frequency set can improve performance. Here, we will check the effectiveness of minimizing the number of common sums in both selection by frequencies and selection by pairs cases.

3.1.1. Selection by frequencies: Even vs. uneven frequency interval

As described in Section 2.3.2, both Method 1 (selection by frequencies with even frequency intervals) and Method 2 (selection by pairs with minimized number of common sums) were on selection by frequencies; Method 1 uses an even frequency interval of 1 Hz and Method 2 selects the same number of frequencies in the range with 0.5 Hz frequency interval, which naturally gives uneven frequency intervals in the selected frequency list. Since Method 1 selects frequencies evenly in the full frequency range, there is no possibility of optimization in Method 1. Method 2 selects frequencies from all candidates using optimization (minimization) on the number of common sums. From Figure 6, we can see that Method 1 did not have a significantly different accuracy to Method 2 ($p_{adj} = 0.98$). However, there are actually two factors that contribute to this result: one is the optimization on the number of common sums, the other is the frequency interval in the selected frequencies. To make a comparison between even and uneven frequency selection in the same frequency range, it is unavoidable to have

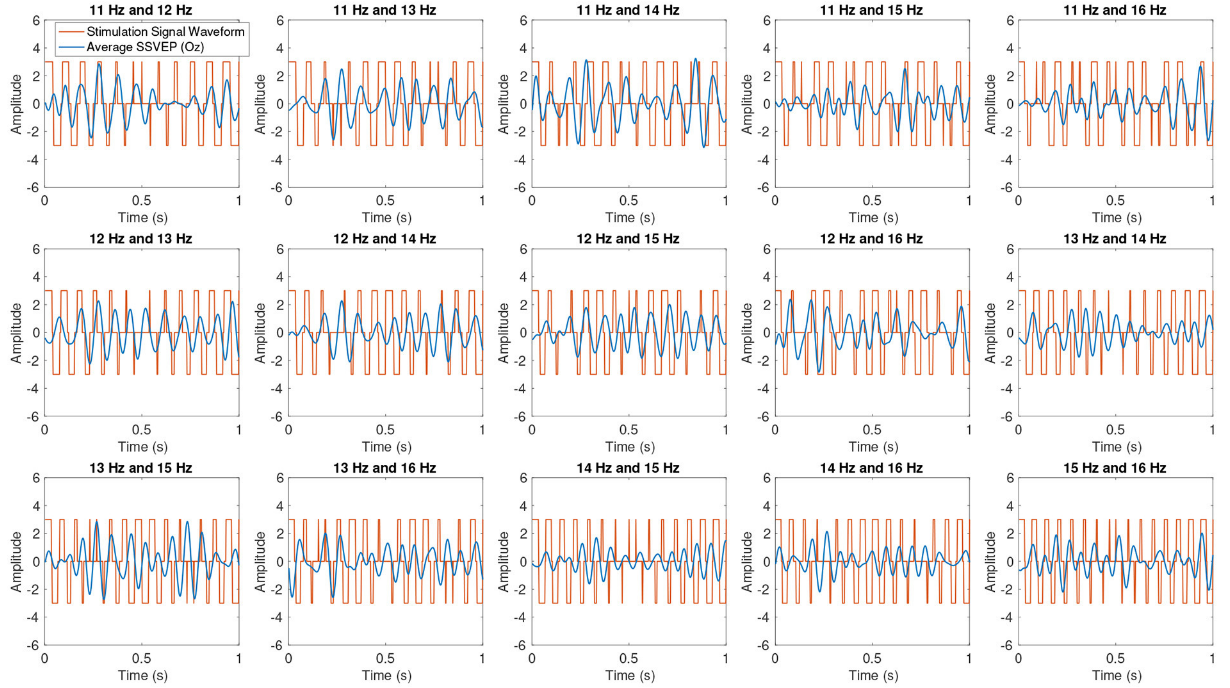

FIGURE 4

Average SSVEP from Test 1 in time domain. Blue lines plot the average SSVEPs from channel Oz after bandpass filtered between 9 and 18 Hz. Orange lines show the waveforms of the dual-frequency stimulation signals.

different frequency intervals in the two frequency sets. The uneven frequency interval, while it minimizes the number of common sums, may result in some intervals that are narrower than that employed in the evenly spaced frequency selection method (Method 1). Therefore, the potential advantage of the optimization may be reduced by the smaller frequency interval.

3.1.2. Selection by pairs: Effectiveness of minimizing the number of common sums compared to minimizing maximum correlation

In all selection by pairs methods (Methods 3–5), a consistent 0.5 Hz frequency interval was used. Therefore, the comparison here potentially reflects the effectiveness of minimizing the number of common sums better.

Methods 3 and 5 are based on different optimization strategies: Method 3 optimizes (minimizes) on the number of common sums while Method 5 optimizes (minimizes) on the maximum correlation between input stimulation signals. Hence, a comparison between Methods 3 and 5 demonstrates the effectiveness of minimizing the number of common sums. It can be seen in Figure 6 that the accuracy of Method 3 was significantly ($p_{adj} = 0.019$) higher than Method 5 by about 10%. This shows that minimizing the number of common sums is an effective optimization strategy in selecting frequency sets with selection by pairs, at least in dual-frequency SSVEP using frequency superposition with ADD, where the two single-frequency square-wave signals each corresponds to half brightness are superimposed on the target.

While both Methods 3 and 5 use decision trees to perform selection by pairs, the fundamental difference between these two optimization strategies is the parameter that is being optimized. Method 3 optimizes (minimizes) the number of common sums, focusing on the frequency domain characteristics of the input/stimulation signals. Method 5 minimizes the maximum correlation between input (stimulation) signals, focusing on the time domain characterization of the expected SSVEP response elicited by the multi-frequency stimulations. Since the brain is a highly non-linear system, optimizing the system output (EEG signals) might further reduce the confusion in the decoding process, hence the difference.

3.2. Selection by frequency vs. selection by pairs with number of common sum minimized frequency selection

The second hypothesis was that selection by pairs results in better performance than selection by frequencies. Here, we compare Methods 2 and 3 as both were optimized (minimized)

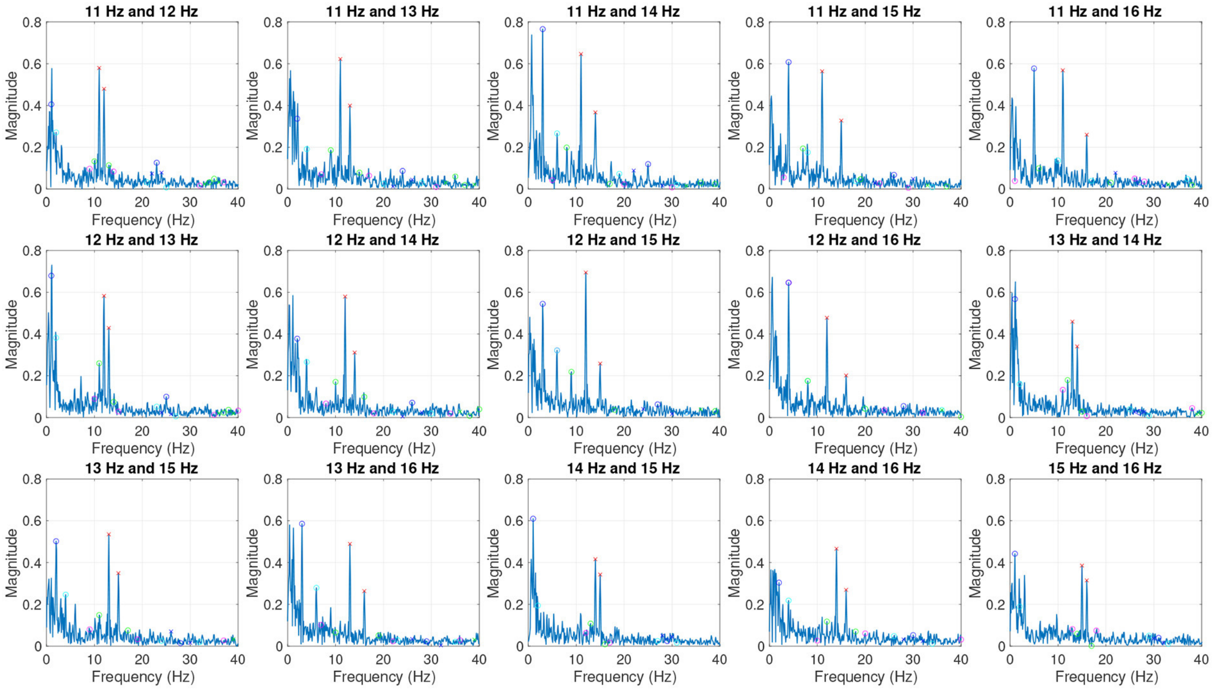

FIGURE 5
Average SSVEP from Test 1 in frequency domain. Red crosses label the two stimulation frequencies. Crosses and circles indicate harmonics and linear combinations of the two frequencies, respectively. Orders N_O are shown with different colors: red−$N_O = 1$; blue−$N_O = 2$; green−$N_O = 3$; cyan−$N_O = 4$; magenta−$N_O = 5$.

on the number of common sums and used 0.5 Hz frequency intervals.

The result from Figure 6 shows that Method 3 had a significantly ($p_{adj} = 0.02$) higher average accuracy compared to Method 2. This showed that, when we have the freedom to select pairs freely in the whole range of frequencies, we could achieve higher accuracy in the interface compared to when we were constrained on the number of frequencies that could be selected. This difference might be amplified when there are larger numbers of frequencies in the candidate set, more frequencies superimposed on the same target, and/or numbers of targets (N_T) increase, because the number of frequency pairs we can select from (N_F) and the number of possible frequency sets becomes larger as shown in Equations 2, 3.

$$N_{F,\text{pair}} = C_N^{N_F}, \tag{2}$$

$$N_{F,\text{set}} = C_{N_T}^{N_{F,\text{pair}}}, \tag{3}$$

where $N_{F,\text{pair}}$ is the total number of possible frequency pairs, $N_{F,\text{set}}$ is the total number of possible frequency sets, N is the number of frequencies superimposed on each target.

3.3. Efficiency of number of common sum minimization

Methods 3 and 4 are explicitly designed to test the efficiency of number of common sum minimization; Method 3 minimizes the number of common sum and Method 4 maximizes the number of common sum. The result from Figure 6 showed an insignificant difference between the average accuracy of the two tests after adjustment for multiple comparisons ($p_{adj} = 0.21$), which is unexpected. This will be discussed in Discussion section.

4. Discussion

4.1. Efficiency of number of common sum minimization

It is interesting to see that Methods 3 and 4 were not significantly different, and Method 4 resulted in a higher average accuracy compared to Method 5. We believe this was because the decision tree method is not the most suited for finding optimal frequency sets based on the number of common sums due to the integer nature of these numbers, which are the number of times the common sums are observed. As a performance measure in an optimization, this metric does not provide very high resolution as it does not entertain fractions and decimals, which are applied to Methods 3 and 4. Method 5, while also utilizing the decision tree mechanism, uses the correlation between input signals as its performance measure in the optimization. This allows a high degree of resolution, as decimals are allowed, providing better outcome of the optimization process. As such, Method 3 and Method 4 do not perform optimally. Table 3 reveals this issue to some extent, where it can be seen that, toward the end, Methods 3 and 4 arrived at the same frequency pair (15.5, 16) after the optimization process even though they were designed to be doing completely opposite tasks.

Method 3 is designed with what we expected to be minimum number of common sums. As it was not optimal, the accuracy was expected to be an underestimate of its potential. However, compared to Method 5, it still yields significantly higher accuracy. Method 4 is designed to maximize the number of common sums. This was expected to yield the lowest accuracy among Methods 3, 4, and 5. As it is not optimal, the resulting accuracy was higher than what was expected.

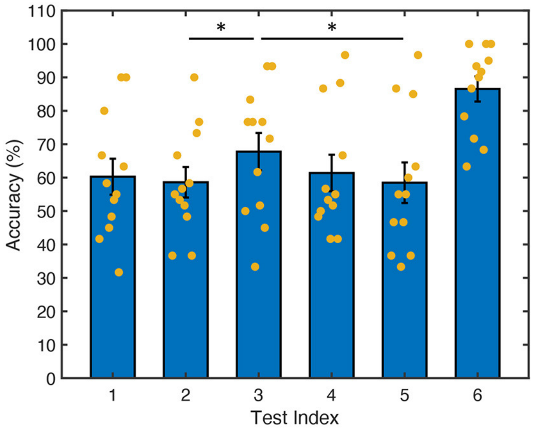

FIGURE 6
Accuracy from the six tests in frequency set selection experiment. Heights of the bars represent the mean accuracy, error bars show standard error of the average accuracies from 12 participants, and yellow dots label the average accuracy from each participant. * Indicates significant difference ($p < 0.05$, corrected) pair-wise between each two tests with ANOVA. Test 1: dual-frequency method 1; test 2: dual-frequency method 2; test 3: dual-frequency method 3; test 4: dual-frequency method 4; test 5: dual-frequency method 5; test 6: single-frequency.

4.2. General SSVEP performance

In terms of time-domain waveform, in Figure 4, we can see that some SSVEP waveforms are highly consistent with the stimulation waveform (e.g., 11 and 12 Hz), whereas some other waveforms are more complex. This is likely because the human brain is a highly nonlinear system that produces complex response to even simple single-frequency stimulation. For the plots that show SSVEPs stimulated by dual-frequency signals, it is expected that there will be more frequency components (interactions between the two input frequencies) in the EEG signal. Thus, when some frequency interactions are dominating the response, the SSVEP waveform may look different to the stimulation waveform.

While the focus of this study was not on boosting the SSVEP performance, we are aware of the difference in performance from our results compared to some studies in the literature for both dual-frequency SSVEP (Liang et al., 2020) and single-frequency SSVEP (Chen et al., 2015). One source of the difference might be attributed to the use of dry electrodes in our study as opposed to wet electrodes commonly used in other studies. It has been shown that there is a 20% accuracy drop when using dry electrodes compared to wet electrodes even though the signals look similar in both time domain and frequency domain (Zhu et al., 2021).

4.3. Limitations

Even though both hypotheses were validated, this work was only tested with the selected multi-frequency stimulation method (frequency superposition). This means that the result may vary if a sufficiently different stimulation method which triggers completely different multi-frequency SSVEP patterns were used. We also acknowledge that only the decision tree method was implemented in optimization in this study and it has its own limitations though its effectiveness compared to global search was already proven (Liang et al., 2020). Furthermore, since MFCCA is the only purposefully designed generalized multi-frequency SSVEP decoder, it was used in this study to avoid extensive training and prolonged experiment duration. However, the accuracies from the dual-frequency tests were at a lower level compared to the single-frequency test. This is not considered a problem here because this study focuses on understanding the difference between different frequency set selection methods in multi-frequency SSVEP and the single-frequency test was included for bench-marking purpose only.

TABLE 4 **Information transfer rate (ITR) from the six tests (mean ± standard deviation).**

Test	1	2	3	4	5	6
ITR (bits/min)	11.5 ± 6.6	10.7 ± 5.5	14.2 ± 7.0	11.9 ± 7.3	11.1 ± 7.6	22.0 ± 6.3

Nonetheless, this suggests that more effort should be spent on developing generalized multi-frequency SSVEP decoding algorithms to improve the overall performance of multi-frequency SSVEP-based BCIs.

4.4. Future work

As part of future work, other optimization methods should be explored to address the potential pitfall in the decision tree when working with the number of common sums. Other optimization strategies regarding the frequency set selection in multi-frequency SSVEP should also be further explored. Last, but not least, a comprehensive comparison between single-frequency and multi-frequency SSVEP should be conducted with finer frequency intervals and larger frequency coverage.

5. Conclusion

The results from the frequency set selection study showed that selection by pairs (compared to selection by frequencies) and optimizing (minimizing) the number of common sums in selection by pairs significantly increased the accuracy of the interface. Furthermore, a potential pitfall was observed in the decision tree method in optimizing the number of common sums, which resulted in a sub-optimal result from the optimization process and subsequently a smaller than expected difference between the best and worst case scenarios in the number of common sums optimization.

Data availability statement

The raw data supporting the conclusions of this article will be made available by the authors, without undue reservation.

Ethics statement

The studies involving human participants were reviewed and approved by University of Melbourne Human Research Ethics Committee. The patients/participants provided their written informed consent to participate in this study.

Author contributions

JM, DG, YT, and DO contributed toward the conception and design of the work, data analysis, and interpretation. JM performed data collection and drafted the manuscript. DG, YT, and DO provided critical revisions of the article. All authors reviewed and approved the submitted version.

Funding

This project was supported by the Valma Angliss Trust.

Acknowledgments

The authors thank Sandy Errey from the University of Melbourne Statistical Consulting Centre for her advice on statistical analyses in this paper.

Conflict of interest

The authors declare that the research was conducted in the absence of any commercial or financial relationships that could be construed as a potential conflict of interest.

Publisher's note

References

Bakardjian, H., Tanaka, T., and Cichocki, A. (2010). Optimization of SSVEP brain responses with application to eight-command brain–computer interface. *Neurosci. Lett.* 469, 34–38. doi: 10.1016/j.neulet.2009.11.039

Chang, M. H., Baek, H. J., Lee, S. M., and Park, K. S. (2014). An amplitude-modulated visual stimulation for reducing eye fatigue in SSVEP-based brain–computer interfaces. *Clin. Neurophysiol.* 125, 1380–1391. doi: 10.1016/j.clinph.2013.11.016

Chen, X., Chen, Z., Gao, S., and Gao, X. (2013). Brain–computer interface based on intermodulation frequency. *J. Neural Eng.* 10, 066009. doi: 10.1088/1741-2560/10/6/066009

Chen, X., Wang, Y., Nakanishi, M., Gao, X., Jung, T. P., and Gao, S. (2015). High-speed spelling with a noninvasive brain–computer interface. *Proc. Natl. Acad. Sci. U. S. A.* 112, E6058–E6067. doi: 10.1073/pnas.1508080112

Hwang, H.-J., Kim, D. H., Han, C.-H., and Im, C.-H. (2013). A new dual-frequency stimulation method to increase the number of visual stimuli for multi-class SSVEP-based brain–computer interface (BCI). *Brain Res.* 1515, 66–77. doi: 10.1016/j.brainres.2013.03.050

Kimura, Y., Tanaka, T., Higashi, H., and Morikawa, N. (2013). SSVEP-based brain–computer interfaces using FSK-modulated visual stimuli. *IEEE Trans. Biomed. Eng.* 60, 2831–2838. doi: 10.1109/TBME.2013.2265260

Liang, L., Lin, J., Yang, C., Wang, Y., Chen, X., Gao, S., et al. (2020). Optimizing a dual-frequency and phase modulation method for SSVEP-based BCIs. *J. Neural Eng.* 17, e046026. doi: 10.1088/1741-2552/abaa9b

Lin, Z., Zhang, C., Wu, W., and Gao, X. (2006). Frequency recognition based on canonical correlation analysis for SSVEP-based BCIs. *IEEE Trans. Biomed. Eng.* 53, 2610–2614. doi: 10.1109/TBME.2006.889197

Liu, B., Huang, X., Wang, Y., Chen, X., and Gao, X. (2020). BETA: a large benchmark database toward SSVEP-BCI application. *Front. Neurosci.* 14, 627. doi: 10.3389/fnins.2020.00627

Mu, J., Grayden, D. B., Tan, Y., and Oetomo, D. (2021a). "Frequency superposition – a multi-frequency stimulation method in SSVEP-based BCIs," in *2021 43rd Annual International Conference of the IEEE Engineering in Medicine Biology Society (EMBC)* (Piscataway, NJ: IEEE), 5924–5927.

Mu, J., Tan, Y., Grayden, D. B., and Oetomo, D. (2021b). "Multi-frequency canonical correlation analysis (MFCCA): a generalised decoding algorithm for multi-frequency SSVEP," in *2021 43rd Annual International Conference of the IEEE Engineering in Medicine and Biology Society (EMBC)* (Piscataway, NJ: IEEE), 6151–6154.

Nicolas-Alonso, L. F., and Gomez-Gil, J. (2012). Brain computer interfaces, a review. *Sensors* 12, 1211–1279. doi: 10.3390/s120201211

Regan, D. (1989). *Human Brain Electrophysiology: Evoked Potentials and Evoked Magnetic Fields in Science and Medicine*. Amsterdam: Elsevier.

Shyu, K. K., Lee, P. L., Liu, Y. J., and Sie, J. J. (2010). Dual-frequency steady-state visual evoked potential for brain computer interface. *Neurosci. Lett.* 483, 28–31. doi: 10.1016/j.neulet.2010.07.043

Volosyak, I., Cecotti, H., and Graser, A. (2009). "Optimal visual stimuli on LCD screens for SSVEP based brain-computer interfaces," in *2009 4th International IEEE/EMBS Conference on Neural Engineering* (Piscataway, NJ: IEEE), 447–450.

Wang, Y., Chen, X., Gao, X., and Gao, S. (2016). A benchmark dataset for SSVEP-based brain–computer interfaces. *IEEE Trans. Neural Syst. Rehabil. Eng.* 25, 1746–1752. doi: 10.1109/TNSRE.2016.2627556

Wolpaw, J. R., Birbaumer, N., Heetderks, W. J., McFarland, D. J., Peckham, P. H., Schalk, G., et al. (2000). Brain-computer interface technology: a review of the first international meeting. *IEEE Trans. Rehabil. Eng.* 8, 164–173. doi: 10.1109/tre.2000.847807

Xu, M., He, F., Jung, T. P., Gu, X., and Ming, D. (2021). Current challenges for the practical application of electroencephalography-based brain–computer interfaces. *Engineering* 7, 1710–1712. doi: 10.1016/j.eng.2021.09.011

Zander, T. O., Kothe, C., Welke, S., and Rötting, M. (2009). "Utilizing secondary input from passive brain-computer interfaces for enhancing human-machine interaction," in *International Conference on Foundations of Augmented Cognition* (Berlin/Heidelberg: Springer), 759–771.

Zhang, Y., Xu, P., Liu, T., Hu, J., Zhang, R., and Yao, D. (2012). Multiple frequencies sequential coding for SSVEP-based brain-computer interface. *PLoS ONE* 7, e29519. doi: 10.1371/journal.pone.0029519

Zhu, D., Bieger, J., Garcia Molina, G., and Aarts, R. M. (2010). A survey of stimulation methods used in SSVEP-based BCIs. *Comput. Intell. Neurosci.* 2010, 702357. doi: 10.1155/2010/702357

Zhu, F., Jiang, L., Dong, G., Gao, X., and Wang, Y. (2021). An open dataset for wearable SSVEP-based brain-computer interfaces. *Sensors* 21, 1256. doi: 10.3390/s21041256

frontiers | Frontiers in Neuroscience

TYPE Original Research
PUBLISHED 06 January 2023
DOI 10.3389/fnins.2022.1100812

A multimodal fusion method for Alzheimer's disease based on DCT convolutional sparse representation

Guo Zhang[1,2†], Xixi Nie[3†], Bangtao Liu[2], Hong Yuan[2], Jin Li[2], Weiwei Sun[4*] and Shixin Huang[1,5*]

[1]School of Communication and Information Engineering, Chongqing University of Posts and Telecommunications, Chongqing, China, [2]School of Medical Information and Engineering, Southwest Medical University, Luzhou, China, [3]Chongqing Key Laboratory of Image Cognition, College of Computer Science and Technology, Chongqing University of Posts and Telecommunications, Chongqing, China, [4]School of Optoelectronic Engineering, Chongqing University of Posts and Telecommunications, Chongqing, China, [5]Department of Scientific Research, The People's Hospital of Yubei District of Chongqing City, Yubei, China

OPEN ACCESS

EDITED BY
Xiaomin Yang,
Sichuan University, China

REVIEWED BY
Kaining Han,
University of Electronic Science and Technology of China, China
Teng Li,
Anhui University, China

*CORRESPONDENCE
Weiwei Sun
✉ sunww@cqupt.edu.cn
Shixin Huang
✉ 15803659045@163.com

†These authors share first authorship

SPECIALTY SECTION
This article was submitted to Neural Technology, a section of the journal Frontiers in Neuroscience

RECEIVED 17 November 2022
ACCEPTED 07 December 2022
PUBLISHED 06 January 2023

CITATION
Zhang G, Nie X, Liu B, Yuan H, Li J, Sun W and Huang S (2023) A multimodal fusion method for Alzheimer's disease based on DCT convolutional sparse representation. *Front. Neurosci.* 16:1100812. doi: 10.3389/fnins.2022.1100812

Introduction: The medical information contained in magnetic resonance imaging (MRI) and positron emission tomography (PET) has driven the development of intelligent diagnosis of Alzheimer's disease (AD) and multimodal medical imaging. To solve the problems of severe energy loss, low contrast of fused images and spatial inconsistency in the traditional multimodal medical image fusion methods based on sparse representation. A multimodal fusion algorithm for Alzheimer' s disease based on the discrete cosine transform (DCT) convolutional sparse representation is proposed.

Methods: The algorithm first performs a multi-scale DCT decomposition of the source medical images and uses the sub-images of different scales as training images, respectively. Different sparse coefficients are obtained by optimally solving the sub-dictionaries at different scales using alternating directional multiplication method (ADMM). Secondly, the coefficients of high-frequency and low-frequency subimages are inverse DCTed using an improved L1 parametric rule combined with improved spatial frequency novel sum-modified SF (NMSF) to obtain the final fused images.

Results and discussion: Through extensive experimental results, we show that our proposed method has good performance in contrast enhancement, texture and contour information retention.

KEYWORDS

Alzheimer, multimodal, sparse, fusion, convolutional

1. Introduction

Alzheimer's disease (AD) is a common neurodegenerative disease with concealed onset and incurable in the elderly. In clinical, AD is characterized by general dementia such as cognitive decline and memory loss (Dubois et al., 2021). Advanced multimodal neuroimaging techniques, such as magnetic resonance imaging (MRI) (Thung et al., 2014; Liu M. et al., 2016; Lian et al., 2018; Fan et al., 2019) and positron emission tomography (PET) (Chetelat et al., 2003; Liu M. et al., 2017) use different imaging mechanisms to reflect the location of organs or lesions from different angles, and can clearly show human tissue or metabolism and blood flow of organs. This technique has the complementarity and irreplaceability of medical information, which provides a good prospect for the early diagnosis of AD (Perrin et al., 2009; Mohammadi-Nejad et al., 2017; Wang et al., 2021).

Medical image fusion includes image decomposition, fusion rules, and image reconstruction. The main purpose of image decomposition is to extract the feature information from the image. The effectiveness of feature extraction determines the quality of fusion results. The current image fusion algorithms can be divided into three categories. The first kind of image fusion is based on wavelet and pyramid transform (Da Cunha et al., 2006; Yang et al., 2010; Miao et al., 2011; Liu S. et al., 2017; Liu X. et al., 2017). Among them, the Laplace pyramid transform has the best robustness in the sampling operator. Wang and Shang (2020) proposed a fast image fusion method based on discrete cosine transform (DCT), which decomposes each source image into a base layer and a detail layer for image fusion. And optimize the calculation method of the base layer to better preserve the structure of the image. In addition, non-subsampled shear wave transforms (NSST) (Kong et al., 2014) are also widely used in AD diagnosis because of their translation invariance and multidirectional. The second kind of image fusion is based on edge-preserving filtering (Farbman et al., 2008; Xu et al., 2011; He et al., 2012; Hu and Li, 2012; Zhang et al., 2014; Kou et al., 2015). This method can filter the image while erasing the details and retaining its strong edge structure. It can decompose the input image into smooth layers and detail layers. The smooth layer contains the main energy information of the image; the detail layer contains texture features. The third type is the feature selection method based on sparse learning, for example, the multiplier alternating directional multiplication method (ADMM) algorithm (Liu and Yan, 2011) organizes the whole learning and decomposition process into vectors, and iterates with a sliding window to achieve the convergence effect.

Sparse representation (SR) is a widely used image representation theory. It deals with the natural sparsity of signals according to the physiological characteristics of the human visual system. It is widely used in image classification (He et al., 2019), image recognition (Liu H. et al., 2016), image feature extraction (Liu et al., 2014), and multimodal image fusion (Zhu et al., 2016). The fusion method based on SR and dictionary learning is widely used in image fusion proposed by compressed sensing theory (Donoho, 2006), and it is generally better than most traditional fusion methods (Zhang and Patel, 2017). It usually represents the source image in the form of a linear combination of overcomplete dictionaries and sparse coefficients. Because the weighted coefficients obtained are sparse, the significant information of the source image can be represented by a small number of non-zero elements in the sparse coefficients. In the methods based on SR, sparse coding is usually based on local image blocks. Yang and Li (2009) first introduces SR into image fusion. This method uses sliding window technology to make the fusion process robust to noise and registration errors. Because the adjacent image blocks overlap each other, the result of each pixel is multi-valued. Ideally, multiple values of each pixel should be equal to maintain the consistency of overlapping image blocks (Gu et al., 2015). However, sparse coding is performed independently on each image block. The correlation between image pixels is ignored, resulting in multiple unequal values for each pixel. At the same time, most fusion methods adopt the strategy of aggregation and averaging to obtain the final value of each pixel, which will cause the image details to be smoothed or even lost in fusion (Rong et al., 2017). Yin et al. (2016) obtained a joint dictionary by using the source image as training data and then fused the image using the maximum weighted multi-norm fusion rule. But the problem of missing details still exists. Zong and Qiu (2017) proposed a fusion method based on classified image blocks, which uses directional gradient histogram (HOG) features to classify image blocks to establish a sub-dictionary. Although the problem of loss of details has been reduced, it still inevitably leads to some details being smoothed. Zhang and Levine (2016) proposed an improved fusion method of multitasking robust SR combined with spatial context information. Like most methods based on SR, this method encodes for local image blocks rather than for the whole image. As a result, it can still lead to poor preservation of details. And usually, the fusion methods based on sparse coding use only one dictionary to represent the different morphological parts of the source image, which is easy to cause the loss of image information.

Therefore, we propose a multimodal fusion method for Alzheimer's disease based on DCT convolution SR to solve the above problems. It was evaluated on the neuroimaging database of Alzheimer's disease (ADNI) (Veitch et al., 2022), and its effectiveness was verified by experiments.

The contribution of this paper has the following three aspects:

1. An improved multiscale decomposition method of DCT is proposed. Firstly, the M × N size image is divided into blocks of 8 × 8 size, and then the DCT transform is applied to each small block separately. The DCT coefficients of each image block are normalized separately and their low-order DCT coefficients

are calculated. The ratio of the energy of the higher-order DCT coefficients to the energy of the lower-order DCT coefficients is used as the focus evaluation function. To solve the problem of fused image capability loss and contrast reduction.

2. A convolutional SR method is proposed to solve the problem of spatial inconsistency of multimodal image fusion by combining the high-frequency and low-frequency components obtained from the multiscale decomposition and adopting the improved rules of spatial frequency and L_1 parametric combination according to the characteristics of AD multimodal images.

3. To address the problem of limited detail preservation capability of medical image fusion methods based on SR and the lack of expression capability of single dictionary, the detail texture and contour of the fused image are enhanced by constructing multiple sub-dictionaries, and finally the fused detail layer image is fused and reconstructed with the fused base layer image to obtain the fused image. The fused AD medical information features are preserved.

2. Materials and methods

In the process of image fusion, the most important thing is how to extract low-high-frequency coefficients and the fusion criteria of low-high-frequency coefficients. First of all, the DCT transform is used to decompose the MRI image in multi-scale; the DCT coefficients of each image block are normalized respectively, and its low-order DCT coefficients are calculated. The ratio of the energy of the higher-order DCT coefficient to that of the lower-order DCT coefficient is used as the focusing evaluation function. Then, the sub-images on each scale are convoluted sparsely encoded, and the sparse coefficients of different sub-images are obtained. The high-frequency sub-image coefficients are combined with the improved L_1 norm and the novel sum-modified SF (NMSF), and the low-frequency sub-images are fused with the improved L_1 norm and regional energy. Finally, the fused low-frequency sub-band and high-frequency sub-band are transformed by inverse DCT transform to get the final fused image. The principle of the image fusion algorithm based on DCT transform is shown in **Figure 1**:

2.1. DCT decomposition

2.1.1. Low-frequency component

The most important part of information for vision is concentrated in the low frequencies of the image. Low frequencies represent the slow variation between image pixels. It is the large flat area of the image that describes the main part of the image and is a comprehensive measure of the intensity of the whole image. In order to maintain the visibility of the image, the low-frequency part of the image is preserved, and changes in the low-frequency part may cause large changes in the image. The low-frequency coefficients of the fused image based on the DCT transform are averaged, assuming that there are p multi-exposure images, which can be defined as:

$$G(i,j)=\sum_{k=1}^{p} w_k G_k(i,j) \tag{1}$$

$$\sum_{k=1}^{p} w_k = 1 \tag{2}$$

$$w_1 = w_2 = \cdots = w_n = \cdots w_p = 1/p \tag{3}$$

where $G_k(i,j)$ is the low-frequency coefficients extracted from the source image after DCT transformation; $G(i,j)$ is the fused low-frequency coefficients; and w_k is the weighting factor.

2.1.2. High-frequency component

The high-frequency coefficients correspond to detailed information in the image, such as edges, and are extracted from the 8 × 8 chunked image after the DCT transform. The standard deviation of the high-frequency coefficients $D\left(i,j\right)$ in the $\left(2k+1\right)\times\left(2k+1\right)$ neighborhood centered on pixel $\left(i,j\right)$ is calculated separately.

$$C(i,j)=\sqrt{\frac{\sum_{m=i-k}^{i+k}\sum_{n=j-k}^{j+k}[D(m,n)-\bar{M}(m,n)]^2}{d-1}} \tag{4}$$

where, D is the number of pixel points in the region $\left(2k+1\right)\times\left(2k+1\right)$; D is the value of the high frequency coefficient corresponding to the (m,n) point; $\overline{M}(m,n)$ is the average value of pixels in the region, which can be defined as:

$$\overline{M}(i,j)=\frac{1}{d}\sum_{m=i-k}^{i+k}\sum_{n-j-k}^{j+k} D(m,n) \tag{5}$$

The regional standard deviation of the high-frequency coefficients for each of the P multi-exposure images is $\left[C1\left(i,j\right), C2\left(i,j\right), \ldots, Cp\left(i,j\right)\right]$, then the weight coefficients corresponding of the extracted high-frequency coefficient is:

$$w_k(i,j)=\frac{\boldsymbol{C_k}(i,j)}{\sum_{k=1}^{p}\boldsymbol{C_k}(i,j)} \tag{6}$$

where, the weights of the P multi-exposure images are compared to them, the fused high-frequency coefficient $D\left(i,j\right)$ is the high-frequency coefficient corresponding to the largest weighting factor.

$$w_k(i,j)=\max\left[w_1(i,j), w_2(i,j),\cdots,w_k(i,j),\cdots,w_p(i,j)\right] \tag{7}$$

$$D(i,\ j)=D_k(i,\ j) \tag{8}$$

2.2. Sparse representation

The medical image fusion method consists of the following four parts: (1) Multi-scale dictionary learning to train sub-dictionaries on different scales of sub-images as training images. (2) Convolutional sparse coding of the dictionaries at different scales to find their convolutional sparse coefficients. (3) Low-frequency sub-band coefficient fusion rules for low-frequency sub-images are fused according to the set fusion rules. (4) High-frequency sub-band coefficient fusion rules fuse high-frequency sub-images at different scales.

2.2.1. Multi-scale dictionary learning

The source images A and B are firstly decomposed by l-level DCT to obtain their decomposition coefficients $\left\{H_A^{l,k}, L_A\right\}$ and $\left\{H_B^{l,k}, L_B\right\}$, respectively. Where, $H_A^{l,k}$ and $H_B^{l,k}$ denote the high-frequency sub-band coefficients of source images A and B at decomposition scale l and orientation k. L_A and L_B are the low-frequency sub-band coefficients of images A and B, respectively. The sub-band images of each scale are used as training images to train the corresponding convolutional sparse sub-dictionaries. The different convolutional sparse sub-dictionaries capture the

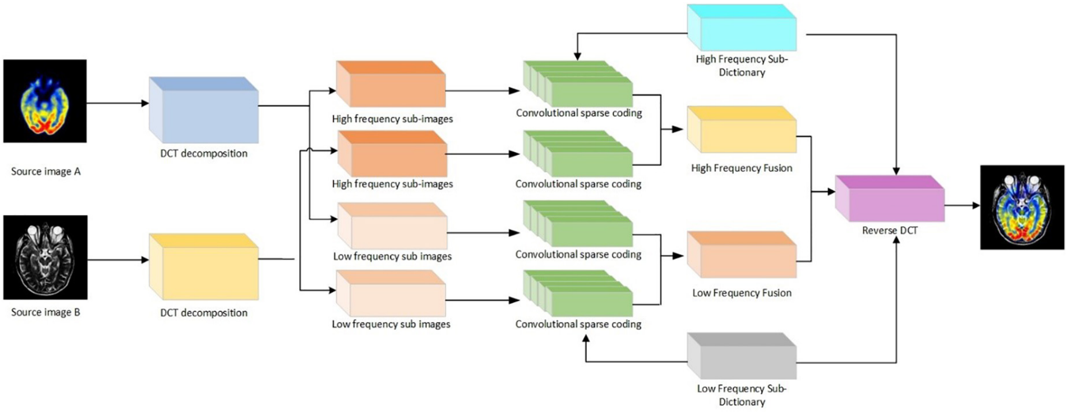

FIGURE 1
Flowchart of image fusion algorithm for discrete cosine transform (DCT) transform.

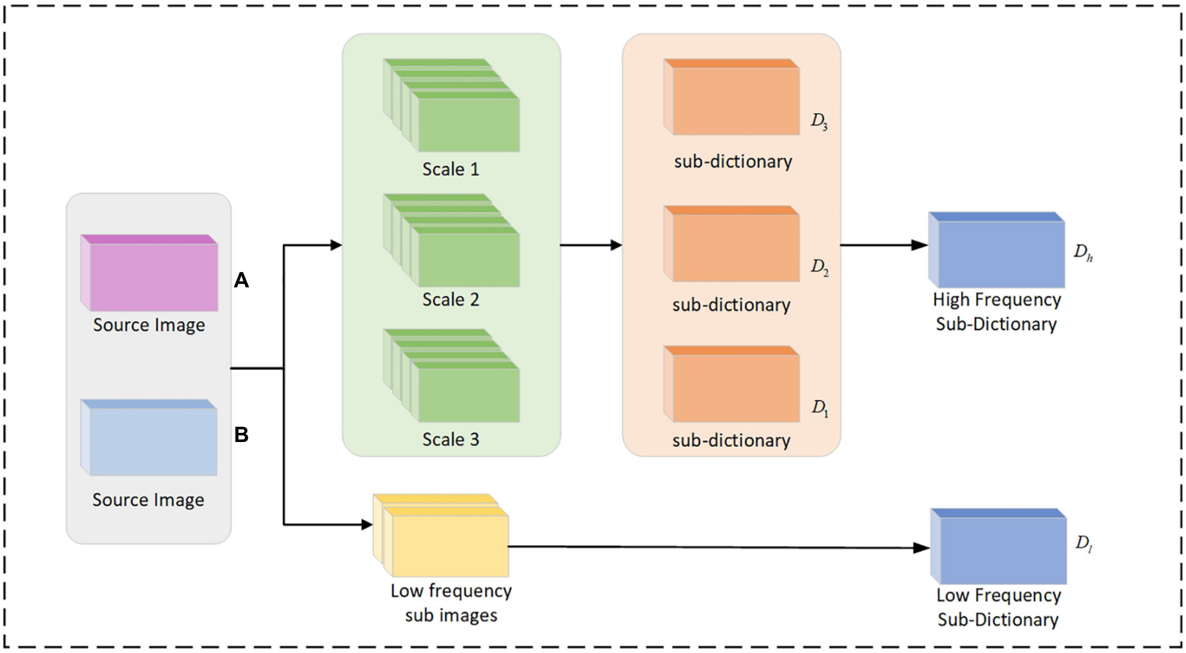

FIGURE 2
Flow chart of multi-scale dictionary learning.

features of the sub-images at different scales. Finally, the low-frequency and high-frequency sub-dictionaries are formed by combining the sub-dictionaries at different scales. The high-frequency first-scale images $H_A^{l,k}$ and $H_B^{l,k}$ of source images A and B are used as training images $\{y_m\}_{m=1}^{M}$, and the corresponding convolutional sparse dictionary learning models are built. The formula is as follows:

$$\arg\min_{d,x} \frac{1}{2}\sum_{m=1}^{M}\left\|y_m-\sum_{k=1}^{K} d_k \times x_{m,k}\right\|_2^2+\lambda\sum_{m=1}^{M}\sum_{k=1}^{K}\left\|x_{m,k}\right\|_1 \tag{9}$$

where, $x_{m,k}$ is the sparse coefficient corresponding to the mth training image; d_k is the corresponding filter; * denotes the two-dimensional convolution operation; λ is the regularization parameter; and $\|\cdot\|_1$ denotes the l_1 parametric number, which represents the sum of the absolute values of the elements.

(1) Dictionary update phase. By keeping the sparse coefficients constant, each filter is optimally updated with the following equation:

$$\arg\min_{d_k} \frac{1}{2}\sum_{m=1}^{M}\left\|y_m-\sum_{k=1}^{K} d_k \times x_{m,k}\right\|_2^2 \tag{10}$$

To optimize the filter in the discrete Fourier domain, the filter d_k needs to be zero-filled to the same size as $x_{m,k}$. Taking into account the normalization of d_k with zero padding, the formula is as follows:

$$\arg\min_{\{d_m\},\{g_m\}} \frac{1}{2}\sum_{k}\left\|\sum_{m} x_{m,k} \times d_m - s_k\right\|_2^2+\sum_{m} l_{C_{PN}}\left(g_m\right) \tag{11}$$

The ADMM algorithm shows that $C_{PN}=\left\{x\in R^N:\left(I-PP^T\right)x=0,\|x\|_2=1\right\}$ represents the

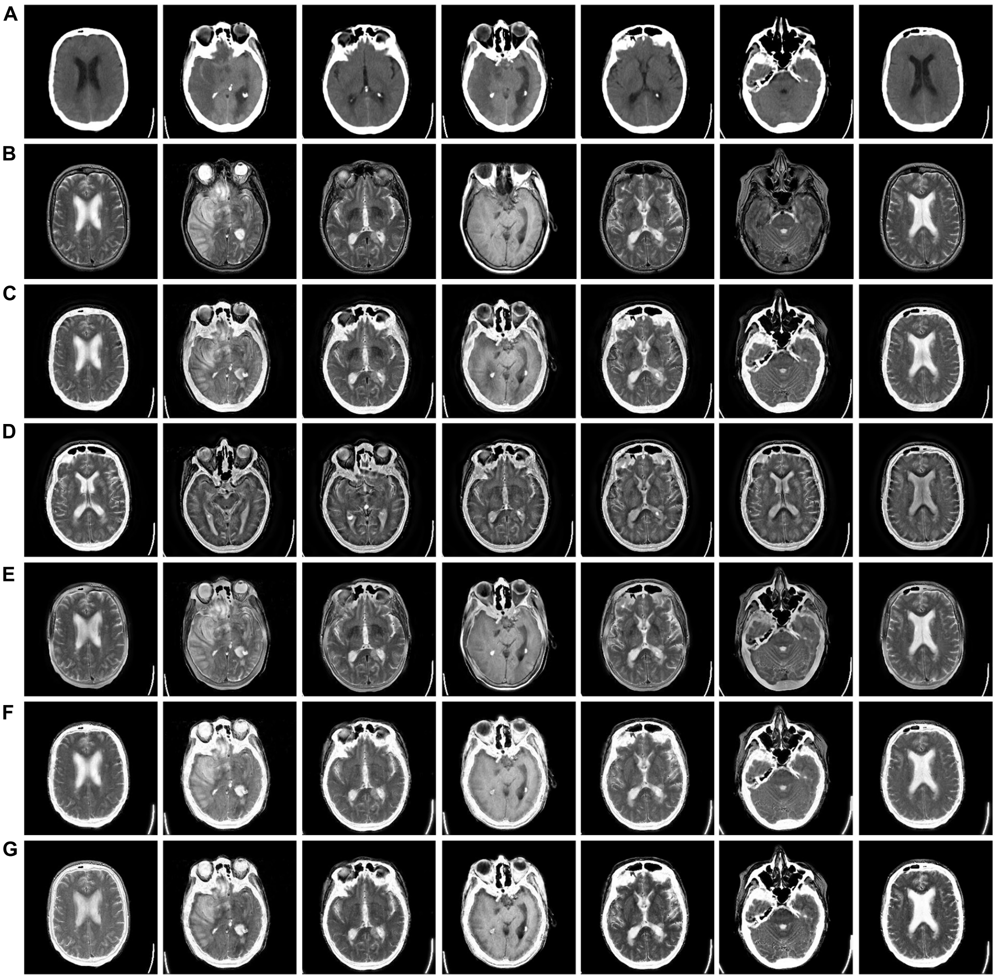

FIGURE 3
CT-MRI fusion images obtained by five fusion methods. **(A)** Computed tomography (CT) source image; **(B)** magnetic resonance imaging (MRI) source image; **(C)** nonsubsampled contourlet (NSCT) fusion result; **(D)** non-subsampled shear wave transform (NSST) fusion result; **(E)** guided filter ng fusion (GFF) fusion result; **(F)** Laplacian redecomposition (ReLP) fusion result; **(G)** fusion result of the proposed method.

constraint range, the indicator function is defined as $l_s(X) = \begin{cases} 0 & \text{if } X \in S \\ \infty & \text{if } X \notin S \end{cases}$, and g_m is an auxiliary variable introduced to facilitate optimal derivation. The resulting updated convolution filter d_k can be obtained.

(2) Convolutional sparse coefficient update phase. Update the coefficients by keeping the filter unchanged:

$$\underset{x_{m,k},z_{m,k}}{\arg\min}\ \frac{1}{2}\sum_{m=1}^{M}\left\| y_m - \sum_{k=1}^{K} d_k \times x_{m,k}\right\|_2^2 + \lambda \sum_{m=1}^{M}\sum_{k=1}^{K}\left\|z_{m,k}\right\|_1 \tag{12}$$

where, $z_{m,k}$ is the introduced auxiliary variable. We obtain the updated convolutional sparse coefficients by alternating iterative solutions.

In **Figure 2**, the cyclic execution of the dictionary and the convolutional sparse coefficients are updated to a predetermined maximum number of cycles or a set parameter threshold to stop. The convolutional sub-dictionary D_1 for the first scale of the high-frequency sub-image is output. The second and third scales of the high-frequency sub-images are dictionary learned separately to obtain the convolutional sub-dictionaries D_2, D_3. By combining each high-frequency sub-dictionary, and the high-frequency dictionary $D_h = [D_1, D_2, D_3]$ is obtained. The low-frequency sub-images are subjected to dictionary learning, and the low-frequency dictionary D_l is obtained.

2.2.2. Convolutional sparse coding

To better capture the detailed texture information of medical images and reduce the influence of artifacts, a high-frequency dictionary D_h and a low-frequency dictionary D_l are obtained by learning. Convolutional sparse coding is performed on the decomposition coefficients $\left\{H_A^{l,k}, L_A\right\}$ of the source image A. The TV regularization is then incorporated into the convolutional sparse coding model. The formula is as follows:

$$\begin{aligned} &\underset{\{x_k\}}{\arg\min}\ \frac{1}{2}\left\| s - \sum_k d_k \times x_k \right\|_2^2 \\ &+\lambda \sum_k \|x_k\|_1 + \lambda_1 TV\left(\sum_{k=1}^{K} d_k * x_k\right) \end{aligned} \tag{13}$$

where, $TV(X) = \left\|g_0 \times x\right\|_1 + \left\|g_0 \times x\right\|_1$, g_0 and g_1 are the filters used to calculate the gradients along the rows and columns of the image, respectively. The sparsity coefficients $\left\{x_{m,L}^A, x_{m,l,k,H}^A\right\}$ and $\left\{x_{m,L}^B, x_{m,l,k,H}^B\right\}$ of the coefficients in the sub-bands of the source images A and B, respectively, are obtained by optimal solution in the discrete Fourier domain. Where, m denotes the number of filters and convolutional sparse coefficient maps; L denotes the low frequency image; Hdenotes the high frequency image; and l and k denote the scale and orientation of the corresponding sub-bands, respectively.

2.2.3. Low-frequency coefficient fusion rules

After DCT decomposition, the energy information of the image is contained in the low-frequency sub-bands L_A and L_B of the source images A and B, which are displayed as basic information such as the contour and brightness of the image. The averaging strategy generally used for low-frequency coefficient fusion tends to lead to a reduction in the contrast of the image. In the case of fusion using the $Max - L_1$ rule with SR, the reduction of contrast can be effectively avoided. However, it can lead to the problem of spatial inconsistency of the image. At the same time, because the region energy can better reflect the energy and significant features of the image, and the convolution sparse coefficients of the L_1 parameter averaging strategy can effectively reduce the effect of misalignment. Therefore, a combination of region energy and averaged L_1 parameter is used to fuse the low-frequency sparse coefficients.

$$L_F = \sum_{m=1}^{M} d_m^l \times x_{m,L}^F \tag{14}$$

2.2.4. High-frequency coefficient fusion rules

The high frequency sub-bands $H_A^{l,k}$ and $H_B^{l,k}$ of the source images A and B contain a large amount of information such as texture details of the images. The convolutional SR of the fusion method has good performance in preserving detail information, and the improved spatial frequency and can well reflect the gradient changes of the image texture. Therefore, the improved spatial frequency combined with the average L_1 parameter strategy is used to fuse the high frequency sparse coefficients.

$$H_F^{l,k} = \sum_{m=1}^{M} d_m^h \times x_{m,l,k,H}^F \tag{15}$$

2.2.5. Multimodal medical image fusion

The problem of spatial inconsistency in multimodal images is caused when the L_1 parametric maximum fusion rule is used in traditional SR-based fusion methods. Therefore, we decompose the source image by performing DCT on it. Different sub-dictionaries are trained for features of different scales. A rule combining region energy and activity coefficients is used for fusion of the low frequency component coefficients, and a modified rule combining spatial frequency and activity

TABLE 1 Average values of index evaluation of different fusion methods for CT-MRI.

Methods	SF	SD	RMSE	GSM	VIF
NSCT	23.5217	1.4275	0.1617	0.9631	0.2376
NSST	23.3269	1.4729	0.1678	0.9620	0.2582
GFF	23.8825	1.4681	0.1604	0.9715	0.2265
ReLP	24.2733	1.4953	0.1539	0.9743	0.2674
Proposed	25.1246	1.5203	0.1482	0.9776	0.2743

coefficients is used for fusion of the high frequency component coefficients. The problems of reduced contrast, blurred details and inadequate information extraction are avoided. The specific steps are as follows:

(1) The DCT decomposition of source images A and B is performed to obtain the respective decomposition coefficients $\left\{H_A^{l,k}, L_A\right\}$ and $\left\{H_B^{l,k}, L_B\right\}$.

(2) In the dictionary learning stage, the images at different scales corresponding to the multimodal source images are used as training sets, and the sub-dictionaries D_0, D_1, D_2, D_3 corresponding of each scale is derived. The low-frequency dictionary is $D_l = D_0$. The high-frequency dictionary is $D_h = [D_1, D_2, D_3]$.

(3) Sparse coding stage. Convolutional sparse coding is performed on the sub-images of different orientations at each scale to obtain the corresponding convolutional sparse $\left\{x_{m,L}^A, x_{m,l,k,H}^A\right\}$ and $\left\{x_{m,L}^B, x_{m,l,k,H}^B\right\}$.

(4) Low-frequency component fusion stage. The regional energies E_A and E_B of L_A and L_B, and the active level maps $\bar{\alpha}_A$ and $\bar{\alpha}_B$ are calculated. The convolution sparsity coefficients $x_{m,L}^F$ are obtained after fusion. Finally, the convolution sparse coefficients are reconstructed with the low-frequency dictionary convolution to obtain the low-frequency sub-band image L_F.

(5) High-frequency component fusion stage. The fused convolutional sparse coefficients C are obtained by calculating the improved spatial frequencies of $H_A^{l,k}$ and $H_B^{l,k}$. Then the high-frequency sub-band images $H_F^{l,k}$ are obtained by convolutional fusion with the high-frequency dictionary D_h.

(6) Finally, the fused image F is obtained by performing inverse DCT on the fused sub-band image $\left\{H_F^{',k}, L_F\right\}$.

3. Results and discussion

3.1. Data set and training parameter settings

(1) Experimental settings

All our experiments are conducted on a computer with Intel Core i7-10750H CPU 2.60 GHz, 16 GB RAM, NVIDIA GeForce

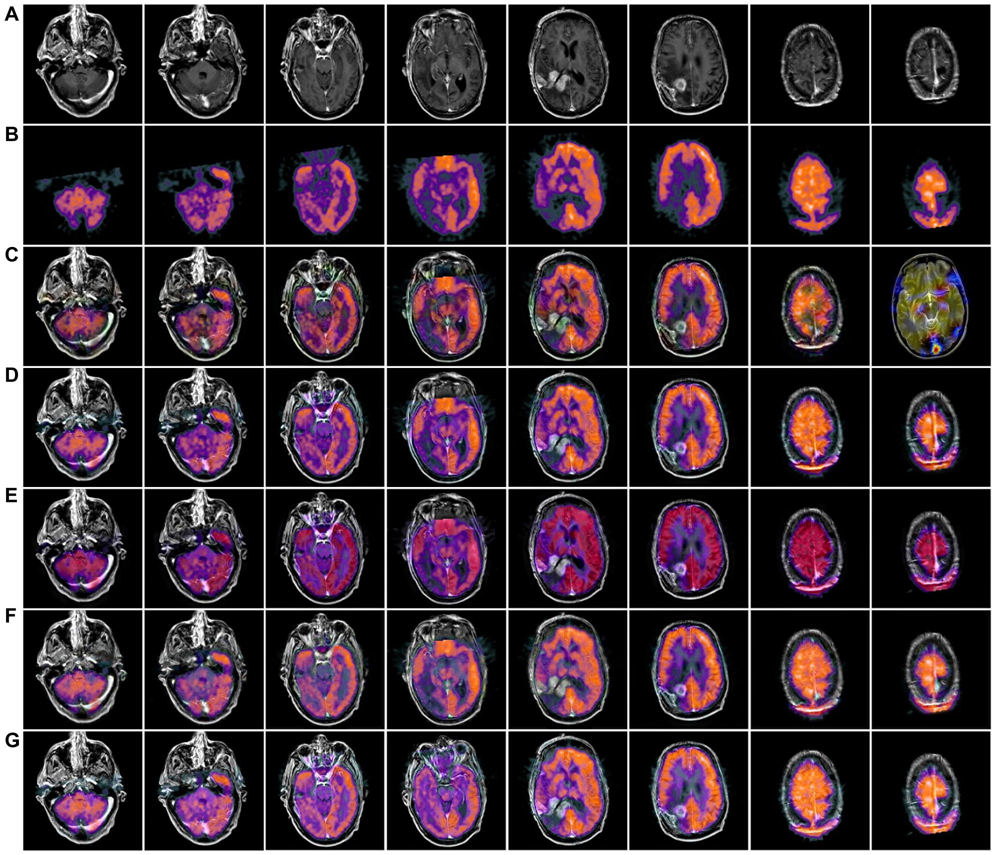

FIGURE 4
MRI-PET fusion images obtained by five methods in Paras1. **(A)** Magnetic resonance imaging (MRI) source image; **(B)** positron emission tomography (PET) source image; **(C)** nonsubsampled contourlet (NSCT) fusion result; **(D)** non-subsampled shear wave transform (NSST) fusion result; **(E)** guided filter ng fusion (GFF) fusion result; **(F)** Laplacian redecomposition (ReLP) fusion result; **(G)** fusion result of the proposed method.

FIGURE 5
MRI-PET fusion images of five methods in Paras2. **(A)** Positron emission tomography (PET) source image; **(B)** magnetic resonance imaging (MRI) source image; **(C)** nonsubsampled contourlet (NSCT) fusion result; **(D)** non-subsampled shear wave transform (NSST) fusion result; **(E)** guided filter ng fusion (GFF) fusion result; **(F)** Laplacian redecomposition (ReLP) fusion result; **(G)** is the fusion result of the proposed method.

TABLE 2 Average values of index evaluation of different fusion methods for MRI-PET.

CT-MRI	Methods	MI	SF	AG	EI	NIQE	TMQI
Paras1	NSCT	3.7269	15.2214	6.1476	45.3264	4.5158	0.8123
	NSST	3.8261	15.3842	6.1842	47.8139	4.5927	0.8546
	GFF	4.1027	16.7253	6.0878	46.9367	4.5231	0.7712
	ReLP	4.1503	17.2636	6.2913	48.4811	4.6080	0.8582
	Proposed	4.2018	17.3059	6.3682	50.6531	4.6675	0.8654
Paras2	NSCT	3.6535	16.1356	6.0631	46.6235	4.6825	0.7403
	NSST	3.7282	16.8575	6.0051	45.3315	4.7057	0.6790
	GFF	3.7451	17.2243	6.2527	46.8728	4.6817	0.7052
	ReLP	3.7871	17.7991	6.3517	46.3297	4.7354	0.7106
	Proposed	3.8010	18.1052	6.4063	47.2031	4.7521	0.7149

GTX 3090 Ti. We train the convolutional sparse and low-rank dictionary with sliding step size set to 1, sliding window size set to 8×8, dictionary size set to 64×512, error set to $\mathcal{E} = 0.03$, and decomposition level set to 3.

(2) Data sets and comparison methods

To validate the performance of the proposed method. We selected 136 sets of aligned AD brain medical images (image size of 256×256 pixels) as the source images to be fused. All image slices were obtained from the Harvard Whole Brain Atlas database (Johnson and Becker, 2001), and the three AD medical image types included 42 sets of CT-MRI images; 42 sets of MRI-PET images; and 52 sets of MRI-SPECT images. Four contrast algorithms were adopted for comparison, including nonsubsampled contourlet (NSCT) (Li and Wang, 2011), NSST (Kong et al., 2014), guided filter ng fusion (GFF) (Li et al., 2013), and Laplacian redecomposition (ReLP) (Li et al., 2020).

(3) Objective evaluation metrics

We selected 10 metrics for objective index evaluation and analysis: mutual information (MI) (Xydeas and Petrovic, 2000), natural image quality evaluator (NIQE) (Mittal et al., 2012), average gradient (AG) (Du et al., 2017), edge intensity (EI) (Wang et al., 2012), tone-mapped image quality index (TMQI) (Yeganeh and Wang, 2012), spatial frequency (SF) (Eskicioglu and Fisher, 1995), SD (Li et al., 2008), root mean square error (RMSE) (Zhang et al., 2018), gradient similarity mechanism (GSM) (Liu et al., 2011), and VIF (Sheikh and Bovik, 2006). SF is the spatial frequency, which is a measure of the richness of image detail and reflects the sharpness of image detail. A larger value means that the image detail is richer. SD is the standard deviation, which measures the contrast of the image; a larger value indicates a better contrast of the image. RMSE is the root mean square error, which measures the difference between the fused image and the source image; a smaller value indicates that the fused image information is closer to the source image. GSM measures the gradient similarity between images; a larger value indicates that the gradient information of the fused image is closer to the source image. NIQE index, the smaller the value, the smaller the distortion. VIF is an image information measure that quantifies the information present in the fused image; larger values indicate better fusion. NIQE measures the simple distance between the model statistic and the distorted image statistic. AG indicates the average gradient, which is used to extract the contrast and texture change features of the image. EI reflects the sharpness of the edges. TMQI index measures the significant features of brightness and contrast between the reference image and the fused image, and measures the structural fidelity of the fused image. Larger values of MI, SF, AG, EI, and TMQI indexes indicate better fusion.

FIGURE 6
MRI-SPECT fusion images of the five methods in Paras1. **(A)** Single photon emission computed tomography (SPECT) source image; **(B)** magnetic resonance imaging (MRI) source image; **(C)** nonsubsampled contourlet (NSCT) fusion result; **(D)** non-subsampled shear wave transform (NSST) fusion result; **(E)** guided filter ng fusion (GFF) fusion result; **(F)** Laplacian redecomposition (ReLP) fusion result; **(G)** fusion result of the proposed method.

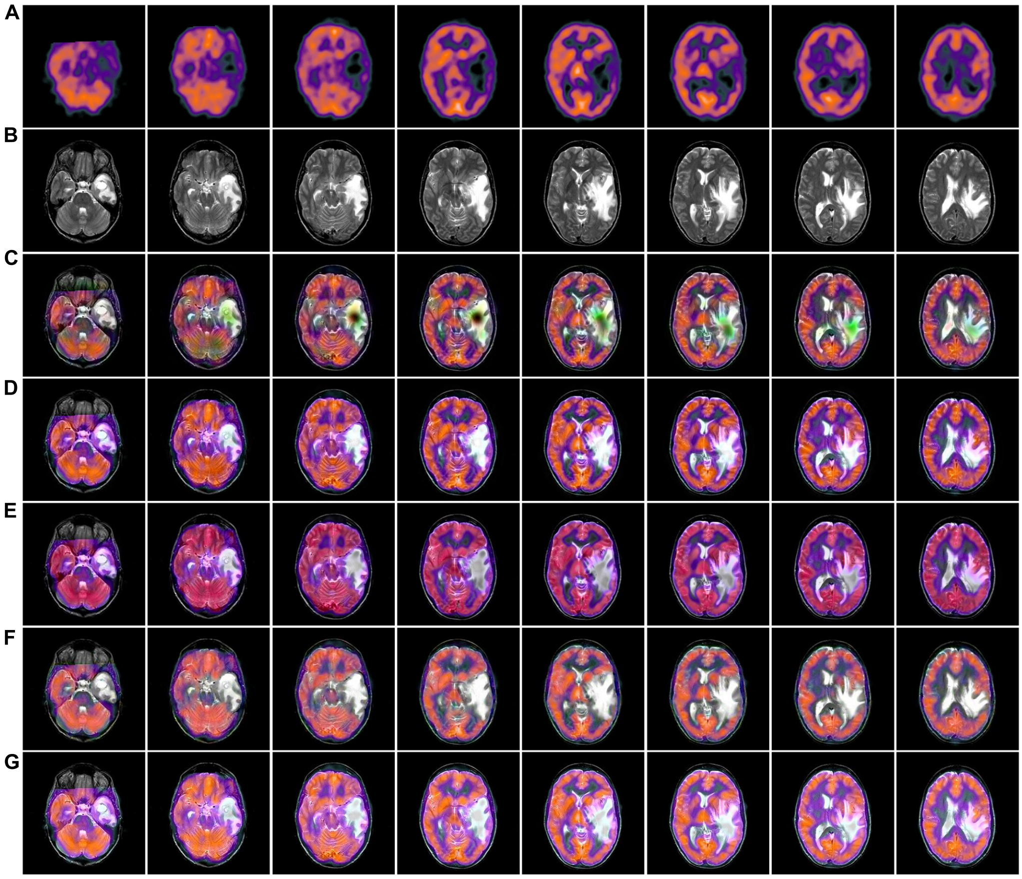

FIGURE 7
MRI-SPECT fusion images of the five methods in Paras2. **(A)** Single photon emission computed tomography (SPECT) source image; **(B)** magnetic resonance imaging (MRI) source image; **(C)** nonsubsampled contourlet (NSCT) fusion result; **(D)** non-subsampled shear wave transform (NSST) fusion result; **(E)** guided filter ng fusion (GFF) fusion result; **(F)** Laplacian redecomposition (ReLP) fusion result; **(G)** fusion result of the proposed method.

TABLE 3 Average values of index evaluation of different fusion methods for MRI-SPECT.

MRI-SPECT	Methods	MI	SF	AG	EI	NIQE	TMQI
Paras1	NSCT	3.6302	16.4106	6.2750	46.6732	4.2038	0.7931
	NSST	3.6231	15.8942	6.1773	47.0792	4.3107	0.7785
	GFF	3.7047	16.5378	6.2035	47.6470	4.2619	0.8063
	ReLP	3.8503	17.0346	6.3106	48.5718	4.3250	0.8307
	Proposed	3.8826	17.2069	6.4209	49.5014	4.4030	0.8526
Paras2	NSCT	3.6057	15.7431	6.1821	47.1003	4.3717	0.7352
	NSST	3.6183	15.7215	6.1040	46.6993	4.4602	0.7075
	GFF	3.6903	15.4903	6.2183	47.2854	4.3736	0.7202
	ReLP	3.7681	16.3107	6.3608	48.5810	4.4071	0.7464
	Proposed	3.7916	16.5012	6.4112	48.7106	4.5306	0.7503

3.2. CT-MRI fusion results comparison

In **Figure 3**, we used 42 sets of CT-MRI fused images and randomly selected seven fused images for comparison. From the figure, we can see that the images fused by NSCT and GFF algorithms are too dark. The images fused by NSST are not only darker but also distorted. The images fused by ReLP algorithm have better brightness but not enough texture details. Our fusion

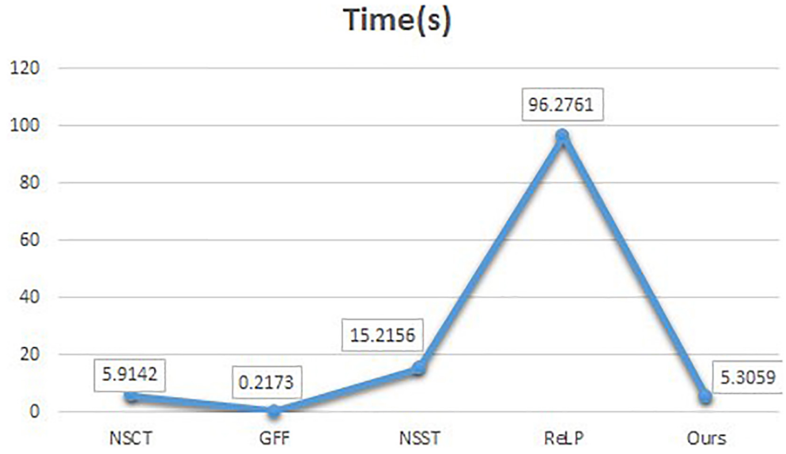

FIGURE 8
Comparison of running time.

algorithm performs best in terms of brightness, detail texture and edge contour.

The mean values of objective evaluation metrics for fusion results corresponding to different rules are given in **Table 1**, where bold indicates that the method ranks best in the metrics. NSCT is low in SD in terms of metrics, indicating insufficient image contrast. NSST is lowest in SF in terms of metrics, with poor image details. ReLP is less distorted with our method in terms of RMSE and GSM. Our proposed method performs better performance in terms of color retention, contrast, and detail retention, and achieves the optimum.

3.3. MRI-PET fusion results comparison

Figures 4, **5** use 42 sets of MRI-PET images from MRI-PET datasets Paras1 and Paras2, respectively. We randomly selected eight fused images. From **Figure 4**, it can be seen that NSCT and GFF show severe distortion, and the fused images of NSST and ReLP algorithms are too dark and have loss of detail information. In **Figure 5**, NSCT and NSST have dark luminance and GFF has distortion, while ReLP and our fusion algorithm have better visual effect.

In **Table 2**, by comparing 42 sets of fused images on the MRI-PET dataset, our proposed algorithm has the best mean value in objective evaluation metrics. Higher contrast, sharper edges and finer details were obtained. The subjective results of the fused images of the two algorithms, NSCT and GFF, were not satisfactory. NSCT and GFF had more color distortion. NSST showed abnormal brightness. ReLP performed better and was close to our average value. So far, it is easy to see that the multi-objective evaluation index of the integrated information is consistent with the conclusions of the subjective analysis. Our proposed algorithm significantly outperforms the average of all algorithms. In summary, we have a more comprehensive advantage over existing algorithms in the evaluation of objective metrics.

3.4. MRI-SPECT fusion results comparison

Figures 6, **7** we used MRI-SPECT datasets Paras1 and Paras2, respectively 52 sets of AD MRI-PET image fusion images for comparison. It can be seen from the figures that NSCT shows severe distortion, NSST fused images are too dark, GFF shows brightness anomalies, and ReLP does not perform well in terms of detail texture. Our fusion algorithm performs best in brightness, detail texture and edge contour.

In **Table 3**, we use 52 sets of fused images on the MRI-SPECT dataset for comparison, and our proposed DCT multiscale decomposition obtains sharper edges and finer details. The improved NMSF fusion rule obtains better brightness and contrast. The superiority of our method over other algorithms is demonstrated.

To compare the advantages of the proposed methods more comprehensively, we calculate the running times of the comparison methods on the same pair of images of 256 × 256 size. **Figure 8** shows the line graphs of the average running times of our method and the four comparison methods. The ReLP method has the longest running time and GFF has the shortest running time. From the line graph, it can be seen that our fusion method has the second best running speed than most of the other algorithms. However, medical image fusion is used to assist in diagnosis and treatment, and the effectiveness of the proposed method is demonstrated from objective and subjective evaluations. Therefore, the proposed method guarantees the quality of fusion results within an acceptable time consumption.

TABLE 4 Subjective quality evaluation of different fusion algorithms.

Method	CT-MRI				MRI-SPECT			
	Contrast ratio↑	Detail↑	Invariance↑	Acceptability↑	Contrast ratio↑	Detail↑	Invariance↑	Acceptability↑
NSCT	3.8 ± 0.52	3.6 ± 0.25	0.5 ± 0.39	3.6 ± 0.97	3.7 ± 0.85	3.8 ± 0.66	0.6 ± 0.14	3.7 ± 0.72
NSST	3.7 ± 0.68	3.7 ± 0.13	0.6 ± 0.37	3.5 ± 0.55	3.7 ± 0.63	3.9 ± 0.45	0.5 ± 0.97	3.6 ± 0.26
GFF	3.9 ± 0.43	3.6 ± 0.07	0.5 ± 0.93	3.7 ± 0.70	3.9 ± 0.51	4.0 ± 0.23	0.7 ± 0.41	3.7 ± 0.91
ReLP	4.0 ± 0.24	3.8 ± 0.64	0.7 ± 0.86	3.8 ± 0.61	4.1 ± 0.07	4.1 ± 0.58	0.7 ± 0.80	4.0 ± 0.96
Proposed	4.1 ± 0.19	3.9 ± 0.40	0.8 ± 0.75	4.0 ± 0.63	4.1 ± 0.79	4.2 ± 0.11	0.8 ± 0.05	4.1 ± 0.18

3.5. Comparison of subjective evaluation

Computed tomography (CT) or MRI unimodal imaging can no longer meet the demand for precise diagnosis in neurosurgery. A multimodality imaging technique that can clearly, visually, and holistically show AD brain atrophy and its association with surrounding cerebral vessels, nerves, and brain tissues can only accommodate the development of neurosurgical precision surgery. Quality assessment of multimodal fusion requires additional medical expertise. Therefore, we invited six chief neurosurgeons with more than 5 years of experience, and we randomly selected a test sample of 10 groups, each group including five fusion images. The subjective evaluation criteria were double stimulus continuous quality scale (DSCQS) including contrast, detail and invariance and acceptability scores of [1 (worst) to 5 (best)]. 1 indicates a non-diagnostic image and 5 indicates a good quality diagnostic image. Pathological invariance was scored as 0 (change) or 1 (no change). Table 4 shows the ratings of six clinicians, and the optimal values are shown in bold.

In Table 4, the subjective physician evaluations of CT-MRI and MRI-SPECT fusion are presented. The NSCT and GFF contrast and brightness were insufficient and therefore rated low. The GFF showed the worst distortion acceptability evaluation. The ReLP was very close to our evaluation among the four evaluation metrics. Our algorithm has the best performance in edge detail, luminance, contrast and spatial coherence, and received the best physician evaluation.

4. Conclusion

Multimodal neuroimaging data have high dimensionality and complexity, and seeking efficient methods to extract valuable features in complex datasets is the focus of current research. To address the shortcomings of AD multimodal fusion images such as contrast reduction, detail blurring and color distortion, we propose a multimodal fusion algorithm for Alzheimer's disease based on DCT convolutional SR. The DCT multi-scale decomposition of the source medical image is performed to obtain the basic layer, local average energy layer and texture layer of the input image, and then the sub-images of different scales are used as training images respectively. The sub-dictionaries at different scales are optimally solved using the ADMM algorithm, and then convolutional sparse coding is performed, and the inverse DCT transform of the subimage coefficients is performed using a combination of improved L_1 parameters and improved NMSF rules to obtain the multimodal fusion images. We experimentally demonstrate that the algorithm has sharper edge details, better color and spatial consistency than other algorithms by fusing medical images in three modalities, CT-MRI, MRI-PET, and MRI-SPECT. This proves that our algorithm outperforms existing state-of-the-art algorithms. In the future, we will use deep learning models for medical image multimodality classification and prediction, and apply them to early clinical diagnosis of AD.

Data availability statement

The original contributions presented in this study are included in the article/supplementary material, further inquiries can be directed to the corresponding author/s.

Ethics statement

Ethical review and approval was not required for the study on human participants in accordance with the local legislation and institutional requirements. Written informed consent for participation was not required for this study in accordance with the national legislation and the institutional requirements.

Author contributions

GZ and XN: investigation, methodology, software, validation, visualization, and writing—original draft. BL, JL, and HY: investigation, methodology, software, and supervision. WS and SH: conceptualization, data curation, formal analysis, funding acquisition, methodology, project administration, resources, supervision, validation, and writing—review and editing.

Funding

This work was supported by the Doctoral Innovative Talents Project of Chongqing University of Posts and Telecommunications (BYJS202107 and BYJS202112), the open project program of Chongqing Key Laboratory of Photo-Electric Functional Materials [K(2022)215], Postdoctoral Science Foundation of Chongqing (cstc2021jcyj-bsh0218), Special financial aid to post-doctor research fellow of Chongqing (2011010006445227), the National Natural Science Foundation of China (U21A20447 and 61971079), the Basic Research and Frontier Exploration Project of Chongqing (cstc2019jcyjmsxmX0666), Chongqing technological innovation and application development project (cstc2021jscx-gksbx0051), the Science and Technology Research Program of Chongqing Municipal Education Commission (KJZD-k202000604), the Innovative Group Project of the National Natural Science Foundation of Chongqing (cstc2020jcyj-cxttX0002), and the Regional Creative Cooperation Program of Sichuan (2020YFQ0025).

Acknowledgments

We thank the School of Optoelectronic Engineering of Chongqing University of Posts and Telecommunications for their assistance in the research.

Conflict of interest

The authors declare that the research was conducted in the absence of any commercial or financial relationships that could be construed as a potential conflict of interest.

Publisher's note

References

Chetelat, G., Desgranges, B., De La Sayette, V., Viader, F., Eustache, F., and Baron, J. C. (2003). Mild cognitive impairment: Can FDG-PET predict who is to rapidly convert to Alzheimer's disease? *Neurology* 60, 1374–1377. doi: 10.1212/01.wnl.0000055847.17752.e6

Da Cunha, A. L., Zhou, J., and Do, M. N. (2006). The nonsubsampled contourlet transform: Theory, design, and applications. *IEEE Trans. Image Process.* 15, 3089–3101. doi: 10.1109/TIP.2006.877507

Donoho, D. L. (2006). Compressed sensing. *IEEE Trans. Inform. Theory* 52, 1289–1306. doi: 10.1109/TIT.2006.871582

Du, J., Li, W., and Xiao, B. (2017). Anatomical-functional image fusion by information of interest in local Laplacian filtering domain. *IEEE Trans. Image Process.* 26, 5855–5866. doi: 10.1109/TIP.2017.2745202

Dubois, B., Villain, N., Frisoni, G. B., Rabinovici, G. D., Sabbagh, M., Cappa, S., et al. (2021). Clinical diagnosis of Alzheimer's disease: Recommendations of the international working group. *Lancet Neurol.* 20, 484–496. doi: 10.1016/S1474-4422(21)00066-1

Eskicioglu, A. M., and Fisher, P. S. (1995). Image quality measures and their performance. *IEEE Trans. Commun.* 43, 2959–2965.

Fan, J., Cao, X., Yap, P. T., and Shen, D. (2019). BIRNet: Brain image registration using dual-supervised fully convolutional networks. *Med. Image Anal.* 54, 193–206. doi: 10.1016/j.media.2019.03.006

Farbman, Z., Fattal, R., Lischinski, D., and Szeliski, R. (2008). Edge-preserving decompositions for multi-scale tone and detail manipulation. *ACM Trans. Graphic.* 27, 1–10. doi: 10.1145/1360612.1360666

Gu, S., Zuo, W., Xie, Q., Meng, D., Feng, X., and Zhang, L. (2015). "Convolutional sparse coding for image super-resolution," in *Proceedings of the international conference on computer vision, Santiago, Chile* (Manhattan, NY: IEEE), 1823–1831.

He, K., Sun, J., and Tang, X. (2012). Guided image filtering. *IEEE Trans. Pattern Anal.* 35, 1397–1409. doi: 10.1109/TPAMI.2012.213

He, Y., Li, G., Liao, Y., Sun, Y., Kong, J., Jiang, G., et al. (2019). Gesture recognition based on an improved local sparse representation classification algorithm. *Cluster Comput.* 22, 10935–10946. doi: 10.1007/s10586-017-1237-1

Hu, J., and Li, S. (2012). The multiscale directional bilateral filter and its application to multisensor image fusion. *Inform. Fusion* 13, 196–206. doi: 10.1016/j.inffus.2011.01.002

Johnson, K. A., and Becker, J. A. (2001). *The whole brain atlas*. Available online at: https://pesquisa.bvsalud.org/portal/resource/pt/lis-LISBR1.1-5215

Kong, W., Zhang, L., and Lei, Y. (2014). Novel fusion method for visible light and infrared images based on NSST–SF–PCNN. *Infrared Phys. Techn.* 65, 103–112. doi: 10.1016/j.infrared.2014.04.003

Kou, F., Chen, W., Wen, C., and Li, Z. (2015). Gradient domain guided image filtering. *IEEE Trans. Image Process.* 24, 4528–4539. doi: 10.1109/TIP.2015.2468183

Li, S., Hong, R., and Wu, X. (2008). "A novel similarity based quality metric for image fusion," in *Proceedings of international conference on audio, language and image processing, Shanghai, China* (Manhattan, NY: IEEE), 167–172.

Li, S., Kang, X., and Hu, J. (2013). Image fusion with guided filtering. *IEEE Trans. Image process.* 22, 2864–2875. doi: 10.1109/TIP.2013.2244222

Li, T., and Wang, Y. (2011). Biological image fusion using a NSCT based variable-weight method. *Inform. Fusion* 12, 85–92. doi: 10.1016/j.inffus.2010.03.007

Li, X., Guo, X., Han, P., Wang, X., Li, H., and Luo, T. (2020). Laplacian redecomposition for multimodal medical image fusion. *IEEE Trans. Instrum. Meas.* 69, 6880–6890. doi: 10.1109/TIM.2020.2975405

Lian, C., Zhang, J., Liu, M., Zong, X., Hung, S. C., Lin, W., et al. (2018). Multi-channel multi-scale fully convolutional network for 3D perivascular spaces segmentation in 7T MR images. *Med. Image Anal.* 46, 106–117. doi: 10.1016/j.media.2018.02.009

Liu, A., Lin, W., and Narwaria, M. (2011). Image quality assessment based on gradient similarity. *IEEE Trans. Image Process.* 21, 1500–1512. doi: 10.1109/TIP.2011.2175935

Liu, G., and Yan, S. (2011). "Latent low-rank representation for subspace segmentation and feature extraction," in *Proceedings of 2011 international conference on computer vision, Barcelona, Spain* (Manhattan, NY: IEEE), 1615–1622. doi: 10.1109/ICCV.2011.6126422

Liu, H., Liu, Y., and Sun, F. (2014). Robust exemplar extraction using structured sparse coding. *IEEE Trans. Neur. Net. Lear.* 26, 1816–1821. doi: 10.1109/TNNLS.2014.2357036

Liu, H., Yu, Y., Sun, F., and Gu, J. (2016). Visual–tactile fusion for object recognition. *IEEE Trans. Autom. Sci. Eng.* 14, 996–1008. doi: 10.1109/TASE.2016.2549552

Liu, M., Zhang, D., and Shen, D. (2016). Relationship induced multi-template learning for diagnosis of Alzheimer's disease and mild cognitive impairment. *IEEE Trans. Med. Imaging* 35, 1463–1474. doi: 10.1109/TMI.2016.2515021

Liu, M., Zhang, J., Yap, P. T., and Shen, D. (2017). View-aligned hypergraph learning for Alzheimer's disease diagnosis with incomplete multi-modality data. *Med. Image Anal.* 36, 123–134. doi: 10.1016/j.media.2016.11.002

Liu, S., Shi, M., Zhu, Z., and Zhao, J. (2017). Image fusion based on complex-shearlet domain with guided filtering. *Multidim. Syst. Sign. Process.* 28, 207–224. doi: 10.1007/s11045-015-0343-6

Liu, X., Mei, W., and Du, H. (2017). Structure tensor and nonsubsampled shearlet transform based algorithm for CT and MRI image fusion. *Neurocomputing* 235, 131–139. doi: 10.1016/j.neucom.2017.01.006

Miao, Q. G., Shi, C., Xu, P. F., Yang, M., and Shi, Y. B. (2011). A novel algorithm of image fusion using shearlets. *Opt. Commun.* 284, 1540–1547. doi: 10.1016/j.optcom.2010.11.048

Mittal, A., Soundararajan, R., and Bovik, A. C. (2012). Making a "completely blind" image quality analyzer. *IEEE Sig. Proc. Lett.* 20, 209–212. doi: 10.1109/LSP.2012.2227726

Mohammadi-Nejad, A. R., Hossein-Zadeh, G. A., and Soltanian-Zadeh, H. (2017). Structured and sparse canonical correlation analysis as a brain-wide multi-modal data fusion approach. *IEEE Trans. Med. Imaging* 36, 1438–1448. doi: 10.1109/TMI.2017.2681966

Perrin, R. J., Fagan, A. M., and Holtzman, D. M. (2009). Multimodal techniques for diagnosis and prognosis of Alzheimer's disease. *Nature* 461, 916–922. doi: 10.1038/nature08538

Rong, Y., Xiong, S., and Gao, Y. (2017). Low-rank double dictionary learning from corrupted data for robust image classification. *Pattern Recogn.* 72, 419–432. doi: 10.1016/j.patcog.2017.06.038

Sheikh, H. R., and Bovik, A. C. (2006). Image information and visual quality. *IEEE Trans. Image Proces.* 15, 430–444. doi: 10.1109/TIP.2005.859378

Thung, K. H., Wee, C. Y., Yap, P. T., Shen, D., and Alzheimer's Disease Neuroimaging Initiative. (2014). Neurodegenerative disease diagnosis using incomplete multi-modality data via matrix shrinkage and completion. *NeuroImage* 91, 386–400. doi: 10.1016/j.neuroimage.2014.01.033

Veitch, D. P., Weiner, M. W., Aisen, P. S., Beckett, L. A., DeCarli, C., Green, R. C., et al. (2022). Using the Alzheimer's disease neuroimaging initiative to improve early detection, diagnosis, and treatment of Alzheimer's disease. *Alzheimer's Dement.* 18, 824–857. doi: 10.1002/alz.12422

Wang, G., Li, W., and Huang, Y. (2021). Medical image fusion based on hybrid three-layer decomposition model and nuclear norm. *Comput. Biol. Med.* 129:104179. doi: 10.1016/j.compbiomed.2020.104179

Wang, M., and Shang, X. (2020). A fast image fusion with discrete cosine transform. *IEEE Sig. Process. Lett.* 27, 990–994. doi: 10.1109/LSP.2020.2999788

Wang, Y., Du, H., Xu, J., and Liu, Y. (2012). "A no-reference perceptual blur metric based on complex edge analysis," in *Proceedings of international conference on network infrastructure and digital content, Beijing, China* (Manhattan, NY: IEEE), 487–491.

Xu, L., Lu, C., Xu, Y., and Jia, J. (2011). "Image smoothing via L_0 gradient minimization," in *Proceedings of the 2011 SIGGRAPH Asia conference, Beijing, China* (New York, NY: ACM), 1–12.

Xydeas, C. S., and Petrovic, V. (2000). Objective image fusion performance measure. *Electron. Lett.* 36, 308–309. doi: 10.1049/el:20000267

Yang, B., and Li, S. (2009). Multifocus image fusion and restoration with sparse representation. *IEEE T. Instrum. Meas.* 59, 884–892. doi: 10.1109/TIM.2009.2026612

Yang, S., Wang, M., Jiao, L., Wu, R., and Wang, Z. (2010). Image fusion based on a new contourlet packet. *Inform. Fusion* 11, 78–84. doi: 10.1016/j.inffus.2009.05.001

Yeganeh, H., and Wang, Z. (2012). Objective quality assessment of tone-mapped images. *IEEE Trans. Image Process.* 22, 657–667. doi: 10.1109/TIP.2012.2221725

Yin, H., Li, Y., Chai, Y., Liu, Z., and Zhu, Z. (2016). A novel sparse-representation-based multi-focus image fusion approach. *Neurocomputing* 216, 216–229. doi: 10.1016/j.neucom.2016.07.039

Zhang, H., and Patel, V. M. (2017). Convolutional sparse and low-rank coding-based image decomposition. *IEEE Trans. Image Process.* 27, 2121–2133. doi: 10.1109/TIP.2017.2786469

Zhang, K., Huang, Y., and Zhao, C. (2018). Remote sensing image fusion via RPCA and adaptive PCNN in NSST domain. *Int. J. Wavelets Multiresolut. Inf. Process.* 16:1850037. doi: 10.1142/S0219691318500376

Zhang, Q., and Levine, M. D. (2016). Robust multi-focus image fusion using multi-task sparse representation and spatial context. *IEEE Trans. Image Process.* 25, 2045–2058. doi: 10.1109/TIP.2016.2524212

Zhang, Q., Shen, X., Xu, L., and Jia, J. (2014). "Rolling guidance filter," in *European conference on computer vision, Zurich, Switzerland: ECCV*, eds D. Fleet, T. Pajdla, B. Schiele, and T. Tuytelaars (Cham: Springer), 815–830.

Zhu, Z., Chai, Y., Yin, H., Li, Y., and Liu, Z. (2016). A novel dictionary learning approach for multi-modality medical image fusion. *Neurocomputing* 214, 471–482. doi: 10.1016/j.neucom.2016.06.036

Zong, J. J., and Qiu, T. S. (2017). Medical image fusion based on sparse representation of classified image patches. *Biomed. Signal Proces.* 34, 195–205. doi: 10.1016/j.bspc.2017.02.005

frontiers | Frontiers in Neuroscience

TYPE Original Research
PUBLISHED 10 January 2023
DOI 10.3389/fnins.2022.1050150

OPEN ACCESS

EDITED BY
Yu Pang,
Chongqing University of Posts
and Telecommunications, China

REVIEWED BY
Julia Izsak,
Sahlgrenska University Hospital,
Sweden
Stephan Theiss,
Heinrich Heine University Düsseldorf,
Germany

*CORRESPONDENCE
Ikuro Suzuki
✉ i-suzuki@tohtech.ac.jp

SPECIALTY SECTION
This article was submitted to
Neural Technology,
a section of the journal
Frontiers in Neuroscience

RECEIVED 21 September 2022
ACCEPTED 14 December 2022
PUBLISHED 10 January 2023

CITATION
Kuroda T, Matsuda N, Ishibashi Y and Suzuki I (2023) Detection of astrocytic slow oscillatory activity and response to seizurogenic compounds using planar microelectrode array. *Front. Neurosci.* 16:1050150. doi: 10.3389/fnins.2022.1050150

Detection of astrocytic slow oscillatory activity and response to seizurogenic compounds using planar microelectrode array

Taeko Kuroda, Naoki Matsuda, Yuto Ishibashi and Ikuro Suzuki*

Department of Electronics, Graduate School of Engineering, Tohoku Institute of Technology, Sendai, Japan

Since the development of the planar microelectrode array (MEA), it has become popular to evaluate compounds based on the electrical activity of rodent and human induced pluripotent stem cell (iPSC)-derived neurons. However, there are no reports recording spontaneous human astrocyte activity from astrocyte-only culture sample by MEA. It is becoming clear that astrocytes play an important role in various neurological diseases, and astrocytes are expected to be excellent candidates for targeted therapeutics for the treatment of neurological diseases. Therefore, measuring astrocyte activity is very important for drug development for astrocytes. Recently, astrocyte activity has been found to be reflected in the low-frequency band < 1 Hz, which is much lower than the frequency band for recording neural activity. Here, we separated the signals obtained from human primary astrocytes cultured on MEA into seven frequency bands and successfully recorded the extracellular electrical activity of human astrocytes. The slow waveforms of spontaneous astrocyte activity were observed most clearly in direct current potentials < 1 Hz. We established nine parameters to assess astrocyte activity and evaluated five seizurogenic drug responses in human primary astrocytes and human iPSC-derived astrocytes. Astrocytes demonstrated the most significant dose-dependent changes in pilocarpine. Furthermore, in a principal component analysis using those parameter sets, the drug responses to each seizurogenic compound were separated. In this paper, we report the spontaneous electrical activity measurement of astrocytes alone using MEA for the first time and propose that the MEA measurement focusing on the low-frequency band could be useful as one of the methods to assess drug response *in vitro*.

KEYWORDS

MEA - microelectrode array, astrocyte, seizure, human, culture, toxicology, iPSC (induced pluripotent stem cell), slow-oscilatory activity

Significance statement

Planar microelectrode array (MEA) is recognized as a useful method for evaluating the toxicity of compounds to *in vitro* human neurons. However, there are no reports directly recording spontaneous human astrocyte activity from astrocyte-only culture sample by MEA, and no drug evaluation methods are established. Here, we successfully recorded extracellular electrical activity of human astrocytes using MEA in low-frequency band. Furthermore, we established a method to assess the activity of primary human astrocytes and human iPSC-derived astrocytes, and evaluated astrocyte drug responses to five seizurogenic compounds. We expect that the MEA-based system for assessing astrocyte activity will not only provide new insights into the mechanisms of neurological diseases, but will also help in the evaluation of drug efficacy in the drug development for diseased astrocytes.

Introduction

The microelectrode array (MEA) is a planar substrate embedded with an array of microelectrodes capable of measuring extracellular potentials. In 1972, Thomas et al. reported activity recordings of cultured cells using MEA (Thomas et al., 1972). Since then, MEA has been used to record from a wide variety of neuronal preparations (Gross et al., 1977; Gross, 1979; Pine, 1980). Furthermore, improvements to the MEA have made it possible to measure from brain slices as well as from cultured neurons (Jobling et al., 1981; Wheeler and Novak, 1986; Novak and Wheeler, 1988). Since then, active research has been conducted mainly using rodent neurons and brain slices. With the development of human induced pluripotent stem cells (iPSCs), it is possible to induce human neurons from iPSCs, and human neural function can be evaluated *in vitro* (Amin et al., 2016; Odawara et al., 2016, 2022; Frega et al., 2017; Grainger et al., 2018; Autar et al., 2022; Pré et al., 2022).

Microelectrode array measurement is a noninvasive, high-temporal-resolution method and can simultaneously measure multiple points of neural network activity. MEA has been proposed as a high-throughput, accurate, and rapid screening method for toxicity testing. Indeed, studies using rodent neurons and human iPSC-derived neurons have reported the usefulness of the MEA method as an evaluation system for identifying seizurogenic compounds (Johnstone et al., 2010; Bradley et al., 2018; Odawara et al., 2018; Tukker et al., 2018, 2020; Fan et al., 2019). We reported that co-culturing neurons and astrocytes on MEA promotes early maturation of neural networks and enhances drug responsiveness (Odawara et al., 2014).

For over a century, glial cells have been regarded as merely passive glue that connects and supports neurons. However, in recent years, they have been found to have diverse roles within the central nervous system (CNS). In particular, astrocytes, the most abundant cell type in the human CNS, are considered to be directly involved in brain signaling via astrocyte–neuron interaction at tripartite synapse (Perea et al., 2009; Bindocci et al., 2017; Martin-Fernandez et al., 2017). Recently, it has been proposed that astrocytes contribute to the progression of various neurodegenerative disorders such as Alzheimer's, Parkinson's, and Alexander's disease (Brenner et al., 2001; Liddelow et al., 2017). Moreover, neurons and astrocytes have been reported to be closely involved in the onset of epileptic seizures (Onodera et al., 2021; Sano et al., 2021). Furthermore, *in vivo* experiments in rats demonstrated that antiepileptic drugs act on astrocytes, which may be related to their antiepileptic actions (Mukai et al., 2018).

From an electrophysiological perspective, epilepsy studies have indicated that wide-band electroencephalogram (EEG) activity in epileptic patients may reflect glial and neural activity. Ikeda et al. (2020) reported that recent improvements in digital electroencephalography have revealed that direct current (DC) potentials, which indicate activity in the low-frequency band below 1 Hz, reflect astrocyte-derived depolarization, whereas high-frequency oscillations (HFOs), which indicate activity in the high-frequency band above 200 Hz, reflect neuron firing activity. On the other hand, Fleischer et al. (2015) have shown that rat primary astrocytes respond to electrical stimulation with HFO. The relationship between DC potentials and HFO remains uncertain. Further studies at the cellular level are required in the future.

Most current MEA measurements focus on the spiking component of neurons in the frequency band above 50 Hz. In recent years, studies focusing on low-frequency components other than the spike component have been reported in MEA analysis of neural activity (Odawara et al., 2018; Trujillo et al., 2019; Yokoi et al., 2021; Sharf et al., 2022). To date, no MEA method has been established to measure glial-derived DC potentials in the lower-frequency band. In this study, we established a new measurement and analysis method focusing on DC potentials and report the first recording of spontaneous slow oscillatory activity of human cultured astrocytes using MEA. Furthermore, we demonstrated that this analysis method could be used to evaluate astrocyte drug responses to seizurogenic compounds.

Materials and methods

Culture of human astrocytes

Human primary astrocytes (Gibco) were cultured at 5.0×10^5 cells/cm^2 on 16 channels per well across 24-well MEA plates (MED-Q2430M; Alpha Med Scientific Inc.) coated with Geltrex (Gibco). Cells were maintained in astrocyte medium: Dulbecco's modified Eagle medium (DMEM; Gibco) containing 10% fetal bovine serum (FBS; Gibco) and N-2 Supplement

(Gibco). For culture on MEAs, a ϕ3.4-mm glass ring was placed in the middle of the MEA probe at the location of the electrode array, and cells were seeded inside the ring. After 1 h, astrocyte medium was added around the ring, and the ring was carefully removed. A frozen vial of human iPSC-derived mature astrocytes purchased from XCell Science was plated at 2.5×10^4 cells/cm^2 in tissue culture plates coated with Geltrex in STEMdiff Astrocyte Maturation Basal Medium kit (STEMCELL technologies). After 7 days, the astrocytes were sub-cultured at 5.0×10^5 cells/cm^2 on 24-well MEA plates in the same manner as above. All cells were maintained in astrocyte medium, and half the medium was replaced after 3 days.

Immunocytochemistry

Sample cultures were fixed with 4% paraformaldehyde in phosphate-buffered saline (PBS) on ice (4°C) for 10 min. Fixed cells were incubated with 0.2% Triton X-100 in PBS for 5 min, followed by preblock buffer (0.05% Triton X and 5% FBS in PBS) at 4°C for 1 h. Samples were then incubated overnight at 4°C with primary antibodies diluted in preblock buffer. Primary antibodies used were glial fibrillary acidic protein (GFAP; 1:100; #3670, Cell Signaling Technology), human nuclei (1:100; MAB1281, Sigma-Aldrich), and MAP2 (1:1000; AB5622, Sigma-Aldrich). After being washed with PBS, samples were incubated with secondary antibodies, Alexa 488- or Alexa 546-conjugated anti-mouse IgG, anti-rabbit IgG (Invitrogen) for 30 min at room temperature. Cell nuclei were counterstained with 1 μg/mL Hoechst 33258 (H341, DOJINDO). All images were taken using an A1 Nikon confocal microscope system (Nikon). Image intensity was adjusted using ImageJ software (NIH).

MEA measurements

This study requires the sensitivity of MEA to analyze signals in the frequency range below 1 Hz. Therefore, we used the MEA systems of Alpha Med Scientific Inc., which are excellent at detecting low-frequency components. Extracellular field potentials were measured using the 24-well MEA system (Presto) with a 20-kHz/channel sampling rate at 37°C under 5% CO_2. The MEA system is implemented with a 0.1 Hz two pole Butterworth high-pass filter and a 5 kHz single pole Butterworth low-pass filter. 16 electrodes per well are arranged in a 4 × 4 array, with each electrode measuring 50 μm × 50 μm and spaced at 300 μm. All MEA measurements were performed in the astrocyte cell culture medium.

Pharmacological test

After 1 week of culture, five seizurogenic compounds and two neutral compounds were cumulatively administered to human astrocytes. The following compounds were used as seizurogenic drugs: the potassium channel blocker 4-aminopyridine (4-AP; 0.3, 1, 3, 10, and 30 μM: 275875-1G, Sigma-Aldrich), the muscarinic receptor agonist pilocarpine (0.3, 1, 3, 10, and 30 μM: P6503-5G, Sigma-Aldrich), the GABAA receptor antagonist picrotoxin (0.1, 0.3, 1, 3, and 10 μM: P1675-1G, Sigma-Aldrich), 1,5-pentamethylene-tetrazole (PTZ; 30, 100, 300, 1,000, and 3,000 μM: P0046, Tokyo Chemical Industry Co.), and the D2 receptor antagonist chlorpromazine (0.1, 0.3, 1, 3, and 10 μM: C8138-5G, Sigma-Aldrich). Acetaminophen (1, 3, 10, 30, and 100 μM: A7085-100G, Sigma-Aldrich) and DMSO (D2650, Sigma-Aldrich) were used as neutral controls. VU0134992 (0.3, 1, 3, 10, 30 μM: 6877, Tocris Bioscience) and cilnidipine (1, 3, 10, 30, 100 μM: C2564, Tokyo Chemical Industry Co.) were used for blockage of Kir4.1 and calcium channels. The final concentrations of these drugs were adjusted to contain 0.1% DMSO. DMSO (0.1%) was administered in all wells as a vehicle control prior to cumulative administration of the compound. Spontaneous activities were recorded for 10 min after 5 min of rest following drug administration ($n \geq 3$).

Analysis parameters

The electrophysiological activity of astrocytes was analyzed by using Presto and Multi-bandpass Analysis software (Alpha Med Scientific). To separate the astrocyte activity to each frequency band, two pole Butterworth high-pass and two pole Bessel low-pass filters were used (DC, 0.1–1 Hz; delta, 1–4 Hz; theta, 4–8 Hz; alpha, 8–14 Hz; beta, 15–30 Hz; gamma, 35–50 Hz; high gamma, 80–150 Hz). The waveforms in each frequency band were converted into root mean square (RMS) histograms, and the threshold value was set at 10% of the highest potential value obtained during the total measurement time in 16 electrodes per well. RMS was calculated with a time window of 100 ms and shifted by 10 ms. Therefore, 90 ms was calculated by overlapping. We established nine analytical parameters for the RMS above the threshold value to evaluate the responses to compound: average total RMS, peak potential RMS, oscillation potential (OP), oscillation width (OW), coefficient of variation (CV) of OW, total OW, total oscillations, interpeak interval (IPI), and CV of IPI (**Table 1**).

Frequency analysis

Power spectral analysis using Short-time Fourier transform (STFT) was performed on the base activity downsampled to 1kHz of primary astrocytes, no cells, fibroblasts, and DMSO 10% treated. A 20 s sliding temporal Hanning window was used in the spectral analysis and spectral power was calculated every 50 ms. To calculate the oscillation intensity without baseline effects, the moving sum of 400 points of the power spectrum was calculated, the minimum sum was defined as the baseline power, and the maximum sum of the spectrum minus the baseline power was calculated as the oscillation power.

Statistical analysis

All data are representative of at least three independent sets of experiments. Analyses were conducted using GraphPad Prism software and the statistical software package R (http://www.r-project.org/). One-way ANOVA followed by Dunnett's test was used to calculate the significant difference between each concentration and the vehicle. Statistical significance is indicated by the following: $^{*}p < 0.05$, $^{**}p < 0.01$. Results are presented as mean ± SEM.

Principal component analysis

We prepared a matrix using all well data (seizurogenic compounds: 4-AP, pilocarpine, picrotoxin, PTZ, and chlorpromazine; neutral controls: DMSO and acetaminophen) with nine analytical parameters obtained using the RMS histogram of DC- and delta-band activity. We performed principal component analysis (PCA) on 502 parameter sets to select two or more from nine analytical parameters using the MATLAB function PCA as previously reported (Ishibashi et al., 2021). One-way MANOVA was used to calculate the significant difference between each concentration and the vehicle in the first two principal components. We identified several parameter sets with significant differences between seizurogenic compounds and neutral compounds as effective parameter sets for detecting drug responses.

TABLE 1 Description of analytical parameters.

Analytical parameter	Description
Average total RMS	Average of RMS calculated in 10 min
Peak potential RMS	Average peak value of RMS for all oscillations
Oscillation potential (OP)	Average of the sum of RMS values per bin for all oscillations
Oscillation width (OW)	Average duration of all oscillations
CV of OW	Coefficient of variation of total oscillation duration
Total OW	Sum of total duration of all oscillations
Total oscillations	The total number of all oscillations in 10 min
Inter peak interval (IPI)	Average time between peaks of all oscillations
CV of IPI	Coefficient of variation of time between peaks for all oscillations

Nine analytical parameters were calculated by multi-bandpass analysis.

Results

Spontaneous activity of human astrocytes detected by MEA measurements

Immunocytochemical staining was performed to confirm that the cultured cell samples on MEA were human astrocytes. Immunostaining with GFAP, a marker for astrocytes, and human nuclei, a marker for nuclei of all human cell types, indicated that the cells were human astrocytes (**Figure 1A** and **Supplementary Figure 1A**). To determine whether these cell populations contained neurons, the cells were stained with MAP2, a marker for mature neurons. No MAP2-positive cells were found in the cultured cells, confirming that astrocytes on MEA did not contain neurons (**Figure 1B** and **Supplementary Figure 1B**).

Spontaneous activity of human primary astrocytes was measured 7 days after the culture on MEA plates. **Figures 1C, D** show representative oscillation waveforms of spontaneous activity of astrocytes. To characterize the astrocyte activity obtained from MEA measurements, the acquired voltage waveforms were low-pass filtered at 50 Hz, and the maximum amplitude in 10 min for each electrode was calculated (n = 24 wells/360 electrodes). **Figure 1E** shows a plot of the maximum amplitude for each well. The minimum and maximum amplitude values of the electrodes at which oscillations were observed were 8.36 and 196.6 μV, respectively. We also observed spontaneous activity of human iPSC-derived astrocytes and compared to the primary astrocytes (**Supplementary Figures 1C, D**). The minimum and maximum amplitude values of the electrodes at which oscillations were observed in iPSC-derived astrocytes were 4.45 and 213.0 μV, respectively (**Supplementary Figure 1E**). Slow oscillatory activity was detected in all wells for human primary astrocyte, and 97% (33/34 wells) for iPS cell-derived astrocytes. The percentage of electrodes per well in which oscillatory activity was detected was 59.4% ± 12.5% (n = 24 wells) for human primary astrocyte and 26.7% ± 2.5% (n = 34 wells) for iPSC-derived astrocytes.

Next, to ensure whether the waveforms obtained reflected spontaneous activity derived from astrocytes, we performed several control experiments. To examine artifacts caused by electronics, we recorded from MEA covered with culture medium without cells for 3 weeks. Power spectral analysis using STFT was performed on the base activity of primary astrocytes and control samples. **Figure 1F** showed the waveform

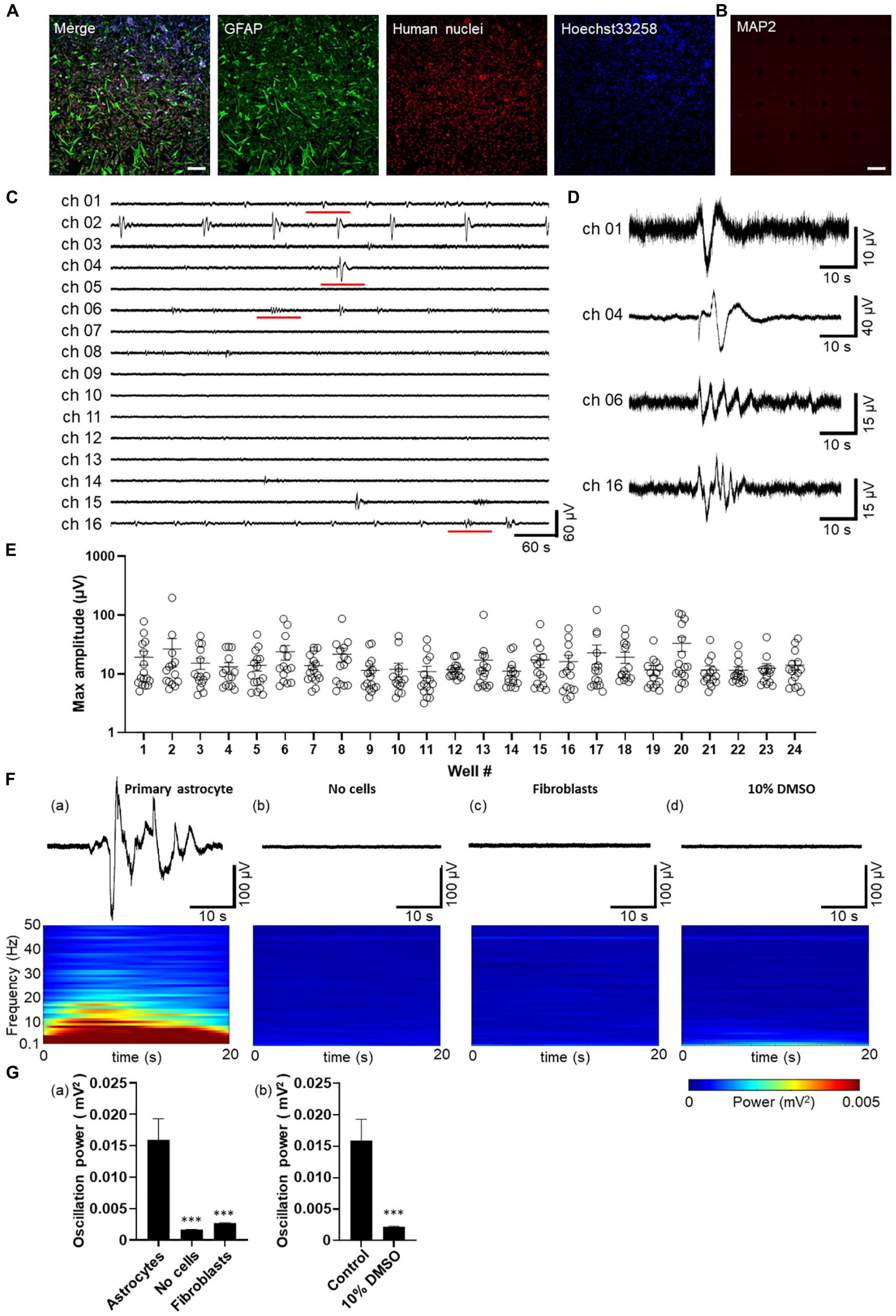

FIGURE 1

Spontaneous activity in human primary astrocytes detected by MEA. **(A,B)** Immunofluorescent images of astrocytes cultured on MEA at 8 days *in vitro* (8 DIV). Immunocytochemistry of GFAP (green), human nuclei (red), cell nuclei by Hoechst 33,258 (blue), merged images in *A*, and MAP2 (red) in **(B)** Scale bar = 200 μm. **(C)** Representative oscillation waveform at the spontaneous activity measurement for 10 min at 7 DIV. **(D)** The magnified waveform of the red underlined time in **(C)**. **(E)** Plot of maximum amplitude in 10 min oscillation waveform of each well. Error bars indicate the SEM. **(F)** Waveforms (upper panel) and their power spectrogram (lower panel) at maximum spectral intensity. (a) astrocytes, (b) no cells, (c) fibroblasts, (d) after 10% DMSO treatment. The vertical axis of the spectrogram shows the linear frequency from 0.1 Hz to 50 Hz, and the color indicates power. A 20 s spectrogram was extracted from the 40 s waveform. (G) Oscillation power of the control experiments. (a) Human primary astrocytes, no cells, fibroblasts, and (b) human primary astrocytes before and after 10% DMSO treatment. unpaired two-tailed *t*-tests, $^{***}p < 0.001$ versus astrocytes. Error bar, SEM.

for the 40-second period of highest oscillation power (upper panel) and the power scalogram calculated from that waveform using STFT (lower panel). The frequency spectrum of astrocyte oscillations showed an intensity distribution in the 0.1 Hz to 10 Hz band [**Figure 1F**(a)]. In contrast, electrode not seeded with cells were observed every 7 days up to 3 weeks, but no oscillation was observed [**Figure 1F**(b)] and mean value and SEM of oscillation power was 0.016 ± 0.003 mV^2 for astrocytes compared to 0.002 ± 0.00003 mV^2 for the medium alone. [**Figure 1G**(a); n = 6 wells/96 electrodes; $^{***}p < 0.001$ versus astrocytes; unpaired two-tailed t-tests]. To test for astrocyte specificity, human fibroblasts were seeded on MEA at high density to cover the electrodes with cells. We observed up to 3 weeks, and any oscillation were not detected [**Figure 1F**(c)]. The oscillation power of fibroblasts was 0.003 ± 0.00008 mV^2 [**Figure 1G**(a); $n = 6$ wells/96 electrodes; $^{***}p < 0.001$ versus astrocytes; unpaired two-tailed *t*-tests]. Finally, to exclude that a layer of biological materials of dead cells could cause the signals, primary astrocytes cultured on MEA were treated by 10% DMSO for killing cells. The oscillation was recorded before and 2 h after addition of DMSO. No oscillations were observed after the treatment [**Figure 1F**(d)] and DMSO addition significantly decreased oscillation power from 0.016 ± 0.003 mV^2 to 0.002 ± 0.00007 mV^2 [**Figure 1G**(b)]; n = 6 wells/96 electrodes; $^{***}p < 0.001$ versus astrocytes; unpaired two-tailed *t*-tests]. These results indicated that the slow oscillations observed by MEA are spontaneous activity of astrocytes on the electrode.

Analytical parameters of spontaneous activity in human primary astrocytes

To assess astrocyte activity, the spontaneous activity of astrocytes was divided into the following frequency bands: DC potentials (0.1–1 Hz), delta (1–4 Hz), theta (4–8 Hz), alpha (8–14 Hz), beta (15–30 Hz), gamma (35–50 Hz), and high gamma (80–150 Hz) (**Figure 2A**). In addition, the waveforms in each frequency band were converted into RMS histograms in **Figure 2B**. The RMS histograms show that the slow waveforms of astrocyte spontaneous activity observed in the MEA measurements were most clearly reflected in DC potentials below 1 Hz, as reported in previous studies using electroencephalographs (**Figure 2B**). In contrast, astrocyte activity was not observed in the frequency bands higher than delta band (**Figure 2B**). Thus, the RMS of DC potential and delta band were used to analyze astrocyte activity. The threshold value was set at 10% of the highest potential value in all electrodes per well, and nine parameters were set for RMS above the threshold value: average total RMS, peak potential RMS, OP, OW, CV of OW, total OW, total oscillations, IPI, and CV of IPI (**Figure 2C** and **Table 1**).

Astrocyte activity depends on ion channel modulations

We next explored a mechanism of the astrocyte spontaneous slow oscillatory activity by using human primary astrocytes. Ikeda et al. reported that DC potential observed in wide-band EEG activity of epileptic patients associated to extracellular potassium, and hypothesized the potassium homeostasis are relative to regulation by Kir4.1 channels in astrocytes. Therefore, we first investigated the effect of extracellular potassium concentration on astrocyte slow oscillations. Based on the chemical composition of ACSF, which maintains comparable electrolyte concentration as cerebrospinal fluid, the extracellular potassium concentration at physiological levels is considered to be 3.0 mM. On the other hand Ullah et al. (2009) measured extracellular neuro-glial potassium concentrations and reported that the extracellular potassium concentration at epileptogenic levels was approximately 40 mM at peak values. They also reported that neuronal firing is induced from an extracellular potassium concentration of 8.5 mM. Medium used for MEA measurements in this study contained 5.3 mM of KCl, and its potassium concentration is close to physiological levels compared to epileptogenic levels and do not reach concentrations that would induce neuronal firing. Therefore, we treated human primary astrocytes with KCl 10 mM, the concentration at which nerve firing can be induced, and KCl 40 mM, the epileptogenic level, and observed changes in oscillation in DC potential. The oscillation frequency decreased with increasing KCl concentrations [**Figure 3A**(a)]. To analyze the effect on astrocyte activity, we examined two parameters: average total RMS, which indicates the intensity of oscillations, and total oscillations, which reflects the frequency of oscillations. A dose-dependent decrease in these two parameters was observed [**Figures 3A**(b, c)]; $n = 5$ wells; $^{*}p < 0.05$, $^{***}p < 0.001$ versus control; one-way ANOVA followed by Dunnett's test]. We next investigated whether regulation of extracellular potassium concentrations by Kir4.1 channels was involved in the formation of astrocyte slow oscillations. The results showed loss of oscillation at 30 μM with 100% inhibitory effect [**Figure 3B**(a)]. We also found significant reductions at 30 μM in average total RMS and total oscillations [**Figures 3B**(b, c); $n = 6$ wells; $^{***}p < 0.001$ versus vehicle; one-way ANOVA followed by Dunnett's test]. These results indicate that extracellular potassium concentration through Kir4.1 channels is involved in slow oscillation formation in astrocytes. Finally, to confirm the effect of calcium, which plays an important role in astrocyte function, we performed experiments with the calcium channel inhibitor cilnidipine. Cilnidipine showed reduced astrocyte slow oscillations in dose-dependent manner and also indicated in average total RMS and in total oscillations (**Figure 3C**; $n = 4$ wells; $^{*}p < 0.05$, $^{**}p < 0.01$, $^{***}p < 0.001$ versus vehicle; one-way ANOVA followed by Dunnett's test). These results suggested that calcium regulation

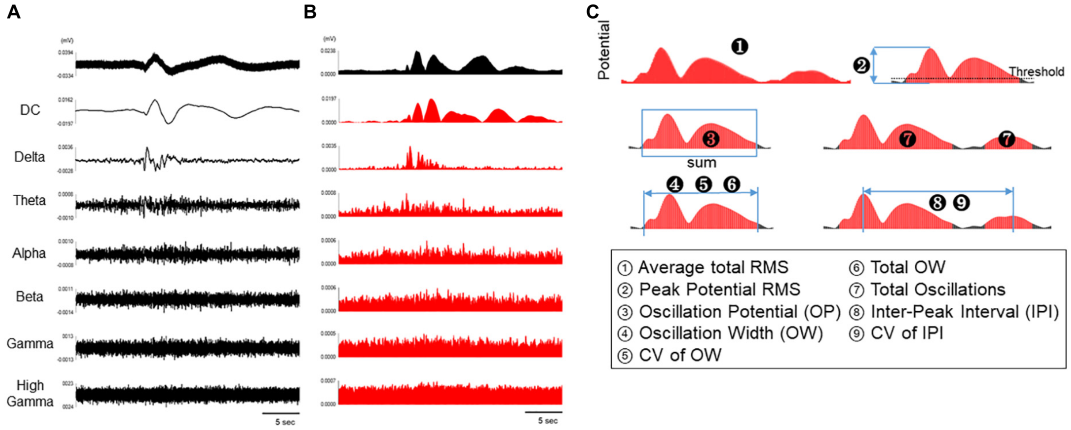

FIGURE 2
Analytical parameters of spontaneous activity in human primary astrocytes. **(A)** Representative oscillation waveform of spontaneous activity in human primary astrocytes at 3 DIV (top), and waveform separated into seven frequency bands (DC, 0.1–1 Hz; delta, 1–4 Hz; theta, 4–8 Hz; alpha, 8–14 Hz; beta, 15–30 Hz; gamma, 35–50 Hz; high gamma, 80–150 Hz). **(B)** The waveforms in each frequency band were converted into RMS histograms. **(C)** Schematic diagram of analysis parameters. The red area are subject to analysis for each parameter.

plays an important role in the formation of slow oscillations in astrocytes.

Drug response of human primary astrocytes in MEA

We assessed the drug responses of astrocytes during 1–3 weeks of culture using nine analytical parameters. Five representative seizurogenic compounds, namely, 4-AP, pilocarpine, picrotoxin, PTZ, and chlorpromazine, were added to the medium of astrocytes cultured on MEA, and the responses of astrocytes against these compounds were examined. Acetaminophen and DMSO responses were used as neutral controls. Figure 4A represents the astrocyte waveforms for each compound. Among the five seizurogenic compounds, the most significant change was observed with the muscarinic receptor agonist pilocarpine, which increased the oscillation frequency on the waveform in a dose-dependent manner [Figure 4A(b)]. Figures 4B, C show the analysis results of the compound responses using nine analysis parameters in DC potential and delta band, respectively (n = 6 wells for each compound; $^{*}p < 0.05$, $^{**}p < 0.01$ versus vehicle; one-way ANOVA followed by Dunnett's test). The rate of change and its significance were indicated when each sample with vehicle only was defined to be 100%. Among those analytical parameters, the average total RMS is graphed in Figure 4D. Pilocarpine administration lead to significantly elevated average total RMS of the DC potential at concentrations above 1 μM [Figures 4B, D(b)]. Pilocarpine also showed some significant increases in other parameters at high concentrations (Figure 4B). Picrotoxin, a GABAA receptor antagonist, showed the highest frequency of oscillations at 0.1 μM, with significant increases in several parameters, including average total RMS [Figures 4A(c), B, D(c)]. With PTZ treatment, the average total RMS increased at 100 μM and showed a dose-dependent decrease with subsequent concentrations [Figures 4A(d), B, D(d)]. Chlorpromazine, a D2 receptor antagonist, showed reduced astrocyte oscillations, with a significant decrease at 3 μM in average total RMS [Figures 4A(e), B, D(e)]. Unlike the other seizurogenic compounds, chlorpromazine demonstrated significant decreases for many parameters. Interestingly, the K-ion channel blocker 4-AP, a typical seizurogenic compound, showed no significant changes, although some parameters tended to increase [Figures 4A](a), B, D(a)]. Although the analytical parameters that showed changes differed among the compounds, the 4-AP results were similar to those of the neutral controls, acetaminophen and DMSO, which showed less significant changes [Figures 4A(f, g), B, D(f, g)].

Analysis of the delta frequency band showed a dose-dependent increase only for pilocarpine in average total RMS (Figures 4C, D; n = 6 wells for each compound; $^{*}p < 0.05$, $^{**}p < 0.01$ versus vehicle; one-way ANOVA followed by Dunnett's test). For the other parameters, there were slightly different parameters and concentrations that showed significant changes for each compound, but the tendency of increase or decrease was similar to the results of the analysis of DC potentials (Figure 4C).

PCA of drug response in human primary astrocytes

To examine whether the response of astrocytes to seizurogenic and neutral controls can be separated, a PCA was performed using the nine parameters in DC potential and delta

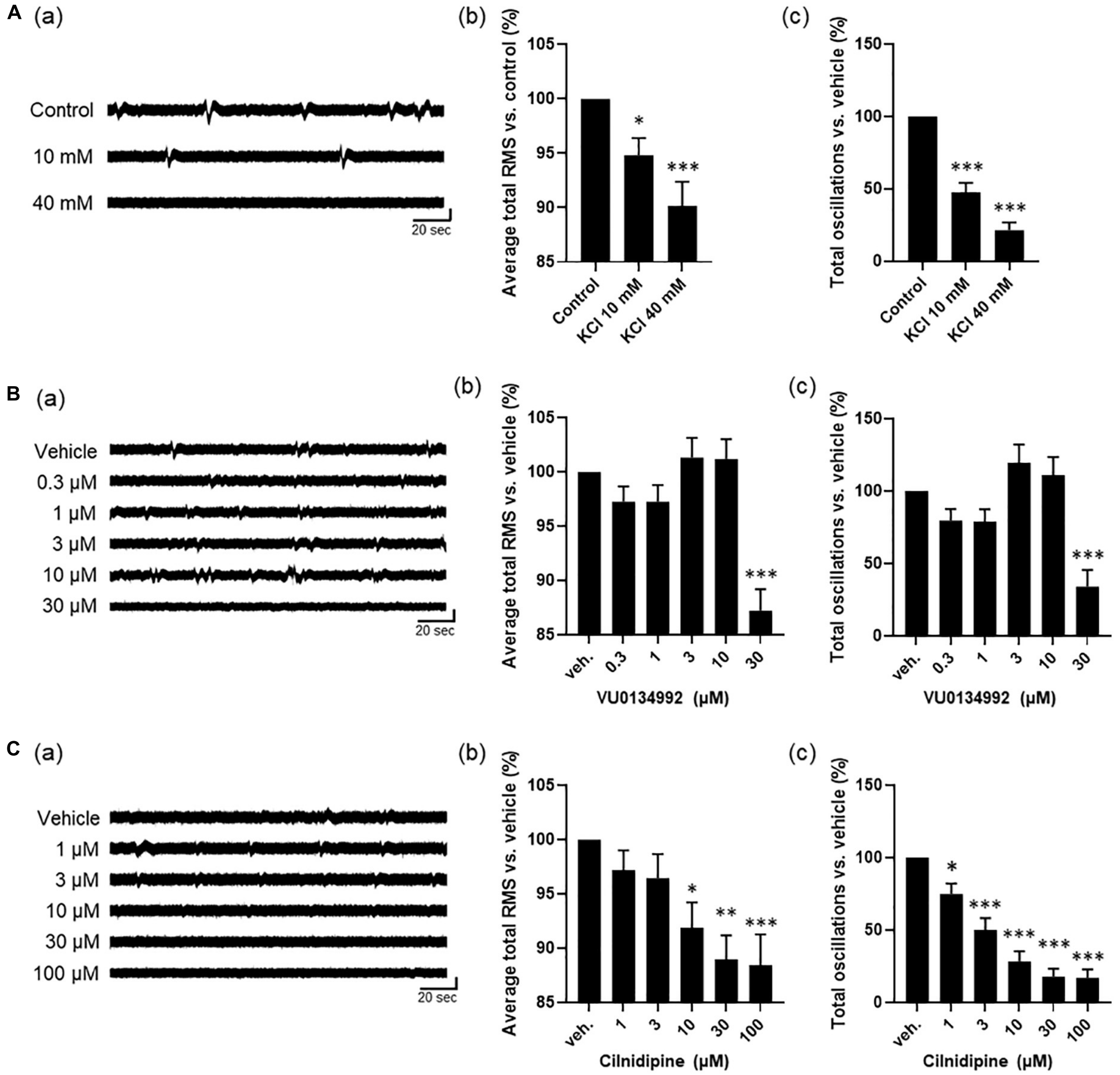

FIGURE 3
Astrocyte activity depends on ion channel modulations. **(A)** high potassium experiments by cumulative administration of KCl (*n* = 5). (a) Representative oscillation waveform. (b) Average total RMS and (c) Total oscillations. **(B)** Inhibitory experiment by VU0134992 (*n* = 6). (a) Representative oscillation waveform. (b) Average total RMS and (c) Total oscillations. **(C)** Inhibitory experiment by cilnidipine (*n* = 4). (a) Representative oscillation waveform. (b) Average total RMS and (c) Total oscillations. KCl and inhibitors were added to astrocytes at 7 DIV. One-way ANOVA followed by Dunnett's test, *$p < 0.05$, **$p < 0.01$, ***$p < 0.001$ versus control/vehicle. Error bar, SEM.

band. Using one-way MANOVA, we identified five parameters that showed no significant differences between neutral controls in PC1 and PC2 and displayed significant differences between seizurogenic and neutral controls and between all seizurogenic compounds (**Table 2**). **Figure 5** shows the results of the PCA with the identified parameters. No significant differences were found between the neutral compounds DMSO and acetaminophen, and significant differences of $p < 0.05$ were detected between the seizurogenic and neutral compounds and between all seizurogenic compounds (**Table 3**). The cumulative contribution of PC1 and PC2 was 73.9%. These results indicate that astrocyte responses to seizurogenic and neutral compounds can be separated by MEA measurements. Furthermore, since the response to each seizurogenic compound was also separable, it was suggested that the mechanism of action of each drug could also be separated by MEA measurement. The most pronounced changes, pilocarpine and chlorpromazine, were at a greater distance from the neutral controls, with pilocarpine exhibiting a dose-dependent change in the upper right diagonal of the PC1–PC2 plot and chlorpromazine in the lower left diagonal. Picrotoxin and PTZ showed a dose-dependent PC1 shift in a negative (leftward) direction, whereas 4-AP showed a slightly upper left diagonal shift. It is suggested that the present results reflect differences in astrocyte drug response (**Figure 5**).

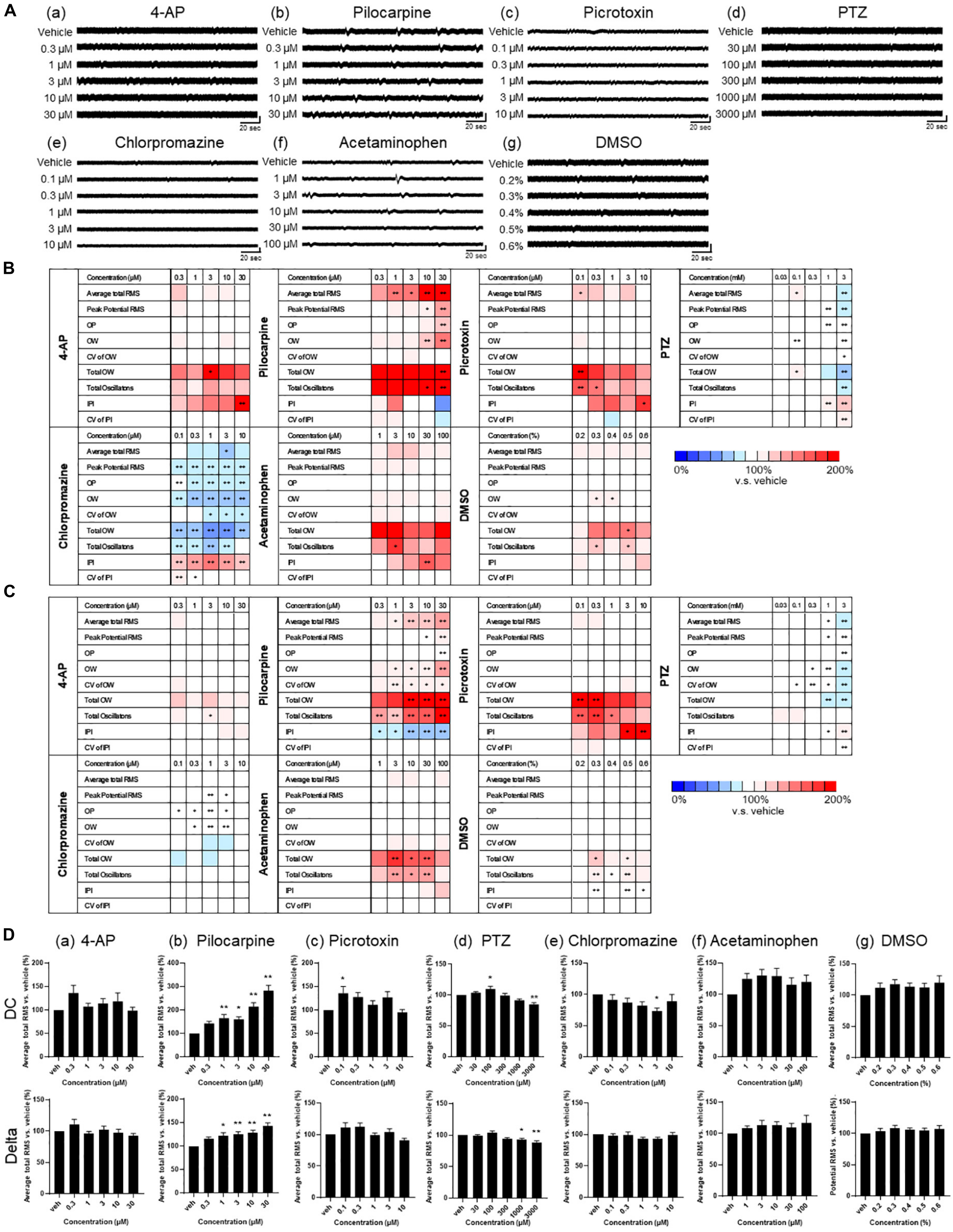

FIGURE 4

Drug responses of primary astrocytes detected by MEA. **(A)** Representative oscillation waveform after the cumulative administration of seizurogenic compounds (a) 4-AP, (b) pilocarpine, (c) picrotoxin, (d) PTZ, and (e) chlorpromazine, and neutral compounds (f) acetaminophen and (g) DMSO. Compounds were added to astrocytes during 1–3 weeks of the culture. Vertical scale bar, 40 μV; horizontal scale bar, 20 ms. **(B,C)** Heatmaps of the analytical parameters of seizurogenic compounds and neutral compounds in DC potential **(B)** and in delta band **(C)**. 4-AP (*n* = 6), pilocarpine (*n* = 6), picrotoxin (*n* = 6), PTZ (*n* = 6), chlorpromazine (*n* = 6), acetaminophen (*n* = 6), and DMSO (*n* = 6). **(D)** Dose-dependent changes of average total RMS in DC potential (upper) and in delta band (lower). One-way ANOVA followed by Dunnett's test, **p* < 0.05, ***p* < 0.01 versus vehicle. Error bar, SEM.

TABLE 2 **Principal component loadings for PCA using effective parameter set for detecting the drug responses in human primary astrocytes.**

	Principal component loadings	
Parameter	PC1	PC2
OW_DC	0.31	0.86
Average total RMS_Delta	0.43	−0.31
Peak potential RMS_Delta	0.56	−0.02
OP_Delta	0.54	0.01
Total oscillations_Delta	0.34	−0.40

Drug response of human iPSC-derived astrocytes in MEA

Next, drug responses of human iPSC-derived astrocytes were examined and compared with those of human primary astrocytes. Five seizurogenic compounds with different mechanisms of action (4-AP, pilocarpine, picrotoxin, PTZ, and chlorpromazine) and two neutral controls (DMSO and acetaminophen) were added to human iPSC-derived astrocytes on MEA during 2–4 weeks of culture (Figure 6A), and astrocyte responses to each drug were evaluated using the nine analytical parameters. The rate of change and its significance of DC and delta bands were indicated when each sample with vehicle only was defined to be 100% (Figures 6B, C; n = 6 wells for each compound; $^{*}p < 0.05$, $^{**}p < 0.01$ versus vehicle; one-way ANOVA followed by Dunnett's test). Comparison of DC potentials and delta band indicated similar changes in both frequency bands, but DC potentials showed a greater rate of change. This suggests that DC potentials below 1 Hz in human iPSC-derived astrocytes as well as in human primary astrocytes more strongly reflect astrocyte responses to drugs. Among the five seizurogenic compounds, pilocarpine demonstrated the most significant changes. Although significant increases were observed at 0.3 μM for average total RMS and CV of OW for DC potential, pilocarpine showed dose-dependent changes in many parameters for both DC potential and delta band (Figures 6B, C). This result was similar to that of primary astrocytes (Figure 4B). Interestingly, significant increases were observed at concentrations higher than 30 μM for 4-AP and 3 μM for picrotoxin (Figures 6B, C). A significant decrease was also observed with PTZ and chlorpromazine compared to vehicle (Figure 6B). For the neutral compounds, there was a significant increase in average total RMS at 0.5% DMSO, but great increase or decrease was not found in both DC potential and delta band (Figures 6B, C). These results indicated that the rate of change was smaller in iPSC-derived astrocytes than in primary astrocytes. Although the concentrations at which significant changes were observed differed in some compounds from those in primary astrocytes, there was a similar trend of increase or decrease depending on the compound.

We next performed a PCA using nine parameters to determine whether responses to the compounds could be separated in iPSC-derived astrocytes. Five parameters were identified that showed no significant differences between neutral compounds in PC1 and PC2, and significant differences between seizurogenic and neutral compounds and between all seizurogenic compounds (Table 4). Figure 7 is the results of a PCA using these parameters. No significant differences were observed between the neutral controls DMSO and acetaminophen; however, significant differences were observed between the seizurogenic and neutral controls, $p < 0.01$

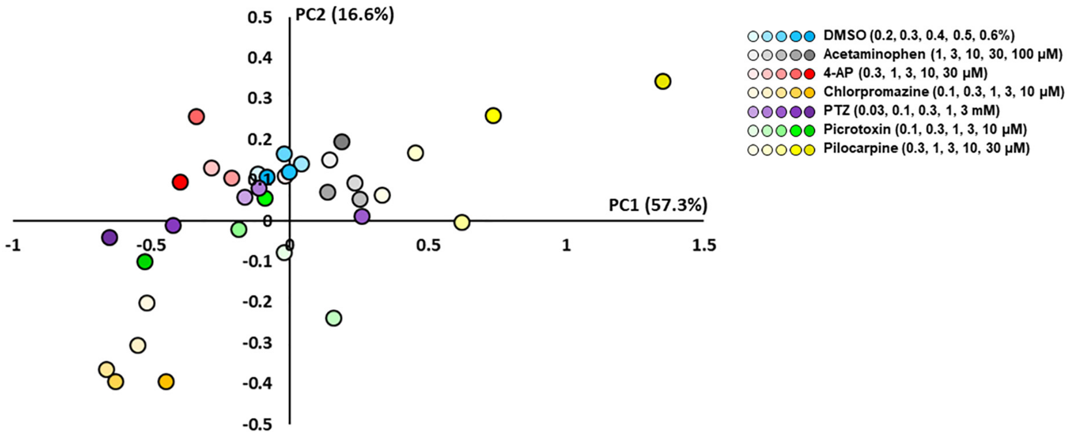

FIGURE 5
Scatterplots of principal component analysis (PCA) using the effective parameter set for detecting the drug responses of primary astrocytes. There was a clear separation between the seizurogenic and neutral compounds and between all seizurogenic compounds. In neutral compounds, DMSO and acetaminophen were not separated. DMSO (n = 6, blue), acetaminophen (n = 6, gray), 4-AP (n = 6, red), chlorpromazine (n = 6, orange), PTZ (n = 6, purple), picrotoxin (n = 6, green), and pilocarpine (n = 6, yellow). Higher concentrations are indicated by darker colored symbols.

TABLE 3 Statistical analysis for PCA using effective parameter set for detecting the drug responses in human primary astrocytes.

	vs. DMSO	vs. Acetaminophen	vs. 4-AP	vs. Chlorpromazine	vs. PTZ	vs. Picrotoxin	vs. Pilocarpine
Compounds	*p* value	*p* value	*p* value	*p* value	*p* value	*p* value	*p* value
DMSO	—	$p = 0.204$	$^{*}p = 0.014$	$^{**}p = 3.71e\text{-}71$	$^{**}p = 1.31e\text{-}05$	$^{**}p = 1.28e\text{-}04$	$^{**}p = 4.33e\text{-}17$
Acetaminophen	$p = 0.204$	—	$^{**}p = 1.27e\text{-}05$	$^{**}p = 2.99e\text{-}33$	$^{**}p = 1.79e\text{-}03$	$^{**}p = 1.13e\text{-}04$	$^{**}p = 1.46e\text{-}06$
4-AP	$^{*}p = 0.014$	$^{**}p = 1.27e\text{-}05$	—	$^{**}p = 8.64e\text{-}33$	$^{**}p = 7.72e\text{-}03$	$^{**}p = 1.50e\text{-}03$	$^{**}p = 1.05e\text{-}21$
Chlorpromazine	$^{**}p = 3.71e\text{-}71$	$^{**}p = 2.99e\text{-}33$	$^{**}p = 8.64e\text{-}33$	—	$^{**}p = 2.78e\text{-}66$	$^{**}p = 8.57e\text{-}13$	$^{**}p = 2.03e\text{-}56$
PTZ	$^{**}p = 1.31e\text{-}05$	$^{**}p = 1.79e\text{-}03$	$^{**}p = 7.72e\text{-}03$	$^{**}p = 2.78e\text{-}66$	—	$^{*}p = 0.015$	$^{**}p = 5.33e\text{-}11$
Picrotoxin	$^{**}p = 1.28e\text{-}04$	$^{**}p = 1.13e\text{-}04$	$^{**}p = 1.50e\text{-}03$	$^{**}p = 8.57e\text{-}13$	$^{*}p = 0.015$	—	$^{**}p = 5.97e\text{-}15$
Pilocarpine	$^{**}p = 4.33e\text{-}17$	$^{**}p = 1.46e\text{-}06$	$^{**}p = 1.05e\text{-}21$	$^{**}p = 2.03e\text{-}56$	$^{**}p = 5.33e\text{-}11$	$^{**}p = 5.97e\text{-}15$	—

4-AP ($n = 6$), pilocarpine ($n = 6$), picrotoxin ($n = 6$), PTZ ($n = 6$), chlorpromazine ($n = 6$), acetaminophen ($n = 6$), and DMSO ($n = 6$). One-way MANOVA. $^{*}p < 0.05$, $^{**}p < 0.01$.

(**Table 5**). There was also a significant difference between all seizurogenic compounds, $p < 0.05$ (**Table 5**). The cumulative contribution of PC1 and PC2 was 82.5%. The PCA result of human iPSC-derived astrocytes indicated that the largest change was observed in pilocarpine and 3 mM of PTZ (**Figure 7**). Similar to the results for human primary astrocytes, pilocarpine showed a dose-dependent change in the upper right diagonal of the PC1–PC2 plot. In PTZ, as same as primary astrocytes, the concentrations under 1 mM showed a dose-dependent PC1 shift in a negative direction, but 3 mM of PTZ showed a big change in the opposite direction. **Figure 7B** shows magnified scatterplots excluding the plots of pilocarpine and PTZ. In the principal component plot, the tendency for pilocarpine and chlorpromazine to increase their distances in the opposite direction was similar to that of primary astrocytes. Picrotoxin demonstrated a dose-dependent change in a different direction (lower right diagonal) from PTZ, chlorpromazine and pilocarpine. 4-AP showed a different distribution from the neutral compounds, although the percentage change was small. These results indicated that it is possible to separate responses to seizurogenic and neutral compounds in iPSC-derived astrocytes as well as in primary astrocytes and that it is also possible to separate responses to each seizurogenic compound.

Discussion

Since the first report of neural activity by Thomas et al. (1972) in, extracellular electrical activity has been recorded in various types of neurons and neural tissues (Thomas et al., 1972; Johnstone et al., 2010). However, to the best of our knowledge, there have been no reports of extracellular electrical activity recorded in human astrocyte-only culture samples using MEA. In this study, we have succeeded in measuring the slow oscillatory activity of cultured astrocytes using MEA. Furthermore, we established a method for assessing astrocyte activity using nine analytical parameters and demonstrated that drug responses to five seizurogenic compounds could be separated by PCA.

In this study, we used two types of commercially available astrocytes, human primary astrocytes and human iPSC-derived astrocytes, and measured their spontaneous activity and responses to the drugs. For spontaneous activity, compared to primary astrocytes, the percentage of oscillations detected was lower in human iPSC-derived astrocytes. The average maximum voltage of oscillation at each electrode was 25.51 ± 1.68 µV ($n = 191$ electrodes) for primary astrocytes and 22.72 ± 1.95 µV ($n = 142$ electrodes) for iPSC-derived astrocytes, $p = 0.28$. This might be due to the immaturity of human iPSC-derived astrocytes compared to primary astrocytes and the relationship between astrocyte maturation and signal acquisition is a future issue.

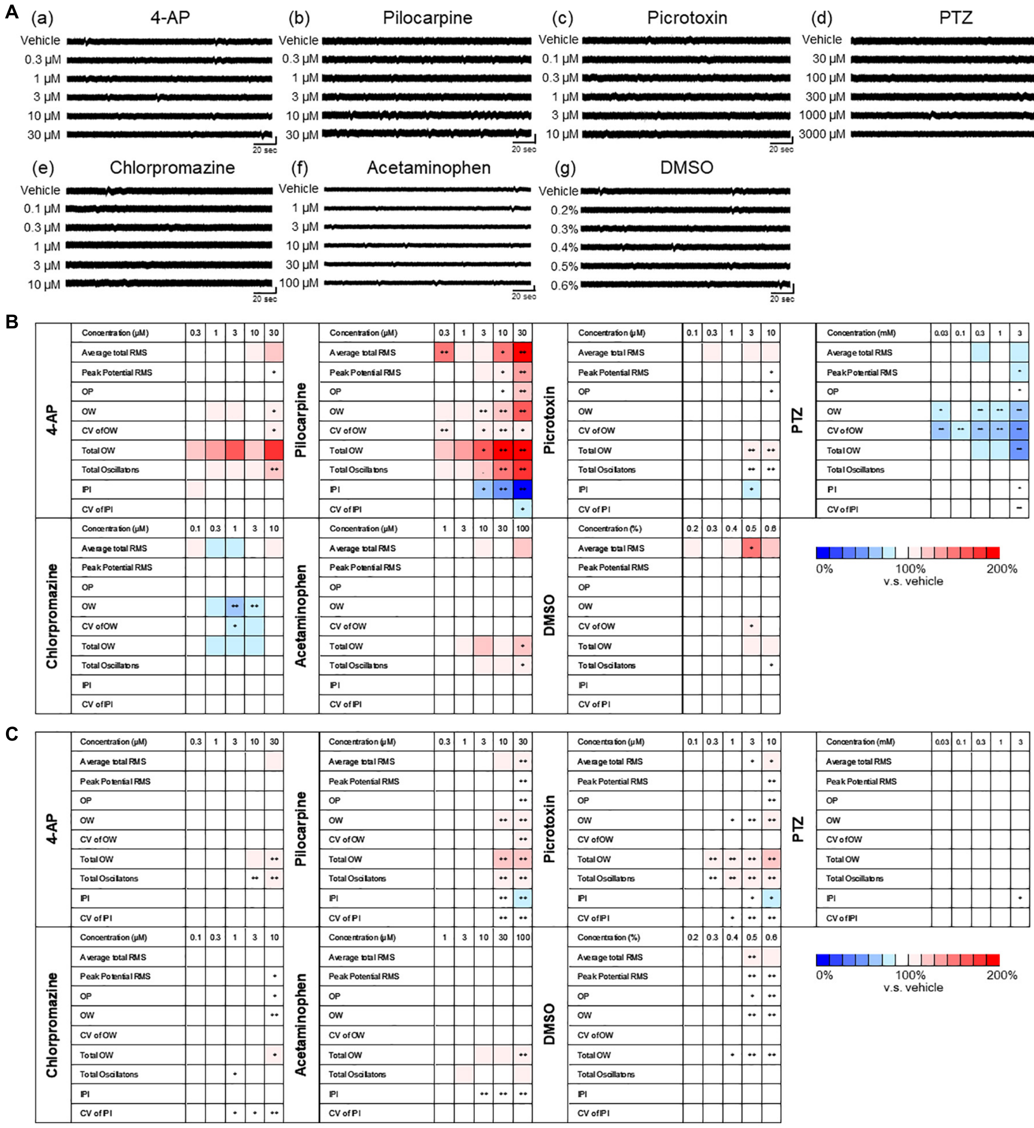

FIGURE 6
Drug responses of human iPSC-derived astrocytes detected by MEA. **(A)** Representative oscillation waveform after the cumulative administration of seizurogenic compounds (a) 4-AP, (b) pilocarpine, (c) picrotoxin, (d) PTZ, and (e) chlorpromazine, and neutral compounds (f) acetaminophen and (g) DMSO. Compounds were added to astrocytes during 2–3 weeks of the culture. Vertical scale bar, 40 μV; horizontal scale bar, 20 ms. **(B,C)** Heatmaps of the analytical parameters of seizurogenic compounds (4-AP, *n* = 6; pilocarpine, *n* = 6; picrotoxin, *n* = 6; chlorpromazine, *n* = 6) and neutral compounds (acetaminophen, *n* = 6; DMSO, *n* = 6) in DC potential **(A)** and in delta band **(B)**. One-way ANOVA followed by Dunnett's test, $*p < 0.05$, $**p < 0.01$ versus vehicle.

We demonstrated that extracellular potassium concentration is involved in generation of astrocyte slow oscillations observed in MEA (**Figures 3A, B**). In Ikeda et al.'s paper, one hypothesis is related to deficient potassium buffering capacity of astrocytes related to Kir4.1 channels and a high extracellular potassium concentration leading to epileptiform activity (Ikeda et al., 2020). However, astrocyte oscillations detected by MEA were significantly reduced in both intensity and frequency when treated with 40 mM KCl at epileptogenic levels (**Figure 3A**). On the other hand, this result was similar to that of Fleischer et al. who recorded stimulation-dependent astrocyte activity of HFOs using MEA (Fleischer et al., 2015). Regarding the effect of calcium modulation, the results of inhibition experiments with cilnidipine showed dose-dependent decrease in astrocyte oscillations, and it was consistent with those reported by Fleischer et al. (**Figure 3C**). In addition, many previous studies reported that intracellular Ca^{2+} concentration in astrocytes dynamically changed in response to drugs (Heuser and Enger, 2021). Therefore, changes in calcium concentration have a role in astrocyte oscillations

TABLE 4 Principal component loadings for PCA using effective parameter set for detecting the drug responses in human iPSC-derived astrocytes.

	Principal component loadings	
Parameter	PC1	PC2
Peak potential RMS_DC	0.47	0.14
OW_DC	0.45	0.57
Total OW_DC	0.42	0.34
OW_Delta	0.45	−0.52
Total OW_Delta	0.44	−0.52

observed in this study. For the baseline signal, we observed a heterogeneity of oscillations. The oscillations were found to be dependent on ion channels, but it is still difficult to define the influx of various ions from the shape of the waveform. The amplitude of the signal varies depending on the location of the electrodes and the cells. In addition, it is the sum of ion influxes from multiple channels. Therefore, we hypothesize that this is the reason for the heterogeneity of the waves. The physiological significance of waveforms and signal propagations are subjects for future study.

To examine astrocyte drug responses, five seizurogenic compounds were added to human primary astrocytes and human iPSC-derived astrocytes. The drug that showed the most significant response in both cells was pilocarpine, a muscarinic receptor agonist. (**Figures 4**, **6**). Pilocarpine is one of the most widely used seizure-inducing compounds to prepare animal models of epilepsy in glia research. Astrocytes, as well as neurons, express muscarinic receptors (Murphy et al., 1986; Guizzetti et al., 1996), and our results of the dose-dependent increase in oscillation frequency indicated that pilocarpine affected muscarinic receptors in astrocytes. The EEG analysis in a rat model of epilepsy using pilocarpine has reported that the low-frequency component DC shift may reflect a disruption of spatial K^+ interference function in astrocytes (Ikeda et al., 2020), suggesting that changes in K^+ concentration may also be affected in the astrocyte oscillation activity observed in our DC potentials in this study.

Chlorpromazine, a D2 receptor antagonist, was observed to reduce oscillation activity in both primary astrocytes and iPSC-derived astrocytes (**Figures 4**, **6**). D2 receptors are known to be expressed in astrocytes (Bal et al., 1994; Zanassi et al., 1999; Miyazaki et al., 2004), but the effects of chlorpromazine on astrocyte D2 receptors are not yet well understood. Chlorpromazine also acts as a calmodulin antagonist, which inhibits the catalytic activity of plasma membrane Ca^{2+}-ATPase to prevent transfer of calcium ions from cytosol into the extracellular space (Khan et al., 2001; Plenge-Tellechea et al., 2018). Our results showing the negative change in astrocyte activity with chlorpromazine treatment suggested that the transfer of calcium ions might have been inhibited by chlorpromazine. Furthermore, Chu et al. (2022) reported that when human primary astrocytes were treated with chlorpromazine at concentrations from 10 to 50 μM for 24 h, cell death was observed at 50 μM, but $[Ca^{2+}]$i measurements using a spectrophotometer with Fura-2-AM showed no change at 10–30 μM. Our MEA measurements successfully captured astrocyte responses at concentrations (0.1–10 μM) even lower than those concentrations.

Interestingly, although both picrotoxin and PTZ are GABAA receptor antagonists, the responses of astrocytes in

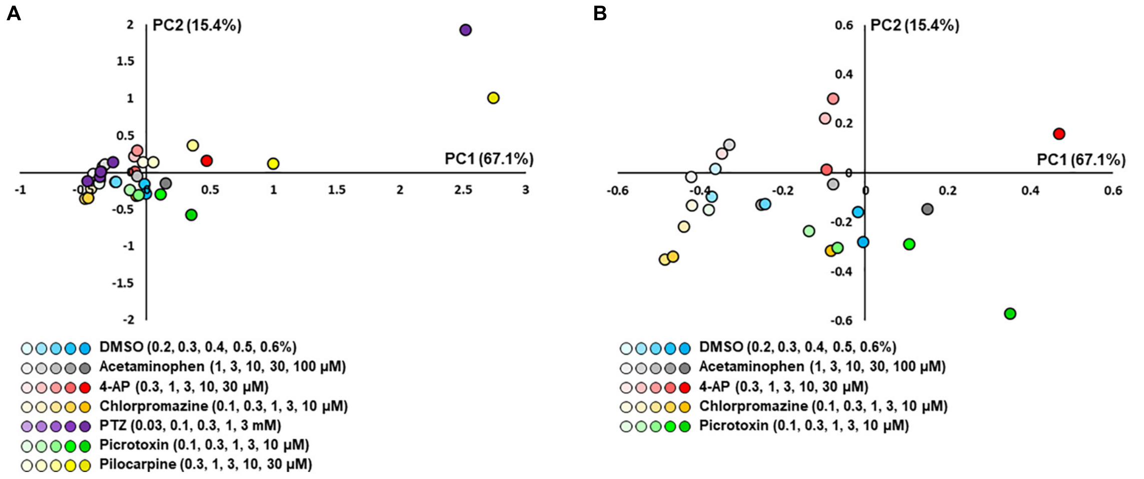

FIGURE 7
Scatterplots of PCA using the effective parameter set for detecting the drug responses of iPSC-derived astrocytes. **(A)** DMSO (*n* = 6, blue), acetaminophen (*n* = 6, gray), 4-AP (*n* = 6, red), chlorpromazine (*n* = 6, orange), PTZ (*n* = 6, purple), picrotoxin (*n* = 6, green), and pilocarpine (*n* = 6, yellow). Higher concentrations are indicated by darker colored symbols. **(B)** The magnified scatterplots excluding the plots of pilocarpine and PTZ.

TABLE 5 Statistical analysis for PCA using effective parameter set for detecting the drug responses in human iPSC-derived astrocytes.

	vs. DMSO	vs. Acetaminophen	vs. 4-AP	vs. Chlorpromazine	vs. PTZ	vs. Picrotoxin	vs. Pilocarpine
Compounds	p value	p value	p value	p value	p value	p value	p value
DMSO	—	p = 0.101	**p = 4.30e-06	**p = 8.50e-07	**p = 1.12e-11	** p = 7.16e-06	**p = 1.92e-21
Acetaminophen	p = 0.101	—	**p = 5.66e-3	**p = 2.35e-09	**p = 2.62e-07	** p = 3.26e-07	**p = 1.35e-17
4-AP	**p = 4.30e-06	**p = 5.66e-3	—	**p = 4.1e-09	*p = 0.032	** p = 5.09e-13	**p = 1.12e-07
Chlorpromazine	**p = 8.50e-07	**p = 2.35e-09	**p = 4.1e-09	—	**p = 2.13e-12	** p = 6.44e-06	**p = 1.94e-22
PTZ	**p = 1.12e-11	**p = 2.62e-07	*p = 0.032	**p = 2.13e-12	—	** p = 1.39e-19	**p = 6.47e-06
Picrotoxin	**p = 7.16e-06	**p = 3.26e-07	**p = 5.09e-13	**p = 6.44e-06	**p = 1.39e-19	—	**p = 7.88e-26
Pilocarpine	**p = 1.92e-21	**p = 1.35e-17	**p = 1.12e-07	$^{**}p$ = 1.94e-22	**p = 6.47e-06	**p = 7.88e-26	—

4-AP ($n = 6$), pilocarpine ($n = 6$), picrotoxin ($n = 6$), PTZ ($n = 6$), chlorpromazine ($n = 6$), acetaminophen ($n = 6$), and DMSO ($n = 6$). One-way MANOVA. $^{*}p < 0.05$, $^{**}p < 0.01$.

this study to each drug showed different trends and were separated in PCA (**Figures 5**, **7**). PTZ has been reported to inhibit the GABAA receptor by interacting with the picrotoxin-barbiturate binding site, closing Cl^{-} channels, and provoking seizures (Qu et al., 2005). Similarly, Fraser et al. (1995) have shown that treatment of astrocytes with picrotoxin inhibits GABAA-activated Cl^{-} conductance by using whole-cell patch clamping. These reports suggested that the astrocyte responses to picrotoxin and PTZ in this study involves changes in Cl ion concentration. However, PTZ has been reported to affect mitochondrial metabolism and glycolysis in cortical and cerebellar astrocytes in culture (Qu et al., 2005). Another group has demonstrated that mitochondria presenting within the fine processes of astrocytes contribute to local Ca^{2+} signaling within the astrocyte (Jackson and Robinson, 2018). These reports suggest that PTZ may be involved in Ca^{2+} signaling as well as Cl^{-} signaling. Experiments on zebrafish compared the effects of picrotoxin and PTZ and demonstrated that each drug has a different mechanism *in vivo* (Yang et al., 2017). Our PCA results demonstrated that the drug responses of PTZ and picrotoxin were separated in the primary and iPSC-derived astrocytes (**Figures 5**, **7**). This indicated that our evaluation system assessed the subtle differences in the mechanism of action of each drug.

4-AP, a typical seizurogenic compound, showed a comparable response to neutral controls in both primary astrocytes and iPSC-derived astrocytes (**Figures 4**, **6**). Recently, it has been reported that astrocytes have a protective function for neurons during seizures induced by 4-AP in neuron-astrocyte co-cultures (Ahtiainen et al., 2021). 4-AP is a voltage-gated K^{+} channel blocker. Astrocytes express voltage-gated K^{+} channels and non-voltage-gated K^{+} channels (e.g., Kir channels, Na^{+}/K^{+}-ATPase, and $Na^{+}/K^{+}/2Cl^{-}$ cotransporters). Ahtiainen et al. (2021) suggested that the protective role of astrocytes under 4-AP treatment may have been due to the non-voltage-gated K^{+} channels in astrocytes that maintained K^{+} homeostasis. In the present study, it was possible that astrocytes may have maintained K^{+} via the non-voltage-gated K^{+} channel, which was not inhibited by 4-AP, resulting in no significant change in K^{+} and a response comparable to that of the negative compound. From these results of drug responses, we demonstrated that it is possible to measure astrocyte drug response using MEA. Our results of the drug response showed that astrocytes responded differently to each drug, suggesting that the oscillation pattern of astrocytes is a phenomenon caused by the balance of factors on which each drug acts, such as K^{+}, Cl^{-}, and Ca^{2+}. The PCA in this study might have captured the changes in oscillation patterns resulted from those ion balance and successfully separated drug reactions (**Figures 5**, **7**). However, the physiological relevance of each parameter and channel responses has not yet been understood. In order to develop MEA measurements of astrocytes, this is an important issue to be resolved in the future.

For drug responses, both astrocytes demonstrated the dose-dependent response to pilocarpine and showed the negative response to chlorpromazine. These results indicated that our MEA method for cultured astrocytes could assess drug responses even in astrocytes derived from different cell sources. However, slightly different responses were observed between the two cell types. Primary astrocytes responded more strongly to drugs than did human iPSC-derived astrocytes. These observed differences between primary astrocytes and iPSC-derived astrocytes may be due to astrocyte maturity, but they may also be due to the diversity of gene expression in astrocytes. Lundin et al. (2018) reported large diversity among astrocytic models derived from various sources using several analytical methods, including transcriptomic and proteomic analyses. The PCA results also suggested that primary astrocytes and iPSC-derived astrocytes have different properties, since the parameter sets of primary and iPSC-derived astrocytes were different. The parameters of the set showed that primary astrocytes had more delta components than iPSC-derived astrocytes. This suggests that different cells may have slightly different main frequency bands for astrocyte signals. The correlation between astrocyte diversity and the differences in drug response in each astrocyte in the MEA measurement should be evaluated in the future.

MEA is a measurement method with high temporal resolution and noninvasiveness that enables long-term electrical activity recording. In the current astrocyte research, two major methods are used to assess real-time astrocyte electrophysiological activity: one is the traditional patch clamp method, and the other is the Ca imaging, which has been used extensively in astrocyte research since the 1990s. In addition to these methods, the evaluation of extracellular potential activity of astrocytes using the MEA method proposed here is expected to enable more detailed analysis of astrocyte activity. In recent years, the involvement of glia in various neurological diseases has been reported, and studies using patient iPSC-derived astrocytes for Rett syndrome, Alexander's disease, Alzheimer's disease, and autism spectrum disorder, in which astrocytes are thought to be involved, are actively conducted (Williams et al., 2014; Kondo et al., 2016; Jones et al., 2017; Russo et al., 2018; Salcedo et al., 2021; Allen et al., 2022). We expect that the MEA-based system for assessing astrocyte activity will not only provide new insights into the mechanisms of neurological diseases, including epilepsy, but will also help in the evaluation of drug efficacy in the drug development for astrocyte related diseases.

Data availability statement

The raw data supporting the conclusions of this article will be made available by the authors, without undue reservation.

Author contributions

TK, NM, and IS designed the research. TK performed the research. TK, NM, and YI analyzed the data. TK and IS wrote the manuscript. All authors contributed to the article and approved the submitted version.

Funding

This study was supported by the grant of AMED, Grant Numbers 20be0304401h0401 and 22be1004203h001.

Acknowledgments

We thank Alpha Med Scientific for supporting this research.

Conflict of interest

The authors declare that the research was conducted in the absence of any commercial or financial relationships that could be construed as a potential conflict of interest.

Publisher's note

Supplementary material

The Supplementary Material for this article can be found online at: https://www.frontiersin.org/articles/10.3389/fnins.2022.1050150/full#supplementary-material

SUPPLEMENTARY FIGURE 1
Spontaneous activity in human iPSC-derived astrocytes detected by MEA. **(A,B)** Immunofluorescent images of astrocytes cultured on MEA at 35 DIV. Immunocytochemistry of GFAP (green), human nuclei (red), cell nuclei by Hoechst 33258 (blue), merged images in **(A)** and MAP2 (red) in **(B)**. Scale bar = 200 μm. **(C)** Representative oscillation waveform at the spontaneous activity measurement for 10 min at 14 DIV. **(D)** The magnified waveform of the red underlined time in **(C)**. **(E)** Plot of maximum amplitude in 10 min oscillation waveform of each well. Error bars indicate the SEM.

References

Ahtiainen, A., Genocchi, B., Tanskanen, J., Barros, M., Hyttinen, J., and Lenk, K. (2021). Astrocytes exhibit a protective role in neuronal firing patterns under chemically induced seizures in neuron–astrocyte co-cultures. *Int. J. Mol. Sci.* 22:12770. doi: 10.3390/ijms222312770

Allen, M., Huang, B., Notaras, M., Lodhi, A., Barrio-Alonso, E., Lituma, P., et al. (2022). Astrocytes derived from ASD individuals alter behavior and destabilize neuronal activity through aberrant Ca2+ signaling. *Mol. Psychiatry* 27, 2470–2484. doi: 10.1038/s41380-022-01486-x

Amin, H., Maccione, A., Marinaro, F., Zordan, S., Nieus, T., and Berdondini, L. (2016). Electrical responses and spontaneous activity of human iPS-derived neuronal networks characterized for 3-month culture with 4096-electrode arrays. *Front. Neurosci.* 10:121. doi: 10.3389/fnins.2016.00121

Autar, K., Guo, X., Rumsey, J., Long, C., Akanda, N., Jackson, M., et al. (2022). A functional hiPSC-cortical neuron differentiation and maturation model and its application to neurological disorders. *Stem Cell Rep.* 17, 96–109. doi: 10.1016/j.stemcr.2021.11.009

Bal, A., Bachelot, T., Savasta, M., Manier, M., Verna, J., Benabid, A., et al. (1994). Evidence for dopamine D2 receptor mRNA expression by striatal astrocytes in culture: In situ hybridization and polymerase chain reaction studies. *Mol. Brain Res.* 23, 204–212. doi: 10.1016/0169-328x(94)90227-5

Bindocci, E., Savtchouk, I., Liaudet, N., Becker, D., Carriero, G., and Volterra, A. (2017). Three-dimensional Ca2+ imaging advances understanding of astrocyte biology. *Science* 356:eaai8185.

Bradley, J., Luithardt, H., Metea, M., and Strock, C. (2018). In vitro screening for seizure liability using microelectrode array technology. *Toxicol. Sci.* 163, 240–253.

Brenner, M., Johnson, A., Boespflug-Tanguy, O., Rodriguez, D., Goldman, J., and Messing, A. (2001). Mutations in GFAP, encoding glial fibrillary acidic protein, are associated with Alexander disease. *Nat. Genet.* 27, 117–120.

Chu, C., Lin, Y., and Liang, W. (2022). The impact of the antipsychotic medication chlorpromazine on cytotoxicity through Ca2+ signaling pathway in glial cell models. *Neurotox. Res.* 40, 791–802. doi: 10.1007/s12640-022-00507-5

Fan, J., Thalody, G., Kwagh, J., Burnett, E., Shi, H., Lewen, G., et al. (2019). Assessing seizure liability using multi-electrode arrays (MEA). *Toxicol. Vitro* 55, 93–100. doi: 10.1016/j.tiv.2018.12.001

Fleischer, W., Theiss, S., Slotta, J., Holland, C., and Schnitzler, A. (2015). High-frequency voltage oscillations in cultured astrocytes. *Physiol. Rep.* 3, 1–20.

Fraser, D., Duffy, S., Angelides, K., Perez-Velazquez, J., Kettenmann, H., and MacVicar, B. (1995). GABAA/benzodiazepine receptors in acutely isolated hippocampal astrocytes. *J. Neurosci.* 15, 2720–2732. doi: 10.1523/JNEUROSCI.15-04-02720.1995

Frega, M., van Gestel, S., Linda, K., van der Raadt, J., Keller, J., van Rhijn, J., et al. (2017). Rapid neuronal differentiation of induced pluripotent stem cells for measuring network activity on micro-electrode arrays. *J. Vis. Exp.* 119:54900. doi: 10.3791/54900

Grainger, A., King, M., Nagel, D., Parri, H., Coleman, M., and Hill, E. (2018). In vitro models for seizure-liability testing using induced pluripotent stem cells. *Front. Neurosci.* 12:590. doi: 10.3389/fnins.2018.00590

Gross, G. (1979). Simultaneous single unit recording in vitro with a photoetched laser deinsulated gold multimicroelectrode surface. *IEEE Trans. Biomed. Eng.* 26, 273–279. doi: 10.1109/tbme.1979.326402

Gross, G., Rieske, E., Kreutzberg, G., and Meyer, A. (1977). A new fixed-array multi-microelectrode system designed for long-term monitoring of extracellular single unit neuronal activity in vitro. *Neurosci. Lett.* 6, 101–105. doi: 10.1016/0304-3940(77)90003-9

Guizzetti, M., Costa, P., Peters, J., and Costa, L. (1996). Acetylcholine as a mitogen: Muscarinic receptor-mediated proliferation of rat astrocytes and human astrocytoma cells. *Eur. J. Pharmacol.* 297, 265–273. doi: 10.1016/0014-2999(95)00746-6

Heuser, K., and Enger, R. (2021). Astrocytic Ca2+ signaling in epilepsy. *Front. Cell. Neurosci.* 15:695380. doi: 10.3389/fncel.2021.695380

Ikeda, A., Takeyama, H., Bernard, C., Nakatani, M., Shimotake, A., Daifu, M., et al. (2020). Active direct current (DC) shifts and "Red slow": Two new concepts for seizure mechanisms and identification of the epileptogenic zone. *Neurosci. Res.* 156, 95–101. doi: 10.1016/j.neures.2020.01.014

Ishibashi, Y., Odawara, A., Kinoshita, K., Okamura, A., Shirakawa, T., and Suzuki, I. (2021). Principal component analysis to distinguish seizure liability of drugs in human iPS cell-derived neurons. *Toxicol. Sci.* 184, 265–275. doi: 10.1093/toxsci/kfab116

Jackson, J., and Robinson, M. (2018). Regulation of mitochondrial dynamics in astrocytes: Mechanisms, consequences, and unknowns. *Glia* 66, 1213–1234. doi: 10.1002/glia.23252

Jobling, D., Smith, J., and Wheal, H. V. (1981). Active microelectrode array to record from the mammalian central nervous systemin vitro. *Med. Biol. Eng. Comput.* 19, 553–560. doi: 10.1007/BF02442768

Johnstone, A., Gross, G., Weiss, D., Schroeder, O., Gramowski, A., and Shafer, T. (2010). Microelectrode arrays: A physiologically based neurotoxicity testing platform for the 21st century. *Neurotoxicology* 31, 331–350. doi: 10.1016/j.neuro.2010.04.001

Jones, V., Atkinson-Dell, R., Verkhratsky, A., and Mohamet, L. (2017). Aberrant iPSC-derived human astrocytes in Alzheimer's disease. *Cell Death Dis.* 8:e2696.

Khan, S., Dyer, J., and Michelangeli, F. (2001). Inhibition of the type 1 inositol 1,4,5-trisphosphate-sensitive Ca2+ channel by calmodulin antagonists. *Cell Signal.* 13, 57–63. doi: 10.1016/s0898-6568(00)00140-6

Kondo, T., Funayama, M., Miyake, M., Tsukita, K., Era, T., Osaka, H., et al. (2016). Modeling Alexander disease with patient iPSCs reveals cellular and molecular pathology of astrocytes. *Acta Neuropathol. Commun.* 4:69.

Liddelow, S. A., Guttenplan, K. A., Clarke, L. E., Bennett, F. C., Bohlen, C. J., Schirmer, L., et al. (2017). Neurotoxic reactive astrocytes are induced by activated microglia. *Nature* 541, 481–487.

Lundin, A., Delsing, L., Clausen, M., Ricchiuto, P., Sanchez, J., Sabirsh, A., et al. (2018). Human iPS-derived Astroglia from a stable neural precursor state show improved functionality compared with conventional Astrocytic models. *Stem Cell Rep.* 10, 1030–1045. doi: 10.1016/j.stemcr.2018.01.021

Martin-Fernandez, M., Jamison, S., Robin, L., Zhao, Z., Martin, E. D., Aguilar, J., et al. (2017). Synapse-specific astrocyte gating of amygdala-related behavior. *Nat. Neurosci.* 20, 1540–1548. doi: 10.1038/nn.4649

Miyazaki, I., Asanuma, M., Diaz-Corrales, F., Miyoshi, K., and Ogawa, N. (2004). Direct evidence for expression of dopamine receptors in astrocytes from basal ganglia. *Brain Res.* 1029, 120–123.

Mukai, T., Kinboshi, M., Nagao, Y., Shimizu, S., Ono, A., Sakagami, Y., et al. (2018). Antiepileptic drugs elevate astrocytic Kir4.1 expression in the rat limbic region. *Front. Pharmacol.* 9:845. doi: 10.3389/fphar.2018.00845

Murphy, S., Pearce, B., and Morrow, C. (1986). Astrocytes have both M1 and M2 muscarinic receptor subtypes. *Brain Res.* 364, 177–180.

Novak, J., and Wheeler, B. (1988). Multisite hippocampal slice recording and stimulation using a 32 element microelectrode array. *J. Neurosci. Methods* 23, 149–159. doi: 10.1016/0165-0270(88)90187-2

Odawara, A., Katoh, H., Matsuda, N., and Suzuki, I. (2016). Physiological maturation and drug responses of human induced pluripotent stem cell-derived cortical neuronal networks in long-term culture. *Sci. Rep.* 6:26181. doi: 10.1038/srep26181

Odawara, A., Matsuda, N., Ishibashi, Y., Yokoi, R., and Suzuki, I. (2018). Toxicological evaluation of convulsant and anticonvulsant drugs in human induced pluripotent stem cell-derived cortical neuronal networks using an MEA system. *Sci. Rep.* 8:10416. doi: 10.1038/s41598-018-28835-7

Odawara, A., Saitoh, Y., Alhebshi, A., Gotoh, M., and Suzuki, I. (2014). Long-term electrophysiological activity and pharmacological response of a human induced pluripotent stem cell-derived neuron and astrocyte co-culture. *Biochem. Biophys. Res. Commun.* 443, 1176–1181. doi: 10.1016/j.bbrc.2013.12.142

Odawara, A., Shibata, M., Ishibashi, Y., Nagafuku, N., Matsuda, N., and Suzuki, I. (2022). In vitro pain assay using human iPSC-derived sensory neurons and microelectrode array. *Toxicol. Sci.* 188, 131–141. doi: 10.1093/toxsci/kfac045

Onodera, M., Meyer, J., Furukawa, K., Hiraoka, Y., Aida, T., Tanaka, K., et al. (2021). Exacerbation of epilepsy by astrocyte alkalization and gap junction uncoupling. *J. Neurosci.* 41, 2106–2118. doi: 10.1523/JNEUROSCI.2365-20.2020

Perea, G., Navarrete, M., and Araque, A. (2009). Tripartite synapses: Astrocytes process and control synaptic information. *Trends Neurosci.* 32, 421–431.

Pine, J. (1980). Recording action potentials from cultured neurons with extracellular microcircuit electrodes. *J. Neurosci. Methods* 2, 19–31.

Plenge-Tellechea, F., Domínguez-Solís, C., Díaz-Sánchez, Á. G., Meléndez-Martínez, D., Vargas-Medrano, J., and Sierra-Fonseca, J. (2018). Chlorpromazine and dimethyl sulfoxide modulate the catalytic activity of the plasma membrane Ca 2 + –ATPase from human erythrocyte. *J. Bioenerg. Biomembr.* 50, 59–69. doi: 10.1007/s10863-017-9741-9

Pré, D., Wooten, A., Biesmans, S., Hinckley, S., Zhou, H., Sherman, S., et al. (2022). Development of a platform to investigate long-term potentiation in human iPSC-derived neuronal networks. *Stem Cell Rep.* 17, 2141–2155. doi: 10.1016/j.stemcr.2022.07.012

Qu, H., Eloqayli, H., and Sonnewald, U. (2005). Pentylenetetrazole affects metabolism of astrocytes in culture. *J. Neurosci. Res.* 79, 48–54.

Russo, F., Freitas, B., Pignatari, G., Fernandes, I., Sebat, J., Muotri, A., et al. (2018). Modeling the interplay between neurons and astrocytes in autism using human induced pluripotent stem cells. *Biol. Psychiatry* 83, 569–578. doi: 10.1016/j.biopsych.2017.09.021

Salcedo, C., Andersen, J. V., Vinten, K., Pinborg, L., Waagepetersen, H., Freude, K., et al. (2021). Functional metabolic mapping reveals highly active branched-chain amino acid metabolism in human astrocytes, which is impaired in iPSC-derived astrocytes in Alzheimer's disease. *Front. Aging Neurosci.* 13:736580. doi: 10.3389/fnagi.2021.736580

Sano, F., Shigetomi, E., Shinozaki, Y., Tsuzukiyama, H., Saito, K., Mikoshiba, K., et al. (2021). Reactive astrocyte-driven epileptogenesis is induced by microglia initially activated following status epilepticus. *JCI Insight* 6:e135391. doi: 10.1172/jci.insight.135391

Sharf, T., van der Molen, T., Glasauer, S., Guzman, E., Buccino, A., Luna, G., et al. (2022). Functional neuronal circuitry and oscillatory dynamics in human brain organoids. *Nat. Commun.* 13:4403. doi: 10.1038/s41467-022-32115-4

Thomas, C., Springer, P., Loeb, G., Berwald-Netter, Y., and Okun, L. (1972). A miniature microelectrode array to monitor the bioelectric activity of cultured cells. *Exp. Cell Res.* 74, 61–66. doi: 10.1016/0014-4827(72)90481-8

Trujillo, C. A., Gao, R., Negraes, P. D., Gu, J., Buchanan, J., Preissl, S., et al. (2019). Complex oscillatory waves emerging from cortical organoids model early human brain network development. *Cell Stem Cell* 25, 558–569.e7. doi: 10.1016/j.stem.2019.08.002

Tukker, A., van Kleef, R., Wijnolts, F., de Groot, A., and Westerink, R. (2020). Towards animal-free neurotoxicity screening: Applicability of hiPSC-derived neuronal models for in vitro seizure liability assessment. *ALTEX* 37, 121–135. doi: 10.14573/altex.1907121

Tukker, A., Wijnolts, F., de Groot, A., and Westerink, R. (2018). Human iPSC-derived neuronal models for in vitro neurotoxicity assessment. *Neurotoxicology* 67, 215–225.

Ullah, G., Cressman, J. R. Jr., Barreto, E., and Schiff, S. J. (2009). The influence of sodium and potassium dynamics on excitability, seizures, and the stability of persistent states: II. Network and glial dynamics. *J. Comput. Neurosci.* 26, 171–183. doi: 10.1007/s10827-008-0130-6

Wheeler, B., and Novak, J. (1986). Current source density estimation using microelectrode array data from the hippocampal slice preparation. *IEEE Trans. Biomed. Eng.* 33, 1204–1212. doi: 10.1109/TBME.1986.325701

Williams, E., Zhong, X., Mohamed, A., Li, R., Liu, Y., Dong, Q., et al. (2014). Mutant astrocytes differentiated from Rett syndrome patients-specific iPSCs have adverse effects on wildtype neurons. *Hum. Mol. Genet.* 23, 2968–2980. doi: 10.1093/hmg/ddu008

Yang, X., Lin, J., Peng, X., Zhang, Q., Zhang, Y., Guo, N., et al. (2017). Effects of picrotoxin on Zebrafish larvae behaviors: A comparison study with PTZ. *Epilepsy Behav.* 70, 224–231. doi: 10.1016/j.yebeh.2017.03.023

Yokoi, R., Shibata, M., Odawara, A., Ishibashi, Y., Nagafuku, N., Matsuda, N., et al. (2021). Analysis of signal components < 500 Hz in brain organoids coupled to microelectrode arrays: A reliable test-bed for preclinical seizure liability assessment of drugs and screening of antiepileptic drugs. *Biochem. Biophys. Rep.* 28:101148. doi: 10.1016/j.bbrep.2021.101148

Zanassi, P., Paolillo, M., Montecucco, A., Avvedimento, E. V., and Schinelli, S. (1999). Pharmacological and molecular evidence for dopamine D1 receptor expression by striatal astrocytes in culture. *J. Neurosci. Res.* 58, 544–552. doi: 10.1002/(sici)1097-4547(19991115)58:4<544::aid-jnr7>3.0.co;2-9

frontiers | Frontiers in Neuroscience

TYPE Original Research
PUBLISHED 10 January 2023
DOI 10.3389/fnins.2022.1003984

OPEN ACCESS

EDITED BY
Yin Tian,
Chongqing University of Posts and Telecommunications, China

REVIEWED BY
Ivan Zubarev,
Aalto University, Finland
Robyn Miller,
Georgia State University, United States

*CORRESPONDENCE
Abner Cardoso Rodrigues
abner.neto@isd.org.br

SPECIALTY SECTION
This article was submitted to Neural Technology, a section of the journal Frontiers in Neuroscience

RECEIVED 26 July 2022
ACCEPTED 22 November 2022
PUBLISHED 10 January 2023

CITATION
de Oliveira IH and Rodrigues AC (2023) Empirical comparison of deep learning methods for EEG decoding. *Front. Neurosci.* 16:1003984. doi: 10.3389/fnins.2022.1003984

Empirical comparison of deep learning methods for EEG decoding

Iago Henrique de Oliveira and Abner Cardoso Rodrigues*

Graduate Program in Neuroengineering, Edmond and Lily Safra International Institute of Neuroscience, Santos Dumont Institute, Macaiba, Brazil

Electroencephalography (EEG) is a technique that can be used in non-invasive brain-machine interface (BMI) systems to register brain electrical activity. The EEG signals are non-linear and non-stationary, making the decoding procedure a complex task. Deep learning techniques have been successfully applied in several research fields, often improving the results compared with traditional approaches. Therefore, it is believed that these techniques can also improve the process of decoding brain signals in BMI systems. In this work, we present the implementation of two deep learning-based decoders and we compared the results with other state of art deep learning methods. The first decoder uses long short-term memory (LSTM) recurrent neural network and the second, entitled EEGNet-LSTM, combines a well-known neural decoder based on convolutional neural networks, called EEGNet, with some LSTM layers. The decoders have been tested using data set 2a from BCI Competition IV, and the results showed that the EEGNet-LSTM decoder has been approximately 23% better than the competition-winning decoder. A Wilcoxon *t*-test showed a significant difference between the two decoders ($Z = 2.524$, $p = 0.012$). The LSTM-based decoder has been approximately 9% higher than the best decoder from the same competition. However, there was no significant difference ($Z = 1.540$, $p = 0.123$). In order to verify the replication of the EEGNet-LSTM decoder on another data, we performed a test with PhysioNet's Physiobank EEG Motor Movement/Imagery dataset. The EEGNet-LSTM presented a higher performance (0.85 accuracy) than the EEGNet (0.82 accuracy). The results of this work can be important for the development of new research, as well as EEG-based BMI systems, which can benefit from the high precision of neural decoders.

KEYWORDS

brain machine interface, deep learning, long short term memory, EEG, machine learning

1. Introduction

Brain-machine interfaces (BMI) aim to translate brain signals into commands that allow the control of machines or computer interfaces (Niemeyer, 2016). One of BMI's best-known paradigms is motor imagery, which refers to the act of imagining a movement without executing it (Mulder, 2007). Thus, if a system can correctly classify the brain signals patterns of motor imagery, patients without motor function can benefit from prostheses, orthoses, exoskeletons, and other neuroprosthetic devices, controlled using thought.

A common method used to record brain electrical activity in non-invasive BMI systems is electroencephalography (EEG) (Bansal and Mahajan, 2019). The EEG signals have complex non-linear properties, low spatial resolution, and are non-stationary (Bhuvaneswari and Kumar, 2015). These limitations make decoding EEG signals a complex and challenging task.

Several statistical methods can be used as neural decoders in BMI systems, such, as an example, Kalman filter (Alarcón-Domínguez, 2017) and linear discriminant analysis (Ahangi et al., 2012). However, as deep learning (DL) is adequate for this purpose, some works are analyzing its feasibility.

Decoders based on convolutional neural networks have been successful in decoding brain signals (Tabar and Halici, 2016; Tang et al., 2017; Lun et al., 2020). EEGNet is a neural decoder based on convolutional neural networks, which was proposed by Lawhern et al. (2018) for the classification of EEG signals showing good performance. Some research has made efforts to improve its performance by combining it with other models, achieving success (Riyad et al., 2020; Wang L. et al., 2020).

The work by Tseng et al. (2019) showed that in some cases, neural decoders based on recurrent neural networks of the long-short term memory (LSTM) type, surpassed traditional decoding methods, such as Kalman filter, wiener filter, and extended Kalman filter.

Besides the relative success in using DL as a decoder in BMI systems, some works are reporting less favorable results, for example, the work of Tseng et al. (2019) employed a LSTM decoder using data from implanted electrodes in three macaques controlling a prosthesis. The results were superior to traditional filter methods for some macaques in some trials but there has not been an overall improvement. These mixed results are due to the large number of hyperparameters that must be evaluated in DL systems, compared to filter methods.

In this work, two neural decoders were implemented. The first neural decoder is based on LSTM, where the characteristics of frequency, time, and space of the signals are extracted separately, through the combination of wavelet packet decomposition (WPD) and common spatial pattern (CSP). This step of pre-processing was chosen based on results presented in the literature (Yang et al., 2012; Feng et al., 2019). The second decoder was called EEGNet-LSTM and combines the features of both models, extracting the characteristics simultaneously with the classification.That decoder is similar to the best decoder implemented by Wang L. et al. (2020), however with differences in the architecture and selection of hyperparameters of the decoder and strategies for data pre-processing.

In both decoders, we exhaustively employed grid search for hyperparameters optimizations, as we believe that is an essential step, to use DL techniques in neural decoding successfully. We detailed all these steps and this may be useful for works that will test DL in BMI in the future.

The neural decoders have been tested with data set 2a from BCI Competition IV (Brunner et al., 2008), which has two motor imaging sessions for four classes (left hand, right hand, both feet, and tongue). To evaluate the performance of the decoders we used two metrics: accuracy and kappa value. We compared the results of the two implemented decoders with each other, as well as with the results obtained by decoders implemented in other works. We found that our deep learning decoders were 23% and 5% better than the best decoder in the competition. We also tested the LSTM-EEG decoder with data from Physiobank EEG Motor Movement/Imagery dataset from PhysioNet, considering two classes of motor imagery (left wrist and right wrist). The EEGNet-LSTM achieved an accuracy of 0.85. The original EEGNet, which was tested by other researchers with the same dataset, showed an accuracy of 0.82.

2. Materials and methods

2.1. Long short-term memory

The recurrent neural networks long short-term memory (LSTM) can process long data sequences while avoiding gradient vanishing problems (Hochreiter and Schmidhuber, 1997). LSTM networks have a memory cell, called cell state, which is long-term memory, capable of storing information for a long period. Besides, LSTM memory cells have three kinds of gates that control the flow of information, namely: forget gate, input gate and output gate (Du et al., 2021). The update of the memory cell, at each time step, is determined by the following equations (Jiao et al., 2020):

$$f_t = \sigma(w_f \cdot [h_{t-1}, x_t] + b_f) \tag{1}$$

The Equation (1) is the forget gate f_t, which indicates the information that will be forgotten in the state of the cell. The w_f symbolizes the forget gate weights, h_{t-1} is the cell's previous output, x_t is the network input, b_f is the bias associated with forget gate.

$$i_t = \sigma(w_i \cdot [h_{t-1}, x_t] + b_i) \tag{2}$$

$$\tilde{C}_t = \sigma(w_c \cdot [h_{t-1}, x_t] + b_c) \tag{3}$$

The input gate i_t is defined by Equation (2), which determines the cell state values that will be updated. The w_i symbolizes the weights and b_i represents the bias associated with the input gate. In Equation (3), $\tilde{C}_t$ is calculated, generating a vector of candidate values for the state of the cell. These values are calculated using the hyperbolic tangent as activation function. The weights and bias of the cell itself are w_c and b_c, respectively.

$$C_t = w_i * C_{t-1} + i_t + \tilde{C}_t \tag{4}$$

TABLE 1 EEGNet architecture based on convolutional block, the output from previous bloc neural networks.

Block	Layer	Filters	Size	Activation	Mode
1	Input				
	Reshape				
	Conv2D	F1	(1, LK)	Linear	Same
	BatchNorm				
	DepthwiseConv2D	D * F1	(C, 1)	Linear	Valid
	BatchNorm				
	Activation			ELU	
	AveragePool2D		(1, 4)		
	Dropout				
2	SeparableConv2D	F2	(1, 16)	Linear	Same
	BatchNorm				
	Activation			ELU	
	AveragePool2D		(1, 8)		
	Dropout				
	Flatten				
Classifier	Dense	N * (F2 * T // 32)		Softmax	

In Equation (4), the result of the previous equations is used to update the state of the cell, where C_t is the current state of the cell.

$$o_t = \sigma(w_o \cdot [h_{t-1}, x_t] + b_o) \tag{5}$$

$$h_t = o_t * \tanh(C_t) \tag{6}$$

Equation (5) is the output gate o_t, which decides the values of the current state of the cell that will be considered in the cell's output. The gate weights are represented by w_o and the bias is b_o. The calculation of the output of cell h_t is shown in Equation (6).

2.2. EEGNet

EEGNet is a deep learning model based on convolutional neural networks proposed by Lawhern et al. (2018) to be used in classification of EEG signals in BCI systems. This model uses deep and separable convolutions, performing the extraction of signal features and classification at same time.

Table 1 shows the model's architecture, where C denotes the number of channels, T represents the number of points in time, $F1$ is the number of time filters, D is the number of spatial filters, $F2$ represents the number of point filters, N is the number of classes and, LK is the kernel size of the first layer, also called the temporal convolution length.

The model has two main blocks and a classification block. In the first block, Conv2D is a convolutional neural network. DepthwiseConv2D is a deep convolution used to learn spatial filters from the temporal convolution performed in the previous layer. The AveragePool2D layers are used in both blocks to reduce the signal-sampling rate. Batch normalization was proposed by Ioffe and Szegedy (2015) to normalize the data for a given layer, in EEGNet it is performed by BatchNorm applied to both blocks. Dropout is the dropout rate and was used in the model to reduce overfitting. In the second block, SeparableConv2D represents separable convolutions, which combine spatial filters in temporal bands. This layer performs a spatial convolution in each input channel and applies a specific convolution to mix the output Chollet (2017). Flatten was used to transform the output of the convolutional layers into a single vector.

In the classification block, the output from previous blocks is transformed by softmax function to perform the multiclass classification.

2.3. Wavelet packet decomposition

Wavelets are mathematical functions used to represent data or other functions, at different scales of time and frequency Jiang and Adeli (2004). The Wavelet Packet Decomposition (WPD) is a type of wavelet transform that decomposes a given signal into low-frequency components (approaches) and high-frequency components (details) Faust et al. (2013). Since WPD presents features in both time and frequency domains, this method is useful for parameters extraction from EEG signals, which are non-stationary and have characteristics of multi-scale and randomness Yang et al. (2016). According to Li and Zhou (2016), WPD can be defined recursively as:

$$\begin{cases} d_{0,0}(t) = x(t), \\ d_{i,2j-1}(t) = \sqrt{2}\sum_k h(k)d_{i-1,j}(2t-k), \\ d_{i,2j}(t) = \sqrt{2}\sum_k g(k)d_{i-1,j}(2t-k). \end{cases} \tag{7}$$

In Equation (7), $x(t)$ is the original signal, $h(k)$ is the high-pass filter, $g(k)$ is the low-pass filter, and $d_(i,j)$ are the coefficients of WPD at the $i-th$ level for the $j-th$ node (Li and Zhou, 2016).

2.4. Common spatial patterns

Common Spatial Patterns (CSP) is a spatial filtering technique widely used for the extraction of EEG features in non-invasive Brain-Computer Interface (BCI) systems (Song and Yoon, 2015). This technique finds spatial filters that will maximize the variance of signals from one class while minimizing the variance from another class, resulting in ideal discriminative features (Cheng et al., 2017). The equations of CSP are presented according to Wang et al. (2005) and

Huang et al. (2010):

$$R_H = \frac{X_H X_H{}^T}{trace(X_H X_H{}^T)} \qquad R_F = \frac{X_F X_F{}^T}{trace(X_F X_F{}^T)} \tag{8}$$

In Equation (8), assuming that the problem has two classes, R_H and R_F represent the normalized spatial co-variance of each class, X_H, and X_F are matrices of the EEG signals of the respective classes, X^T is the transposed from matrix X and, $trace(A)$ is the sum of the diagonal elements of matrix A.

$$R = \overline{R_H} + \overline{R_F} = U_0 D U_0{}^T \tag{9}$$

In Equation (9), the composite spatial co-variance R is calculated. $\overline{R_H}$ and $\overline{R_F}$ are the average normalized covariance, calculated using the average of the co-variance matrices of examples in each class. U_0 is the eigenvector matrix and D is the diagonal eigenvalue matrix of R.

$$P = D^{-1/2} U_0{}^T \tag{10}$$

In Equation (10), the bleaching matrix P is calculated, which equalizes the variance in the space defined by U_0.

$$S_H = P\overline{R_H}P^T \qquad S_F = P\overline{R_F}P^T \tag{11}$$

$$S_H = U D_H U^T \qquad S_F = U D_F U^T \qquad I = D_H + D_F \tag{12}$$

In Equation (11), the bleaching transformation is applied to $\overline{R_H}$ and $\overline{R_F}$, obtaining matrices S_H and S_F, which share the same eigenvectors. The identity matrix I is presented in Equation (12). The eigenvectors that have higher eigenvalues for S_H have smaller eigenvalues for S_F, that is, these quantities are inversely proportional, differentiating the classes.

$$W = U^T P \tag{13}$$

Equation (13) calculates the projection matrix W, which allows obtaining non-correlated components of the EEG signals.

$$Z = WX \tag{14}$$

In Equation (14), Z are the components of the signal X, aggregating common and class-specific components.

2.5. Description of the datasets

2.5.1. BCI competition IV

This paper used data set 2a from the BCI Competition IV (Brunner et al., 2008), which were registered and made publicly available by Graz University of Technology, located in Austria.

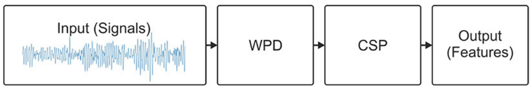

FIGURE 1
Features extraction steps for the LSTM decoder.

Nine subjects participated in the experiment, which consisted of two motor imaging sessions, held on different days. The objective of the experiment was to imagine four movements, namely, the movement of the left hand, right hand, both feet and, tongue. In each session, 288 attempts at motor imagery have been recorded, with 72 attempts for each movement. It is worth mentioning that each sample of motor imagery has 7.5 s, a time that includes the initial preparation, the realization of motor imagery, and a pause. During the experiment, 22 EEG channels and 3 electro-oculography (EOG) channels were recorded, with sampling rate of 250 Hz. The EEG and EOG electrodes can be consulted in Brunner et al. (2008).

The signals were filtered using a bandpass filter between 0.5 and 100 Hz. In addition, a notch filter was applied at 50 Hz to suppress the noise from the electrical network.

The EOG signals were not recorded correctly for the fourth subject. Therefore, this subject was not considered in this research.

2.5.2. Physiobank EEG motor movement/imagery dataset

To verify the replicability of the best neural decoder developed in this paper, we used the Physiobank EEG Motor Movement/Imagery dataset, freely available from PhysioNet (Goldberger et al., 2000).

One hundred and nine subjects participated in the experiment, which consisted in different tasks of movement execution and motor imagery. However, this paper focuses only on the task of imagining the opening and closing of the left or right wrist, that is, two classes of motor imagery.

During the experiment, a target was displayed on the left or right side of the screen and the subject imagined opening and closing the corresponding fist, until this target disappeared. Over three sessions, subjects performed a total of 45 trials, imagining one of the movements for 4 s. During the execution of the experiment, the brain signals of the subjects were recorded through 64 EEG channels using the international 10–10 system and the BCI2000 toolkit (Schalk et al., 2004), with a sampling rate of 160 Hz.

2.6. Implementation of the LSTM decoder

The extraction of features is an important step in the classification of EEG signals (Amin et al., 2017). Some works have used the combination of WPD and CSP to extract features and have achieved better results compared to the use of CSP only (Yang et al., 2012; Feng et al., 2019). In this research, we use a combination of WPD and CSP to extract important resources for the LSTM-based neural decoder. Initially, the preprocessed EEG signals are used as input to the four-level WPD, obtaining the coefficients of the wavelet transform. Then, the extraction of features from these coefficients was performed through the CSP. This process is shown in Figure 1.

For the implementation of the neural decoders, the python programming language (Python, 2020) and the keras library (Keras, 2020) were used. For the implementation of the LSTM-based decoder, an input layer was initially added to the model, allowing the input of features obtained through WPD and CSP. Inspired by the model that obtained the best performance in the work by Tseng et al. (2019), two LSTM layers were included in the model. After each LSTM layer, batch normalization was applied to normalize the outputs, and the dropout to avoid overfitting the model. Finally, a dense layer was inserted with the number of units equal to the number of classes in the data set used, and a softmax activation function was added, allowing multiclass classification. The architecture of the LSTM decoder is shown in Figure 2.

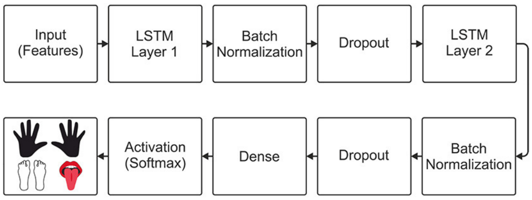

FIGURE 2
Architecture of the LSTM neural decoder.

2.7. Implementation of the EEGNet-LSTM decoder

For the implementation of the model proposed here, the two main blocks of the EEGNet model were used, as specified by Lawhern et al. (2018). Then, a layer was used to reshape the output of the last block of the EEGNet model and connect its output to the 2 LSTM layers. After each LSTM layer, batch normalization and dropout were used. A dense layer with the number of units equal to the number of classes and a softmax activation function for multiclass classification. The architecture of the EEGNet-LSTM decoder is shown in Figure 3.

2.8. Data pre-processing

2.8.1. Data preprocessing from BCI competition IV dataset 2a

As the preprocessing step is very important for the good performance of neural decoders, we tested four different bandpass filters. The first one was a bandpass filter between 0.5 and 100 Hz, the second was between 8 and 13 Hz (mu rhythm), the third was between 15 and 30 Hz (beta rhythm), and the fourth was between 8 and 30 Hz (mu and beta rhythms). The frequency ranges referring to mu and beta rhythms were defined according to Bear et al. (2020).

The labels of the four classes of motor imagery (left hand, right hand, both feet and tongue) were coded using one-hot encoding, respectively, in four-dimensional vectors: {[1, 0, 0, 0], [0, 1, 0, 0], [0, 0, 1, 0], [0, 0, 0, 1]}.

Then, only 4 s of each sample were selected. Among the 7.5 s of each sample, only signals registered between 2 and 6 s were considered, during which time a suggestion of motor imagery was presented on the screen and was performed by the subject. Finally, the data was normalized between −1 and 1.

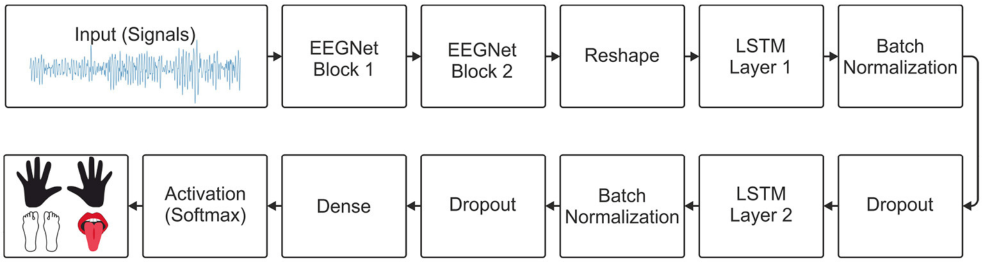

FIGURE 3
Architecture of the EEGNet-LSTM neural decoder.

TABLE 2 Common hyperparameters of both models.

Hyperparameter	Values
Optimizer	Adam, RMSprop, SGD
Learning rate	0.0001, 0.001, 0.01
Batch size	32, 64, 128
Regularization of L2	0.1, 0.2, 0.3
Dropout	0.1, 0.2, 0.3
Epochs	100, 200, 300, 400, 500, 1,000

2.8.2. Data preprocessing from the Physiobank EEG Motor Movement/Imagery dataset from PhysioNet

The same bandpass filters applied in the BCI Competition IV dataset 2a were applied to Physiobank data. As Wang X. et al. (2020) did not report the application of any filter, we also tested the use of raw signals, without any filtering. Additionally, we also tested a bandpass filter between 0.5 and 45 Hz.

Each motor imagery attempt has a duration of 4 s. However, we select only the first 3 s, as suggested by Wang X. et al. (2020). Thus, for each motor imagery attempt we have 480 samples for each of the 64 EEG channels.

Next, we separate the training and test data according to Wang X. et al. (2020). Data from subjects 1 (S001) to 84 (S084) were used as a training set. Subjects 85 (S085) to 109 (S109) were used as a test set.

In their paper, Wang X. et al. (2020) mentioned the removal of four subjects, but did not specify which ones. Thus, we removed subjects 88 (S088), 92 (S092), 100 (S100) and 104 (S104) because they were damaged, according to Varsehi and Firoozabadi (2021) and Fan et al. (2021).

The labels of the two classes of motor imagery (left wrist and right wrist) were coded using one-hot coding. Finally, we scaled brain signals between –1 and 1.

2.9. Hyperparameter optimization

2.9.1. Hyperparameter optimization of LSTM and EEGNet-LSTM decoders for BCI Competition IV dataset 2a

The hyperparameter optimization was performed using the data from first subject of the data set. Then, we freeze the parameters and used them to train the models for the other subjects.

The data set has two sessions, one used for training and the other for testing. For each configuration test, accuracy and value of the kappa coefficient (Cohen, 1960) were recorded, so that the best configuration was identified. Table 2 presents the common hyperparameters between the LSTM based decoder and the EEGNet plus LSTM decoder.

TABLE 3 Hyperparameters specific to the LSTM decoder.

Hyperparameter	Values
Neurons layer one	32, 64, 128, 256
Neurons layer two	32, 64, 128, 256

TABLE 4 Hyperparameters specific to the EEGNet decoder.

Hyperparameter	Values
LK	16, 32, 64, 128
F1	4, 6, 8, 16
F2	4, 6, 8, 16
D	1, 2, 4, 6

2.9.2. Adjusting hyperparameters of the LSTM decoder

Initially, the LSTM-based decoder was trained with 32 neurons in each layer, with different configurations shown in Table 2. The best configuration was maintained based on the highest accuracy and kappa value, and the decoder was tested with different amounts of neurons, according to Table 3.

Based on these tests, it was possible to identify an ideal configuration for the decoder and this configuration was used for the other subjects.

2.9.3. Adjusting hyperparameters of the EEGNet-LSTM decoder

The EEGNet-LSTM decoder has been trained with LK = 64, F1 = 8, *D* = 2 and F2 = 16, which are standard for EEGNet. In the LSTM layers, the same number of neurons obtained through tests with the LSTM-based decoder was maintained. Then, all configurations in Table 2 were tested, obtaining the best configuration for the model. Soon after, the hyperparameters of Table 4 were tested to identify the best configuration of the specific hyperparameters of EEGNet.

2.9.4. Hyperparameter optimization of the EEGNet-LSTM decoder for the Physiobank EEG motor movement/imagery dataset

To adjust the EEGNet-LSTM decoder hyperparameters for the Physiobank EEG Moviment/Imagery dataset, we performed the same steps performed for the previous dataset. The only difference is that for this dataset, we used a 30% of the data from the training set to use as a test during hyperparamer search, instead of using the first subject as we did with BCI data.

3. Results

3.1. Best hyperparameters for the implemented decoders

3.1.1. Best hyperparameters for decoders LSTM and EEGNet-LSTM using BCI Competition IV dataset 2a

After automatically making all possible combinations of the hyperparameters, the best settings for the two neural decoders were obtained. Table 5 presents the configurations (common between the two decoders) that provided the best results. Regarding the specific hyperparameters of the LSTM-based neural decoder, it presented better results with 32 neurons in each layer. For the EEGNet-LSTM neural decoder, the specific EEGNet configurations that generated the best results were F1 = 16, *D* = 6, F2 = 16 and FK = 16.

Regarding the filtering configuration, the best results were obtained through the standard filtering of the data set, that is, between 0.5 and 100 Hz. The best filtering and the best hyperparameters were used to decode the signals of all subjects.

3.1.2. Best hyperparameters for the EEGNet-LSTM decoder using the physiobank EEG motor movement/imagery dataset from PhysioNet

Table 6 presents the large search result, which returned the best combination of hyperparameters for the EEGNet-LSTM decoder, when using the Physiobank EEG Movement/Imagery dataset.

The best results were achieved after applying a bandpass filter between 0.5 and 45 Hz. This filtering and the best hyperparameters were used to train the EEGNet-LSTM and decode the data from the test dataset.

TABLE 5 Best selected hyperparameters for the decoders considering the data set 2a from BCI Competition IV.

Hyperparameter	LSTM	EEGNet-LSTM
Optimizer	Adam	Adam
Learning rate	0.0001	0.001
Batch size	64	32
Regularization of L2	0.2	0.2
Dropout	0.2	0.2
Epochs	200	400

TABLE 6 Best selected hyperparameters for the EEGNet-LSTM decoder considering the data set Physiobank EEG Motion/Imagery from PhysioNet.

Hyperparameter	EEGNet-LSTM
F1	16
D	4
F2	16
FK	16
Optimizer	Adam
Learning rate	0.01
Batch size	128
Regularization of L2	0.2
Dropout	0.2
Epochs	200

3.2. Comparison between the implemented decoders using BCI competition IV dataset 2a

Using the best configurations, the neural decoders were trained with the data from one session and tested with the data from another session, making it possible to evaluate their performance, in the classification of four classes of motor imagery.

Figure 4 shows the comparison graph between the accuracy of each subject, obtained through the two neural decoders implemented: LSTM and EEGNet-LSTM. The second decoder obtained a better result for all subjects, except subject 3, in which the two decoders presented equal accuracy. The average accuracy for the EEGNet-LSTM neural decoder was 0.86 and for the LSTM decoder, it was 0.72. Therefore, the average accuracy of the EEGNet-LSTM neural decoder was about 14% higher than the average accuracy of the LSTM decoder. A Wilcoxon *t*-test showed a significant difference between the accuracy of the neural decoders ($Z = 2.366$, $p = 0.018$).

Figure 5 shows the comparison bar plot between the kappa values obtained for each subject and the average value for each decoder. The LSTM decoder presented the average kappa value equal to 0.63 and the decoder that combines EEGNet and LSTM resulted in an average kappa value equal to 0.81. According to the interpretation suggested by Landis and Koch (1977), the first decoder presented a strong agreement, and the second, an almost perfect agreement. The average kappa value obtained using the EEGNet-LSTM neural decoder was approximately 18% higher than the average kappa value achieved by the LSTM decoder. A Wilcoxon *t*-test indicated a significant difference between the kappa values of the two decoders ($Z = 2.371$, $p = 0.018$).

3.3. Comparison with other results published in the literature that made use of the BCI competition IV dataset 2a

Table 7 presents a comparison between the kappa values obtained through the decoders implemented in the present

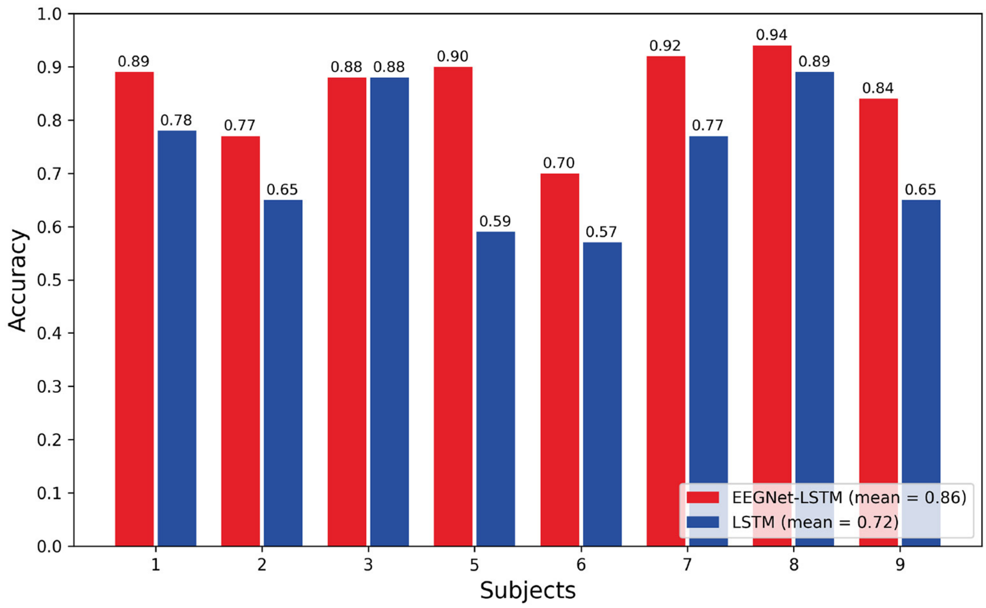

FIGURE 4
Comparison of the accuracy obtained through the decoders.

work and the kappa values achieved by decoders developed in other works.

Based on the average kappa value, the EEGNet-LSTM neural decoder was about 23% higher than the method proposed by Ang et al. (2012), first place in the BCI Competition IV, which used the filter bank common spatial pattern (FBCSP) for the extraction of characteristics and the naive bayesian Parzen window (NBPW) for the classification. A Wilcoxon *t*-test indicated a significant difference between the two decoders ($Z = 2.524$, $p = 0.012$). The EEGNet-LSTM decoder provided a result approximately 14% higher than the Incep-EEGNet developed by Riyad et al. (2020). There was a statistically significant difference ($Z = 2.028$, $p = 0.043$). This decoder was about 17% higher than the decoder entitled series compact convolutional recurrent neural network (SCCRNN), proposed by Wang L. et al. (2020). The test indicated a significant difference ($Z = 2.527$, $p = 0.012$). The average kappa value was also approximately 17% above the filter bank spatial filtering and temporal-spatial convolutional neural network (FBSF-TSCNN), presented by Chen et al. (2020). There was a statistically significant difference ($Z = 2.527$, $p = 0.018$).

The LSTM-based decoder achieved a result about 5% higher than the result obtained using the Ang et al. (2012) method. However, there was no significant difference ($Z = 1.540$, $p = 0.123$). The LSTM neural decoder presented a result approximately 4% lower than the result obtained through the Riyad et al. (2020) method. However, there was no significant difference ($Z = 0.981$, $p = 0.326$). The LSTM decoder gave a result about 2% below the result of Wang L. et al. (2020). However, there was no significant difference ($Z = 0.141$, $p = 0.888$). This decoder obtained a result approximately 1% lower than the result achieved by the Chen et al. (2020) method. However, there was no statistically significant difference ($Z = 0.314$, $p = 0.753$).

3.4. EEGNet-LSTM decoder performance with Physiobank EEG Motor movement/imagery dataset

Considering the two classes of motor imagery (left wrist and right wrist) from the Physiobank EEG Motion/Imagery dataset from PhysioNet, the EEGNet-LSTM decoder presented an accuracy of 0.85 in the test set. Using the same dataset, Wang X. et al. (2020) tested EEGNet and achieved an accuracy of 0.82. Using Filter Bank Common Spatial Pattern (FBCSP) and Support Vector Machine (SVM), Handiru and Prasad (2016) achieved approximately 0.64 accuracy.

4. Discussion

This work aimed to develop accurate neural decoders. The EEGNet-LSTM and LSTM decoders achieved, respectively, accuracies equal to 0.86 and 0.72. The high hit rate suggests that the decoders developed have great potential for future applications in EEG-based BMI systems.

In this work, a combination of WPD and CSP was performed to extract the characteristics of the signals, for the LSTM-based

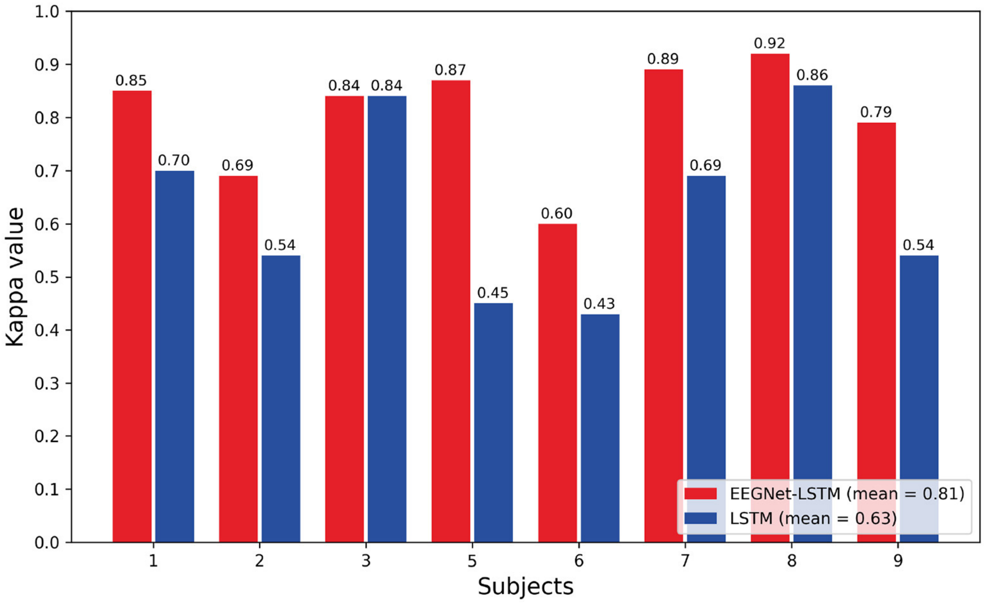

FIGURE 5
Comparison of the kappa values obtained through the decoders.

TABLE 7 Comparison with the kappa values achieved by other studies.

Methods	Subjects								Mean	Standard deviation	p value (Wilcoxon)	
	1	2	3	5	6	7	8	9			EEGNet-LSTM	LSTM
EEGNet-LSTM (Proposed method)	0.85	0.69	0.84	0.87	0.60	0.89	0.92	0.79	0.81	0.109	-	0.018
LSTM (Proposed method)	0.70	0.54	0.84	0.45	0.43	0.69	0.86	0.54	0.63	0.167	0.018	-
FBCSP e NBPW (Ang et al., 2012)	0.68	0.42	0.75	0.40	0.27	0.77	0.75	0.61	0.58	0.192	0.012	0.123
Incep-EEGNet (Riyad et al., 2020)	0.71	0.37	0.87	0.48	0.47	0.88	0.76	0.79	0.67	0.198	0.043	0.326
SCCRNN (Wang L. et al., 2020)	0.77	0.38	0.75	0.54	0.47	0.76	0.78	0.70	0.64	0.157	0.012	0.888
FBSF-TSCNN (Chen et al., 2020)	0.81	0.47	0.84	0.32	0.43	0.77	0.76	0.74	0.64	0.202	0.018	0.753

decoder. According to Yang et al. (2012), this combination provides better results compared to the use of CSP only, due to the time and frequency characteristics of the WPD. Using WPD, the signals were represented in different scales of frequency and time, and the spatial characteristics were extracted through the CSP.

LSTM-type networks can store information for long periods in their memory (Tseng et al., 2019). Therefore, these networks allowed the retention of information of imagined movements and, provided good performance in the decoding of the signals. The decoder surpassed the best result of BCI competition IV, but the results were slightly lower than the results obtained by other researchers, who used decoders that made use of convolutional neural networks (Chen et al., 2020; Riyad et al., 2020; Wang L. et al., 2020).

Although the average kappa value was slightly worse compared to decoders that used convolutional neural networks, for some specific subjects the LSTM decoder provided greater or equal results. The average kappa value provided by the LSTM decoder was approximately 2% lower than the decoders of Wang L. et al. (2020) and Chen et al. (2020). Therefore, the percentage difference was very small.

The other decoder implemented in this paper, called EEGNet-LSTM, combined the features of the two models, aiming to obtain a better performance. Wang L. et al. (2020) developed some neural decoders and the best was SCCRNN, similar to the decoder implemented here, since both combine EEGNet with two LSTM layers. The frequency and spatial characteristics can be extracted by CNN, and the temporal characteristics can be extracted by the LSTM layers.

However, unlike the network model implemented in this paper, Wang L. et al. (2020) used a fully connected layer before the first LSTM layer. In the EEGNet-LSTM decoder, implemented in the present paper, only the two main EEGNet blocks were used and the characteristics extracted through these blocks were passed directly to the LSTM layers. After each LSTM layer, batch normalization and dropout layers were also added to avoid overfitting the model. The use of these layers was not mentioned by Wang L. et al. (2020).

In addition, after testing different frequency ranges of the signals, bandwidth filtering between 0.5 and 100 Hz was considered, which generated the best results. In the research by [3], a bandpass filter between 4 and 35 Hz was applied. In the present work, the labels of the imagined movements were encoded in binary vectors, using the one-hot encoding method, being another difference that can influence the results. Other works used in the comparison also did not mention the use of this technique.

The EEGNet-LSTM decoder implemented in this research, surpassed the results of current decoders (Chen et al., 2020; Riyad et al., 2020), including the best decoder proposed by Wang L. et al. (2020), which has an architecture similar to the decoder implemented in this work. The additional layers, the exhaustive selection of hyperparameters, the strategies used in the pre-processing of the signals, and the fact of passing the characteristics extracted by the EEGNet blocks, directly to the LSTM layers, is what must be behind the better performance.

The combination of WPD and CSP allows the extraction of time-frequency and space features. However, using these methods, the extraction of characteristics and, the classification through LSTM decoder, are steps performed separately. According to Wang L. et al. (2020), performing the feature extraction and classification, separately, may not provide ideal results, and it is recommended to perform the extraction and classification stage together, since the extraction of characteristics can be adjusted automatically, based on the classification. The EEGNet-LSTM decoder performs the extraction of characteristics and, the classification, together, providing better results in comparison to the decoder based on LSTM, with the extraction of resources through WPD and CSP.

Wang X. et al. (2020) demonstrated that there is a reduction in performance metrics of the model, as the number of motor imagery classes increases. We noticed that the EEGNet-LSTM presents a similar result to the original EEGNet in a simpler problem, involving two classes of motor imagery from the Physiobank EEG Motor Movement/Imagery dataset. However, we noticed that in a more complex problem, involving the four classes of motor imagery from the BCI Competition IV dataset 2a, the EEGNet-LSTM presented significantly higher results than the Incep-EEGNet, an improved version of the EEGNet. Therefore, additional LSTM layers increase the hit rate, especially in more complex problems. The EEGNet-LSTM presented satisfactory results for two different datasets, one simpler and the other more complex. Considering that brain-machine interface systems can be used to control multiple actuators coupled to prostheses, orthoses and exoskeletons, the model presented is useful, as it maintains a high success rate in a more difficult problem.

5. Conclusion

Through this work, it was possible to observe better results, when feature extraction and classification are performed together. It was noted that the selection of hyperparameters and the pre-processing of the data are essential for the good performance of the decoders. It was also possible to notice that when combined with other models, LSTM-type networks have the potential to improve results, mainly due to their temporal capacity. The EEGNet-LSTM neural decoder showed satisfactory results for two different datasets, proving the potential for replicability and ability to maintain a high rate of success in simpler problems (two classes of motor imagery) and more complex (four classes of motor imagery). Given the good results compared to competing neural decoders, the EEGNet-LSTM decoder implemented in this research can be a good alternative for accurate decoding of EEG signals in BMI systems. Therefore, it can serve as a starting point for the development of future works.

Data availability statement

Publicly available datasets were analyzed in this study. This data can be found here: https://www.bbci.de/competition/iv.

Ethics statement

Ethical review and approval were not required for the study on human participants in accordance with the local legislation and institutional requirements. The patients/participants provided their written informed consent to participate in this study.

Author contributions

IO implemented the algorithms and wrote the manuscript. AR conceived and supervised the project. Both authors contributed to the article and approved the submitted version.

Funding

This study was financed by the Coordenação de Aperfeiçoamento de Pessoal de Nível Superior – Brasil (CAPES) – Finance Code 001, Conselho Nacional de Desenvolvimento Científico e Tecnológico (CNPq), and Ministério da Educação (MEC).

Acknowledgments

The authors thank Mariane de Araujo, Master's student in Neuroengineering, for reading the paper and suggesting some grammatical corrections, as she is fluent in English.

Conflict of interest

The authors declare that the research was conducted in the absence of any commercial or financial relationships that could be construed as a potential conflict of interest.

Publisher's note

References

Ahangi, A., Karamnejad, M., Mohammadi, N., Ebrahimpour, R., and Bagheri, N. (2012). Multiple classifier system for eeg signal classification with application to brain-computer interfaces. *Neural Comput. Appl.* 23, 1319–1327. doi: 10.1007/s00521-012-1074-3

Alarcón-Domínguez, J. (2017). Uso de interfaces cerebro-computador para la decodificación de la cinemática de miembro superior e inferior. *Revista Doctorado UMH* 2, 1. doi: 10.21134/doctumh.v2i1.1260

Amin, H. U., Mumtaz, W., Subhani, A. R., Saad, M. N. M., and Malik, A. S. (2017). Classification of eeg signals based on pattern recognition approach. *Front. Comput. Neurosci.* 11, 103. doi: 10.3389/fncom.2017.00103

Ang, K. K., Chin, Z. Y., Wang, C., Guan, C., and Zhang, H. (2012). Filter bank common spatial pattern algorithm on bci competition iv datasets 2a and 2b. *Front. Neurosci.* 6, 39. doi: 10.3389/fnins.2012.00039

Bansal, D., and Mahajan, R. (2019). "EEG-based brain-computer interfacing (BCI)," in *EEG-Based Brain-Computer Interfaces* (Amsterdam: Elsevier), 21–71.

Bear, M., Connors, B., and Paradiso, M. (2020). *Neuroscience: Exploring the Brain*, Enhanced Edition: Exploring the Brain. Jones and Bartlett Learning.

Bhuvaneswari, P., and Kumar, J. S. (2015). Influence of linear features in nonlinear electroencephalography (EEG) signals. *Procedia Comput. Sci.* 47, 229–236. doi: 10.1016/j.procs.2015.03.202

Brunner, C., Leeb, R., Müller-Putz, G., Schlögl, A., and Pfurtscheller, G. (2008). *BCI Competition 2008–Graz data set A.* Institute for Knowledge Discovery (Laboratory of Brain-Computer Interfaces), Graz University of Technology, Graz, Austria. 16, 1–6.

Chen, J., Yu, Z., Gu, Z., and Li, Y. (2020). Deep temporal-spatial feature learning for motor imagery-based brain-computer interfaces. *IEEE Trans. Neural Syst. Rehabil. Eng.* 28, 2356–2366. doi: 10.1109/TNSRE.2020.3023417

Cheng, M., Lu, Z., and Wang, H. (2017). Regularized common spatial patterns with subject-to-subject transfer of eeg signals. *Cogn. Neurodyn.* 11, 1–9. doi: 10.1007/s11571-016-9417-x

Chollet, F. (2017). *Deep Learning with Python*. Manning Publications Company.

Cohen, J. (1960). A coefficient of agreement for nominal scales. *Educ. Psychol. Meas.* 20, 37–46. doi: 10.1177/001316446002000104

Du, J., Vong, C. M., and Chen, C. L. P. (2021). Novel efficient rnn and lstm-like architectures: recurrent and gated broad learning systems and their applications for text classification. *IEEE Trans. Cybern.* 51, 1586–1597. doi: 10.1109/TCYB.2020.2969705

Fan, C., Yang, H., Hou, Z.-G., Ni, Z.-L., Chen, S., and Fang, Z.-J. (2021). Bilinear neural network with 3-D attention for brain decoding of motor imagery movements from the human EEG. *Cogn. Neurodyn.* 15, 181–189. doi: 10.1007/s11571-020-09649-8

Faust, O., Yu, W., and Kadri, N. A. (2013). Computer-based identification of normal and alcoholic eeg signals using wavelet packets and energy measures. *J. Mech. Med. Biol.* 13, 13500334. doi: 10.1142/S0219519413500334

Feng, G., Hau, L., and Nuo, G. (2019). "Feature extraction algorithm based on csp and wavelet packet for motor imagery EEG signals," in *2019 IEEE 4th International Conference on Signal and Image Processing (ICSIP)* (Wuxi: IEEE), 798–802.

Goldberger, A. L., Amaral, L. A. N., Glass, L., Hausdorff, J. M., Ivanov, P. C., Mark, R. G., et al. (2000). PhysioBank, PhysioToolkit, and PhysioNet: components of a new research resource for complex physiologic signals. *Circulation* 101, e215-e220. doi: 10.1161/01.CIR.101.23.e215

Handiru, V. S., and Prasad, V. A. (2016). Optimized bi-objective eeg channel selection and cross-subject generalization with brain-computer interfaces. *IEEE Trans. Hum. Mach. Syst.* 46, 777–786. doi: 10.1109/THMS.2016.2573827

Hochreiter, S., and Schmidhuber, J. (1997). Long short-term memory. *Neural Comput.* 9, 1735–1780. doi: 10.1162/neco.1997.9.8.1735

Huang, G., Liu, G., Jianjun, M., Zhang, D., and Zhu, X. (2010). Model based generalization analysis of common spatial pattern in brain computer interfaces. *Cogn. Neurodyn.* 4, 217–223. doi: 10.1007/s11571-010-9117-x

Ioffe, S., and Szegedy, C. (2015). "Batch normalization: accelerating deep network training by reducing internal covariate shift," in *Proceedings of the 32nd International Conference on Machine Learning, volume 37 of Proceedings of Machine Learning Research*, eds F. Bach and D. Blei (Lille: PMLR), 448–456.

Jiang, X., and Adeli, H. (2004). Wavelet packet-autocorrelation function method for traffic flow pattern analysis. *Comput. Aided Civil Infrastruct. Eng.* 19, 324–337. doi: 10.1111/j.1467-8667.2004.00360.x

Jiao, Y., Deng, Y., Luo, Y., and Lu, B.-L. (2020). Driver sleepiness detection from eeg and eog signals using gan and lstm networks. *Neurocomputing* 408, 100–111. doi: 10.1016/j.neucom.2019.05.108

Keras (2020). *About keras*. Available online at: https://keras.io/about/

Landis, J. R., and Koch, G. G. (1977). The measurement of observer agreement for categorical data. *Biometrics* 33, 159–174. doi: 10.2307/2529310

Lawhern, V. J., Solon, A. J., Waytowich, N. R., Gordon, S. M., Hung, C. P., and Lance, B. J. (2018). EEGNet: a compact convolutional neural network for EEG-based brain–computer interfaces. *J. Neural Eng.* 15, 056013. doi: 10.1088/1741-2552/aace8c

Li, T., and Zhou, M. (2016). Ecg classification using wavelet packet entropy and random forests. *Entropy* 18, 285. doi: 10.3390/e18080285

Lun, X., Yu, Z., Chen, T., Wang, F., and Hou, Y. (2020). A simplified cnn classification method for mi-eeg via the electrode pairs signals. *Front. Hum. Neurosci.* 14, 338. doi: 10.3389/fnhum.2020.00338

Mulder, T. (2007). Motor imagery and action observation: Cognitive tools for rehabilitation. *J. Neural Transm.* 114, 1265–1278. doi: 10.1007/s00702-007-0763-z

Niemeyer, J. E. (2016). Brain-machine interfaces: assistive, thought-controlled devices. *Lab. Anim.* 45, 359–361. doi: 10.1038/laban.1115

Python (2020). *What is python? Executive Summary*. Available online at: https://www.python.org/doc/essays/blurb/

Riyad, M., Khalil, M., and Adib, A. (2020). "Incep-eegnet: a convnet for motor imagery decoding," in *Image and Signal Processing*, eds A. El Moataz,

D. Mammass, A. Mansouri, and F. Nouboud (Cham: Springer International Publishing), 103–111.

Schalk, G., Mcfarland, D., Hinterberger, T., Birbaumer, N., and Wolpaw, J. (2004). Bci2000: a general-purpose brain-computer interface (bci) system. *IEEE Trans. Biomed. Eng*. 51, 1034–1043. doi: 10.1109/TBME.2004.827072

Song, X., and Yoon, S.-C. (2015). Improving brain-computer interface classification using adaptive common spatial patterns. *Comput. Biol. Med*. 61, 150–160. doi: 10.1016/j.compbiomed.2015.03.023

Tabar, Y. R., and Halici, U. (2016). A novel deep learning approach for classification of EEG motor imagery signals. *J. Neural Eng*. 14, 016003. doi: 10.1088/1741-2560/14/1/016003

Tang, Z., Li, C., and Sun, S. (2017). Single-trial eeg classification of motor imagery using deep convolutional neural networks. *Optik* 130, 11–18. doi: 10.1016/j.ijleo.2016.10.117

Tseng, P.-H., Urpi, N., Lebedev, M., and Nicolelis, M. (2019). Decoding movements from cortical ensemble activity using a long short-term memory recurrent network. *Neural Comput*. 31, 1–29. doi: 10.1162/neco_a_01189

Varsehi, H., and Firoozabadi, S. M. P. (2021). An EEG channel selection method for motor imagery based brain-computer interface and neurofeedback using granger causality. *Neural Netw*. 133, 193–206. doi: 10.1016/j.neunet.2020.11.002

Wang, L., Huang, W., Yang, Z., and Zhang, C. (2020). Temporal-spatial-frequency depth extraction of brain-computer interface based on mental tasks. *Biomed. Signal Process. Control* 58, 101845. doi: 10.1016/j.bspc.2020.101845

Wang, X., Hersche, M., Tömekce, B., Kaya, B., Magno, M., and Benini, L. (2020). "An accurate eegnet-based motor-imagery brain-computer interface for low-power edge computing," in *2020 IEEE International Symposium on Medical Measurements and Applications (MeMeA)* (Bari: IEEE), 1–6.

Wang, Y., Gao, S., and Gao, X. (2005). "Common spatial pattern method for channel selelction in motor imagery based brain-computer interface," in *2005 IEEE Engineering in Medicine and Biology 27th Annual Conference* (Shanghai: IEEE), 5392–5395.

Yang, B., Li, H., Wang, Q., and Zhang, Y. (2016). Subject-based feature extraction by using fisher wpd-csp in brain-computer interfaces. *Comput. Methods Programs Biomed*. 129, 21–28. doi: 10.1016/j.cmpb.2016.02.020

Yang, B., Lu, W., He, M., and Liu, L. (2012). Novel feature extraction method for bci based on WPD and CSP. *Chin. J. Sci. Instrument* 33, 2560–2565.

frontiers | Frontiers in Neuroscience

TYPE Original Research
PUBLISHED 02 March 2023
DOI 10.3389/fnins.2023.1128646

OPEN ACCESS

EDITED BY
Yu Pang,
Chongqing University of Posts
and Telecommunications, China

REVIEWED BY
Maxwell Bond Wang,
Carnegie Mellon University, United States
Xuan Bu,
Beijing Normal University, China

*CORRESPONDENCE
Xiaobo Li
✉ xli.aecom@gmail.com;
✉ xiaobo.li@njit.edu

SPECIALTY SECTION
This article was submitted to
Neural Technology,
a section of the journal
Frontiers in Neuroscience

RECEIVED 21 December 2022
ACCEPTED 17 February 2023
PUBLISHED 02 March 2023

CITATION
Cao M, Wu K, Halperin JM and Li X (2023) Abnormal structural and functional network topological properties associated with left prefrontal, parietal, and occipital cortices significantly predict childhood TBI-related attention deficits: A semi-supervised deep learning study.
Front. Neurosci. 17:1128646.
doi: 10.3389/fnins.2023.1128646

Abnormal structural and functional network topological properties associated with left prefrontal, parietal, and occipital cortices significantly predict childhood TBI-related attention deficits: A semi-supervised deep learning study

Meng Cao[1], Kai Wu[2], Jeffery M. Halperin[3] and Xiaobo Li[1,4]*

[1]Department of Biomedical Engineering, New Jersey Institute of Technology, Newark, NJ, United States, [2]School of Biomedical Sciences and Engineering, South China University of Technology, Guangzhou, China, [3]Department of Psychology, Queens College, City University of New York, New York, NY, United States, [4]Department of Electrical and Computer Engineering, New Jersey Institute of Technology, Newark, NJ, United States

Introduction: Traumatic brain injury (TBI) is a major public health concern in children. Children with TBI have elevated risk in developing attention deficits. Existing studies have found that structural and functional alterations in multiple brain regions were linked to TBI-related attention deficits in children. Most of these existing studies have utilized conventional parametric models for group comparisons, which have limited capacity in dealing with large-scale and high dimensional neuroimaging measures that have unknown nonlinear relationships. Nevertheless, none of these existing findings have been successfully implemented to clinical practice for guiding diagnoses and interventions of TBI-related attention problems. Machine learning techniques, especially deep learning techniques, are able to handle the multi-dimensional and nonlinear information to generate more robust predictions. Therefore, the current research proposed to construct a deep learning model, semi-supervised autoencoder, to investigate the topological alterations in both structural and functional brain networks in children with TBI and their predictive power for post-TBI attention deficits.

Methods: Functional magnetic resonance imaging data during sustained attention processing task and diffusion tensor imaging data from 110 subjects (55 children with TBI and 55 group-matched controls) were used to construct the functional and structural brain networks, respectively. A total of 60 topological properties were selected as brain features for building the model.

Results: The model was able to differentiate children with TBI and controls with an average accuracy of 82.86%. Functional and structural nodal topological properties associated with left frontal, inferior temporal, postcentral, and medial occipitotemporal regions served as the most important brain features for accurate classification of the two subject groups. Post hoc regression-based machine learning analyses in the whole study sample showed that among these most important neuroimaging features, those associated with left postcentral area, superior frontal region, and medial occipitotemporal regions had significant value for predicting the elevated inattentive and hyperactive/impulsive symptoms.

Discussion: Findings of this study suggested that deep learning techniques may have the potential to help identifying robust neurobiological markers for post-TBI attention deficits; and the left superior frontal, postcentral, and medial occipitotemporal regions may serve as reliable targets for diagnosis and interventions of TBI-related attention problems in children.

KEYWORDS

pediatric, traumatic brain injury, attention deficits, diffusion tensor imaging, functional magnetic resonance imaging, graph theory, autoencoder, semi-supervised deep learning technique

1. Introduction

Traumatic brain injury (TBI) is a major public health concern. For children in the United State, TBI-related emergency department visits exceeded 600,000 every year (Dewan et al., 2016). Children with TBI have elevated risks in developing neurocognitive impairments and behavioral abnormalities (Konigs et al., 2015; Polinder et al., 2015; Lumba-Brown et al., 2018). Significant attention deficits are among the most common cognitive consequences that can be observed in more than 35% of children two years post-TBI (Max et al., 2005). The attention problems in children post-TBI can persist into late adolescence and have been linked to the development of severe psychopathology and impairments in overall functioning (Le Fur et al., 2019; Narad et al., 2019). Without having established neurobiological signatures, treatments and interventions of TBI-related attention deficits in children have been based on subjective observations from clinicians and have resulted in suboptimal efficacy (Backeljauw and Kurowski, 2014; Kurowski et al., 2019; LeBlond et al., 2019).

In the past two decades, a number of clinical and neuroimaging studies have tried to investigate the neuroanatomical and functional substrates associated with TBI-related attention problems in children. Several diffusion tensor imaging (DTI) studies reported that the white matter integrity in corpus collosum, superior longitudinal fasciculus, and inferior fronto-occipital fasciculus were linked with impaired attention function in children with chronic TBI (Wozniak et al., 2007; Kurowski et al., 2009; Dennis et al., 2015; Konigs et al., 2018). Task-based functional magnetic resonance imaging (fMRI) studies have also reported functional alterations in frontal, parietal, and occipital regions during inhibition and sustained attention process (Kramer et al., 2008; Tlustos et al., 2011, 2015; Strazzer et al., 2015).

Known as a foundation of neuroscience, human brain regions do not work in an isolated manner. The existing voxel- and region-of-interest (ROI)-based studies have limitations in addressing how, in the systems-level, certain brain regions are vulnerable to TBI and contribute to related cognitive and behavioral consequences. The graph theoretical technique (GTT)-based approaches have been increasingly implemented in human brain imaging data to construct structural and/or functional brain networks in a systems-level, and to characterize the network integration, segregation, centrality, and small-worldness in both the global and regional (sub-network) scales (Bullmore and Sporns, 2009). Studies have reported that children with TBI demonstrated a less integrated structural or functional brain network compared to healthy controls (Caeyenberghs et al., 2012; Konigs et al., 2017; Yuan et al., 2017; Botchway et al., 2022; Ware et al., 2022). Our recent GTT-based studies in both DTI and task-based fMRI data reported that, compared to group-matched typically developing children (TDC), children with diagnosed TBI-related attention deficits (TBI-A) had significant regional topological alterations associated with frontal, parietal, and temporal lobes in both structural and functional networks, with the altered regional topological properties associated with parietal and temporal regions significantly linking to elevated inattentive symptoms in children with TBI-A (Cao et al., 2021a,b). These existing studies suggest that TBI-related attention deficits in children have close relationships with systems-level functional and structural abnormalities associated with multiple brain regions. However, all these studies have adopted conventional parametric models (such as *t*-test, analysis of variance, etc.) for group comparisons, which have very limited capacities to deal with the large-scale and nonlinearly related neuroimaging measures.

Compared to conventional parametrical models, machine learning techniques have the capacity in learning the joint effects of measures in high dimensional space and have the sensitivity in detecting subtle information that have high discriminative/predictive power (Nielsen et al., 2020). When aided with feature selection methods and cross-validation methods, machine learning techniques can deliver efficient and robust classifications between different groups. A few existing studies in children with TBI have applied machine learning techniques. By constructing classification model using support vector machine (SVM) and edge density image, one study was able to differentiate 14 children with TBI and 10 controls with an area under the receiver-operating-characteristic-curve (AUC) of 0.94 (Raji et al., 2020). Another study built an SVM-based classification model using structural MRI data and DTI data from 29 student athletes (aged from 15 to 20 years) and 27 controls and achieved an AUC of 0.84 (Tamez-Pena et al., 2021). A longitudinal study reported that when combining resting-state MRI data and structural MRI data in 99 children with TBI at 4 weeks after the injury, SVM algorithm was able to predict the recovery of post-concussion symptoms at 8 weeks with an AUC of 0.86 (Iyer et al., 2019). However, the majority of these machine learning studies in children with TBI applied supervised models that only focused on discriminating labels of the two diagnostic groups, and none of these studies have intended to detect the neurobiological features associated with the most common TBI-related cognitive deficits.

In this study, we propose to utilize a deep learning technique, semi-supervised autoencoder, to identify the robust functional and structural brain signatures of TBI-related attention deficits in children. Deep learning techniques were highly effective in generating feature representations by learning the deep linear or nonlinear relationships within a high dimensional space of the study measures (LeCun et al., 2015). Based on results of previous study from our and other teams (Wozniak et al., 2007; Kramer et al., 2008; Kurowski et al., 2009; Tlustos et al., 2011; Dennis et al., 2015; Strazzer et al., 2015; Tlustos et al., 2015; Konigs et al., 2018; Cao et al., 2021a,b), we hypothesize that topological anomalies associated with frontal, parietal, and temporal regions in the functional and structural brain networks not only play the most important role in characterizing children with TBI when compared to controls, but also most significantly contribute to TBI-related attention deficits in the affected children.

2. Materials and methods

2.1. Participants

A total of 110 children, including 55 children with TBI and 55 group-matched controls, were initially involved in this study. The TBI subjects were recruited from the New Jersey Pediatric Neuroscience Institute, Saint Peter's University Hospital, and local communities in New Jersey. Controls were solicited from the local communities by advertisement in public places. The study received institutional review board approval at the New Jersey Institute of Technology and Saint Peter's University Hospital. Prior the study, all the participants and their parents or guardians provided written informed assent and consent, respectively.

The inclusion criteria for the TBI group were: (1) has history of at least one clinical diagnosed mild or moderate non-penetrating TBI (Teasdale and Jennett, 1974); (2) has no overt focal brain damages or hemorrhages during all the TBI incidences; (3) the first TBI incidence was at least 6 months prior to the study date; (4) has no significant inattention or hyperactive problems before the injury. The control group included children with no history of diagnosed TBI or no history of diagnosed attention deficit/hyperactivity disorder (ADHD). Conners 3^{rd} Edition-Parent Short form (Conners 3-PS) were assessed during the study visit to characterize the inattention problems and hyperactivity/impulsivity problems in both groups (Conners, 2008).

To further improve the homogeneity of the study sample, the general inclusion criteria for both groups included (1) only right-handed, to remove handedness-related potential effects on brain structures, which the handedness were evaluated using the Edinburgh Handedness Inventory (Oldfield, 1971); (2) full scale IQ $\geq$ 80, which were estimated by the Wechsler Abbreviated Scale of Intelligence II (WASI-II) (Wechsler, 2011); (3) has no current or previous diagnosis of Autism spectrum disorders, pervasive development disorder, psychosis, major mood disorders (except dysthymia not under treatment), post-traumatic stress disorder, obsessive compulsive disorder, conduct disorder, anxiety (except simple phobias), or substance use disorders, based on Diagnostic and Statistical Manual of Mental Disorders 5 (DSM-5) (Association, 2013) and supplemented by the Kiddie Schedule for Affective Disorders and Schizophrenia for School-Age Children-Present and Lifetime Version (K-SADS-PL) (Kaufman et al., 2000); (4) has no learning disabilities, neurological disorders, or any types of diagnosed chronic medical illnesses, from the medical history. None of the subjects involved in this study had any treatments with long-acting stimulants or non-stimulant psycho-tropic medications within the past month nor any contraindications for MRI scanning, such as claustrophobia, tooth braces, or other metal implants.

After initial processing of the neuroimaging data from each subject, three subjects from the TBI group and two subjects from the control group were excluded due to low imaging quality or excessive motions in either DTI data or functional MRI data. Therefore, a total of 52 children with TBI and 53 controls were included in the group-level analyses. All the demographic information was shown in **Table 1**.

2.2. Neuroimaging data acquisition protocol

For each subject, a DTI scan, a task-based functional MRI scan, and a high-resolution T1-weighed MRI scan were collected using a 3-Tesla Siemens TRIO (Siemens Medical Systems, Germany) scanner at Rutgers University Brain Imaging Center. The DTI data were acquired using a single-shot echo planar sequence, with the following parameters: voxel size = 2.0 mm × 2.0 mm × 2.5 mm,

TABLE 1 Demographic and clinical characteristics in the study sample.

	Controls Mean (SD)	TBI Mean (SD)	*t* or χ^2-value	*P*-value
N	55	55		
Male/female	30/25	33/22	0.334 (χ^2)	0.563
Socio-economic status	16.47 (2.13)	15.70 (2.09)	1.450	0.151
Full scale IQ	113.00 (11.23)	110.97 (13.72)	1.402	0.165
Age	13.06 (2.03)	13.63 (2.28)	−1.370	0.174
Ethnicity/race			4.259 (χ^2)	0.119
Caucasian	30	36		
Hispanic	8	11		
Others	17	8		
Conners 3rd edition-parent short form (*T*-score)				
Inattention	46.15 (6.02)	64.73 (13.49)	−9.145	< 0.001
Hyperactivity/ impulsivity	48.38 (5.42)	58.44 (14.43)	−4.747	< 0.001

TBI, children with traumatic brain injury; SD, standard deviation; N, number of subjects; M, males; F, females.

repetition time (TR) = 7,700 ms, echo time (TE) = 103 ms, field of view (FOV) = 250 mm × 250 mm, 30 diffusion-sensitizing gradient directions with b-value = 700 s/mm^2, and one image with b-value = 0 s/mm^2. The fMRI data were acquired using a whole brain gradient echo-planar sequence, with the following parameters: voxel size = 1.5 mm × 1.5 mm × 2.0 mm, TR = 1,000 ms, TE = 28.8 ms, and FOV = 208 mm. A high-resolution T1-weighted structural image was also collected with a sagittal multi-echo magnetization-prepared rapid acquisition gradient echo sequence with the following parameters: voxel size = 1 mm^3 isotropic, TR = 1,900 ms, TE = 2.52 ms, flip angle = 9°, FOV = 250 mm × 250 mm, and 176 sagittal slices. The T1-weighted image were used for fMRI co-registration and creation of individualized brain region masks in DTI-based structural brain network construction.

2.3. Visual sustained attention task for fMRI

In the current study, the fMRI data for each subject were collected during an enhanced continuous performance task, the visual sustained attention task (VAST), which was designed to achieve optimal power in maintaining sustained attention and to assess related functional brain pathways in children (Li et al., 2012; Cao et al., 2021a). The VAST is a block-designed task which included five task stimulations block that interleaved with five resting blocks. The total duration is 5 min with each block last 30 s. During task blocks, subjects were asked to remember a sequence of three numbers and responds when the stimulus sequences match the target. To ensure full understanding of the instructions, practical trials of the task were provided to each subject before the scan session.

2.4. Individual level structural MRI and DTI data processing and structural brain feature generation

Each individual's structural MRI data was visually checked for artifacts and excessive motions. Then the preprocessing steps, including registration into Talairach space, skull-stripping, and intensity normalization, were performed using Freesurfer v6.0.0 (Fischl, 2012). The preprocessed structural MRI data were parcellated using Desikan atlas and were used for node generation in constructing the structural brain network.

To construct the structural network, the DTI data were preprocessed using the Diffusion Toolbox from FMRIB Software Library v6.0 (FSL) (Woolrich et al., 2001). The preprocessing steps included head-motions correction, non-brain voxels removal, and intensities normalization. The head motions and eddy-current distortion were then corrected with affine transformation and predictions estimated by a Gaussian Process (Andersson and Sotiropoulos, 2016). Heavy head movement is a critical issue that can significantly affect the quality of imaging data and cause inaccurate results of tractography. In this study, the cutoffs of heavy head movements were defined as data with> 2 mm translational displacement, > 5° rotational displacement, or > 0.2 mm mean volume-by-volume displacement. Three subjects from TBI group and one subject from control group were excluded due to heavy head motion. Then, the probabilistic tractography parameters of each voxel were estimated with a two-fiber model in each individual's native space. For each subject, a total of 78 ROIs were selected as the nodes for structural brain network, including 34 cortical regions and 5 subcortical regions per hemisphere. The mask for each ROI was generated based on the parcellation in the preprocessed structural MRI data and transformed into the native diffusion space. Probabilistic tractography were used to estimate the connecting fibers between each pair of the seed masks. Five thousand streamlines per voxel were then initiated from each seed mask, with 0.5 step distance. A fiber was terminated when (1) it reached other seed masks; (2) it exceeded 2,000 step limits; (3) it looped back to the same streamline; or (4) its curvature exceeded 80. The streamlines between seed masks were averaged in both directions to determine the structural connectivity between network nodes. Due to the connection density bias, the white matter bundle with higher anisotropy usually generate significantly higher streamline counts in the probabilistic tractography process (Jones, 2010; Zhang et al., 2022). Therefore, in this study, the weight of a non-zero edge was evaluated by log-transformed streamline count and normalized by dividing the maximum edge weight in the same network to increase the discriminability of low edge weights (Ashourvan et al., 2019; Hansen et al., 2022). Then for each subject, a 78 × 78 symmetric connectivity matrix was generated for construction of the weighted structural brain network.

After the weighted structural brain network was constructed for each subject, the network topological properties were calculated [technical details for computations were provided in our previous publications (Cao et al., 2021b)]. The nodal-level topological properties for weighted network, including the nodal strength, nodal global efficiency, nodal local efficiency, clustering coefficient, and betweenness centrality, were calculated for each node in the structural brain networks to serve as structural brain features. All structural network topological properties were calculated using the Brain Connectivity Toolbox (Rubinov and Sporns, 2010). A total of 390 structural brain features were generated for building the semi-supervised autoencoder.

2.5. Individual level fMRI data processing and functional brain feature generation

The preprocessing of the fMRI data was carried out using FEAT Toolbox from FSL v6.0 (Woolrich et al., 2001). For fMRI data, the same cutoffs of heavy head motions that used in DTI preprocessing were applied, with which two subjects from TBI group (overlapped with excluded subjects in DTI preprocessing) and one subject from control group were excluded. After motion correction and slice timing correction, the fMRI data of each subject was co-registered to standard Montreal Neurological Institute (MNI) space using high-resolution structural MRI. The hemodynamic response to the task-related condition was modeled using the general linear model with 24 motion parameters. The activated voxels were identified by cluster-based thresholding on the Z statistic map with $Z > 2.3$ and $p < 0.05$. To construct the functional brain network for each subject, the network nodes were generated by defining a spherical region with a radius of 5 mm at the local maximum of any clusters that have more than 100 activated voxels. A total of 59 ROIs were generated based on the automatic anatomical labeling atlas (Tzourio-Mazoyer et al., 2002). The connectivity of a ROI-pair was represented by the Pearson's correlation coefficient of the blood-oxygen-level-dependent (BOLD) signal in each of the two ROIs. The connectivity matrix was then binarized using the network cost range that satisfied small-network property to construct the binarized functional brain network (Achard and Bullmore, 2007).

The nodal-level topological properties for binarized network, including the nodal degree, nodal global efficiency, nodal local efficiency, clustering coefficient, and betweenness centrality, were calculated for each node in the functional brain networks [technical details for computations were provided in our previous publications (Cao et al., 2021a)]. The individual-level analysis was performed using pipeline tool GAT-FD (Cao et al., 2022), where all network topological properties were calculated by calling functions from the Brain Connectivity Toolbox (Rubinov and Sporns, 2010). A total of 295 nodal topological properties were calculated from the functional brain networks to serve as the functional brain features of each subject for building the semi-supervised autoencoder.

2.6. Modeling of semi-supervised autoencoder

To increase training robustness and reduce overfitting risk, combination of three approaches, including two-sample *t*-test, mutual information-based method (Ross, 2014), and Lasso-based method (Muthukrishnan and Rohini, 2016), were utilized for feature reduction. At the end, a total of 60 top features from the 685 source brain features derived from structural and functional brain networks were selected for training in the model. Before passing to the autoencoder model, all these features were normalized to a range of 0 to 1 using min-max normalization.

The semi-supervised autoencoder consisted of three major components, the encoder, the decoder, and the classifier, as shown in **Figure 1**. The encoder and decoder were part of a regular autoencoder model, which learns a compressed representation of the original brain features by optimizing the reconstructed brain features in an unsupervised manner (Hinton and Salakhutdinov, 2006). The encoder transformed inputs from original feature space into a latent space by compressing the information in the inputs. The encoder in the proposed model contained one input layer with a size of 60, one hidden layer of 40 neurons, and one output layer of 20 neurons. Then the autoencoder-generated features, i.e., AE-features, in the latent space were passed into the decoder to reconstruct the original input. The decoder included an input layer with a size of 20, a hidden layer of 40 neurons, and one output layer of 60 neurons. An additional classifier was included in the proposed autoencoder to work as a constrain in the learning of the compressed AE-features in the latent space. The classifier took 20 AE-features in the latent space to predict the group label for each sample. The classifier included a hidden layer with 20 neurons and an output layer of 1 neuron. Sigmoid function was used as the activation function for all the artificial neurons in the semi-supervised autoencoder neural network.

Two different loss functions were used compensate the different training speeds of the regression task (the decoder) and the classification task (the classifier). Mean squared error (MSE) was selected as the loss function of the reconstruction process, which was calculated using the following formula,

$$MSE = \frac{1}{n}\sum_{i=1}^{n}\left[\frac{1}{f}\sum_{j=1}^{f}\left(x'_{ij}-x_{ij}\right)^{2}\right],$$

where n is the number of subjects in the training data, f is the number of brain features, x'_{ij} is the reconstructed value for feature j of subject i, and $x_{ij}$is original value for feature j of subject i. Binary cross-entropy were selected as the loss function of the classification process, which was calculated using the following formula,

$$H_{binary} = -\frac{1}{n}\sum_{i=1}^{n}\left[y\log p + (1-y)\log(1-p)\right],$$

where H_{binary} is binary cross-entropy, n is the number of subjects in the training data, y is the binary indicator of the class label, and p is probability of y is 1.

In order to force the model to learn the latent AE-features for reconstruction earlier than for classification, loss of the decoder model was assigned with a higher weight than the loss of the classifier model. The loss function of the full model was calculated using the following formula,

$$L_{full-model} = 0.7 \times MSE + 0.3 \times H_{binary},$$

where the weight of the decoder loss is 0.7 and the weight of the classifier loss is 0.3.

2.7. Model training and evaluation

Training of the model was performed using python v3.8.0 and Tensorflow v2.10 (Abadi et al., 2016). Adam optimizer was used for the back-propagation process (Kingma and Ba, 2014). To increase the robustness of the model, a five-fold cross validation were employed in the training process. For details, the data were split into five stratified folds such that each fold consisted of balanced 20% of the entire data. For each iteration, four-folds were dedicated for training data and the remaining one for validation. To avoid potential leakage effect in the training process, the feature selection algorithms only used training data in each cross validation (Pereira et al., 2009). To further minimize the risk of overfitting in the training process, a gaussian noise with a mean of zero and standard deviation of 0.02 was randomly induced to 20% of the input features, before feeding into the encoder model. The training process stops when the accuracy of the training data exceeds 95% or reach a total of 1,000 epochs.

The performance of the reconstruction process of the semi-supervised autoencoder model were measured using the MSE of the validation data and averaged for all the five cross validations. The classification performance was measured in terms of classification accuracy and AUC in the validation data, which also averaged for all five cross validations.

In comparison, a conventional machine learning model was also constructed using the same training and validation procedure. The model used principal component analysis (PCA) for feature reduction and SVM for classification.

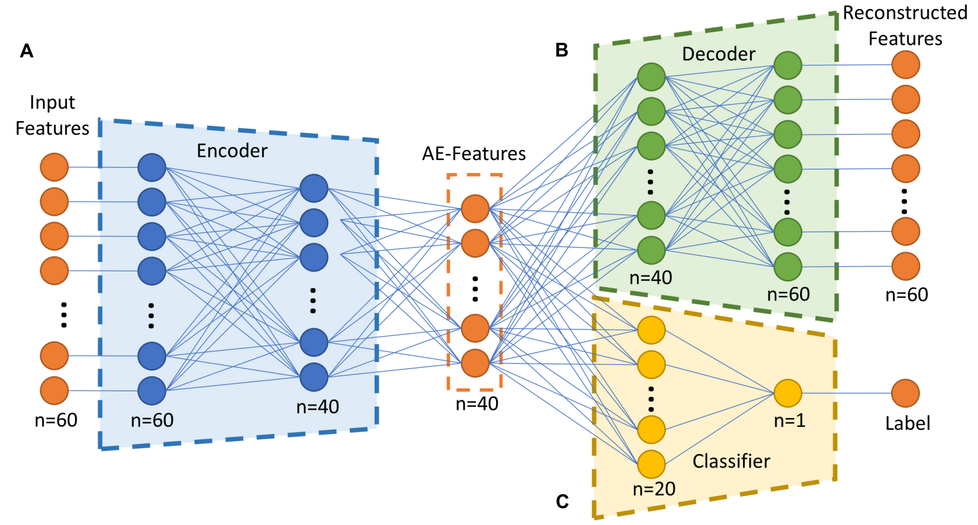

FIGURE 1
Overall structure of the semi-supervised autoencoder. **(A)** The encoder model, which transform the inputs from original brain feature space into a latent space. **(B)** The decoder model, which reconstruct the input by transforming the encoded features. **(C)** The classifier model, which predict if a subject is in the TBI group or in the control group based on the encoded features. AE-Features: autoencoder-generated features.

2.8. Feature importance score calculation

To identify the most important brain features for successful classification process, a permutation-based method was used to calculate the importance score of each input feature (Breiman, 2001). A feature's importance was determined by the amount of error caused by shuffling the feature's value over all the samples (Fisher et al., 2019). For the classification process, the feature importance for a feature was characterized by the binary cross-entropy, which was calculated using the following formula,

$$FI_{class} = \frac{1}{m}\sum_{k=1}^{m}\left(H_{binary} - H'_{binary}\right)^{2},$$

where m is the number of random shuffling, H_{binary} is the cross-entropy of the original input, and H'_{binary} is the cross-entropy of the shuffled input. The importance score for features in the current study was calculated by shuffling for 1,000 times. Features with importance score that two standard deviation higher than the mean importance score of all features were identified as important features (Sun et al., 2020).

2.9. Modeling of brain-behavior relationships

Regression-based machine learning, a support vector regression (SVR) model, was first constructed to study the relations between the most important brain features for successful group discriminations and the severity measures of inattentive and hyperactive/impulsive symptoms (T-scores derived from Conners 3-PS) in the whole study sample. To minimize overfitting, five-fold cross validation were used for training and validation. The R^2 and MSE were used to evaluate the performance of the SVR model. Permutation importance score were used to evaluate the importance of the brain features.

To further validate the robustness of the relationships between the identified important brain features and clinical measures, a partial least squares structural equation modeling (PLS-SEM) was conducted (Hair et al., 2011). The rationale of the PLS-SEM was to test whether the important brain features for classification were associated with any AE-features, and whether those AE-features were associated with the clinical measures, while accounting for the effects of age, sex, handedness, SES, and IQ. The PLS-SEM analysis was carried out using R 4.1.3 and SEMinR 2.3.2 (Hair et al., 2021). First, Pearson's correlation between the AE-features in the latent space and T-scores of the inattentive and hyperactive/impulsive subscales from Conners 3-PS were performed within the whole study sample. The correlation analyses were controlled for potential multiple comparisons (for 20 features in the latent space), by using the Bonferroni correction with a threshold of significance at corrected α 0.05. The AE-features in the latent space that showed significant correlation with the clinical scores were selected as the intermediate variables in the PLS-SEM. Bootstrap with 5,000 random samples were performed to determine the significant levels of the path coefficients in the PLS-SEM analysis (Henseler and Chin, 2010).

3. Results

3.1. Demographic and clinical/behavioral measures

There were no significant between-group differences in any demographic measures in our sample. Among the subjects in TBI group, 14 subjects had no significant inattentive or hyperactive problems, 27 had significant inattentive problems, 2 had significant

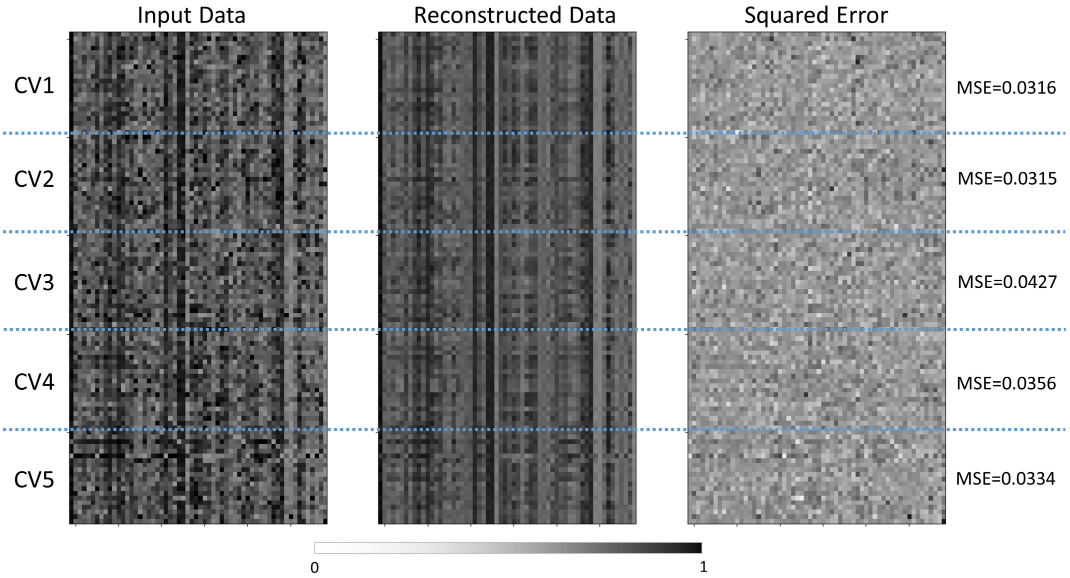

FIGURE 2
Comparisons between the normalized features and reconstructed features by the semi-supervised autoencoder model. The normalized input data was shown on the left, the reconstructed data was shown in the middle, and the squared error was shown on the right. The vertical axis represented the subjects in each cross-validation set, and the horizontal axis represented the features. CV, cross-validation; MSE, mean squared error.

hyperactive/impulsive problems, and 12 had significant problems in both inattention and hyperactivity/impulsivity. In the TBI group, the range between first TBI incidence and MRI scan was from 6 to 90 months (7 years 6 months), with average of 33.8 ± 24.2 months. The results showed that children with TBI had significantly more inattentive ($t = -9.145$, $p < 0.001$) and hyperactive/impulsive ($t = -4.747$, $p < 0.001$) symptoms measured using the T-scores in Conners 3-PS, when compared to controls. No significant correlations were observed between the time after injury and inattention or hyperactivity/impulsivity T-scores. The demographic and clinical information was shown in Table 1.

3.2. Performance of the semi-supervised autoencoder

The semi-supervised autoencoder model was able to differentiate children with TBI and controls with a classification accuracy of 82.86% ± 07.97% and an AUC of 0.860 ± 0.061. At the same time, the model was able to reconstruct the original brain features with an MSE of 0.035 ± 0.005, as shown in Figure 2. In comparison, the PCA+SVM model was able to achieve a classification accuracy of 78.09% ± 11.47% with an AUC of 0.825 ± 0.114.

3.3. Most important brain features for classification

Network topological properties associated with left inferior and superior frontal, postcentral, inferior temporal and medial occipitotemporal regions were identified as the most important brain features for successful discrimination between children with TBI and controls. Specifically, the functional nodal clustering coefficient of left inferior temporal gyrus and left medial occipitotemporal gyrus, the functional nodal local efficiency of left postcentral gyrus, the structural nodal local efficiency of left inferior frontal gyrus, the structural nodal clustering coefficient of left frontal pole, and the structural betweenness centrality of left superior frontal gyrus had significantly higher importance scores than other selected brain features (Table 2).

TABLE 2 Importance score of the most important brain features in accurately differentiating children with TBI and controls.

Region	Topological property	Network	Importance score
Left inferior temporal gyrus	Nodal clustering coefficient	Functional	0.0430
Left superior frontal gyrus	Betweenness centrality	Structural	0.0421
Left inferior frontal gyrus	Nodal local efficiency	Structural	0.0339
Left medial occipitotemporal gyrus	Nodal clustering coefficient	Functional	0.0338
Left postcentral gyrus	Nodal local efficiency	Functional	0.0308
Left frontal pole	Nodal clustering coefficient	Structural	0.0277

3.4. Regression model performance and brain-behavior relationships

The SVR model using the top 6 most important brain features was able to explain 9.44% of the variance (R^2 of 9.44% ± 4.02%) in the inattentive symptom T-score in the study

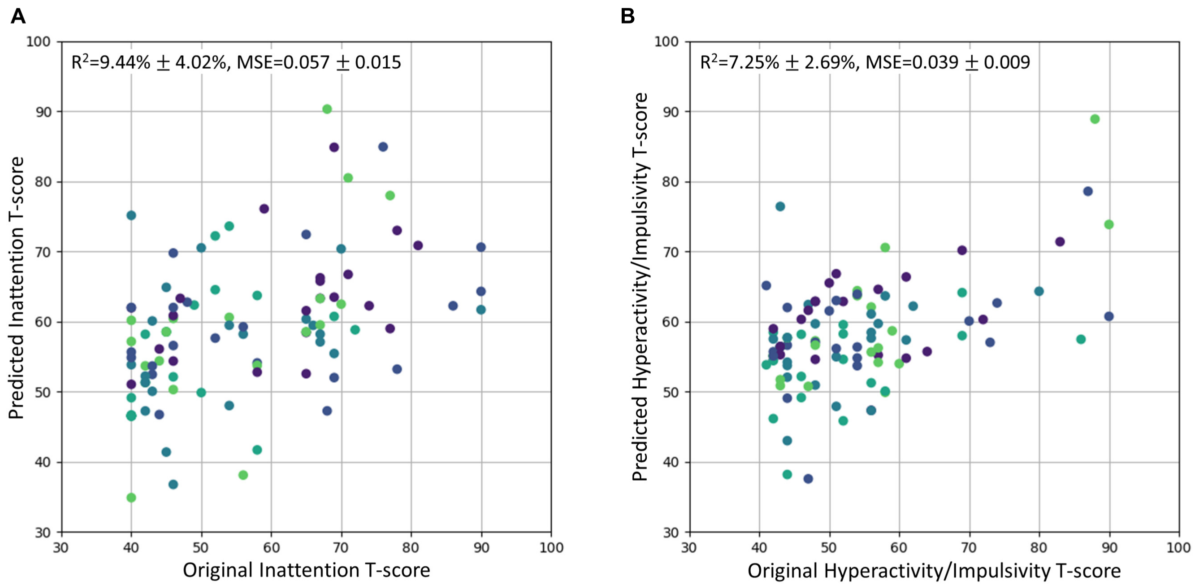

FIGURE 3

The original *T*-scores of the inattentive and hyperactive/impulsive subscales vs. the predicted *T*-scores using regression model. The predicted values were scaled back to the normal T-score range. The R^2 and MSE were reported as mean ± standard deviation. Different cross-validation sets were represented with different colors. **(A)** Original inattention *T*-score vs. Predicted inattention *T*-score. **(B)** Original hyperactivity/impulsivity *T*-score vs. Predicted hyperactivity/impulsivity *T*-score. MSE, mean squared error.

sample (Figure 3A). And the predicted inattentive symptom *T*-score yielded an MSE of 0.057 ± 0.015. The functional nodal clustering coefficient of left medial occipitotemporal gyrus and the functional nodal local efficiency of left postcentral gyrus showed the highest predictive values, with feature importance scores of 0.132 and 0.104, respectively. For the SVR model in predicting hyperactive/impulsive symptom *T*-score, the R^2 was 7.25% ± 2.69% and the MSE was 0.039 ± 0.009 (Figure 3B). The most important brain features for predicting hyperactive/impulsive symptoms were the structural betweenness centrality of left superior frontal gyrus, with an importance score of 0.114, and the functional nodal clustering coefficient of left medial occipitotemporal gyrus, with an importance score of 0.050 (Table 3).

In the PLM-SEM analysis, AE-feature 17 showed significant direct effect on the inattentive symptoms *T*-score, and both AE-features 4 and 17 showed significant direct effects on the hyperactive/impulsive symptoms *T*-score in the whole study sample. Important brain features in left inferior temporal, medial occipitotemporal, postcentral, and superior frontal regions showed significant direct effects on AE-features 4 and 17. The detailed results of the PLM-SEM analysis were shown in Figure 4.

4. Discussion

To our best knowledge, this is the first study in the field applying deep learning approach in multimodal neuroimaging data to identify the neural signatures associated with post-TBI attention deficits in children. By constructing a semi-supervised autoencoder in task-based fMRI and DTI data from 110 children, this study has identified 6 most predictive brain features, involving functional and structural network topological properties associated with left frontal, parietal, temporal, and occipital lobes. Regression-based machine learning analysis in our study sample further showed that, among these most important brain features, those associated with left postcentral area showed significant predictive value for inattentive symptoms; those associated with left superior frontal gyrus showed significant predictive value for hyperactive/impulsive symptoms; while those associated with left medial occipitotemporal gyrus showed significant predictive value for both inattentive and hyperactive/impulsive symptoms.

In the current study, our semi-supervised autoencoder model has well-behaved in terms of effectiveness and robustness in successful discrimination between children with TBI and controls, with satisfactory accuracy and AUC. The reconstructed features also showed minimal error, measured using MSE, when compared to the input features. Compared to the conventional PCA+SVM model, our semi-supervised autoencoder model achieved higher classification accuracy and AUC. The reconstruction process preserved the distinctive information while reducing the feature dimensionality for the classification process (Hinton and Salakhutdinov, 2006; Kamal and Bae, 2022). In addition, the added gaussian noise to input features during the training process of the semi-supervised autoencoder model further improve the generalization performance of the constructed deep neural network model (Audhkhasi et al., 2016; Noh et al., 2017). Therefore, relative to those reported in the majority of existing conventional model-based studies, our identified brain substrates for childhood TBI and its related attention deficits are more reliable and have more significant value in guiding tailored diagnoses and interventions in affected children.

Our study observed the important roles of the structural topological alterations of left inferior frontal gyrus, left superior frontal gyrus, and left frontal pole in differentiating children with TBI and controls. In addition, the betweenness centrality (which represent the capacity of serving as a bridging node) of left superior frontal gyrus showed significant value for successfully predicting severity of the hyperactive/impulsive symptoms in the whole study sample. Those regions were part of the prefrontal cortex, which is an essential component in the top-down control pathway that facilitate the selective attention, inhibition, and sensory modulation (Buschman and Miller, 2007; Rossi et al., 2009; Katsuki and Constantinidis, 2014). Structural MRI and DTI studies have consistently reported decreased gray matter volume, reduced cortical thickness, and disrupted white matter integrity in left prefrontal area in children with TBI (Wilde et al., 2012a; Mayer et al., 2015; Dennis et al., 2016). Our previous investigation also reported significant structural topological alterations in left inferior frontal gyrus in children with TBI-A (Cao et al., 2021b). Linking with these existing findings, our findings of altered structural connectivity within left prefrontal cortex and between left prefrontal and other brain regions may be related to the axonal damages caused TBI; and the persisted structural alterations in the left prefrontal area in children with chronic TBI might disrupt the attention processing pathways and contribute to the emergence of hyperactive/impulsive symptoms.

Meanwhile, the functional nodal local efficiency (which represent regional integration in the whole network) in the left postcentral gyrus were identified as one of the most important brain features for accurate group classification as well as one of the most valuable brain features in predicting severity of inattentive symptoms in the whole study sample. The postcentral gyrus is responsible for transferring tactile information during the spatial attention, which is a key region in the attention top-down and bottom-up pathways (Macaluso et al., 2000; Buschman and Miller, 2007; Katsuki and Constantinidis, 2014). Existing task-based fMRI studies have reported functional alterations of postcentral gyrus in children with TBI during inhibitory control (Tlustos et al., 2015) and sustained attention (Cao et al., 2021b). Our functional network study also reported that the increased nodal local efficiency in left postcentral gyrus was significantly correlated with reduced inattentive symptoms in children with TBI-A (Cao et al., 2021b). Together with existing evidence, this study further validated that functional alterations associated with left postcentral gyrus are highly vulnerable that may disrupt normal attention processing and contribute to the onset of attention deficits in children with TBI.

TABLE 3 Importance score of the most important brain features in the regression-based machine learning model for predicting inattentive and hyperactive/impulsive symptom *T*-scores in the whole study sample.

Region	Topological property	Network	Importance score
Importance scores for predicting inattentive *T*-score			
Left medial occipitotemporal gyrus	Nodal clustering coefficient	Functional	0.132
Left postcentral gyrus	Nodal local efficiency	Functional	0.104
Left inferior temporal gyrus	Nodal clustering coefficient	Functional	0.061
Left superior frontal gyrus	Betweenness centrality	Structural	0.014
Left frontal pole	Nodal clustering coefficient	Structural	0.013
Left inferior frontal gyrus	Nodal local efficiency	Structural	0.011
Importance scores for predicting hyperactive/impulsive *T*-score			
Left superior frontal gyrus	Betweenness centrality	Structural	0.114
Left medial occipitotemporal gyrus	Nodal clustering coefficient	Functional	0.050
Left inferior frontal gyrus	Nodal local efficiency	Structural	0.021
Left inferior temporal gyrus	Nodal clustering coefficient	Functional	0.017
Left postcentral gyrus	Nodal local efficiency	Functional	0.016
Left frontal pole	Nodal clustering coefficient	Structural	−0.007

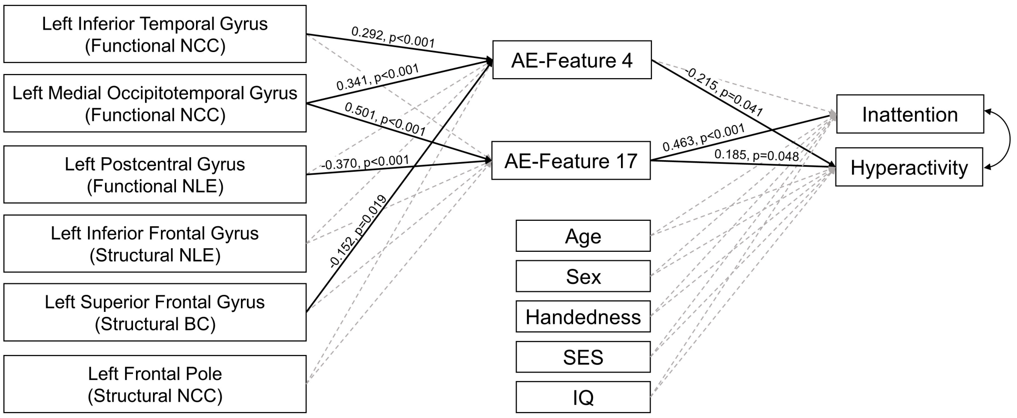

FIGURE 4

Results of partial least square structural equation modeling analysis. The paths with significant direct effects were shown in black solid line. The paths without significant effects were shown in gray dashed line. The numbers next to the significant paths were standardized path coefficient. The *p*-values were calculated by applying bootstrapping with 5,000 random samples. AE-Features: autoencoder-generated features; NCC, nodal clustering coefficient; NLE, nodal local efficiency; BC, betweenness centrality; SES, socioeconomic status, was calculated using the average education years of the parents.

Intriguingly, our study also found that the functional nodal clustering coefficient (which represent the regional connectivity) in left medial occipitotemporal gyrus was an important brain feature in differentiating TBI and control, as well as a significant predictor for both inattentive and hyperactive/impulsive symptoms. The occipitotemporal gyrus has been associated with visual information processing, especially letter process (Mechelli et al., 2003; Vinckier et al., 2007), and was also found to play important role in visual imagery and internally directed cognition (Benedek et al., 2016; Ceh et al., 2021). Structural MRI studies have reported reductions in gray matter volume of the medial occipitotemporal gyrus in children with TBI, and the reduction can persist years after the injury (Wilde et al., 2012b; Dennis et al., 2016). However, no existing studies have reported functional alterations in medial occipitotemporal gyrus in children with TBI. One of the reasons might be that the conventional parametric models lack the sensitivity in detecting the subtle functional alterations in medial occipitotemporal gyrus.

There are some limitations associates with the current study. First, although we have a total of 110 subjects involved in the study, this sample size is still relatively modest in the deep learning field. Such sample size still has potential risk for having overfitted model and limited generalizability. To minimize such risk, we utilized multiple feature selection methods, applied cross-validation, and implemented an additional gaussian noise layer during the training process. Future research with an even larger sample size is expected to further validate the findings of this study. Second, streamline count-based structural brain network can be biased using probabilistic tractography (Zhang et al., 2022). To reduce potential effects, estimation of streamline count was performed in the native diffusion space using individualized brain parcellations and edge weights were normalized in the individual-level analysis. Other graph theory techniques on structural brain network, like fiber density-based (Smith et al., 2015), connectivity probability-based (Cao et al., 2013), and microstructural measure-based (Girard et al., 2017), can be explored to validate the significance of the current findings. Third, the sex factor associated with post-TBI attention deficits was not investigated in this study. Recent clinical studies with large sample size (> 500) reported that girls with TBI had significantly higher risk in developing attention problems than boys (Keenan et al., 2018; Wade et al., 2020). We did not investigate sex-specific neural markers, considering the sample size limitation mentioned above. To partially remove the potential confounding effects, sex was added in our *post hoc* analysis and showed no significant associations with inattentive or hyperactive symptoms. Future studies with much larger samples are required to thoroughly investigate the sex-specific neural markers of post-TBI attention deficits in children.

In summary, the current study has constructed a semi-supervised autoencoder to effectively and robustly discriminate children with TBI and controls while preserve the intrinsic neuroimaging characteristics in the reconstruction of brain features. All the predominant brain features in differentiating children with TBI and controls were in the left hemisphere, including the functional and structural topological alterations involving left frontal regions, postcentral regions, and temporal regions. More importantly, the highly discriminative brain features in left frontal regions, parietal regions, and medial occipitotemporal regions demonstrated significant value for predicting elevated inattentive and/or hyperactive/impulsive symptoms in children post-TBI. The findings of this study suggest that deep learning techniques may have the potential to help identifying robust neurobiological markers for post-TBI attention deficits; and the left superior frontal, postcentral, and medial occipitotemporal regions may serve as reliable targets for the diagnosis and interventions of TBI-related attention problems in children.

Data availability statement

The raw data supporting the conclusions of this article will be made available by the authors, without undue reservation.

Ethics statement

The studies involving human participants were reviewed and approved by Institutional Review Board at the New Jersey Institute of Technology and Institutional Review Board at Saint Peter's University Hospital. Written informed consent to participate in this study was provided by the participants or their legal guardian/next of kin.

Author contributions

XL and JH designed the study. MC worked on literature searching, clinical and imaging data analyses, and wrote the first draft of the manuscript. MC, KW, JH, and XL edited and revised the manuscript. All authors contributed to and have approved the final manuscript.

Funding

This work was partially supported by research grants from the National Institute of Mental Health (R03MH109791, R15MH117368, and R01MH126448) and the New Jersey Commission on Brain Injury Research (CBIR17PIL012 and CBIR22PIL002).

Conflict of interest

The authors declare that the research was conducted in the absence of any commercial or financial relationships that could be construed as a potential conflict of interest.

Publisher's note

References

Abadi, M., Agarwal, A., Barham, P., Brevdo, E., Chen, Z., Citro, C., et al. (2016). Tensorflow: Large-scale machine learning on heterogeneous distributed systems. *arXiv [preprint]*

Achard, S., and Bullmore, E. (2007). Efficiency and cost of economical brain functional networks. *PLoS Comput. Biol.* 3:e30017. doi: 10.1371/journal.pcbi.0030017

Andersson, J. L. R., and Sotiropoulos, S. N. (2016). An integrated approach to correction for off-resonance effects and subject movement in diffusion MR imaging. *Neuroimage* 125, 1063–1078. doi: 10.1016/j.neuroimage.2015.10.019

Ashourvan, A., Telesford, Q. K., Verstynen, T., Vettel, J. M., and Bassett, D. S. (2019). Multi-scale detection of hierarchical community architecture in structural and functional brain networks. *PLoS One* 14:e0215520. doi: 10.1371/journal.pone.0215520

Association, A. P. (2013). *Diagnostic and statistical manual of mental disorders (DSM-5®)*. Worcester, MA: APA. doi: 10.1176/appi.books.9780890425596

Audhkhasi, K., Osoba, O., and Kosko, B. (2016). Noise-enhanced convolutional neural networks. *Neural Netw.* 78, 15–23. doi: 10.1016/j.neunet.2015.09.014

Backeljauw, B., and Kurowski, B. G. (2014). Interventions for attention problems after pediatric traumatic brain injury: what is the evidence? *PM R* 6, 814–824. doi: 10.1016/j.pmrj.2014.04.004

Benedek, M., Jauk, E., Beaty, R. E., Fink, A., Koschutnig, K., and Neubauer, A. C. (2016). Brain mechanisms associated with internally directed attention and self-generated thought. *Sci. Rep.* 6:22959. doi: 10.1038/srep22959

Botchway, E., Kooper, C. C., Pouwels, P. J. W., Bruining, H., Engelen, M., Oosterlaan, J., et al. (2022). Resting-state network organisation in children with traumatic brain injury. *Cortex* 154, 89–104. doi: 10.1016/j.cortex.2022.05.014

Breiman, L. (2001). Random forests. *Mach. Learn.* 45, 5–32. doi: 10.1023/A:1010933404324

Bullmore, E., and Sporns, O. (2009). Complex brain networks: graph theoretical analysis of structural and functional systems. *Nat. Rev. Neurosci.* 10, 186–198. doi: 10.1038/nrn2575

Buschman, T. J., and Miller, E. K. (2007). Top-down versus bottom-up control of attention in the prefrontal and posterior parietal cortices. *Science* 315, 1860–1862. doi: 10.1126/science.1138071

Caeyenberghs, K., Leemans, A., De Decker, C., Heitger, M., Drijkoningen, D., Linden, C. V., et al. (2012). Brain connectivity and postural control in young traumatic brain injury patients: A diffusion MRI based network analysis. *Neuroimage Clin.* 1, 106–115. doi: 10.1016/j.nicl.2012.09.011

Cao, M., Halperin, J. M., and Li, X. (2021a). Abnormal functional network topology and its dynamics during sustained attention processing significantly implicate post-TBI attention deficits in children. *Brain Sci.* 11:1348. doi: 10.3390/brainsci11101348

Cao, M., Luo, Y., Wu, Z., Mazzola, C. A., Catania, L., Alvarez, T. L., et al. (2021b). Topological aberrance of structural brain network provides quantitative substrates of post-traumatic brain injury attention deficits in children. *Brain Connect.* 11, 651–662. doi: 10.1089/brain.2020.0866

Cao, M., Wu, Z., and Li, X. (2022). GAT-FD: An integrated MATLAB toolbox for graph theoretical analysis of task-related functional dynamics. *PLoS One* 17:e0267456. doi: 10.1371/journal.pone.0267456

Cao, Q., Shu, N., An, L., Wang, P., Sun, L., Xia, M. R., et al. (2013). Probabilistic diffusion tractography and graph theory analysis reveal abnormal white matter structural connectivity networks in drug-naive boys with attention deficit/hyperactivity disorder. *J. Neurosci.* 33, 10676–10687. doi: 10.1523/JNEUROSCI.4793-12.2013

Ceh, S. M., Annerer-Walcher, S., Koschutnig, K., Korner, C., Fink, A., and Benedek, M. (2021). Neurophysiological indicators of internal attention: An fMRI-eye-tracking coregistration study. *Cortex* 143, 29–46. doi: 10.1016/j.cortex.2021.07.005

Conners, C. K. (2008). *Conners 3*. Toronto, ON: MHS.

Dennis, E. L., Hua, X., Villalon-Reina, J., Moran, L. M., Kernan, C., Babikian, T., et al. (2016). Tensor-based morphometry reveals volumetric deficits in moderate = severe pediatric traumatic brain injury. *J. Neurotrauma* 33, 840–852. doi: 10.1089/neu.2015.4012

Dennis, E. L., Jin, Y., Villalon-Reina, J. E., Zhan, L., Kernan, C. L., Babikian, T., et al. (2015). White matter disruption in moderate/severe pediatric traumatic brain injury: advanced tract-based analyses. *Neuroimage Clin.* 7, 493–505. doi: 10.1016/j.nicl.2015.02.002

Dewan, M. C., Mummareddy, N., Wellons, J. C. III, and Bonfield, C. M. (2016). Epidemiology of global pediatric traumatic brain injury: qualitative review. *World Neurosurg.* 91:e491. doi: 10.1016/j.wneu.2016.03.045

Fischl, B. (2012). FreeSurfer. *Neuroimage* 62, 774–781. doi: 10.1016/j.neuroimage.2012.01.021

Fisher, A., Rudin, C., and Dominici, F. (2019). All models are wrong, but many are useful: learning a variable's importance by studying an entire class of prediction models simultaneously. *J. Mach. Learn. Res.* 20, 1–81.

Girard, G., Daducci, A., Petit, L., Thiran, J. P., Whittingstall, K., Deriche, R., et al. (2017). AxTract: Toward microstructure informed tractography. *Hum. Brain Mapp.* 38, 5485–5500. doi: 10.1002/hbm.23741

Hair, J. F. Jr., Hult, G. T. M., Ringle, C. M., Sarstedt, M., Danks, N. P., and Ray, S. (2021). *Partial least squares structural equation modeling (PLS-SEM) using R: A workbook*. Berlin: Springer Nature. doi: 10.1007/978-3-030-80519-7

Hair, J. F., Ringle, C. M., and Sarstedt, M. (2011). PLS-SEM: Indeed a silver bullet. *J. Market. Theor. Pract.* 19, 139–152. doi: 10.2753/MTP1069-6679190202

Hansen, J. Y., Shafiei, G., Vogel, J. W., Smart, K., Bearden, C. E., Hoogman, M., et al. (2022). Local molecular and global connectomic contributions to cross-disorder cortical abnormalities. *Nat. Commun.* 13:4682. doi: 10.1038/s41467-022-32420-y

Henseler, J., and Chin, W. W. (2010). A comparison of approaches for the analysis of interaction effects between latent variables using partial least squares path modeling. *Struct. Eq. Model.* 17, 82–109. doi: 10.1080/10705510903439003

Hinton, G. E., and Salakhutdinov, R. R. (2006). Reducing the dimensionality of data with neural networks. *Science* 313, 504–507. doi: 10.1126/science.1127647

Iyer, K. K., Zalesky, A., Barlow, K. M., and Cocchi, L. (2019). Default mode network anatomy and function is linked to pediatric concussion recovery. *Ann. Clin. Transl. Neurol.* 6, 2544–2554. doi: 10.1002/acn3.50951

Jones, D. K. (2010). Challenges and limitations of quantifying brain connectivity in vivo with diffusion MRI. *Imaging Med.* 2:341. doi: 10.2217/iim.10.21

Kamal, I. M., and Bae, H. (2022). Super-encoder with cooperative autoencoder networks. *Pattern Recogn.* 126:108562. doi: 10.1016/j.patcog.2022.108562

Katsuki, F., and Constantinidis, C. (2014). Bottom-up and top-down attention: different processes and overlapping neural systems. *Neuroscientist* 20, 509–521. doi: 10.1177/1073858413514136

Kaufman, J., Birmaher, B., Brent, D. A., Ryan, N. D., and Rao, U. (2000). *K-Sads-Pl.* doi: 10.1097/00004583-200010000-00002

Keenan, H. T., Clark, A. E., Holubkov, R., Cox, C. S., and Ewing-Cobbs, L. (2018). Psychosocial and executive function recovery trajectories one year after pediatric traumatic brain injury: the influence of age and injury severity. *J. Neurotrauma* 35, 286–296. doi: 10.1089/neu.2017.5265

Kingma, D. P., and Ba, J. (2014). Adam: A method for stochastic optimization. *arXiv [preprint]*

Konigs, M., Heij, H. A., Van Der Sluijs, J. A., Vermeulen, R. J., Goslings, J. C., Luitse, J. S., et al. (2015). Pediatric traumatic brain injury and attention deficit. *Pediatrics* 136, 534–541. doi: 10.1542/peds.2015-0437

Konigs, M., Pouwels, P. J., Ernest Van Heurn, L. W., Bakx, R., Jeroen Vermeulen, R., Goslings, J. C., et al. (2018). Relevance of neuroimaging for neurocognitive and behavioral outcome after pediatric traumatic brain injury. *Brain Imaging Behav.* 12, 29–43. doi: 10.1007/s11682-017-9673-3

Konigs, M., Van Heurn, L. W. E., Bakx, R., Vermeulen, R. J., Goslings, J. C., Poll-The, B. T., et al. (2017). The structural connectome of children with traumatic brain injury. *Hum. Brain Mapp.* 38, 3603–3614. doi: 10.1002/hbm.23614

Kramer, M. E., Chiu, C. Y., Walz, N. C., Holland, S. K., Yuan, W., Karunanayaka, P., et al. (2008). Long-term neural processing of attention following early childhood traumatic brain injury: fMRI and neurobehavioral outcomes. *J. Int. Neuropsychol. Soc.* 14, 424–435. doi: 10.1017/S1355617708080545

Kurowski, B., Wade, S. L., Cecil, K. M., Walz, N. C., Yuan, W., Rajagopal, A., et al. (2009). Correlation of diffusion tensor imaging with executive function measures after early childhood traumatic brain injury. *J. Pediatr. Rehabil. Med.* 2, 273–283. doi: 10.3233/PRM-2009-0093

Kurowski, B. G., Epstein, J. N., Pruitt, D. W., Horn, P. S., Altaye, M., and Wade, S. L. (2019). Benefits of methylphenidate for long-term attention problems after traumatic brain injury in childhood: a randomized. double-masked, placebo-controlled, dose-titration, crossover trial. *J. Head Trauma Rehabil.* 34, E1–E12. doi: 10.1097/HTR.0000000000000432

Le Fur, C., Camara-Costa, H., Francillette, L., Opatowski, M., Toure, H., Brugel, D., et al. (2019). Executive functions and attention 7years after severe childhood traumatic brain injury: Results of the Traumatisme Grave de l'Enfant (TGE) cohort. *Ann. Phys. Rehabil. Med.* 63, 270–279. doi: 10.1016/j.rehab.2019.09.003

LeBlond, E., Smith-Paine, J., Riemersma, J. J., Horn, P. S., Wade, S. L., and Kurowski, B. G. (2019). Influence of methylphenidate on long-term neuropsychological and everyday executive functioning after traumatic brain injury in children with secondary attention problems. *J. Int. Neuropsychol. Soc.* 25, 740–749. doi: 10.1017/S1355617719000444

LeCun, Y., Bengio, Y., and Hinton, G. (2015). Deep learning. *Nature* 521, 436–444. doi: 10.1038/nature14539

Li, X., Sroubek, A., Kelly, M. S., Lesser, I., Sussman, E., He, Y., et al. (2012). Atypical pulvinar-cortical pathways during sustained attention performance in children with attention-deficit/hyperactivity disorder. *J. Am. Acad. Child. Adolesc. Psychiatry* 51:e1194. doi: 10.1016/j.jaac.2012.08.013

Lumba-Brown, A., Yeates, K. O., Sarmiento, K., Breiding, M. J., Haegerich, T. M., Gioia, G. A., et al. (2018). Diagnosis and management of mild traumatic brain injury in children: a systematic review. *JAMA Pediatr.* 172:e182847. doi: 10.1001/jamapediatrics.2018.2847

Macaluso, E., Frith, C. D., and Driver, J. (2000). Modulation of human visual cortex by crossmodal spatial attention. *Science* 289, 1206–1208. doi: 10.1126/science.289.5482.1206

Max, J. E., Schachar, R. J., Levin, H. S., Ewing-Cobbs, L., Chapman, S. B., Dennis, M., et al. (2005). Predictors of secondary attention-deficit/hyperactivity disorder in children and adolescents 6 to 24 months after traumatic brain injury. *J. Am. Acad. Child Adolesc. Psychiatry* 44, 1041–1049. doi: 10.1097/01.chi.0000173292.05817.f8

Mayer, A. R., Hanlon, F. M., and Ling, J. M. (2015). Gray matter abnormalities in pediatric mild traumatic brain injury. *J. Neurotrauma* 32, 723–730. doi: 10.1089/neu.2014.3534

Mechelli, A., Gorno-Tempini, M. L., and Price, C. J. (2003). Neuroimaging studies of word and pseudoword reading: consistencies, inconsistencies, and limitations. *J. Cogn. Neurosci.* 15, 260–271. doi: 10.1162/089892903321208196

Muthukrishnan, R., and Rohini, R. (2016). "LASSO: A feature selection technique in predictive modeling for machine learning," in *Proceedings of the 2016 IEEE International Conference on Advances in Computer Applications (ICACA)*, 18–20. doi: 10.1109/ICACA.2016.7887916

Narad, M. E., Riemersma, J., Wade, S. L., Smith-Paine, J., Morrison, P., Taylor, H. G., et al. (2019). Impact of Secondary ADHD on long-term outcomes after early childhood traumatic brain injury. *J. Head Trauma Rehabil.* 35, E271–E279. doi: 10.1097/HTR.0000000000000550

Nielsen, A. N., Barch, D. M., Petersen, S. E., Schlaggar, B. L., and Greene, D. J. (2020). Machine learning with neuroimaging: evaluating its applications in psychiatry. *Biol. Psychiatry Cogn. Neurosci. Neuroimaging* 5, 791–798. doi: 10.1016/j.bpsc.2019.11.007

Noh, H., You, T., Mun, J., and Han, B. (2017). Regularizing deep neural networks by noise: Its interpretation and optimization. *Adv. Neural Inform. Process. Syst.* 30, 5115–5124.

Oldfield, R. C. (1971). The assessment and analysis of handedness: the Edinburgh inventory. *Neuropsychologia* 9, 97–113. doi: 10.1016/0028-3932(71)90067-4

Pereira, F., Mitchell, T., and Botvinick, M. (2009). Machine learning classifiers and fMRI: a tutorial overview. *Neuroimage* 45, S199–S209. doi: 10.1016/j.neuroimage.2008.11.007

Polinder, S., Haagsma, J. A., Van Klaveren, D., Steyerberg, E. W., and Van Beeck, E. F. (2015). Health-related quality of life after TBI: a systematic review of study design, instruments, measurement properties, and outcome. *Popul. Health Metr.* 13:4. doi: 10.1186/s12963-015-0037-1

Raji, C. A., Wang, M. B., Nguyen, N., Owen, J. P., Palacios, E. M., Yuh, E. L., et al. (2020). Connectome mapping with edge density imaging differentiates pediatric mild traumatic brain injury from typically developing controls: proof of concept. *Pediatr. Radiol.* 50, 1594–1601. doi: 10.1007/s00247-020-04743-9

Ross, B. C. (2014). Mutual information between discrete and continuous data sets. *PLoS One* 9:e87357. doi: 10.1371/journal.pone.0087357

Rossi, A. F., Pessoa, L., Desimone, R., and Ungerleider, L. G. (2009). The prefrontal cortex and the executive control of attention. *Exp Brain Res* 192, 489–497. doi: 10.1007/s00221-008-1642-z

Rubinov, M., and Sporns, O. (2010). Complex network measures of brain connectivity: uses and interpretations. *Neuroimage* 52, 1059–1069. doi: 10.1016/j.neuroimage.2009.10.003

Smith, R. E., Tournier, J. D., Calamante, F., and Connelly, A. (2015). SIFT2: Enabling dense quantitative assessment of brain white matter connectivity using streamlines tractography. *Neuroimage* 119, 338–351. doi: 10.1016/j.neuroimage.2015.06.092

Strazzer, S., Rocca, M. A., Molteni, E., De Meo, E., Recla, M., Valsasina, P., et al. (2015). Altered recruitment of the attention network is associated with disability and cognitive impairment in pediatric patients with acquired brain injury. *Neural Plast.* 2015:104282. doi: 10.1155/2015/104282

Sun, Y., Zhao, L., Lan, Z., Jia, X. Z., and Xue, S. W. (2020). Differentiating boys with ADHD from those with typical development based on whole-brain functional connections using a machine learning approach. *Neuropsychiatr. Dis. Treat.* 16, 691–702. doi: 10.2147/NDT.S239013

Tamez-Pena, J., Rosella, P., Totterman, S., Schreyer, E., Gonzalez, P., Venkataraman, A., et al. (2021). Post-concussive mTBI in Student Athletes: MRI features and machine learning. *Front. Neurol.* 12:734329. doi: 10.3389/fneur.2021.734329

Teasdale, G., and Jennett, B. (1974). Assessment of coma and impaired consciousness. A practical scale. *Lancet* 2, 81–84. doi: 10.1016/S0140-6736(74)91639-0

Tlustos, S. J., Chiu, C. Y., Walz, N. C., Holland, S. K., Bernard, L., and Wade, S. L. (2011). Neural correlates of interference control in adolescents with traumatic brain injury: functional magnetic resonance imaging study of the counting stroop task. *J. Int. Neuropsychol. Soc.* 17, 181–189. doi: 10.1017/S1355617710001414

Tlustos, S. J., Peter Chiu, C. Y., Walz, N. C., and Wade, S. L. (2015). Neural substrates of inhibitory and emotional processing in adolescents with traumatic brain injury. *J. Pediatr. Rehabil. Med.* 8, 321–333. doi: 10.3233/PRM-150350

Tzourio-Mazoyer, N., Landeau, B., Papathanassiou, D., Crivello, F., Etard, O., Delcroix, N., et al. (2002). Automated anatomical labeling of activations in SPM using a macroscopic anatomical parcellation of the MNI MRI single-subject brain. *Neuroimage* 15, 273–289. doi: 10.1006/nimg.2001.0978

Vinckier, F., Dehaene, S., Jobert, A., Dubus, J. P., Sigman, M., and Cohen, L. (2007). Hierarchical coding of letter strings in the ventral stream: dissecting the inner organization of the visual word-form system. *Neuron* 55, 143–156. doi: 10.1016/j.neuron.2007.05.031

Wade, S. L., Kaizar, E. E., Narad, M. E., Zang, H., Kurowski, B. G., Miley, A. E., et al. (2020). Behavior problems following childhood TBI: the role of sex, age, and time since injury. *J. Head Trauma Rehabil.* 35, E393–E404. doi: 10.1097/HTR.0000000000000567

Ware, A. L., Yeates, K. O., Geeraert, B., Long, X., Beauchamp, M. H., Craig, W., et al. (2022). Structural connectome differences in pediatric mild traumatic brain and orthopedic injury. *Hum. Brain Mapp.* 43, 1032–1046. doi: 10.1002/hbm.25705

Wechsler, D. (2011). *Wechsler Abbreviated Scale of Intelligence–Second Edition (WASI-II)*. Bloomington, MN: NCS Pearson. doi: 10.1037/t15171-000

Wilde, E. A., Ayoub, K. W., Bigler, E. D., Chu, Z. D., Hunter, J. V., Wu, T. C., et al. (2012a). Diffusion tensor imaging in moderate-to-severe pediatric traumatic brain injury: changes within an 18 month post-injury interval. *Brain Imaging Behav.* 6, 404–416. doi: 10.1007/s11682-012-9150-y

Wilde, E. A., Merkley, T. L., Bigler, E. D., Max, J. E., Schmidt, A. T., Ayoub, K. W., et al. (2012b). Longitudinal changes in cortical thickness in children after traumatic brain injury and their relation to behavioral regulation and emotional control. *Int. J. Dev. Neurosci.* 30, 267–276. doi: 10.1016/j.ijdevneu.2012.01.003

Woolrich, M. W., Ripley, B. D., Brady, M., and Smith, S. M. (2001). Temporal autocorrelation in univariate linear modeling of FMRI data. *Neuroimage* 14, 1370–1386. doi: 10.1006/nimg.2001.0931

Wozniak, J. R., Krach, L., Ward, E., Mueller, B. A., Muetzel, R., Schnoebelen, S., et al. (2007). Neurocognitive and neuroimaging correlates of pediatric traumatic brain injury: a diffusion tensor imaging (DTI) study. *Arch. Clin. Neuropsychol.* 22, 555–568. doi: 10.1016/j.acn.2007.03.004

Yuan, W., Treble-Barna, A., Sohlberg, M. M., Harn, B., and Wade, S. L. (2017). Changes in structural connectivity following a cognitive intervention in children with traumatic brain injury. *Neurorehabil. Neural. Repair.* 31, 190–201. doi: 10.1177/1545968316675430

Zhang, F., Daducci, A., He, Y., Schiavi, S., Seguin, C., Smith, R. E., et al. (2022). Quantitative mapping of the brain's structural connectivity using diffusion MRI tractography: A review. *Neuroimage* 249:118870. doi: 10.1016/j.neuroimage.2021.118870

frontiers | Frontiers in Neuroscience

TYPE Original Research
PUBLISHED 04 April 2023
DOI 10.3389/fnins.2023.1174005

Epileptic prediction using spatiotemporal information combined with optimal features strategy on EEG

Lisha Zhong[1,2†], Jiangzhong Wan[2†], Fangji Yi[3], Shuling He[1], Jia Wu[1,2], Zhiwei Huang[2], Yi Lu[1,4], Jiazhang Yang[5]* and Zhangyong Li[3]*

[1]School of Communication and Information Engineering, Chongqing University of Posts and Telecommunications, Chongqing, China, [2]School of Medical Information and Engineering, Southwest Medical University, Luzhou, Sichuan, China, [3]Research Center of Biomedical Engineering, Chongqing University of Posts and Telecommunications, Chongqing, China, [4]Central Nervous System Drug Key Laboratory of Sichuan Province, Luzhou, Sichuan, China, [5]Yongchuan Women and Children Hospital, Chongqing, China

OPEN ACCESS

EDITED BY
Xiaomin Yang,
Sichuan University, China

REVIEWED BY
Kusumika Krori Dutta,
Ramaiah Institute of Technology, India
Vassiliy Tsytsarev,
University of Maryland, Baltimore, United States

*CORRESPONDENCE
Jiazhang Yang
✉ 1668412087@qq.com
Zhangyong Li
✉ lizy@cqupt.edu.cn

†These authors have contributed equally to this work

SPECIALTY SECTION
This article was submitted to Neural Technology, a section of the journal Frontiers in Neuroscience

RECEIVED 25 February 2023
ACCEPTED 21 March 2023
PUBLISHED 04 April 2023

CITATION
Zhong L, Wan J, Yi F, He S, Wu J, Huang Z, Lu Y, Yang J and Li Z (2023) Epileptic prediction using spatiotemporal information combined with optimal features strategy on EEG.
Front. Neurosci. 17:1174005.
doi: 10.3389/fnins.2023.1174005

Objective: Epilepsy is the second most common brain neurological disease after stroke, which has the characteristics of sudden and recurrence. Seizure prediction is seriously important for improving the quality of patients' lives.

Methods: From the perspective of multiple dimensions including time-frequency, entropy and brain network, this paper proposed a novel approach by constructing the optimal spatiotemporal feature set to predict seizures. Based on strong independence and large information capabilities, the two-dimensional feature screening algorithm is performed to eliminate unnecessary redundant features. In order to verify the effectiveness of the optimal feature set, support vector machine (SVM) was used to classify the preictal and interictal states on both the Kaggle intracranial EEG and CHB-MIT scalp EEG dataset.

Results: This model achieved an average accuracy of 98.01%, AUC of 0.96, F-Score of 98.3% and FPR of 0.0383/h on the Kaggle dataset; On the CHB-MIT dataset, the average accuracy, AUC, F-score and FPR were 95.93%, 0.92, 94.97% and 0.0473/h, respectively. Further ablation experiments have confirmed that the temporal and spatial features fusion has better performance than the individual temporal or spatial features.

Conclusion: Compared to the state-of-the-art methods, our approach outperforms most of these existing techniques. The results show that our approach can effectively extract the spatiotemporal information of epileptic EEG signals to predict epileptic seizures with high performance.

KEYWORDS

epilepsy, spatiotemporal features, fuzzy entropy, power spectral density, brain network, EEG

1. Introduction

Epilepsy is a neurological disease of brain activity, caused by excessive and synchronous electrical discharges. As the second most common disease after stroke, epilepsy affects approximately 70 million people worldwide, which is nearly 1% of the global population, and approximately 80% in developing countries according to the World Health Organization. The sudden and recurring seizures are catastrophic for patients, easily resulting in loss of consciousness, injury and even death by accidents (Lenkov et al., 2013; Zhong et al., 2022c). Therefore, reliable seizure prediction is prime important, as it can greatly improve the quality of patients lives. Electroencephalogram (EEG) which reflects the discharges of neurons, provides plenty of valuable information about brain activities. Due to the advantages of cheap price and high temporal resolution, EEG becomes one of the most useful tools in the diagnosis and prediction of epilepsy (Freestone et al., 2017; Jia et al., 2022; Peng et al., 2022). Contrasting to the obvious difference in the ictal states, EEG signals in the preictal states are similar to the interictal states, which leads to a great challenge in how to accurately forecast epileptic seizures. Therefore, the essence of epilepsy prediction is to identify preictal EEG signals, that is, to accurately distinguish between preictal and interictal states (Chu et al., 2017).

Over the past few decades, with the development of machine learning and deep learning, seizure prediction based on EEG recordings has attracted extensive attention. Nejedly et al. (2019) proposed an automatic seizure prediction approach using CNN with an average sensitivity of only 79%. Usman et al. (2021) extracted handcrafted and automatic features, which were then fed into an ensemble classifier of SVM, CNN, and LSTM, and finally achieved a high accuracy of 95.5%. Chen et al. (2021) put forward an online seizure prediction method with an average sensitivity of 84%. Successive variational mode decomposition and transformers deep learning network has been proposed and achieved an average sensitivity of 0.86 and FPR of 0.18/h on iEEG signals (Wu et al., 2022). Although the good performance of deep learning approach in seizure prediction, its lack of interpretability has limited its clinical application. Therefore, this paper still focuses on machine learning that requires handcrafted features. The prediction performance using machine learning mainly depends on whether the EEG features are effectively extracted and screened.

Entropy, as a good non-linear feature for the complexity evaluation of EEG signals, has been widely proposed for seizure prediction in previous studies (Xiang et al., 2015; Song and Zhang, 2016; Zhang et al., 2018). Zhang et al. (2018) put forward the fuzzy distribution entropy to automatically detect seizure. Sample entropy-based features and extreme learning machine to distinguish interictal and preictal iEEG signals with a sensitivity of 86.75% and a specificity of 83.80% (Song and Zhang, 2016). Some methods are focused on time-frequency features such as power spectral density (PSD) (Zhong et al., 2022b), empirical mode decomposition (EMD) (Cho et al., 2016), and wavelet transform (Faust et al., 2015; Sharma et al., 2015). A dual self-attention residual network proposed by Yang et al. (2021) has extracted the spectrograms by using a short-time Fourier transform and achieved an accuracy of 92.07% on 13 patients in the CHB-MIT dataset. Another important feature during the process of epileptic seizures is synchronization, which can quantify the degree of mutual coupling among brain regions. Previous studies have reported that EEG synchronization can be employed to predict seizures (Ibrahim and Majzoub, 2017; Zhang et al., 2021). Some researchers combined the spatiotemporal features to construct the multi-dimensional feature set. Zhong et al. (2022a) proposed a novel method based on both entropy and synchronization of iEEG signals, and achieved an accuracy of 82.95% on the Kaggle dataset. However, the frequency domain has not been considered.

Although spatial synchronization, entropy, or time-frequency features could be utilized to predict seizures, most of these methods only consider a certain aspect of EEG signals characteristics. Even some methods with multiple features have been resulting in unsatisfactory performance due to not implementing proper screening algorithms. Most of those current methods can only achieve good results in a specific dataset. On the one hand, the reason is that EEG signals in different datasets lack unified labels. On the other hand, the types of epilepsy are diverse, and the dynamics of epilepsy vary greatly among different patients. Therefore, the typical EEG features of some patients may not be suitable for others. Seizures can be seen as the accumulation of abnormal fluctuations over time, and then spread across brain regions through spatial synchronicity, and are also affected by waveforms in different frequency bands. To solve these problems mentioned above, this paper extracts comprehensive multi-dimensional features including non-linearity, time-frequency and spatial domains from the perspective of spatiotemporal information. In order to select the optimal feature set, a feature screening algorithm that takes into account independence and information capabilities is designed. And then the optimal feature set was as the input to the SVM for training and testing. Our approach achieved good prediction performances on both scalp and intracranial EEG signals.

2. Materials and methods

2.1. Dataset description

In this study, the proposed model is tested on two public EEG datasets, the CHB-MIT scalp EEG dataset[1] and the Kaggle competition iEEG dataset.[2] These two public EEG datasets included long-term EEG signals and multiple seizures have been recorded for each subject.

CHB-MIT dataset consists of continuous scalp EEG recordings of 23 epileptic patients from Boston Children's Hospital over many days. Multi-channel EEG signals were recorded with a sampling rate of 256 Hz using the international 10–20 system. In this

---

[1] https://physionet.org/content/chbmit/

[2] https://www.kaggle.com/c/seizure-detection/data

paper, the preictal state was defined as a 30 min signal before the seizure onset; and the interictal state was determined as at least 4 h far away from any seizure. The upcoming seizure is excluded with an interval of less than half an hour between two adjacent seizures to ensure the preictal states with the length of 30 min. Patients with at least three recorded preictal and interictal states were screened. The reason is that less than three preictal or interictal states would lead to an overfitting problem. A total of 14 patients are available for considering all these definitions and constraints. **Table 1** summarizes the details of these 14 patients used in our experiments.

The Kaggle competition dataset consists of intracranial EEG signals recorded from five dogs with naturally occurring epilepsy using an ambulatory monitoring system. The iEEG recordings were collected from 16 electrodes with a sampling rate of 400 Hz. Preictal states were determined as 1 h before seizure onset and 1 h interictal iEEG signals were restricted to be at least 1 week before or after seizure in this dataset. All canines had experienced at least four seizures, and a total of 44 seizures were recorded in this experiment. The detailed information is shown in **Table 2**.

2.2. Methodology

The flow chart of the algorithm for seizure prediction using the spatiotemporal information with the optimal features strategy is shown in **Figure 1**, and the detailed steps are as below:

2.2.1. Pre-processing

The amplitude of scalp EEG signals is weak, making it easily disturbed by the external environment, such as electrode contact, power frequency interference, etc. In addition, various physiological activities inside the human body also produce artifacts, such as electrooculogram (EOG) artifacts caused by eye movement and blinking, electromyogram (EMG) artifacts caused by muscle shaking, and electrocardiogram (ECG) artifacts caused by heart beating. These artifacts often affect and interfere with the experimental results. In comparison, intracranial EEG signals are less susceptible to interference, and their signals are relatively clean and less affected by the environment. Therefore, different pre-processing procedures are applied to intracranial and scalp EEG signals, as described below:

The pre-processing of intracranial EEG signals is relatively simple to avoid removing valuable information. Baseline drift was removed by subtracting the mean value of the iEEG signal from each data point (Wu et al., 2009). Then a simple fourth-order Butterworth bandpass filter with a range of 0.5∼70 Hz was used to filter the iEEG signal. For scalp EEG, in addition to the above-mentioned pre-processing steps, the following measures were taken to remove interference: a 50 Hz notch filter was used to remove the power-line interference and independent component analysis (ICA) has been developed to effectively remove artifacts in EEG signals (Du et al., 2016). Artifacts such as eye movement, eye blink, and muscle artifacts were removed by using ICA in the EEGLAB toolbox (Delorme and Makeig, 2004) with the guidelines (Urigüen and Garcia-Zapirain, 2015). Artifacts that cannot be removed through signal processing, such as severe crying or intense head movement, are excluded directly from the experimental data. The results after pre-processing are shown in **Figure 2**. The EEG signals become smoother, and the burr, interference as well as EOG artifacts are effectively removed from the raw EEG signals.

The long-term continuous EEG recordings need to be segmented. The duration of the segment is commonly performed from 5 to 30 s. In our method, a 5 s non-overlapping moving window was used to divide the clean EEG signals into 5 s epochs. EEG analysis and feature extraction were performed with the software package MATLAB R2016b (The MathWorks, Inc., Natick, MA, United States) and its EEGlab and statistics toolbox.

2.2.2. Features extraction

Accurate extraction of the EEG features that can distinguish between preictal and interictal states is the key to improving the prediction accuracy. This paper analyses epileptic EEG signals from multiple dimensions such as non-linear, time-frequency and brain networks with the purpose of deeply mining the signals' spatiotemporal features. The temporal features include the non-linear feature fuzzy entropy and the spectral features; and the spatial features are jointly constructed from the statistical parameters and the synchronization of the brain network. The principle of these spatiotemporal features is as follows:

2.2.2.1. Fuzzy entropy

Entropy originally measures the degree of chaos in a thermodynamic system, and it can also describe the probability of the occurrence of new events in a time-series signal. Fuzzy entropy (FuzzyEn) was proposed by Chen et al. (2007) to measure the complexity of time series, which is then used as a non-linear feature to evaluate the complexity of EEG. FuzzyEn can be obtained by the following steps:

For a time series of N points $U = \{u(i), i = 1, \ldots, N\}$, m-dimensional vectors $X(i)$ are formed as:

$$X(i) = [u(i), u(i+1), \cdots, u(i+m-1)] - u_0(i), \quad (1)$$
$$i = 1, 2, \cdots, N-m+1$$

where $u_0(i) = \frac{1}{m}\sum_{j=0}^{m-1} u(ij)$ and m indicates the embedding dimension.

The distance matrix d_{ij}^m between vectors $X(i)$ and $X(j)$ is constructed as:

$$d_{ij}^m = d[X(i), X(j)] = \max_{p=1,2,\cdots,m} \{|u(i+p-1) - u_0(i)| - |u(j+p-1) - u_0(j)|\} \quad (2)$$

where k indicates the sequence number of elements of the reconstructed vector.

The similarity degree A_{ij}^m can be calculated through the fuzzy function $A(x)$:

$$A(x) = \begin{cases} 1, & x = 0 \\ \exp\left[-ln(2)\left(\frac{x}{y}\right)^2\right], & x > 0 \end{cases} \quad (3)$$

$$A_{ij}^m = exp\left[-ln(2) \cdot (d_{ij}^m/r)^2\right], j = 1, 2, N-m+1 \quad (4)$$
$$and\, j \neq i$$

TABLE 1 Summary of the 14 patients in the CHB-MIT dataset.

Patients	Gender	Age	No. of seizures	Total record time (h)	No. of electrodes
chb01	Female	11	7	40.55	23
chb03	Female	14	7	28	23
chb05	Female	7	5	39	23
chb06	Female	1.5	9	66.7	23
chb07	Female	14.5	3	68.1	23
chb08	Male	3.5	5	20	23
chb09	Female	10	4	67.8	23
chb10	Male	3	7	50	23
chb14	Female	9	8	26	23
chb15	Male	16	20	40	31
chb18	Female	18	6	36	22
chb20	Female	6	8	29	28
chb21	Female	13	4	33	28
chb23	Female	6	7	28	28

TABLE 2 Information for the canines in the Kaggle competition dataset.

Dogs	No. of seizures	Interictal states (10 min)	Preictal states (10 min)	No. of electrodes
Dog1	4	480	24	16
Dog2	7	500	42	16
Dog3	12	1440	72	16
Dog4	16	804	97	16
Dog5	5	450	30	15

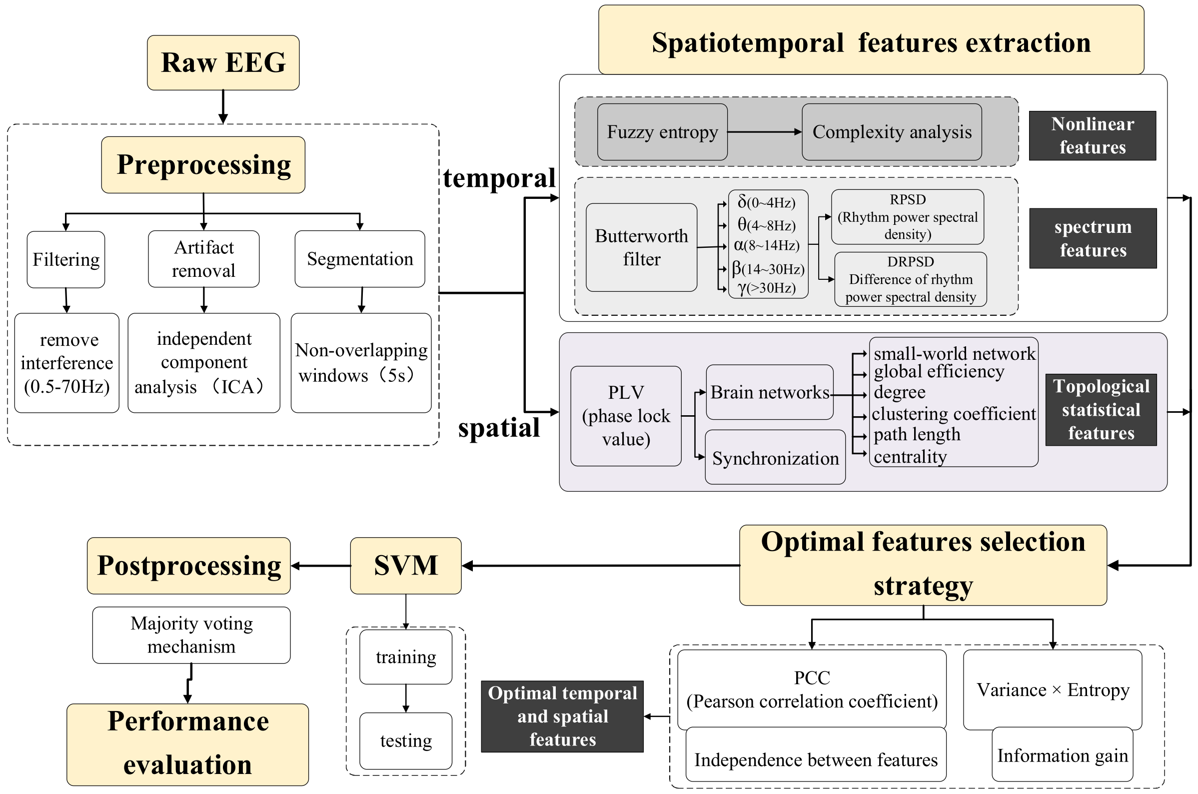

FIGURE 1
The flow chart of the algorithm.

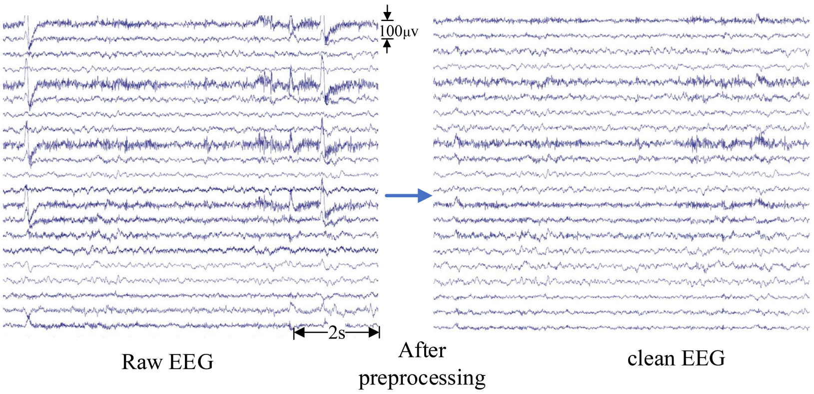

FIGURE 2
The clean electroencephalogram (EEG) signals after pre-processing.

Define the function $\Phi^m(r)$ as:

$$C_i^m(r) = \frac{1}{N-m}\sum_{j=1, j\neq i}^{N-m+1} A_{ij}^m \quad (5)$$

$$\Phi^m(r) = \frac{1}{N-m+1}\sum_{i=1}^{N-m+1} C_i^m(r) \quad (6)$$

Similarly, $\Phi^{m+1}(r)$can be calculated by the above process. For a finite set, FuzzyEn can be estimated by

$$FuzzyEn(m, r, N) = ln\phi^m(r) - ln\phi^{m+1}(r) \quad (7)$$

This paper set the dimension $m = 2$ and the tolerance$r = 0.2 \times std$(standard deviation).

2.2.2.2. Power spectral density (PSD)

Welch method was used to calculate the PSD of EEG signals with the advantages of fast calculation speed and multiple windows for selection (Zhang and Parhi, 2016). In accordance with Welch's periodogram method, the PSD of the EEG segment in each frequency band was estimated by the following steps (Welch, 1967):

First, the EEG signal $x_N(n), n = \{0, 1, , N-1\}$ is divided into L segments. Each segment has M points and the PSD for the ith segment is obtained as:

$$P_i(w) = \frac{1}{U}\left|\sum_{n=0}^{M-1} x_{N_i}(n)\, d_2(n)\, e^{-jwn}\right|^2, i = 1, 2, M-1 \quad (8)$$

where $U = \frac{1}{M}\sum_{n=0}^{M-1} d_2^2(n)$ and $d_2(n)$ is the window function.

Then, the PSD of the $x_N(n)$ can be expressed as:

$$P(w) = \frac{1}{L}\sum_{i=1}^{L} P_i(w) \quad (9)$$

Mathematically, the PSD in the ith frequency band (*delta, theta, alpha, beta, and gamma*) is calculated as (Zhang and Parhi, 2016):

$$P_i = \log \sum_{\omega\in \text{band}i} P(\omega), \left\{ i = delta, theta, alpha, beta, gamma. \right\} \quad (10)$$

where delta (0∼4 Hz), theta(4∼8 Hz), alpha(8∼14 Hz), beta(14∼30 Hz) and gamma (>30 Hz). Therefore, Rhythm Power Spectral Density (RPSD) can be calculated according to formula (10). Spectral power ratio (SPR) represents the difference between the PSDs in two different bands in the same time window. SPR of the spectral power in band k over that in band l can be computed as:

$$P_{k-l} = P_k - P_l \quad (11)$$

where P_k represents the PSD in band k; P_l represents the PSD in the band l.

For a single-channel EEG signal, all possible combinations of five frequency bands lead to a total number of 10 SPR and 5 RPSD features. SPR and RPSD features have been confirmed to be good features for seizure detection (Bandarabadi et al., 2014) and prediction (Parhi and Zhang, 2013). Compared to the RPSD features, certain SPR features are stronger indicators of an upcoming seizure (Zhang and Parhi, 2016).

2.2.2.3. Spatial features based on brain networks

PLV, as an independent of amplitude, is suitable to measure the phase synchronization of EEG signals, which can be computed as follow (Lachaux et al., 1999):

$$PLV(t,f) = \frac{1}{N}\left|\sum_{n=1}^{N} \exp\left(j\left\{\Delta\phi(t,f)\right\}\right)\right| \quad (12)$$

where $\Delta\Phi(t,f)$ is the instantaneous phase difference between a pair of EEG channels at time t and frequency f. Taking channels 1 and 2 for example, $\Delta\Phi(t,f)$ is calculated as:

$$\Delta\Phi(t,f) = \Phi_{ch1}(t,f) - \Phi_{ch2}(t,f) \quad (13)$$

where $\Phi_{ch1}(t,f)$ and $\Phi_{ch2}(t,f)$ are the instantaneous phases of the EEG signals in channel 1 and channel 2, respectively. Instantaneous phase $\phi(t)$ is obtained by the Hilbert transform (Ihlen, 2009). The value of PLV ranges from 0 to 1. The larger the PLV value, the stronger the synchronization of the signal, and vice versa.

From the perspective of graph theory, the complex phase-synchronized brain network established by PLV belongs to the undirected connection graph, which contains rich topological

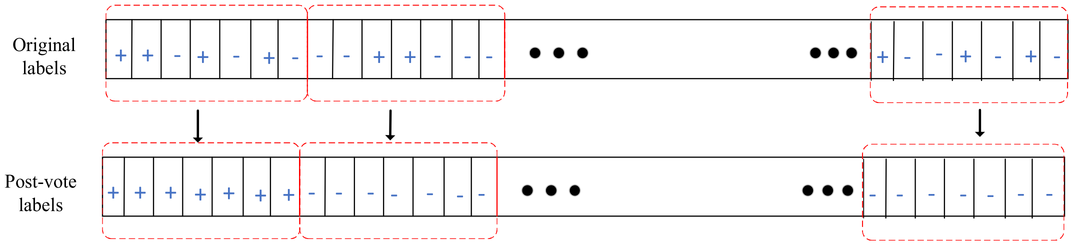

FIGURE 3
Majority voting diagram.

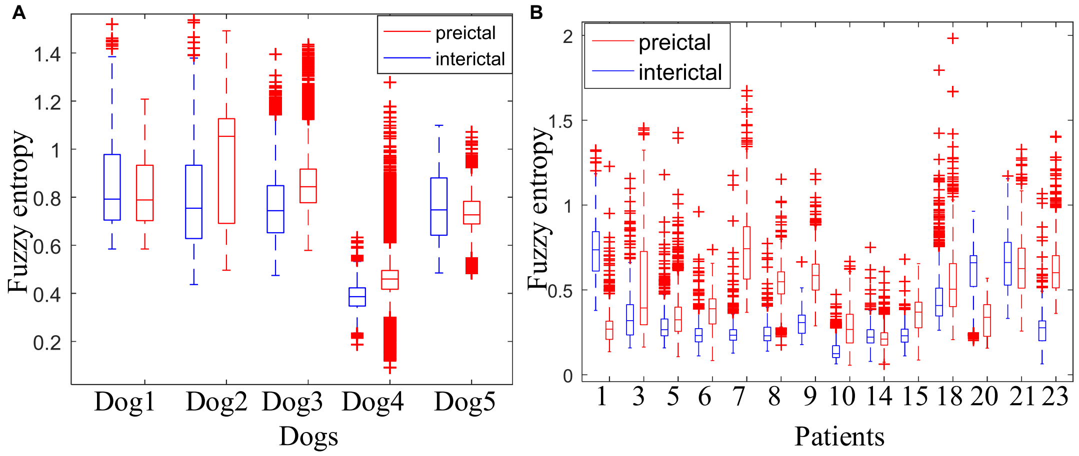

FIGURE 4
Comparison of the fuzzy entropy between the preictal and interictal states. **(A)** Is the fuzzy entropy for dogs in the Kaggle dataset and **(B)** is for patients in the CHB-MIT dataset.

statistical features. In addition to the synchronization, 6 statistical features including small-world attributes (Humphries et al., 2006), global efficiency, degree, clustering coefficient, characteristics path length and eigenvector centrality (Rubinov and Sporns, 2010) have been chosen as the spatial features.

2.2.3. Optimal spatiotemporal feature set selection

In summary, for each electrode, 23 spatiotemporal features, which include 1 FuzzyEn, 5 RPSD, 10 SPRs, and 7 topological statistical features are extracted every 5 s. As more and more features have been extracted for multi-channel long-term EEG signals, there are a large number of irrelevant redundant features in the spatiotemporal features. This greatly reduces the performance of the classifier, causing the curse of dimensionality. Therefore, the feature selection algorithm is essential. The critical strategy is to select the most important EEG features that can best express the characteristics of preictal states, thereby removing the redundant features to reduce the dimension of features. This paper proposed a two-dimensional feature selection algorithm based on independence and information capability in order to form the optimal epilepsy spatiotemporal feature set. The stronger the independence of the features (lower the correlation between the features) contained in the feature set, the less redundancy of the features is guaranteed. The larger the information content of the feature set, the more comprehensive and effective features can be obtained to measure the epileptic EEG signals. Therefore, the spatiotemporal feature set selection algorithm should satisfy strong independence and large information.

Pearson correlation coefficient (Barakchian et al., 2020) has been used to calculate the correlation between features. The

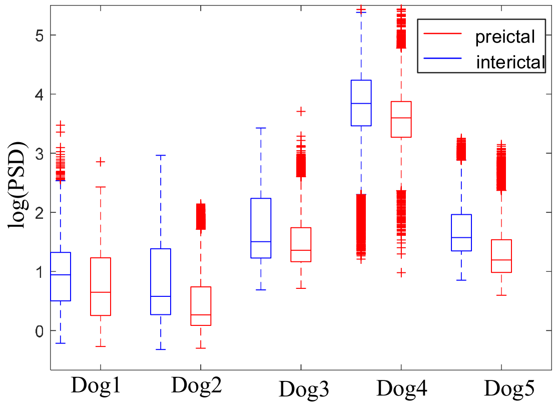

FIGURE 5
Comparison of power spectral density (PSD) between preictal and interictal states for five canines in the Kaggle dataset.

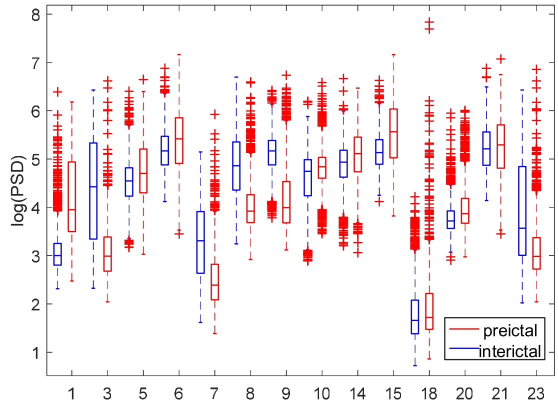

FIGURE 6
Comparison of PSD between preictal and interictal states for 14 patients in the CHB-MIT dataset.

independence of the ith feature ind_ican be evaluated as:

$$r_{i,k} = \frac{\sum_{j=1}^{n} \left(f_{ji} - \overline{f_i}\right)\left(f_{jk} - \overline{f_k}\right)}{\sqrt{\sum_{j=1}^{n} (f_{ji} - \overline{f_i})^2 (f_{jk} - \overline{f_k})^2}} \tag{14}$$

$$i, k = 1, 2, \cdots, m(i \neq k); j = 1, 2, \cdots, n.$$

$$ind_i = \sum_{k=1}^{m} \left(1 - \left|r_{i,k}\right|\right) \tag{15}$$

where $r_{i,k}$ represent Pearson correlation coefficient between two features i and k with n samples; f_{ji} and f_{jk} represent the value of the features i and k at the jth sample, $\overline{f_i}$and $\overline{f_k}$ represent the means of f_{ji} and f_{jk}, respectively. m is the number of all features and n is the total number of samples.

In terms of the features' information capacity, this paper used the variance entropy product to measure the amount of information (Daoud and Bayoumi, 2019). Variance is used to evaluate the fluctuation of features, and entropy can measure the complexity of features. First, calculate the variance and information entropy of the ith feature. The variance $\sigma^2(X_i)$ and the entropy $H(X_i)$ were defined by formulas (17) and (18), respectively. Then, multiply the variance and entropy to measure the information of features (formula 19). Finally, the features are selected with the highest variance entropy product.

$$\sigma^2(X_i) = \frac{1}{N} \sum_{j=1}^{N} \left(x_i(j) - \mu_i\right)^2 \tag{16}$$

$$(X_i) = -\sum_{j=1}^{N} p\left(x_i(j)\right) \log_2 p\left(x_i(j)\right) \tag{17}$$

$$inf_i = ó(X_i) \cdot H(X_i) \tag{18}$$

where X_i, μ_i and N are the ith feature, the mean of the ith feature, and the total number of features, respectively. $p\left(x_i(j)\right)$ is the probability mass function of the ith feature.

In the two-dimensional space with independence as the abscissa and information amount as the ordinate, the features with high independence and a large amount of information are screened out. $Score_i$ is defined to represent the independence and information of the ith feature as:

$$Score_i = inf_i \cdot ind_i \tag{19}$$

Then features with high *Scores* are selected to form the optimal spatiotemporal feature set.

2.2.4. Classification and post-processing

SVM, as a common classifier in EEG signals, is used for training and classification. The kernel function selected for SVM in this paper is the default parameter radial basis function: $K(x, x_i) = exp(-ã|x - x_i|^2)$. In order to improve the recognition performance of the algorithm, post-processing is to reprocess the classification results of EEG signals in continuous time windows. Specifically, a majority vote is performed on the output results within a 1 min time window and the majority voting diagram is shown in Figure 3.

2.3. Evaluation metrics

In order to verify whether the epileptic EEG spatiotemporal feature set constructed by the algorithm proposed in this paper can distinguish between the preictal and interictal states, four indicators including accuracy rate (ACC), the area under the receiver operating characteristic curve (AUC), F-score, and false positive rate (FPR) were introduced to evaluate the performance. The evaluation measures are defined as follows (Moridani et al., 2019):

$$ACC = \frac{TN + TP}{TN + FP + TP + FN} \times 100\% \tag{20}$$

$$F - score = \frac{2TP}{2TP + FP + FN} \times 100\% \tag{21}$$

$$FPR = \frac{FP}{FP + TN} \times 100\% \tag{22}$$

where *TP*, *TN*, *FP*, and *FN* refer to true positive, true negative, false positive and false negative, respectively.

3. Results and discussion

3.1. Spatiotemporal feature analysis

3.1.1. Fuzzy entropy

Figure 4 shows the comparison of the fuzzy entropy between the preictal states and the interictal states. The change of fuzzy entropy for each sample is inconsistent. For Dog2, Dog3, and Dog4, the fuzzy entropy in the preictal state was significantly greater than that of the interictal state, making it relatively easy to distinguish between the preictal and the interictal states. However, fuzzy

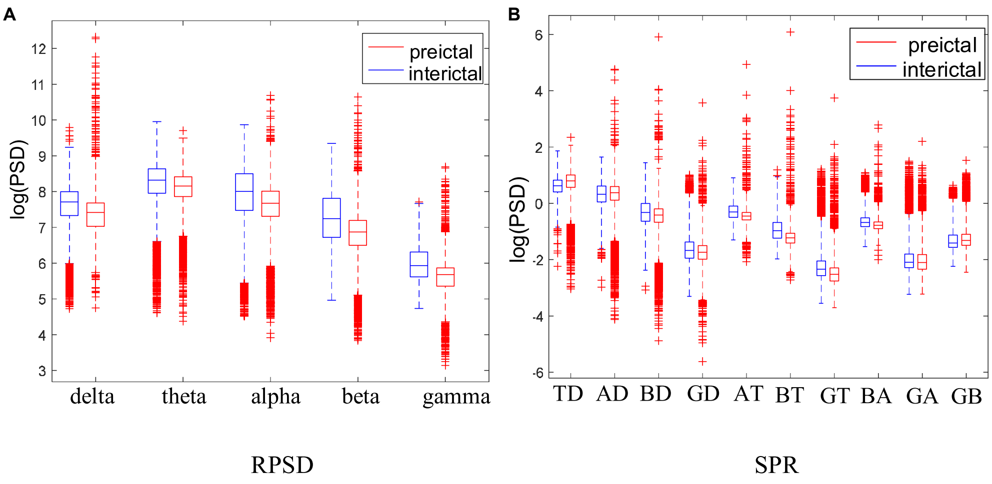

FIGURE 7
Comparison of the RPSD and DRPSD in Dog4. **(A)** Is the RPSD and **(B)** is the SPR. Note that the abscissa label of panel **(B)** represents the difference values obtained by subtracting two different RPSDs. Specifically, TD, theta minus delta; AD, alpha minus delta; BD, beta minus delta; GD, gamma minus delta; AT, alpha minus theta; BT, beta minus theta; GT, gamma minus theta; BA, beta minus alpha; GA, gamma minus alpha; GB, gamma minus beta.

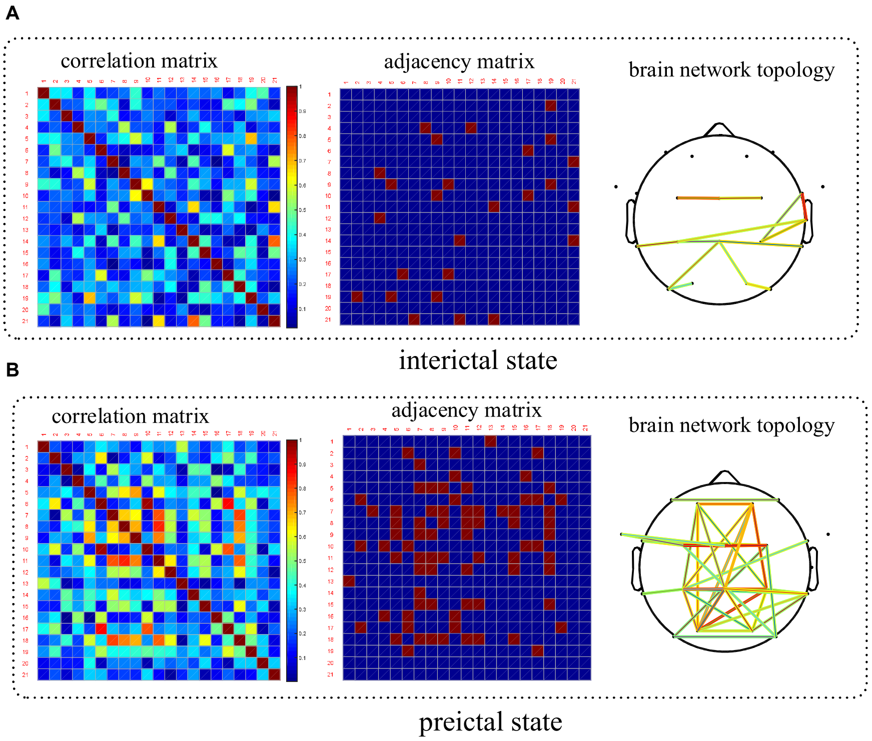

FIGURE 8
Comparison of the spatial features based on brain network between the interictal and preictal states. Patient number chb06 has been taking as an example. **(A)** Brain network in the interictal state and **(B)** is in the preictal state.

entropy of Dog1 and Dog5 are basically overlapped in these two states, making it difficult to distinguish between these two states. For epileptic patients in the CHB-MIT dataset, except patients chb01, chb14, and chb20, the fuzzy entropy in the preictal states is greater than that of the interictal states. The experimental results show that the fuzzy entropy of the epileptic EEG in most of the patients is significantly larger than the interictal states, indicating that the brain activity has changed before the seizure. And the higher complexity of EEG occurs in the preictal states, indicating the upcoming seizure. The experimental results also show that the fuzzy entropy of epileptic EEG signals has large individual differences. Some samples have good classification effect, while others are not sensitive, making it not suitable for each subject. Therefore, although fuzzy entropy can be regarded as an important feature to predict epileptic seizures, it is not suitable as a single feature of epileptic EEG for seizure prediction.

3.1.2. PSD

Figure 5 shows the comparison of PSD between the preictal and interictal iEEG signals for five canines. The results indicate that the PSDs in the interictal states were higher than that in the preictal states. And there are more outliers in both the preictal and interictal states for Dog4. The individual differences exist in the PSD of epileptic EEG signals. As shown from Figure 5, there is some overlap in the overall trend between the interictal states and the preictal states for each subject. Figure 6 compares the PSD of preictal and interictal scalp EEG of 14 patients in the CHB-MIT database. Most of these patients had significant differences in PSD between the preictal and interictal states. Especially for patients chb01, chb03, chb07, chb08, and chb09, the PSD of their EEG signals could be available for distinguishing between preictal and interictal states. However, for an individual patient (such as patient chb21), it is almost impossible to classify the preictal and interictal states using PSD due to the overlapping of PSD in these two states. Therefore, only using PSD as a feature to classify the interictal and the preictal EEG signals is inappropriate and cannot achieve good prediction accuracy.

In order to further analyze the PSD variation of each rhythm, this paper calculated the RPSD and SPR of each subject. Taking Dog4 as an example, the results are shown in Figure 7. Except for theta rhythm, RPSD is higher in the interictal states than in the preictal states. RPSD of beta and gamma rhythms have more outliers in the preictal states. Meanwhile, the RPSD of theta has no significant differences between the preictal and the interictal states while the SPR associated with theta rhythm was significantly different. For BT (beta-theta) and AT (alpha-theta), the SPTs in the interictal states are greater than those in the preictal states, and more outliers appear in preictal states. These results suggest that BT and AT may be good features to distinguish between interictal and preictal states. However, some other SPRs, such as GA (gamma-alpha) and GB (gamma-beta), are difficult to distinguish these two states. For each subject, some specific features may be more suitable. Therefore, RPSD and SPR are combined to further screen the optimal features set.

3.1.3. Spatial features based on brain networks

PLV which is a good measure of phase synchronization was used to construct brain networks in this paper. CHB-MIT scalp EEG dataset has electrode position information, which makes the display of the constructed brain network more convenient and intuitive. Therefore, taking a patient in this dataset as an example to compare the spatial features between the preictal and interictal states, and the results are shown in Figure 8. The results showed that the synchronization between the electrodes in the preictal states was higher than that in the interictal states, indicating that the abnormal EEG signals had begun to spread and affect more brain regions before the seizure onset. Spatial coupling and connectivity can also be observed from the brain network topology drawn from the adjacency matrix. Topological connectivity has been altered in the preictal states with significant enhancement and been covered with most areas of the brain. The results show that the statistical characteristics of network topology can effectively extract epilepsy information before seizures and can be further applied to seizure prediction.

3.2. Comparing the optimal spatiotemporal features selection algorithms

An ablation study is carried out to verify the feature selection algorithm on both the Kaggle competition and CHB-MIT datasets. Four feature selection schemes, namely without features selection, independence-based, information-based, and the feature score proposed in this paper, are compared. The results are shown in Table 3, the accuracy rate without feature selection is the lowest, followed by independent-based or information-based feature selection with an accuracy rate below 80%. The feature score algorithm composed of the independence and the information achieved the highest accuracy, reaching 98.01% on the Kaggle competition dataset and 95.93% on the CHB-MIT dataset. The experimental results illustrate that our proposed feature selection algorithm can effectively extract the optimal spatiotemporal features and accurately distinguish between the preictal and interictal states.

3.3. Prediction performance verification

3.3.1. Performance evaluation of seizure prediction based on the Kaggle dataset

Table 4 shows the performances of preictal and interictal iEEG signal classification for five epileptic dogs on the Kaggle dataset. Our method achieved an average ACC of up to 98.01%, an average AUC of 0.96 and an average F-score is 98.30% with an FPR of only 3.83%. Dog4 has the highest prediction accuracy, reaching 100%. The reason may be that, on the one hand, our proposed spatiotemporal features can better express the epileptic information about impending seizures for Dog4; on the other hand, Dog4 has the largest amount of preictal iEEG data (16 seizures), making more data available for training and testing, which improves the performance of the classifier. Compared to other canines, the accuracy of Dog5 is relatively low, especially the FPR is up to 11%. The reason may be the small sample size (only 5 seizures occurred). Alternatively, it is also possible that Dog5 has a damaged electrode that has been removed in the pre-processing, which may lead to a loss of spatial information. Overall, the optimal spatiotemporal features proposed in this paper can well distinguish the preictal and interictal states.

To explore the impact of features on epilepsy prediction, an ablation study is conduct to compare our proposed method with two other methods that use either temporal features or spatial features alone. As shown in Table 5, only temporal features are used as the input to the classifier with average accuracy, AUC, F-score, and FPR of 87.7, 0.84, 87.91, and 4.42%, respectively. Using only brain network-based spatial features to distinguish between interictal and preictal states, the results yielded an average accuracy of 81.75%, an average AUC of 0.73, an F-score of 80.91%, and an FPR of 19.64%. It is evident that our proposed method which fuses spatial and temporal features greatly improves the performance of

TABLE 3 Comparison of four feature selection schemes.

Dataset	ACC (%)			
	Without features selection	Independence-based	Information-based	Feature score
Kaggle competition	69.86 ± 27.19	78.07 ± 8.27	75.84 ± 4.06	98.01 ± 2.60
CHB-MIT	66.14 ± 18.11	73.57 ± 3.57	79.96 ± 2.75	95.93 ± 5.74

TABLE 4 Performance evaluation of our proposed method on the Kaggle dataset.

Subjects	ACC (%)	AUC	F-score (%)	FPR (%)
Dog1	99.65 ± 0.69	0.99 ± 0.01	99.66 ± 0.69	0.70 ± 1.39
Dog2	96.28 ± 9.68	0.93 ± 0.19	97.03 ± 7.70	7.43 ± 19.35
Dog3	99.77 ± 0.60	0.99 ± 0.01	99.76 ± 0.61	0.13 ± 0.44
Dog4	100.00 ± 0.00	1.00 ± 0.00	100 ± 0.00	0.00 ± 0.00
Dog5	94.34 ± 7.93	0.89 ± 0.16	95.04 ± 6.77	11.04 ± 15.94
Total	98.01 ± 2.60	0.96 ± 0.05	98.30 ± 2.19	3.83 ± 5.05

TABLE 5 Comparing the proposed spatiotemporal features method for seizure prediction to the temporal or spatial features method on the Kaggle dataset.

	Features	ACC (%)	AUC	F-score (%)	FPR (%)
Spatial features	Brain networks	81.75 ± 8.72	0.73 ± 0.12	80.91 ± 10.89	19.64 ± 15.01
Temporal features	FuzzyEn + PSD	87.7 ± 4.17	0.84 ± 0.08	87.91 ± 5.12	4.42 ± 5.09
Our method	FuzzyEn + PSD + Brain networks	98.01 ± 2.60	0.96 ± 0.05	98.30 ± 2.19	3.83 ± 5.05

TABLE 6 Performance evaluation of our proposed method on the CHB-MIT dataset.

Patients	ACC (%)	AUC	F-score (%)	FPR (%)
chb01	99.95 ± 0.11	0.99 ± 0.01	99.95 ± 0.11	0.05 ± 0.11
chb03	97.36 ± 1.41	0.96 ± 0.01	98.32 ± 1.36	0.15 ± 0.33
chb05	99.36 ± 0.48	0.99 ± 0.01	99.36 ± 0.48	0.39 ± 0.87
chb06	99.65 ± 0.61	0.99 ± 0.01	99.65 ± 0.60	0.28 ± 0.58
chb07	85.19 ± 14.50	0.80 ± 0.29	74.14 ± 12.51	22.22 ± 38.49
chb08	85.28 ± 20.01	0.71 ± 0.40	87.77 ± 13.51	19.50 ± 43.60
chb09	88.33 ± 21.51	0.77 ± 0.43	79.76 ± 38.67	1.18 ± 2.36
chb10	99.72 ± 0.38	0.99 ± 0.01	99.71 ± 0.38	0.56 ± 0.77
chb14	91.09 ± 19.35	0.82 ± 0.38	93.74 ± 13.00	17.82 ± 38.69
chb15	99.12 ± 0.49	0.98 ± 0.01	99.16 ± 0.78	0.94 ± 1.25
chb18	99.48 ± 0.86	0.98 ± 0.02	99.49 ± 0.84	0.90 ± 1.81
chb20	99.17 ± 0.69	0.98 ± 0.01	99.16 ± 0.71	0.22 ± 0.49
chb21	98.57 ± 1.15	0.98 ± 0.01	98.68 ± 1.01	1.78 ± 1.45
chb23	99.72 ± 0.28	0.99 ± 0.01	99.73 ± 0.27	0.22 ± 0.50
Average	95.93 ± 5.74	0.92 ± 0.10	94.97 ± 8.40	4.73 ± 8.25

TABLE 7 Comparing the proposed spatiotemporal features method for seizure prediction with only temporal or spatial features on the CHB-MIT dataset.

Features		ACC (%)	AUC	F-score (%)	FPR (%)
Temporal features	FuzzyEn + PSD	86.40 ± 4.78	0.81 ± 0.05	84.49 ± 5.78	7.01 ± 6.45
Spatial features	Brain networks	82.19 ± 4.79	0.77 ± 0.10	82.66 ± 4.93	11.17 ± 8.74
Our method	FuzzyEn + PSD + Brain networks	95.93 ± 5.74	0.92 ± 0.10	94.97 ± 8.40	4.73 ± 8.25

TABLE 8 The comparison results between the proposed method and other existing state-of-the-art techniques.

References	Features	Classifier	Dataset	ACC (%)	AUC	F-Score (%)	FPR (/h)
Usman et al., 2021	CNN, Statistical and spectral moments	Ensemble of SVM, CNN and LSTM	Kaggle	95.53	–	SPE:95.81SEN:94.20	–
			CHI-MIT	96.05	–	SPE:96.28SEN:95.65	–
Hussein et al., 2021	Continuous wavelet transform	SDCN	Kaggle	–	0.928	SPE: 85.6SEN:88.45	–
			CHB-MIT	98.82	0.97	SPE:98.90SEN:98.75	0.06
Xu et al., 2020	CNN	CNN	Kaggle	–	0.981	SEN:93.5	0.063
			CHB-MIT	–	0.988	SEN:98.8	0.074
Truong et al., 2018	Spectrogram	CNN	Kaggle	–	–	SEN:75	0.25
			CHB-MIT	–	–	SEN:81.4	0.06
This manuscript	FuzzyEn + PSD + Brain networks	SVM	Kaggle	98.01	0.96	98.3	0.038
			CHB-MIT	95.93	0.92	94.97	0.047

seizure prediction. Therefore, it is necessary to consider both spatial and temporal features when analyzing epileptic EEG signals.

3.3.2. Performance evaluation of seizure prediction based on the CHB-MIT dataset

Table 6 shows that our approach has also achieved a good prediction performance on the CHB-MIT scalp EEG signals. The results obtained an average accuracy, AUC, F-score and FPR of 95.93%, 0.92, 94.97%, and 0.0473/h, respectively. The prediction accuracy of most patients exceeds 99% such as chb01, chb05, chb06, chb10, chb15, chb18, chb20, and chb23. However, not all patients have good prediction accuracy such as chb07, chb08, and chb14, which have an accuracy of less than 90%. The reason may be that these patients had relatively few training samples (3—5 seizures). Among them, the chb07 with only three seizures had the lowest accuracy of 85.12%. And FPR may be another reason for this unsatisfactory classification effect of chb07 and chb08. For these two patients, the FPR shows that it is easy to misjudge the interictal states as preictal states. Overall, our proposed approach was validated for predicting epileptic seizures, indicating that the optimal spatiotemporal feature set is effective. It was also found that the prediction performance varies greatly between different patients.

Table 7 shows that the average accuracy, AUC, F-score and FPR of using temporal features are 86.4, 0.81, 84.49, and 7.01%, respectively. While using the spatial features related to the brain network, the average accuracy, AUC, F-score and FPR are 82.19, 0.77, 82.66, and 11.17%, respectively. These results are consistent with that on the Kaggle dataset, indicating that the optimal set generated by fusing spatiotemporal features can significantly improve the prediction performance of epileptic seizures.

3.3.3. Comparison with existing state-of-the-art methods

Table 8 provides the comparison results on seizure prediction performance between our method and other existing state-of-the-art methods using the same datasets (American epilepsy society-Kaggle iEEG dataset and the CHB-MIT scalp EEG dataset). Syed (Usman et al., 2021) performed a deep learning approach that extracts both the handcrafted and the automated features as the input to an ensemble classifier of SVM, CNN, and LSTM, resulting in an accuracy of 95.53 and 96.05% on Kaggle and CHB-MIT datasets, respectively. A semi-dilated convolutional network (SDCN) was proposed by Hussein et al. (2021) which EEG signals were converted into a mage-like format by continuous wavelet transforms. The results finally achieved the AUC of 0.928 on the Kaggle dataset and a high accuracy of 98.82% on the CHB-MIT dataset. Xu et al. (2020) developed an end-to-end deep learning method with a higher AUC of 0.981 and 0.988 on the Kaggle dataset and CHB-MIT dataset, respectively. Truong et al. (2018) proposed a convolutional neural network extracting time and frequency domain information by using short-time Fourier transform (STFT), which has only obtained an average sensitivity of 75% and FPR of 0.21/h on the Kaggle dataset and the average sensitivity of 81.4% on CHB-MIT dataset.

Compared to the other existing state-of-the-art methods, our proposed approach achieves better FPR on both of these two datasets, illustrating that the probability of our error warning in predicting seizures is the lowest. Meanwhile, our method also obtains better performance than other methods on the Kaggle database. For the CHB-MIT dataset, the accuracy of our model is slightly lower than that of Hussein et al. (2021) and Usman et al. (2021), but the complex features and three classifiers combination required in the method proposed by Usman has caused high complexity and the sensitivity; and Hussein's paper only achieved the accuracy of 88.45% on iEEG dataset. Furthermore, both of these two methods are not provided the indicator FPR. In summary, compared with the existing advanced techniques, our method still has certain advantages in seizure prediction on both intracranial and scalp EEG signals.

4. Conclusion

In this paper, epileptic spatiotemporal information is deeply mined from comprehensive multiple dimensions of time-frequency, non-linearity and brain network. A novel prediction model is proposed by using spatiotemporal information with optimal features strategy for seizures early warning. The optimal spatiotemporal features set was formed by screening the high independence and rich information of the extracted features. This feature set has been input into SVM for training and recognition. On the Kaggle intracranial EEG dataset, this model achieved an average accuracy of 98.01%, AUC of 0.96, F-Score of 98.3% and FPR of 0.0383/h, respectively; and On the CHB-MIT scalp EEG dataset, the average accuracy, AUC, F score and FPR were 95.93%, 0.92, 94.97%, and 0.0473/h, respectively. An ablation study was performed to compare our model with two other methods using only temporal features or spatial features. The results show that our method achieves more effective performance. Compared to other existing state-of-the-art approaches on the same datasets, this present method has certain advantages in prediction performance. It is further confirmed that our spatiotemporal information can effectively identify the preictal states, which is helpful to the early warning of seizures for the clinical epileptic patients.

Data availability statement

The original contributions presented in this study are included in the article/supplementary material, further inquiries can be directed to the corresponding authors.

Author contributions

LZ and FY designed the work and wrote the original manuscript. JZW, SH, and ZH contributed to the analysis of data. YL, JW, JY, and ZL contributed to the review and editing. ZL mainly responsible for this project. All authors contributed to the article and approved the submitted version.

Funding

This work was supported by the National Natural Science Foundation of China (62171073), the Doctoral Training Program of Chongqing University of Posts and Telecommunications (BYJS202103), the Sichuan Science and Technology Program (2022NSFSC0508 and 2022YFS0616), the Open Project of Central Nervous System Drug Key Laboratory of Sichuan Province (200027-01SZ, 210022-01SZ, and 230005-01SZ), and the Project of Southwest Medical University (2021ZKZD019).

Acknowledgments

We thank the Research Center of Biomedical Engineering of Chongqing University of Posts and Telecommunications for their assistance in the research.

Conflict of interest

The authors declare that the research was conducted in the absence of any commercial or financial relationships that could be construed as a potential conflict of interest.

Publisher's note

References

Bandarabadi, M., Teixeira, C. A., Netoff, T. I., Parhi, K. K., and Dourado, A. (2014). "Robust and low complexity algorithms for seizure detection," in *Proceedings of the 36th Annual international conference of the IEEE engineering in medicine and biology society*, (Chicago, IL), 4447–4450. doi: 10.1109/EMBC.2014.6944611

Barakchian, S. N., Shati, M., Mortazavi, S. S., Nikanfar, M., and Charsouei, S. (2020). Psychometric properties of the Persian version of the patient-weighted quality of life in epilepsy inventory-10-P. *Epilepsy Behav.* 111:107243. doi: 10.1016/j.yebeh.2020.107243

Chen, H. H., Shiao, H. T., and Cherkassky, V. (2021). Online prediction of lead seizures from iEEG data. *Brain Sci.* 11, 1554. doi: 10.3390/brainsci11121554

Chen, W., Wang, Z., Xie, H., and Yu, W. (2007). Characterization of surface EMG signal based on fuzzy entropy. *IEEE Trans. Neural Syst. Rehabil. Eng.* 15, 266–272.

Cho, D., Min, B., Kim, J., and Lee, B. (2016). EEG-based prediction of epileptic seizures using phase synchronization elicited from noise-assisted multivariate empirical mode decomposition. *IEEE Trans. on Neural Syst. Rehabil. Eng.* 25, 1309–1318. doi: 10.1109/TNSRE.2016.2618937

Chu, H., Chung, C. K., Jeong, W., and Cho, K. H. (2017). Predicting epileptic seizures from scalp EEG based on attractor state analysis. *Comput. Methods Programs Biomed.* 143, 75–87. doi: 10.1016/j.cmpb.2017.03.002

Daoud, H., and Bayoumi, M. A. (2019). Efficient epileptic seizure prediction based on deep learning. *IEEE Trans. Biomed. Circuits Syst.* 13, 804–813. doi: 10.1109/TBCAS.2019.2929053

Delorme, A., and Makeig, S. (2004). EEGLAB: an open source toolbox for analysis of single-trial EEG dynamics including independent component analysis. *J. Neurosci. Methods.* 134, 9–21. doi: 10.1016/j.jneumeth.2003.10.009

Du, Y., Allen, E. A., He, H., Sui, J., Wu, L., and Calhoun, V. D. (2016). Artifact removal in the context of group ICA: a comparison of single-subject and group approaches. *Hum. Brain Mapp.* 37, 1005–1025. doi: 10.1002/hbm.23086

Faust, O., Acharya, U. R., Adeli, H., and Adeli, A. (2015). Wavelet-based EEG processing for computer-aided seizure detection and epilepsy diagnosis. *Seizure* 26, 56–64. doi: 10.1016/j.seizure.2015.01.012

Freestone, D. R., Karoly, P. J., and Cook, M. J. (2017). A forward-looking review of seizure prediction. *Curr. Opin. Neurol.* 30, 167–173. doi: 10.1097/WCO.0000000000000429

Humphries, M., Gurney, K., and Prescott, T. (2006). The brainstem reticular formation is a small world, not scale-free, network. *Proc. R. Soc. Lond B Biol. Sci.* 273, 503–511. doi: 10.1098/rspb.2005.3354

Hussein, R., Lee, S., Ward, R., and McKeown, M. J. (2021). Semi-dilated convolutional neural networks for epileptic seizure prediction. *Neural Netw.* 139, 212–222. doi: 10.1016/j.neunet.2021.03.008

Ibrahim, S., and Majzoub, S. (2017). Adaptive epileptic seizure prediction based on EEG synchronization. *J. Biomimetics Biomater. Biomed. Eng.* 33, 52–58.

Ihlen, E. A. F. (2009). A comparison of two Hilbert spectral analyses of heart rate variability. *Med. Biol. Eng. Comput.* 47, 1035–1044. doi: 10.1007/s11517-009-0500-x

Jia, M., Liu, W., Duan, J., Chen, L., Chen, C. P., Wang, Q., et al. (2022). Efficient graph convolutional networks for seizure prediction using scalp EEG. *Front. Neurosci.* 16:967116. doi: 10.3389/fnins.2022.967116

Lachaux, J. P., Rodriguez, E., Martinerie, J., and Varela, F. J. (1999). Measuring phase synchrony in brain signals. *Hum. Brain Mapp.* 8, 194–208. doi: 10.1002/(SICI)1097-019319998:4<194::AID-HBM4<3.0.CO;2-C

Lenkov, D., Volnova, A., Pope, A., and Tsytsarev, V. (2013). Advantages and limitations of brain imaging methods in the research of absence epilepsy in humans and animal models. *J. Neurosci. Methods* 212, 195–202. doi: 10.1016/j.jneumeth.2012.10.018

Moridani, M. K., Heydar, M., and Behnam, S. S. J. (2019). "A reliable algorithm based on combination of EMG, ECG and EEG signals for sleep apnea detection:(a reliable algorithm for sleep apnea detection)," in *Proceedings of the 5th Conference on knowledge based engineering and innovation (KBEI)*, (Tehran), 256–262. doi: 10.1109/KBEI.2019.8734992

Nejedly, P., Kremen, V., Sladky, V., Nasseri, M., Guragain, H., Klimes, P., et al. (2019). Deep-learning for seizure forecasting in canines with epilepsy. *J. Neural Eng.* 16:036031. doi: 10.1088/1741-2552/ab172d

Parhi, K. K., and Zhang, Z. (2013). "Seizure prediction using ratio of spectral power from single EEG electrode," in *Proceedings of the 6th international workshop on seizure prediction (IWSP6)*, (San Diego, CA), 39.

Peng, P., Song, Y., Yang, L., and Wei, H. (2022). Seizure prediction in EEG signals using STFT and domain adaptation. *Front. Neurosci.* 15:1880. doi: 10.3389/fnins.2021.825434

Rubinov, M., and Sporns, O. (2010). Complex network measures of brain connectivity: uses and interpretation. *Neuroimage* 52, 1059–1069. 2009.10.003 doi: 10.1016/j.neuroimage

Sharma, R., Pachori, R. B., and Acharya, U. R. (2015). An integrated index for the identification of focal electroencephalogram signals using discrete wavelet transform and entropy measures. *Entropy* 17, 5218–5240. doi: 10.3390/e17085218

Song, Y., and Zhang, J. (2016). Discriminating preictal and interictal brain states in intracranial EEG by sample entropy and extreme learning machine. *J. Neurosci. Methods* 257, 45–54. doi: 10.1016/j.jneumeth.2015.08.026

Truong, N. D., Nguyen, A. D., Kuhlmann, L., Bonyadi, M. R., Yang, J., Ippolito, S., et al. (2018). Convolutional neural networks for seizure prediction using intracranial and scalp electroencephalogram. *Neural Netw.* 105, 104–111. doi: 10.1016/j.neunet.2018.04.018

Urigüen, J. A., and Garcia-Zapirain, B. (2015). EEG artifact removal state-of-the-art and guidelines. *J. Neural Eng.* 12, 1–23. doi: 10.1088/1741-2560/12/3/031001

Usman, S. M., Khalid, S., and Bashir, S. (2021). A deep learning based ensemble learning method for epileptic seizure prediction. *Comput. Biol. Med.* 136, 104710. doi: 10.1016/j.compbiomed.2021.104710

Welch, P. (1967). The use of fast Fourier transform for the estimation of power spectra: a method based on time averaging over short, modified periodograms. *IEEE Trans. Audio Electroacoustics.* 15, 70–73. doi: 10.1109/TAU.1967.1161901

Wu, J., Zhang, J., and Yao, L. (2009). "An automated detection and correction method of EOG artifacts in EEG-based BCI," in *Proceedings of the International conference on complex medical engineering*, (Tempe, AZ), 1–5. doi: 10.1109/ICCME.2009.4906624

Wu, X., Zhang, T., Zhang, L., and Qiao, L. (2022). Epileptic seizure prediction using successive variational mode decomposition and transformers deep learning network. *Front. Neurosci.* 16:982541. doi: 10.3389/fnins.2022.982541

Xiang, J., Li, C., Li, H., Cao, R., Wang, B., Han, X., et al. (2015). The detection of epileptic seizure signals based on fuzzy entropy. *J. Neurosci. Methods.* 243, 18–25.

Xu, Y., Yang, J., Zhao, S., Wu, H., and Sawan, M. (2020). "An end-to-end deep learning approach for epileptic seizure prediction," in *Proceedings of the 2nd IEEE International Conference on Artificial Intelligence Circuits and Systems (AICAS)*, 266–270. doi: 10.1109/AICAS48895.2020.9073988

Yang, X., Zhao, J., Sun, Q., Lu, J., and Ma, X. (2021). An effective dual self-attention residual network for seizure prediction. *IEEE Trans. Neural Syst. Rehabil. Eng.* 29, 1604–1613. doi: 10.1109/TNSRE.2021.3103210

Zhang, S., Chen, D., Ranjan, R., Ke, H., Tang, Y., and Zomaya, A. Y. (2021). A lightweight solution to epileptic seizure prediction based on EEG synchronization measurement. *J. Supercomput.* 77, 3914–3932. doi: 10.1007/s11227-020-03426-4

Zhang, T., Chen, W., and Li, M. (2018). Fuzzy distribution entropy and its application in automated seizure detection technique. *Biomed. Signal Process. Control.* 39, 360–377. doi: 10.1016/j.bspc.2017.08.013

Zhang, Z., and Parhi, K. K. (2016). Low-complexity seizure prediction from iEEG/sEEG using spectral power and ratios of spectral power. *IEEE Trans. Biomed. Circuits Syst.*10, 693–706.

Zhong, L., Wu, J., He, S., Yi, F., Zeng, C., Li, X., et al. (2022c). Epileptic seizure prediction in intracranial EEG using critical nucleus based on phase transition. *Comput. Methods Programs Biomed.* 226:107091. doi: 10.1016/j.cmpb.2022.107091

Zhong, L., Wan, J., Wu, J., He, S., Zhong, X., Huang, Z., et al. (2022b). Temporal and spatial dynamic propagation of electroencephalogram by combining power spectral and synchronization in childhood absence epilepsy. *Front. Neuroinform.* 16:962466.

Zhong, L., He, S., Yi, F., Li, X., Wei, L., Zeng, C., et al. (2022a). Spatio-temporal evaluation of epileptic intracranial EEG based on entropy and synchronization: a phase transition idea. *Biomed. Signal Process. Control.* 77:103689. doi: 10.1016/j.bspc.2022.103689

frontiers | Frontiers in Neuroscience

TYPE Original Research
PUBLISHED 14 April 2023
DOI 10.3389/fnins.2023.1175451

OPEN ACCESS

EDITED BY
Xiaomin Yang,
Sichuan University,
China

REVIEWED BY
Su Zhihua,
Guizhou University of Finance and Economics,
China
Shi Shenghui,
Chongqing University of Technology,
China

*CORRESPONDENCE
Xiuxin Wang
✉ wangxx@cqupt.edu.cn
Hongzhong Li
✉ lihz001@gdcp.edu.cn

SPECIALTY SECTION
This article was submitted to
Neural Technology,
a section of the journal
Frontiers in Neuroscience

RECEIVED 27 February 2023
ACCEPTED 24 March 2023
PUBLISHED 14 April 2023

CITATION
Wang X, Yang Y, Wu T, Zhu H, Yu J, Tian J and Li H (2023) Energy minimization segmentation model based on MRI images.
Front. Neurosci. 17:1175451.
doi: 10.3389/fnins.2023.1175451

Energy minimization segmentation model based on MRI images

Xiuxin Wang[1,2]*, Yuling Yang[1], Ting Wu[1], Hao Zhu[1], Jisheng Yu[1], Jian Tian[1] and Hongzhong Li[3]*

[1]Chongqing University of Posts and Telecommunications, Chongqing, China, [2]Institute for Advanced Sciences, Chongqing University of Posts and Telecommunications, Chongqing, China, [3]School of Civil Engineering, Guangdong Communication Polytechnic, Guangzhou, China

Introduction: Medical image segmentation is an important tool for doctors to accurately analyze the volume of brain tissue and lesions, which is important for the correct diagnosis of brain diseases. However, manual image segmentation methods are time-consuming, subjective and lack of repeatability, it needs to develop automatic and reliable methods for image segmentation.

Methods: Magnetic Resonance Imaging (MRI), a non-invasive imaging technique, is commonly used to detect, characterize and quantify tissues and lesions in the brain. Partial volume effect, gray scale in homogeneity, and lesions presents a great challenge for automatic medical image segmentation methods. So, the paper is dedicated to address the impact of partial volume effect and multiple sclerosis lesions on the segmentation accuracy in MRI. The objective function of the improved model and the post-processing method of lesion filling are researched based on the fuzzy clustering space and energy model.

Results: In particular, an energy-minimized segmentation algorithm is proposed. Through experimental verification, the AR-FCM algorithm can better overcome the problem of low segmentation accuracy of the RFCM algorithm for tissue boundary voxels and improve the segmentation accuracy of this algorithm. Meanwhile, a multi-channel input energy-minimization segmentation method with lesion filling and anatomical mapping is further proposed.

Discussion: The feasibility of the lesion filling strategy using post-processing can be confirmed and the segmentation accuracy is increased by comparison experiments.

KEYWORDS

image segmentation, MRI, anatomical atlas, lesions filling, energy

1. Introduction

In recent years, brain diseases are becoming more and more dangerous to human health, and their prevention and treatment are gradually becoming the most important concerns in the medical field. The number of patients with brain diseases such as cerebral thrombosis, cerebral infarction and multiple sclerosis accounts for 30% of the total number of human diseases (Feigin et al., 2021). Multiple sclerosis (MS) is one of the chronic autoimmune diseases of the central nervous system. It is characterized by the demyelination of axons in the cerebral cortex and other gray matter (GM) and white matter (WM) regions, forming focal inflammatory lesions accompanied by the production of symptoms such as pain, impaired mobility, and poor vision (Lassmann, 2018). According to research, the incidence of this disease has been increasing worldwide, and the number of patients with multiple sclerosis currently exceeds more than 2 million cases (Browne et al., 2014). In research and clinical practice, magnetic resonance imaging (MRI) is often used as the most important tool for the diagnosis of MS because of its high sensitivity, good imaging quality, and low radiation output, which can well detect MS plaques and quantify the number and volume of lesions (Filippi et al., 2016). In general, MRI sequences are divided into different categories, including T1-weighted, T2-weighted, proton density (PD), and fluid attenuation inversion recovery (FLAIR). MS lesions usually appear as areas of low signal intensity (low signal to normal white matter) on T1-weighted images and focal areas of high signal intensity (high signal) on T2-weighted images, reflecting tissue water content. Except for cerebrospinal fluid (CSF) suppression, FLAIR images have similar features to T2-w images (Poser et al., 1983). The identification of the number and volume of MS lesions is a critical process in diagnosis, and for the presence of white matter lesions, they are usually depicted manually by specialists in hospitals (Wang et al., 2019). However, manual segmentation of MS lesions is very time consuming and there is a large variation in the depiction of different experts (Gva et al., 2020), in contrast, automated segmentation of MS lesions can save time and reduce the dependence on the observer. However, the presence of grayscale unevenness and noise in MRI, among others (Bajracharya and Rawal, 2015), make accurate segmentation a challenge.

Image segmentation is a common method for extracting tissues such as white matter, gray matter, and CSF from MRI images for quantitative brain tissue analysis (Dora et al., 2017). Over that last decades, many researchers focus on medical image segmentation, which has led to the rapid development of medical image techniques. Brain tissue segmentation methods can be broadly classified into five categories: manual segmentation, region-based segmentation methods, threshold-based segmentation methods, clustering-based segmentation methods, and methods with feature extraction and classification (Jiang et al., 2022). In brain tissue segmentation, clustering methods are statistical techniques based on pixels or voxels and are usually processed for T1-weighted MR images. Among the clustering algorithms based on minimization objective functions, the most theoretically sound and most applied clustering method is the Fuzzy C-Means (FCM) algorithm. The FCM algorithm was proposed by Dunn et al. Although it has better segmentation performance than hard clustering methods, it has poor noise immunity and does not segment noisy MR images well (Tian et al., 2021). To reduce the sensitivity of the FCM algorithm to noise, Pham proposed a new objective function for adding spatial context to the fuzzy c-mean algorithm (Pham, 2001). Its objective function includes a penalty term, which is similar to the Markov random field prior, and is consistent with the desired behavior of the affiliation function determined by the values of the fuzzy factor parameters thus improving it compared to the FCM algorithm, but is more sensitive to the boundaries of the organization (Dobson and Giovannoni, 2019). However, these classical segmentation methods also face some challenges when dealing with images in the presence of lesions, as the intensity of the lesion portion is usually similar to that of normal tissue (Zhao et al., 2018).

In order to handle brain MRI that contain both grayscale unevenness, noise, and MS focal regions, this paper presents anatomical mapping based on the RFCM algorithm, as well as a focal filling strategy using post-processing, which is applied to segment normal brain tissue on brain MRI images suffering from MS. It is demonstrated that the improved RFCM algorithm strategy improves the accuracy of brain MRI image segmentation.

2. Methods

2.1. Atlas Robust Fuzzy C-mean algorithm

The fuzzy clustering space model is an earlier method that uses penalty terms to achieve smoothing of images without being too sensitive to noise, but the model is less effective for segmentation of tissue boundary parts, which is due to the volume effect that can exist in magnetic resonance images, and the volume effect causes the boundaries of brain structures in images to become discontinuous and unclear (Wang et al., 2018). To address this problem, an energy minimization algorithm based on anatomical mapping is proposed in this paper. The model links fuzzy clustering and statistical probability probability mapping by constructing a constraint term in the objective function of the fuzzy clustering space model, called the AR-FCM algorithm (Atlas Robust FCM, AR-FCM). This model inherits the advantages of the fuzzy clustering space model, uses statistical probability mapping to constrain the segmentation of brain tissue, and uses morphological mapping to redistribute voxels at tissue boundaries after segmentation to reduce the effect of partial volume effects. The flow of the method is shown in Figure 1 below.

2.2. S-Lesion Filling algorithm

From an image processing perspective, MS lesions can affect tissue segmentation, causing GM and WM to be classified in the wrong category. MS lesions may affect the estimation of segmentation parameters, leading to changes in tissue boundaries (Ma et al., 2010; Prados et al., 2016), which can affect subsequent morphological studies, including atrophy measurements, tissue volume measurements, etc. Therefore, lesion filling is needed to reduce the negative impact that MS lesions may have on image analysis in order to improve tissue segmentation accuracy (Tian et al., 2022). Briefly, the lesion filling process uses WM image intensities to synthetically estimate filled WM lesions.

S-Lesion Filling (SLF) algorithm is a combined global and local method for filling WM lesions (Valverde et al., 2014; Makropoulos et al., 2018). The filling process of the lesions was performed by taking each axial slice that constituted the 3D image and calculating the mean and standard deviation of the NAWM tissue signal intensity. The calculated mean and standard deviation values are used to generate a normal distribution with a mean value equal to the calculated NAWM mean intensity and a standard deviation equal to half of the calculated NAWM standard deviation. The standard deviation was always fixed to half of the WM mean, independent of the data set used, and this value was chosen empirically to balance the accuracy of the method for 1.5 and 3 T images. The lesion voxel intensities of the current image slice were then replaced by random values of the generated distribution. The process is repeated until all image slices are completed. The flow of the algorithm is shown in Figure 2.

2.3. Lesion Filling and Atlas RFCM algorithm

Pathophysiological studies have shown that conventional magnetic resonance imaging has limited sensitivity to small

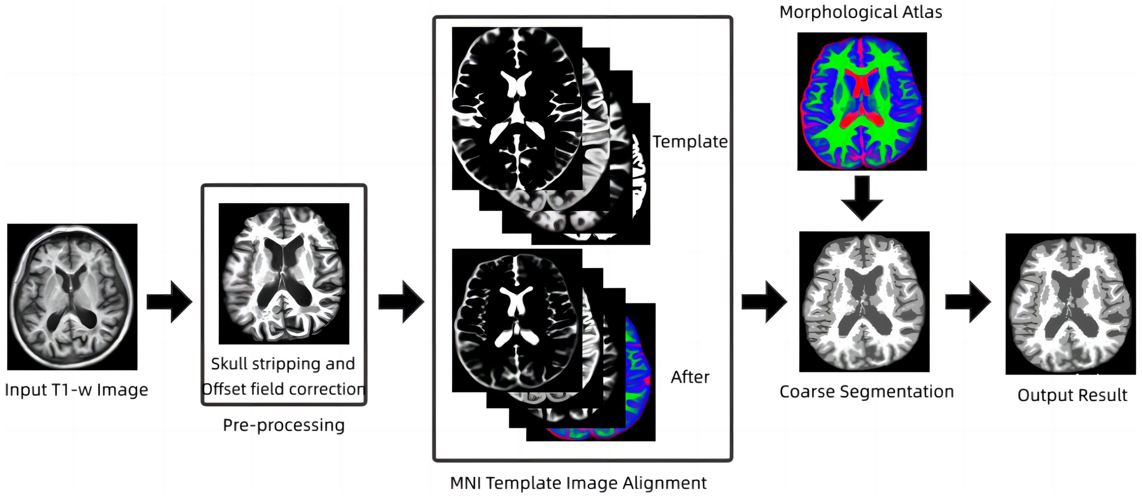

FIGURE 1
Flowchart of energy minimization algorithm based on anatomical mapping.

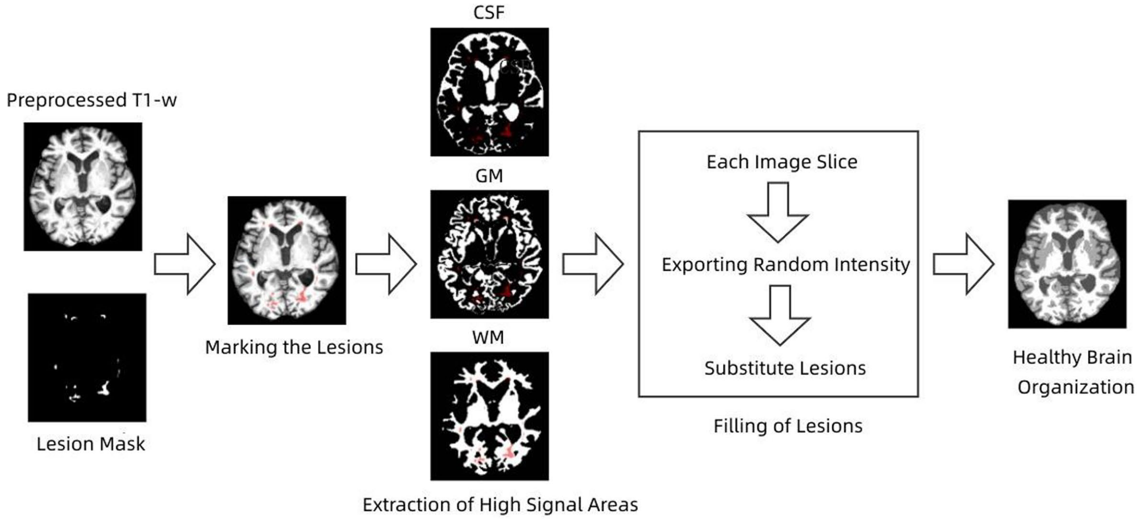

FIGURE 2
Flow chart of lesion filling.

structural changes, both in lesions and normal gray and white matter (Fan et al., 2016; Weiskopf et al., 2021). This suggests that quantitative volumetric analysis of brain tissue and lesions directly from MRI images is not feasible and therefore requires extraction of brain structures such as cerebrospinal fluid, white matter, gray matter, and lesions using image segmentation techniques prior to quantitative analysis (Wang et al., 2014). Multiple sclerosis lesions are an autoimmune neurodegenerative disease whose main feature is the presence of white matter lesions (WM Lesion, WML), which are damaged white matter tissues associated with increased CSF levels. Some classical segmentation methods also face some challenges when dealing with images with lesions, because the intensity of the lesion part is often similar to that of normal tissue and the AR-FCM algorithm proposed in this paper does not segment the brain tissue with lesions well. In general, MS lesions in FLAIR sequences are less severe than CSF, exhibit high signal abnormalities in GM, and can be identified based on contrast (Pohl et al., 2007; Fransen et al., 2020). Based on this feature, lesion areas can be processed using focal filling prior to segmentation, effectively reducing misclassification of CSF and white matter tissue. According to this strategy, an energy minimization algorithm based on lesion filling and anatomical mapping, namely the LFA-FCM algorithm (Lesion Filling and Atlas RFCM), is proposed in this paper. The method requires input T1-w images and FLAIR images, screening out focal regions on FLAIR images using the segmentation lesion method, and then using lesion filling to fill in and replace abnormal values in T1-w images to construct healthy brain MRI images, and finally completing the segmentation using the AR-FCM method. The flow of the method is shown in Figure 3.

2.4. Evaluation indicators

Three commonly used evaluation metrics are selected to measure the segmentation results of this method and other methods, namely Dice similarity coefficient (DSC), Volumetric similarity (*VS*), and Hausdorff distance (HD). These three metrics are chosen because the Dice coefficient is sensitive to the internal organization of the segmentation, while the Hausdorff distance is sensitive to the boundaries of the segmentation, and the volumetric similarity shows the overall segmentation effect.

The Dice similarity coefficient is an ensemble similarity measure function that is widely used to calculate the similarity of two samples and takes values in the range of [0,1]. In image processing, the Dice coefficient is mainly used to measure the accuracy of segmentation within a tissue. The Dice similarity coefficient is calculated by both the gold standard image (GT) and the computational segmentation mask (SEG) as follows:

$$DSC = \frac{2|SEG \cap GT|}{|SEG| \cup |GT|} \tag{1}$$

The closer the Dice similarity coefficient is to 100 indicates that the segmentation results are closer to those of the expert manual segmentation. To make the results more accurate, the DSC value is multiplied by 100 in this paper.

Hausdorff distance is a measure describing the degree of similarity between two sets of points, and it is a defined form of distance between two sets of points. It is mainly used in image segmentation to measure the segmentation accuracy of the boundary. It is calculated by the distance (95th percentile) between the segmentation points in the gold standard image and the segmentation points in the segmentation mask as follows:

$$HD = \max_{p \in SEG_c} \min_{p' \in GT_c} |p - p'| \tag{2}$$

The closer the Hausdorff distance is, the better the segmentation is indicated.

The volume similarity is also calculated by both the gold standard image and the computed segmentation mask, and the more the value converges to 100, the better the segmentation effect:

$$VS = 1 - \left|\frac{GT - SEG}{GT + SEG}\right| \tag{3}$$

3. Results

In this paper, two sets of experiments were conducted, and the first set of experiments was selected to compare the AR-FCM algorithm with the RFCM algorithm, and the segmentation categories were set to three categories: CSF, gray matter and white matter, and the parameter settings of the two methods are shown in Table 1 below. The second group of experiments is to use RFCM algorithm, AR-FCM algorithm and LFA-FCM algorithm for brain tissue segmentation respectively, and the parameter settings of the three methods are shown in Table 2 below. The parameters of the AR-FCM algorithm as well as the LFA-FCM algorithm were required to be consistent in the experiment, which was to verify whether the strategy of increasing

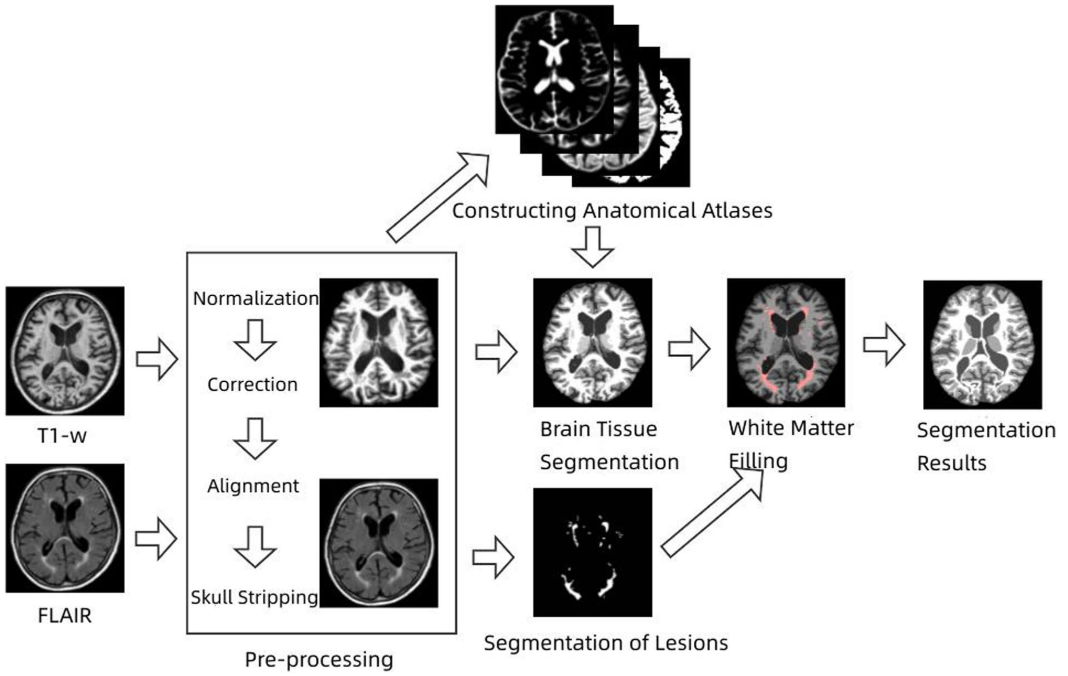

FIGURE 3
Flow chart of energy minimization algorithm based on lesion filling and anatomical mapping.

TABLE 1 RFCM and AR-FCM parameter setting table.

Methods	q	γ	w	β	n	thr
RFCM	2	-	-	1	500	0.001
AR-FCM	2	0.025	1	-	200	0.001

TABLE 2 Parameter settings for RFCM, AR-FCM and LFA-FCM methods.

Methods	q	γ	w	β	n	thr
RFCM	2	–	–	1	500	0.001
AR-FCM	2	0.025	1	–	200	0.001
LFAR-FCM	2	0.025	1	–	200	0.001

TABLE 3 Table of experimental software and hardware parameters.

Category	Parameters
Operating system	Windows 10
CPU	Intel(R) Core(TM) i5-9400F CPU 2.90GHz
RAM	16GB
Simulation software	Matlab 2019b

lesion filling could improve the accuracy of tissue segmentation with the same parameters. Two experiments were done on the MICCAI 2018 MRI brain segmentation challenge data set, and the hardware platform and software used for the experiments are shown in Table 3.

In Figure 4A, shows the original image, and Figure 4B,C show the results of AR-FCM and RFCM algorithm segmentation. Comparing the gold standard image and the result image obtained by the two algorithms, observing the part of the image (c) circled by green circles, we can see that many gray matter parts of the RFCM algorithm are divided into white matter, which leads to too low accuracy of gray matter segmentation and too high accuracy of white matter segmentation. On the contrary, the gray matter around CSF was preserved because AR-FCM used morphological maps to re-divide part of the volume of tissue after tissue segmentation. The second column from left to right is the result of segmentation of cerebrospinal fluid, gray matter and white matter for RFCM, and the third column from left to right is the result of segmentation of cerebrospinal fluid, gray matter and white matter for AR-FCM. The comparison between the second and third columns above shows that RFCM is less effective than AR-FCM in segmenting gray and white matter. Moreover, AR-FCM is better for the tissue segmentation between the boundaries and retains more details, which is achieved by using morphological mapping to re-divide some of the volume regions. The method in this paper improves the segmentation accuracy of the RFCM algorithm and requires only fewer iterations than the RFCM algorithm. However, the part circled in red in image (b) is incorrectly segmented as gray matter tissue, which is the presence of focal tissue in the data set used. It can be seen that the AR-FCM algorithm also does not segment the brain tissue with the presence of lesions better.

In addition, other examples in the data set are processed in this paper using the AR-FCM algorithm. Figure 5 shows the results of applying the energy-minimization segmentation algorithm based on anatomical mapping to other examples in the data set. The first and third rows are the T1-w images of the subject, and the second and fourth rows are the results of segmentation using the AR-FCM algorithm. The black part is CSF, the light gray part is gray matter, and the white part is white matter. Comparing the T1-w images with the segmented result images, it can be seen that the segmented parts of the brain tissue are more consistent with the structures shown in the T1 images. In addition, this method is stable and fully automated, which can yield satisfactory results in practical applications.

Table 4 shows the mean DSC, *VS* and HD values obtained by the RFCM algorithm for each subject, and Figure 6 show the results of the data visualization in the table, respectively. By comparing the average DSC, *VS*, and HD values obtained by the two clustering algorithms, AR-FCM and RFCM, the overall data shows that the average, as well as the values obtained by the AR-FCM algorithm are higher than those of the RFCM algorithm, which indicates that the overall performance of the AR-FCM algorithm is better than that of the RFCM algorithm. The red box plots in Figure 6A, through image (c), represent the AR-FCM segmentation results, and the gray box plots represent the RFCM segmentation results. It is found that both algorithms have higher segmentation accuracy for white matter compared to other tissues, while the AR-FCM algorithm has higher average DSC values for CSF, gray matter, and white matter, which indicates that the AR-FCM algorithm is more accurate for segmenting voxels within brain tissue, which is related to the statistical probability mapping as a constraint. The results in Figure 7 show that the AR-FCM algorithm segmented all three tissues to obtain higher Hausdorff distance values than the RFCM algorithm, and the AR-FCM algorithm segmented each tissue to obtain a minimum HD value greater than the RFCM algorithm obtained a maximum HD value. It indicates that the AR-FCM algorithm is more accurate for segmentation of boundaries, and verifies the feasibility of the strategy of post-processing and re-dividing some volume regions using morphological spectrograms in this paper. In terms of *VS* scores, the difference between the AR-FCM algorithm and the RFCM algorithm for CSF and GM tissue segmentation is not significant, but the AR-FCM algorithm has improved the average *VS* score for WM. In conclusion, AR-FCM is better than RFCM for segmentation of brain tissues in MRI images.

The results of the second group experiments with RFCM, AR-FCM and LFA-FCM are shown in Figure 8A. shows the gold standard image provided in the dataset, Figure 8B–D show the brain tissue segmented using RFCM, AR-FCM, and LFA-FCM, respectively. Comparing image (a) with image (b), the regions circled in green belong to gray matter tissue in the gt image, while the RFCM algorithm classifies all these regions as white matter, which will result in large volume measurements of white matter tissue and small volume measurements of gray matter tissue. Observe image (c) and image (d), the regions circled in red in (c), which belong to white matter tissue in the gt image, and the AR-FCM algorithm incorrectly divides these regions into gray matter tissue. Image (d) shows the result of improved segmentation by the AR-FCM algorithm using lesion filling. It can clearly be seen that the incorrectly segmented gray matter tissue in image (c) is correctly segmented into normal white matter tissue after processing using focal filling, which indicates that the segmentation accuracy of white matter tissue with gray matter tissue can be improved using the post-processing focal filling strategy.

Figure 7 shows the segmentation results of other examples in the LFA-FCM algorithm segmentation dataset. The first and third rows are the T1-w images of the subjects, and the second and fourth rows are

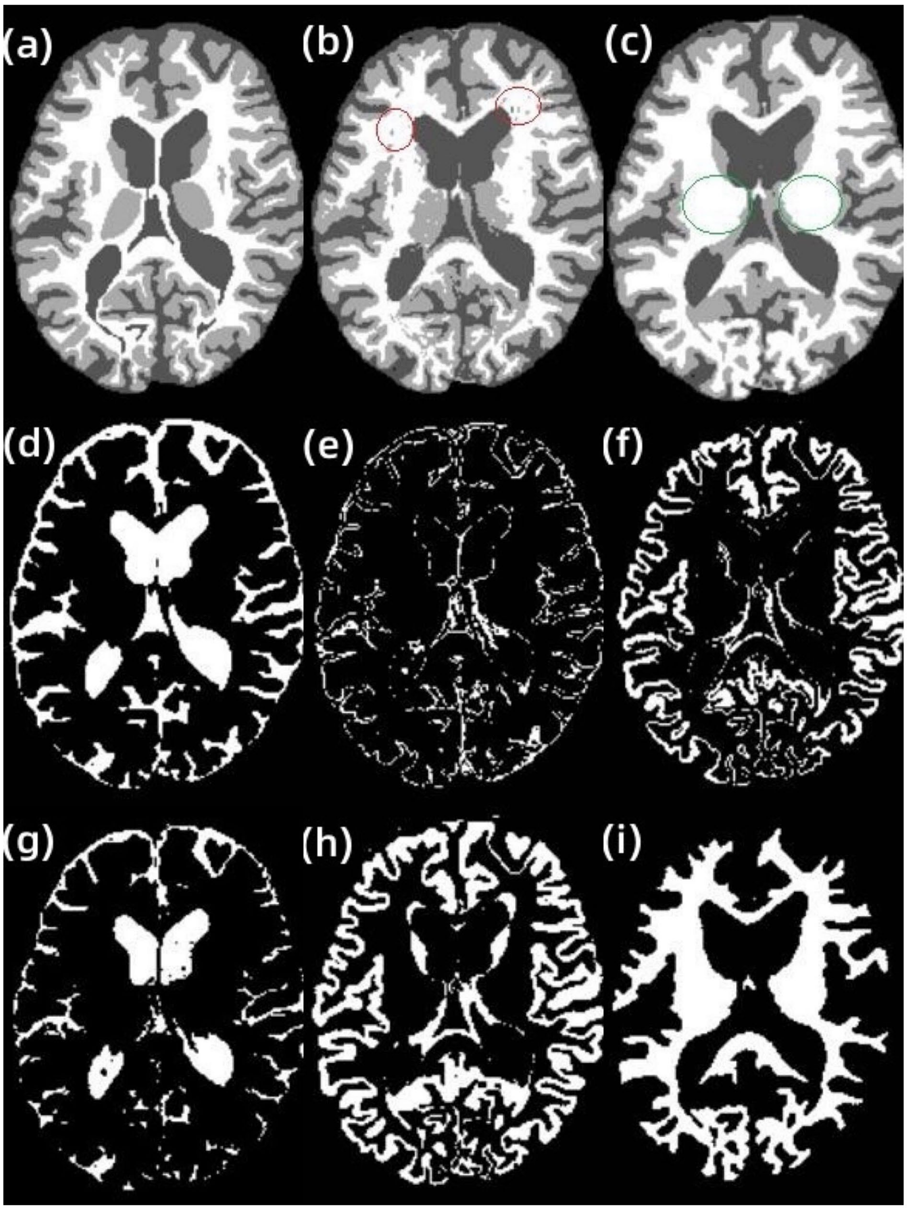

FIGURE 4
Segmentation results of AR-FCM and RFCM algorithms. **(A)** gt image, **(B)** AR-FCM, **(C)** RFCM, **(D)** cerebrospinal fluid, **(E)** gray matter, **(F)** white matter, **(G)** cerebrospinal fluid, **(H)** gray matter, and **(I)** white matter.

the results of segmentation using the LFA-FCM algorithm. The black part is the CSF, the light gray part is the gray matter, and the white part is the white matter. From the above figure, it can be seen that the method segmented the brain tissue better, and it is almost consistent with the brain tissue structure demonstrated by the T1-w images.

The results of segmentation by the three methods were quantitatively analyzed. The results of the three methods to obtain the three index scores are shown in Table 5, and Figure 9 show the results of data visualization in the table, respectively. By the results shown, Figure 9A, LFA-FCM obtained the highest DSC scores, especially the DSC values of segmented white matter tissue and gray matter tissue, and the worst results obtained in all seven sets of images processed were better than the best performance obtained by the other two methods. This is directly related to the operation of adding white matter filling before segmentation, indicating that lesion filling can effectively reduce the effect of T1-w multiple sclerosis lesions with low signal intensity on automatic brain tissue segmentation, thus improving the segmentation accuracy of the segmentation algorithm for white and gray matter tissues. As seen in Figure 9B, the LFA-FCM algorithm is an overall improvement in the accurate measurement of the volume of each part of the brain tissue. Figure (c), shows the average HD values obtained by the three algorithms, and although the average Hausdorff distance calculated by RFCM is closer, the overall result is still worse than the performance of the other two methods. In particular, the CSF tissue is far better than on the other two methods. In Figure 9C, the difference between the average Hausdorff distance calculated by the two methods, AR-FCM and LFA-FCM, is not significant, indicating that the white matter filling algorithm is not effective in improving the border tissue segmentation.

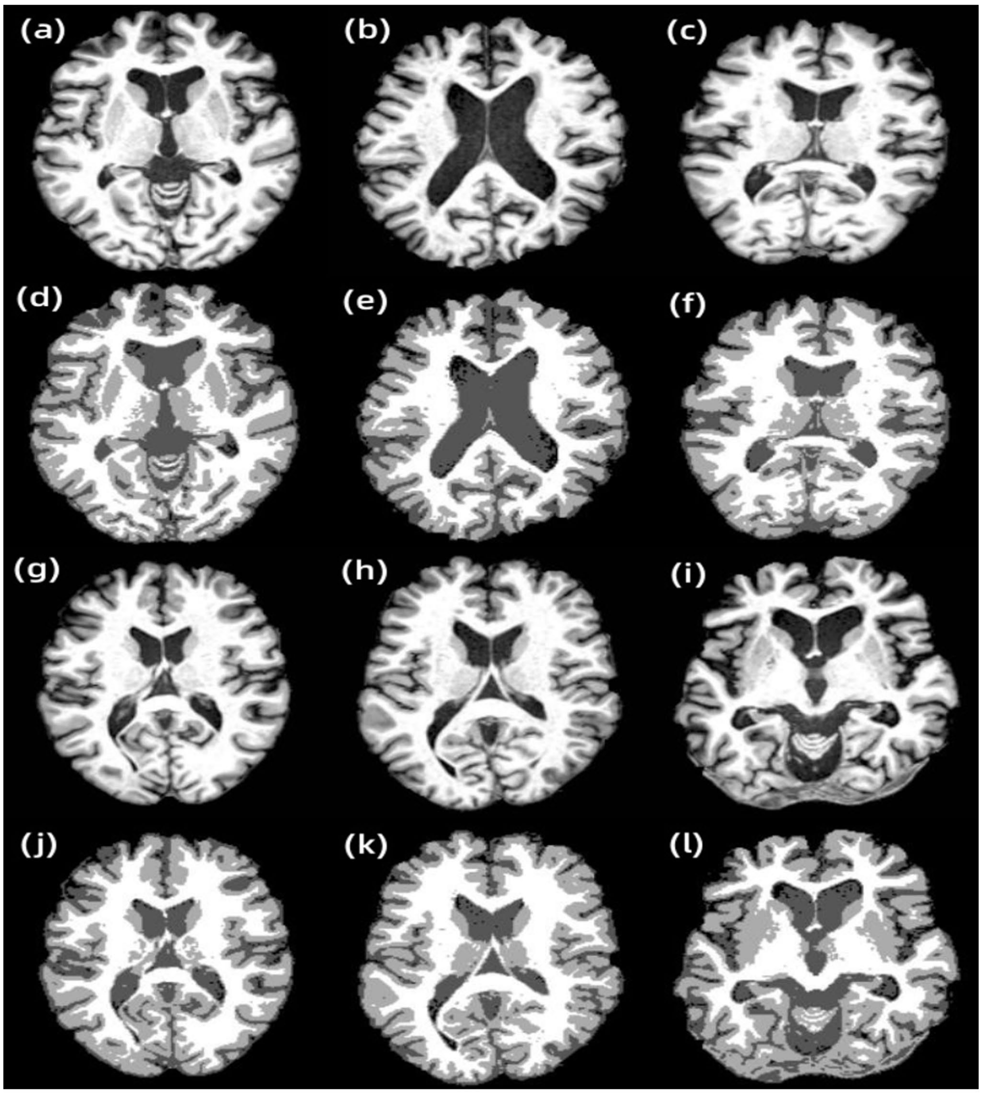

FIGURE 5
Results of other examples of AR-FCM algorithm segmentation. **(A)** Subject 1, **(B)** subject 2, **(C)** subject 3, **(D)** subject 1 segmentation result, **(E)** subject 2 segmentation result, **(F)** subject 3 segmentation result, **(G)** subject 4, **(H)** subject 5, **(I)** subject 6, **(J)** subject 4 segmentation result, **(K)** subject 5 segmentation result, and **(L)** subject 6 segmentation result.

TABLE 4 Average DSC, *VS* and HD values for AR-FCM and RFCM.

Models	Indicators	CSF	GM	WM
RFCM	DSC	76.33 ± 2.94	76.86 ± 1.78	80.67 ± 1.51
	VS	89.95 ± 4.36	90.22 ± 3.87	90.46 ± 3.23
	HD	4.06 ± 0.53	3.59 ± 0.27	3.23 ± 0.36
AR-FCM	DSC	77.32 ± 2.09	78.21 ± 1.01	82.98 ± 1.56
	VS	91.41 ± 3.07	91.34 ± 2.06	92.83 ± 4.11
	HD	3.03 ± 0.23	3.05 ± 0.12	2.81 ± 0.42

4. Discussions

An anatomical atlas-based energy minimization algorithm (Atlas Robust FCM) is firstly proposed for problems such as offset fields and lesions in brain image segmentation. In the objective function of a fuzzy clustering space model, the constraints are constructed to link the fuzzy clustering and the statistical probability graph. Statistical probability mapping is used as a constraint to limit the over-segmentation of brain tissue. After the brain tissue is segmented, the voxels of the volume part are redistributed using morphological

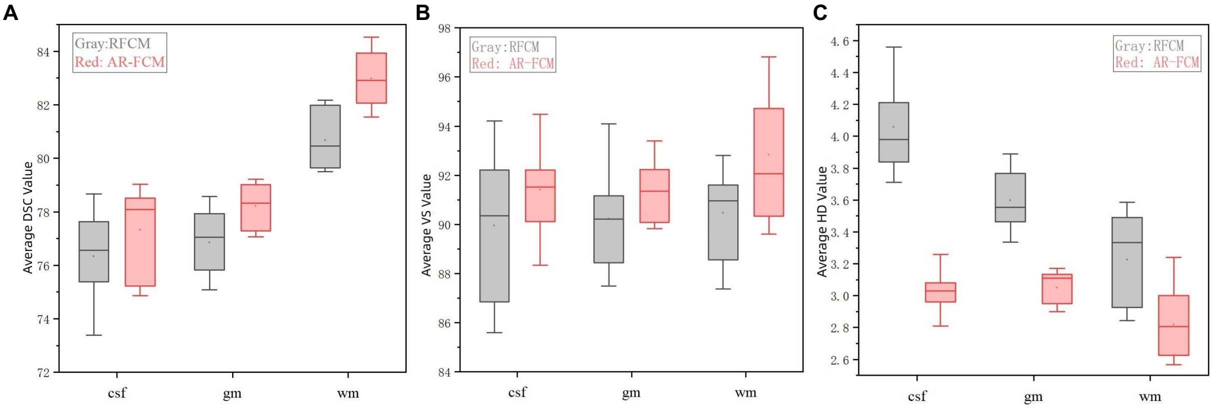

FIGURE 6
Indicator data visualization results. **(A)** Average DSC values of AR-FCM and RFCM, **(B)** average *VS* values of AR-FCM and RFCM, and **(C)** average HD values of AR-FCM and RFCM.

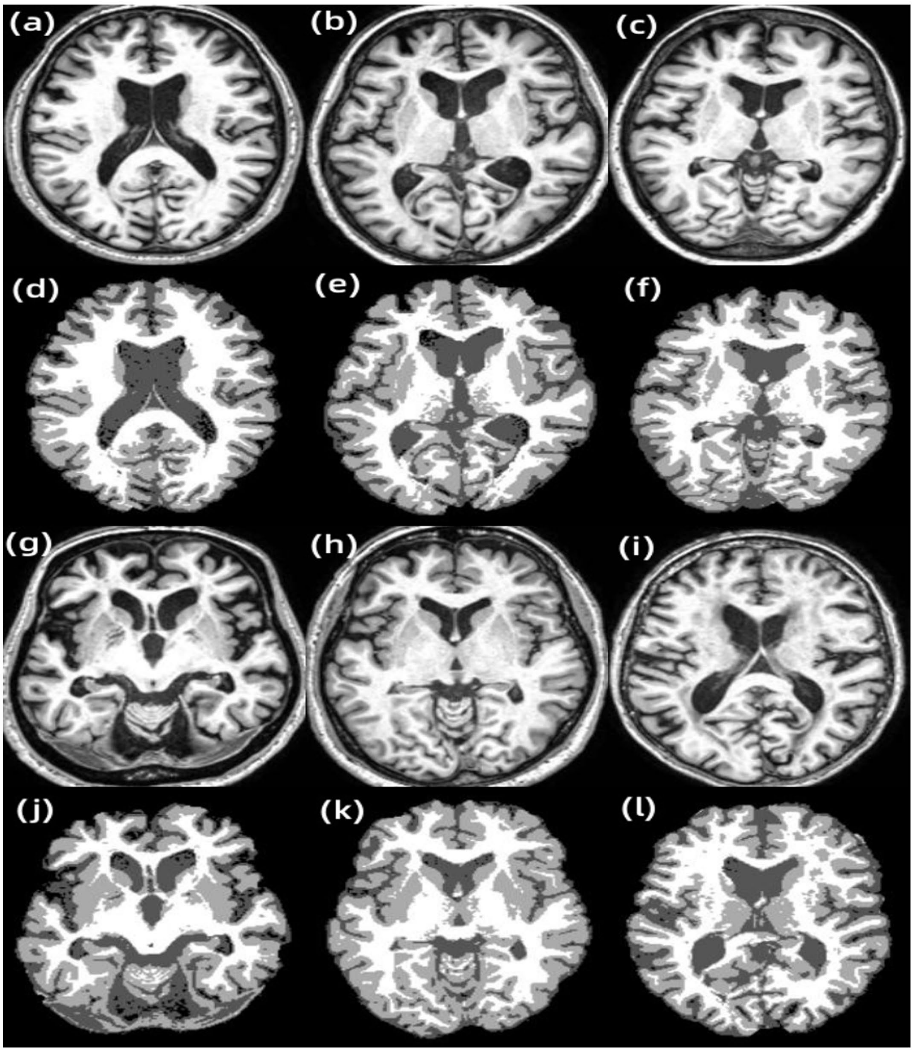

FIGURE 7
Results of other examples of LF-ARFCM algorithm segmentation. **(A)** Subject 1, **(B)** subject 2, **(C)** subject 3, **(D)** subject 1 segmentation result, **(E)** subject 2 segmentation result, **(F)** subject 3 segmentation result, **(G)** subject 4, **(H)** subject 5, **(I)** subject 6, **(J)** subject 4 segmentation result, **(K)** subject 5 segmentation result, and **(L)** subject 6 segmentation result.

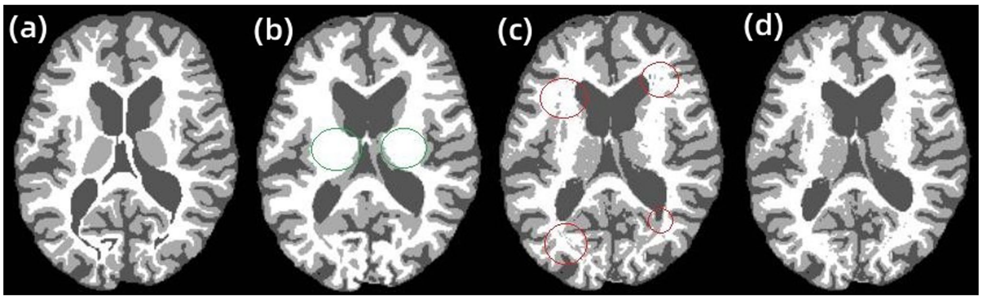

FIGURE 8
RFCM, AR-FCM, and LFA-FCM segmentation results. **(A)** gt, **(B)** RFCM, **(C)** AR-FCM, and **(D)** LFA-FCM.

TABLE 5 Average DSC, *VS* and HD values for RFCM, AR-FCM and LFA-FCM.

Models	Indicators	CSF	GM	WM
RFCM	DSC	76.33 ± 2.94	76.86 ± 1.78	80.67 ± 1.51
	VS	89.95 ± 4.36	90.22 ± 3.87	90.46 ± 3.23
	HD	4.06 ± 0.53	3.59 ± 0.27	3.23 ± 0.36
AR-FCM	DSC	77.32 ± 2.09	78.21 ± 1.01	82.98 ± 1.56
	VS	91.41 ± 3.07	91.34 ± 2.06	92.83 ± 4.11
	HD	3.03 ± 0.23	3.05 ± 0.12	2.81 ± 0.42
LFA-FCM	DSC	80.32 ± 2.53	81.73 ± 1.72	86.77 ± 1.46
	VS	92.88 ± 2.36	94.17 ± 3.08	94.11 ± 3.13
	HD	2.81 ± 0.21	3.01 ± 0.12	2.33 ± 0.43

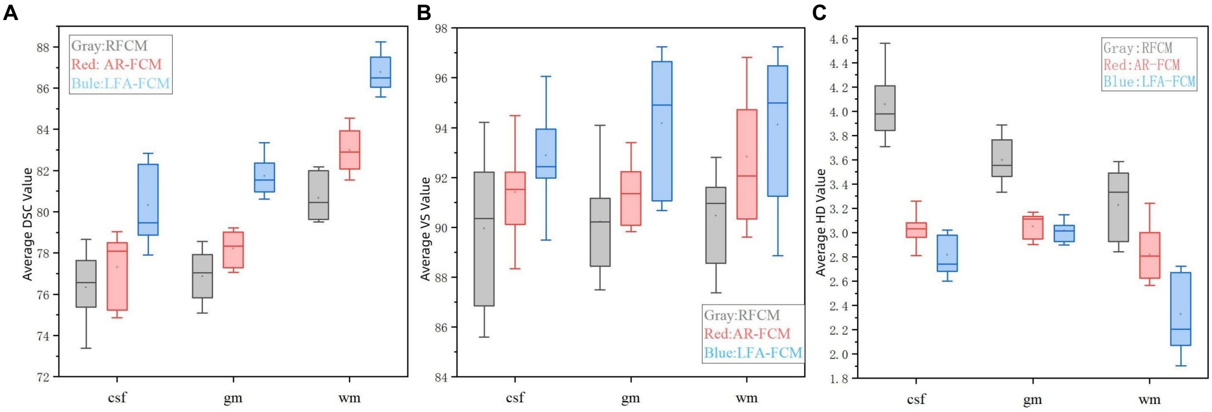

FIGURE 9
Indicator data visualization results. **(A)** Average DSC values of RFCM, AR-FCM and LFA-FCM, **(B)** average *VS* values of RFCM, AR-FCM and LFA-FCM, and **(C)** average HD values of RFCM, AR-FCM and LFA-FCM.

mapping, which resolves the unclear and discontinuous boundary of the target structure. It will lead to the problem that the model of fuzzy clustering space is not accurate when organize the boundary region of classification. The AR-FCM clustering algorithm is verified by comparison experiments to overcome the problem of low accuracy of RFCM clustering algorithm for boundary tissue segmentation and improve the segmentation accuracy of RFCM algorithm.

An energy minimization algorithm (Lesion Filling and Atlas FCM) based on lesion filling and anatomical mapping was proposed for brain tissues with lesions that were not well segmented by the AR-FCM algorithm. Based on the feature that MS lesions in FLAIR sequences are lighter than CSF and exhibit high signal abnormalities in GM, lesion regions are filtered out on FLAIR images using the lesion segmentation method (SLF). The T1-w images were coarsely segmented using a clustered segmentation algorithm, and only the tissue with possible lesions was processed. Among the structures coarsely segmented out of T1-w, the part related to GM was selected and filtering conditions were set to filter out the overlapping region that met the conditions in the coarsely segmented brain tissue and the focal region. For this region, the abnormal values in the T1-w image are filled and replaced by using the lesion filling, and a healthy T1-w image is constructed, and finally the AR-FCM algorithm is used again to complete the segmentation. The average DSC, HD and *VS* scores of LFA-FCM are found to be higher than those of AR-FCM through comparison experiments, which indicates that the strategy of using post-processing lesion filling is indeed feasible and the segmentation accuracy is indeed improved.

Innovative improvements are made to solve the problems of partial volume effect, gray scale inhomogeneity, and sensitivity of the fuzzy clustering space model to tissue boundaries in magnetic resonance images. The specific improvements are based on the fuzzy clustering space model, using statistical probability mapping as a constraint term in the energy function to limit the over-segmentation of brain tissue, and after segmentation, using morphological mapping to reassign voxels between tissue boundaries; the energy minimum segmentation algorithm segments MRI brain images in the presence of white matter lesions, which may misjudge the focal regions and lead to the assessment of brain white matter volume inadequate. The specific improvement method uses the focal segmentation method to estimate the focal region on FLAIR images, screens out the lesioned tissue, and replaces the abnormal values by filling them using the focal filling method.

5. Conclusion

In this paper, the MRI brain image segmentation algorithm makes an intensive study, mainly considering the effects of offset field, cranial bone, volume effect and lesion on the segmentation results. A large number of MRI images are segmented and compared with existing related algorithms in terms of the effectiveness and accuracy of segmentation results. Experiments have verified that the algorithm proposed reduces the effects of partial volume effects and lesions; achieves accurate and efficient brain image segmentation by MRI. Therefore, it can better diagnose the brain disease, manage the patients effectively in the early stage and reduce the possibility of the brain disease worsening.

Data availability statement

The original contributions presented in the study are included in the article/supplementary material, further inquiries can be directed to the corresponding authors.

Author contributions

XW contributed to the experiments design and conception. TW, HZ, and JY performed experiments and data analysis. YY, JT, and HL contributed to data analysis. All authors edited the manuscript.

Funding

This work was sponsored in part by the National Natural Science Foundation of China (Grant No. 61605021); in part by Science and Technology Research Program of Chongqing Municipal Education Commission (Grant No. KJQN202000624); in part by Opening Foundation of Key Laboratory of Opto-technology and Intelligent Control (Lanzhou Jiaotong University), The Ministry of Education (KFKT 2020–08); and in part by the eleventh Chongqing fledgling Eagle Project (No. CY220617).

Conflict of interest

The authors declare that the research was conducted in the absence of any commercial or financial relationships that could be construed as a potential conflict of interest.

Publisher's note

References

Bajracharya, U., and Rawal, P. (2015). In vitro study of magnetic resonance imaging artifacts of anesthetic devices. *J. Soc. Anesthesiol. Nepal* 2:13. doi: 10.3126/jsan.v2i1.13551

Browne, P., Chandraratna, D., Angood, C., Tremlett, H., Baker, C., Taylor, B. V., et al. (2014). Atlas of multiple sclerosis 2013: a growing global problem with widespread inequity. *Neurology* 83, 1022–1024. doi: 10.1212/WNL.0000000000000768

Dobson, R., and Giovannoni, G. (2019). Multiple sclerosis–a review. *Eur. J. Neurol.* 26, 27–40. doi: 10.1111/ene.13819

Dora, L., Agrawal, S., Panda, R., and Abraham, A. (2017). State-of-the-art methods for brain tissue segmentation: A review. *IEEE Rev. Biomed. Eng.* 10, 235–249. doi: 10.1109/RBME.2017.2715350

Fan, X., Chen, P., Cheng, H., and Liu, R. (2016). A reproducible comparative study on registration packages for toddler MRI images. *J. Med. Imaging Health Inform.* 6, 1409–1418. doi: 10.1166/jmihi.2016.1820

Feigin, V. L., Stark, B. A., Johnson, C. O., Roth, G. A., Bisignano, C., Abady, G. G., et al. (2021). Global, regional, and national burden of stroke and its risk factors, 1990–2019: a systematic analysis for the global burden of disease study 2019. *Lancet Neurol.* 20, 795–820. doi: 10.1016/S1474-4422(21)00252-0

Filippi, M., Rocca, M. A., Ciccarelli, O., de Stefano, N., Evangelou, N., Kappos, L., et al. (2016). MRI criteria for the diagnosis of multiple sclerosis: MAGNIMS consensus guidelines. *Lancet Neurol.* 15, 292–303. doi: 10.1016/S1474-4422(15)00393-2

Fransen, N. L., Hsiao, C. C., van der Poel, M., Engelenburg, H. J., Verdaasdonk, K., Vincenten, M. C. J., et al. (2020). Tissue-resident memory T cells invade the brain parenchyma in multiple sclerosis white matter lesions. *Brain* 143, 1714–1730. doi: 10.1093/brain/awaa117

Gva, B., Ao, A., Yh, B., Lladó, X., and Landman, B. A. (2020). A fully automated pipeline for brain structure segmentation in multiple sclerosis. *NeuroImage Clin.* 27:102306. doi: 10.1016/j.nicl.2020.102306

Jiang, Y., Li, H., Pang, Y., Ling, J., Wang, H., Yang, Y., et al. (2022). Cell image reconstruction using digital holography with an improved GS algorithm. *Front. Physiol.* 13:1040777. doi: 10.3389/fphys.2022.1040777

Lassmann, H. (2018). Multiple sclerosis pathology. *Cold Spring Harb. Perspect. Med.* 8:a028936. doi: 10.1101/cshperspect.a028936

Ma, Z., Tavares, J., Jorge, R. N., and Mascarenhas, T. (2010). A review of algorithms for medical image segmentation and their applications to the female pelvic cavity. *Comput. Methods Biomech. Biomed. Engin.* 13, 235–246. doi: 10.1080/10255840903131878

Makropoulos, A., Counsell, S. J., and Rueckert, D. (2018). A review on automatic fetal and neonatal brain MRI segmentation. *NeuroImage* 170, 231–248. doi: 10.1016/j.neuroimage.2017.06.074

Pham, D. L. (2001). Spatial models for fuzzy clustering. *Comput. Vis. Image Underst.* 84, 285–297. doi: 10.1006/cviu.2001.0951

Pohl, K. M., Bouix, S., Nakamura, M., Rohlfing, T., McCarley, R. W., Kikinis, R., et al. (2007). A hierarchical algorithm for MR brain image parcellation. *IEEE Trans. Med. Imaging* 26, 1201–1212. doi: 10.1109/TMI.2007.901433

Poser, C. M., Paty, D. W., Scheinberg, L., McDonald, W. I., Davis, F. A., Ebers, G. C., et al. (1983). New diagnostic criteria for multiple sclerosis: Guidelines for research protocols. *Ann. Neurol.* 13, 227–231. doi: 10.1002/ana.410130302

Prados, F., Cardoso, M. J., Kanber, B., Ciccarelli, O., Kapoor, R., Gandini Wheeler-Kingshott, C. A. M., et al. (2016). A multi-time-point modality-agnostic patch-based method for lesion filling in multiple sclerosis. *NeuroImage* 139, 376–384. doi: 10.1016/j.neuroimage.2016.06.053

Tian, J., Xie, J., He, Z., Ma, Q., and Wang, X. (2021). A device employing a neural network for blood pressure estimation from the oscillatory pressure pulse wave and PPG signal. *Sens. Rev.* 41, 74–86. doi: 10.1108/SR-09-2020-0216

Tian, J., Xie, J., He, Z., Qin, D., and Wang, X. (2022). Modeling of an impedimetric biosensor with ultrasonic-assisted cell alignment for the detection of yeast. *J. Sens.* 2022, 1–14. doi: 10.1155/2022/4514218

Valverde, S., Oliver, A., and Lladó, X. (2014). A white matter lesion-filling approach to improve brain tissue volume measurements. *NeuroImage Clin.* 6, 86–92. doi: 10.1016/j.nicl.2014.08.016

Wang, X., Jiang, Y., Li, Z., Wang, W., and Li, Z. (2019). Sensitivity characteristics of microfiber Fabry-Perot interferometric photoacoustic sensors. *J. Lightwave Technol.* 37, 4229–4235. doi: 10.1109/JLT.2019.2922223

Wang, X., Jin, L., Li, J., Ran, Y., and Guan, B. O. (2014). Microfiber interferometric acoustic transducers. *Opt. Express* 22, 8126–8135. doi: 10.1364/OE.22.008126

Wang, X. X., Li, Z. Y., Tian, Y., Wang, W., Pang, Y., and Tam, K. Y. (2018). Two dimensional photoacoustic imaging using microfiber interferometric acoustic transducers. *Opt. Commun.* 419, 41–46. doi: 10.1016/j.optcom.2018.02.048

Weiskopf, N., Edwards, L. J., Helms, G., Mohammadi, S., and Kirilina, E. (2021). Quantitative magnetic resonance imaging of brain anatomy and in vivo histology. *Nat. Rev. Phys.* 3, 570–588. doi: 10.1038/s42254-021-00326-1

Zhao, Y., Guo, S., Luo, M., Shi, X., Bilello, M., Zhang, S., et al. (2018). A level set method for multiple sclerosis lesion segmentation. *Magn. Reson. Imaging* 49, 94–100. doi: 10.1016/j.mri.2017.03.002

frontiers | Frontiers in Neuroscience

TYPE Original Research
PUBLISHED 03 May 2023
DOI 10.3389/fnins.2023.1117340

OPEN ACCESS

EDITED BY
Yin Tian,
Chongqing University of Posts and Telecommunications, China

REVIEWED BY
Hao Guo,
Taiyuan University of Technology, China
Peng Ji,
Fudan University, China

*CORRESPONDENCE
Jiqian Zhang
✉ zhangcdc@ahnu.edu.cn

RECEIVED 06 December 2022
ACCEPTED 11 April 2023
PUBLISHED 03 May 2023

CITATION
Lu X, Wang T, Ye M, Huang S, Wang M and Zhang J (2023) Study on characteristic of epileptic multi-electroencephalograph base on Hilbert-Huang transform and brain network dynamics.
Front. Neurosci. 17:1117340.
doi: 10.3389/fnins.2023.1117340

Study on characteristic of epileptic multi-electroencephalograph base on Hilbert-Huang transform and brain network dynamics

Xiaojie Lu[1,2], Tingting Wang[2], Mingquan Ye[2], Shoufang Huang[1], Maosheng Wang[1] and Jiqian Zhang[1]*

[1]School of Physics and Electronic Information, Anhui Normal University, Wuhu, China, [2]Research Center of Health Big Data Mining and Applications, School of Medicine Information, Wan Nan Medical College, Wuhu, China

Lots of studies have been carried out on characteristic of epileptic Electroencephalograph (EEG). However, traditional EEG characteristic research methods lack exploration of spatial information. To study the characteristics of epileptic EEG signals from the perspective of the whole brain，this paper proposed combination methods of multi-channel characteristics from time-frequency and spatial domains. This paper was from two aspects: Firstly, signals were converted into 2D Hilbert Spectrum (HS) images which reflected the time-frequency characteristics by Hilbert-Huang Transform (HHT). These images were identified by Convolutional Neural Network (CNN) model whose sensitivity was 99.8%, accuracy was 98.7%, specificity was 97.4%, F1-score was 98.7%, and AUC-ROC was 99.9%. Secondly, the multi-channel signals were converted into brain networks which reflected the spatial characteristics by Symbolic Transfer Entropy (STE) among different channels EEG. And the results show that there are different network properties between ictal and interictal phase and the signals during the ictal enter the synchronization state more quickly, which was verified by Kuramoto model. To summarize, our results show that there was different characteristics among channels for the ictal and interictal phase, which can provide effective physical non-invasive indicators for the identification and prediction of epileptic seizures.

KEYWORDS

Hilbert-Huang transform, CNN, symbolic transfer entropy, brain network, Kuramoto model

1. Introduction

Epilepsy is a neurological disease caused by sudden abnormal hyper-synchronization discharge behavior of neurons in the brain, causing involuntary behavior and seizures. Electroencephalogram (EEG) signals could be used to monitor the electrical activity in the brain. They record the electrical wave changes during brain activity and are the overall reflection of the electrophysiological activities of brain nerve cells on the scalp surface. EEG contains abundant brain information and is one of the means of clinical diagnosis of brain diseases (Proix et al., 2018).

Diagnosis of epilepsy by EEG requires a well-trained clinician or neurophysiologist, however, detecting through artificial intelligence has the potential to improve the quality of medical care by shortening diagnosis time, reducing manual errors, and relieving physician fatigue. Many analyzing and processing techniques of signals have been proposed for studying EEG signals (Shoeibi et al., 2021). The time-frequency analysis methods have attracted the attention of many scholars. Hilbert Huang Transform (HHT) are commonly used to process non-stationary signals (Wu and Huang, 2009; Supriya et al., 2020). Empirical Mode Decomposition (EMD) (Tsai et al., 2016) is the key step of HHT. HHT is employed to assess the time-frequency characteristics in some references (Hopfengärtner et al., 2014; Biju et al., 2017). Hopfengärtner et al. (2014) obtained adaptive energy thresholding in the sub band.

In addition, the applications of Convolutional Neural Network (CNN) toward the detection of epileptic seizures have been implemented. Acharya et al. (2018) found that a 13-layer deep CNN showed an accuracy of 88.67% by using the database of the University of Bonn. The EEG image study based on CNN showed that the true positive rate was 74.0% between seizures and non-seizures EEG activities (Emami et al., 2019). Especially, the research taking time-frequency analysis as the features and combining with CNN is also increasing. The highest classification accuracy of 82.85 and 88.30% was achieved using transfer learning and extract image features approach, respectively, (Raghu et al., 2020). Ansari et al. (2019) achieved the seizure detection rate of 77.0% by using deep CNN with 26 neonates. San-Segundo et al. (2019) used EMD and CNN to classify focal and non-focal signals, which achieved an accuracy of 98.9%.

The above researches are based on the time-frequency domain of multi-channel EEG. Furthermore, multi-channel EEG connectivity in spatial domain is represented by brain networks. With the development of medical imaging technology, more and more evidence shows that some brain diseases, such as epilepsy, Alzheimer's disease, depression and schizophrenia, have abnormal brain function connections (Bansal et al., 2019). Therefore, researchers' exploration of the brain has gradually shifted from structural analysis to the functional connections among brain regions. In addition to quantifying and modeling observations in laboratory animals, researchers can perform whole-region simulations of the human brain based on noninvasive imaging data (Lynn and Bassett, 2019). The scalp EEG is more convenient to collect and the cost is lower than other types of data (Lu et al., 2021), so a brain network is built by using scalp EEG in this paper. Transfer entropy (TE) is an information-theoretic measure method originally introduced by Schreiber (2000) to evaluate effective connectivity and it is often used to estimate "information flow" in the brain and analyze EEG signals. The rules defining nodes and edges in association networks are not the same for different medical data. For example, the number of EEG channels, such as 23 channels, 64 channels, 128 channels, etc., determines the number and distribution of network nodes. The calculation methods of the correlation among signals, such as mutual information, TE, phase lock value, Granger causality, Pearson correlation, etc., determine the edge weight of the network. TE is often used to measure the strength of functional connection of neurons (Schreiber, 2000). In this paper, symbolic transfer entropy(STE) based on symbolic dynamics is selected because it is insensitive to signal noise and does not require high parameter coordination (Li et al., 2020).

To research the properties of brain networks, the researchers use the topological properties which include global efficiency, cluster coefficient, average path length, etc. (Wang et al., 2014; Shimono and Beggs, 2015). Besides, the others reveal the dynamic mechanisms of brain network to explain large-scale neural behavior emerging from individual neurons (Lv et al., 2021). Kuramoto model is often used to describe the large-scale neural activity. Majhi et al. (2018) summarized that recent research had shown that the coexistence of coherent and incoherent states, known as chimera states or simply chimeras, is particularly important and characteristic for neuronal systems.

It is clear from the literature that no successful combined studies (in terms of characteristic of epileptic multi-EEG) have been proposed for the multi-channel scalp EEG. Therefore, to explore the characteristics of epileptic EEG signals from the perspective of whole brain were studied by using multi-channel scalp EEG in this paper. Our research work was carried out from the following: firstly, the 1D signals were converted into HS images stack, then, the concatenated images were fed into CNN. Secondly, the 23 channels signals were converted into brain networks by STE among different channels EEG. Thirdly, the networks properties and synchronous behavior by brain network analysis toolbox and Kuramoto model in which the coupling matrix was the above networks were observed. The results show that compared to the previous approach, these methods achieve comparable identification results, besides, our research method can provide effective physical markers for epileptic seizures.

2. Methodology

2.1. Hilbert-Huang transform

HHT can reflect the energy information of multi-channel EEG in time-frequency domain. HHT is a method composed of EMD and Hilbert Transform (HT). The signal is adaptively decomposed into different IMFs by EMD, and then each IMF is transformed by HT. EMD is a decomposition method to generate IMFs by repeatedly averaging the envelope of maximum and minimum values (Huang et al., 1998). It can be decomposed directly without prior analysis and research for an unknown signal. This method automatically divides the signal according to some fixed modes and levels without manual setting and intervention. The original signal can be obtained by EMD decomposition.

The analytic signal of a single frequency component signal can be obtained through HT, assuming that the analytic signal $z(t)$ is:

$$z(t)=c(t)+jy(t)=a(t)e^{j\theta(t)} \tag{1}$$

$a(t)=\sqrt{c(t)^2+y(t)^2}$ represents instantaneous amplitude. $\theta(t)=\arctan\dfrac{y(t)}{c(t)}$ represents instan-taneous phase. $\omega(t)=\dfrac{d\theta(t)}{dt}$ represents instantaneous frequency. The signal can be expressed as:

$$x(t)=a(t)e^{j\int\omega(t)dt} \tag{2}$$

If $|a(t)|^2$ is used as the instantaneous energy, the instantaneous energy distribution of the signal can be drawn on the time-frequency plane, and this distribution spectrum is Hilbert Spectrum (HS) which is marked as $H(\omega,t)$. The 1D original signal is refined into different components and expanded into the 2D image by HHT. The scale of data will be expanded from the dimensions of time, phase and frequency domain. According to its frequency, amplitude and physiological characteristics, the EEG signal with conventional bands includes $\alpha(8\sim13\,\text{Hz})$, $\beta(14\sim30\,\text{Hz})$, $\theta(4\sim7\,\text{Hz})$, $\delta(0.5\sim3\,\text{Hz})$.

HS can reflect the energy distribution of different frequency bands. The HS presents the amplitude, instantaneous frequency and time of the original wave simultaneously. In wave dynamics, the squared amplitude is frequently used to represent the energy density of the original wave, hence, the HS represents the Hilbert energy of the original wave. Hilbert Marginal Spectrum(HMS) is the integral of HS in time. From the perspective of integration, all amplitudes in time are added up for any first order frequency to reflect the amplitude accumulation of each frequency in all times and reflect the relationship between the frequency and amplitude of the signal. The HMS offers a measure of total energy contribution from each frequency value and corresponds to energy density at frequency *f*. The HMS represents the cumulated energy of the EEG over the entire data span in a probabilistic sense (Fu et al., 2015).

2.2. Symbolic transfer entropy

TE is a parameter that measures the degree of correlation between two time sequences. Because *TE* is based on the transition probability and is asymmetric, it mixes directional and dynamic information. *TE* is defined as follows (Staniek and Lehnertz, 2008).

$$TE_{J\to I}=\sum p\left(i_{n+1},i_n^{(k)},j_n^{(l)}\right)\times\log\frac{p\left(i_{n+1}|i_n^{(k)},j_n^{(l)}\right)}{p\left(i_{n+1}|i_n^{(k)}\right)}\qquad(3)$$

i_n, j_n represent the state of sequence *I* and *J* at time *n* respectively, $i_n^{(k)}$ refers to a string of length k, $i_{n-k+1},\cdots,i_n$, similarly, $j_n^{(l)}$ refers to a string of length l, $j_{n-l+1},\cdots,j_n$. The *TE* of *J* to *I* is information flow transferred from *J* to *I*, which can be used as an indicator of causality.

The above-mentioned *TE* is more sensitive to noise, so STE which has the advantage of being insensitive to noise and is more suitable for non-stationary continuous time series is employed (Staniek and Lehnertz, 2009). Providing symbolic sequence of signal ${}^{I}S_n$ and ${}^{J}S_n$, the STE can be calculated as:

$$STE_{J\to I}=\sum p\left({}^{I}S_{n+1},{}^{I}S_n,{}^{J}S_n\right)\log\frac{p\left({}^{I}S_{n+1}\,{}^{I}S_n,{}^{J}S_n\right)}{p\left(\frac{{}^{I}S_{n+1}}{{}^{I}S_n}\right)}\qquad(4)$$

2.3. Brain networks and Kuramoto model

Because TE is directional, the brain network constructed is a positive and negative coupling network. Based on these studies, we use STE to build a brain functional network. The network is a weighted directed network with the characteristics of time, structure and direction.

The nodes correspond to different channels and the edge weight is the value of STE. The brain network is treated as a coarse-grained representation of neuron cluster network, which is used as the coupling matrix of the coupled dynamic equation to find out the synchronous behavior of the neuron cluster. To facilitate the simulation of the synchronous behavior of these networks, the Kuramoto model is used as a simplified neural mass model to provide the basis for testing the synchronization of the neural oscillation (Rodrigues et al., 2016; Ma and Tang, 2017). The Kuramoto model is as follows:

$$\frac{d\theta_i}{dt}=\omega_i+\frac{K}{N}\sum_{j=1}^{N}G_{ij}\sin\left(\theta_j-\theta_i\right)\qquad(5)$$

Where θ_i and θ_j are the phase of the *i*-th and *j*-th oscillator, ω_i is intrinsic frequency, and *K* is the coupling constant, G_{ij} is coupling matrix which represents an $N\times N$ matrix with $N=23$, the reason is that the EEG signals in the dataset in this paper have 23 channels.

2.4. Electroencephalograph signals dataset and processing

CHB-MIT dataset is the EEG signals from Children's Hospital of Boston (CHB) included in the Massachusetts Institute of Technology (MIT) EEG database. The EEG data with the sampling frequency of 256 Hz are taken from the open dataset collected by a team of investigators from CHB-MIT[1] (Shoeb, 2009). This dataset contains scalp EEG records of 22 epileptic patients (5 males, 3 to 22 years old, 17 females, 1.5 to 19 years old). These EEG signals are recorded for 1 h using the international 10–20 EEG electrode position and naming system. Most EEG signals files contain 23 channels in this dataset. In each file containing the data of the seizure that has occurred, the dataset of the beginning and end of 182 seizures are annotated. We divided the one-hour EEG signals into multiple segments of 10 s, and separated the inter stages from the interictal stage state. Figure 1 shows the flow chart of the preprocessing method, which includes EEG signal preprocessing, feature extraction, and classification of interictal and ictal states to detect seizures. The ictal signals contain many types of abnormal waveforms and their amplitude and frequency have changed greatly.

It is well known that the above CHB-MIT dataset is scalp EEG dataset, which contains a lot of noise and artifacts, including blink artifact, eye movement artifact, myoelectricity interference, electrocardio interference, power frequency interference, amplifier saturation, pulse interference, etc. It is necessary to clean up these interference signals before studying the EEG signals. Thus, after comparing and analyzing various EEG processing tools, a new tool based on Python-MNE library, namely MNELAB is selected (Gramfort et al., 2013). The Python-MNE library is one of the python libraries designed to deal with EEG specifically. The preprocessing method in this paper is to use the MNELAB tools for commonly

---

[1] https://www.physionet.org/content/chbmit/1.0.0/

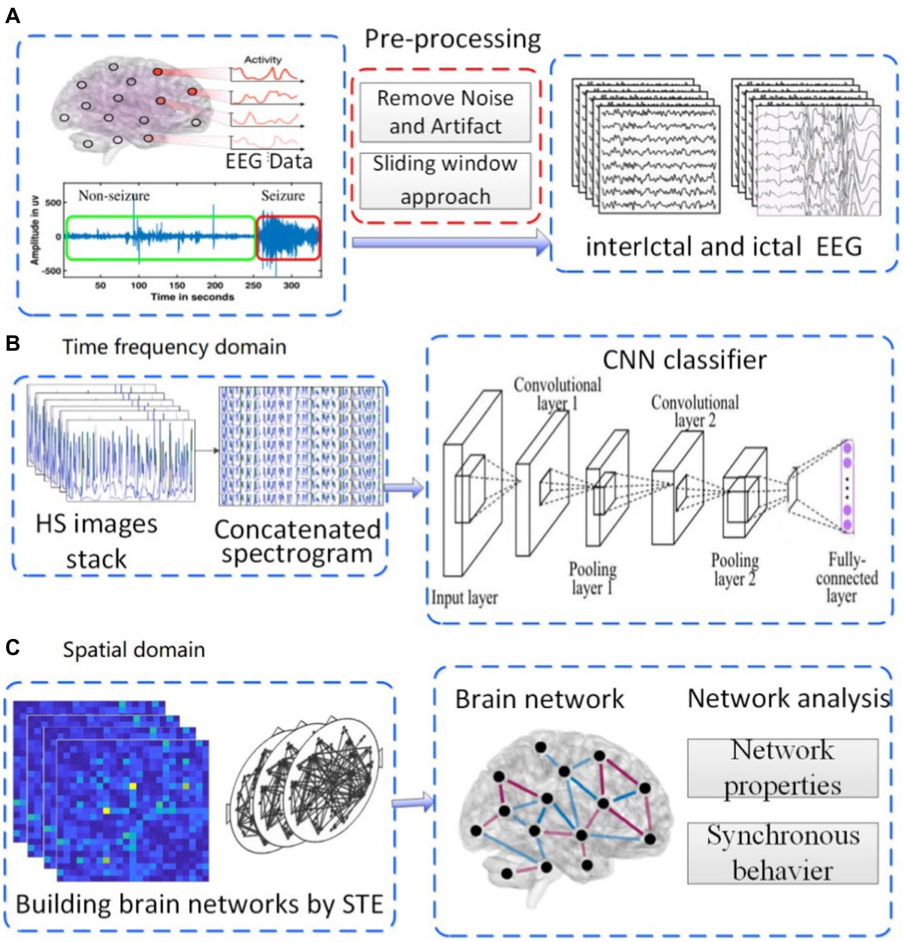

FIGURE 1
Experimental roadmap. (**A**) pre-processing of EEG. (**B**) analysis in time-frequency domain. (**C**) analysis in spatial domain.

denoising in EEG signals by using frequency limiting and fast Independent Component Analysis (ICA) (Antony et al., 2022).

After preprocessing and screening, and reference to previous literature(Acharya et al., 2018; Emami et al., 2019), we finally extracted 2,500 s interictal EEG and 2,500 s ictal EEG from the dataset. Then, a total of 5,000 s EEG signals with 23 channels were split into segments of 10s each and then converted them into HS images stack. Therefore, 500 EEG segments were generated, which contained 250 interictal and 250 ictal EEG segments.

3. Results and discussion

To study the characteristics of epileptic EEG signals from the perspective of the whole brain，this paper proposed an approach of multi-channel characteristics from time-frequency and spatial domains. Thus in this paper, the experimental scheme was carried out in the following three steps shown in Figure 1.

(i) The original EEG signals were preprocessed according to the following steps: Firstly, the background noise and artifact in original signal were removed. Denoised signals were split into segments of 10s each (Figure 1A). Secondly, the processed signals were converted into HS images, then, in a 23 channels EEG signal segment, HS images stack was concatenated into a single spectrogram. Thirdly, the concatenated images were used as the input layer of CNN classifier to identify the ictal EEG (Figure 1B). (ii) The brain function network was constructed by using the processed EEG signals, information transfer among different channels was investigated by using the network, and the network properties were calculated(Figure 1C). (iii) According to the mean field theory, the whole neural networks could be coarse-grained into network of brain regions. The Kuramoto model was used to study the synchronous behavior of these networks.

3.1. Seizure identification by HS and CNN

The HS reflects the instantaneous frequency and amplitude and the energy distribution characteristics of the signals in time-frequency domain, while the HMS represents the energy contribution from each frequency value. Some studies have reported that analyzing EEG signals in the frequency domain could be used effectively for subsequent pattern recognition tasks. Inspired by these results, the recorded EEG time series signal into HS images which reflected the Time-frequency characteristics were transformed in our paper. To observe the EEG time-frequency characteristic, HS and HMS images of three segments of single

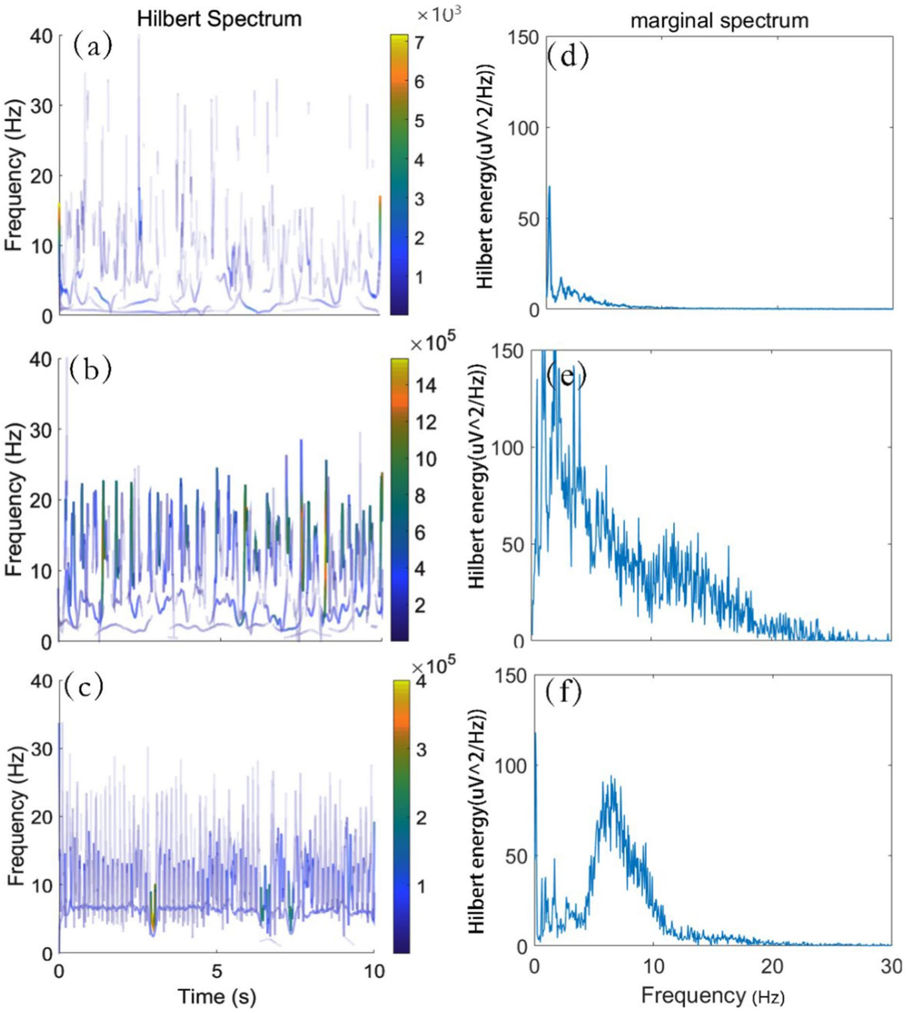

FIGURE 2
HS and HMS of ictal and interictal EEG. **(A)** HS of interictal EEG. **(B,C)** HS of ictal EEG. **(D)** HMS of interictal EEG. **(E,F)** HMS of ictal EEG.

channel signals were selected and plotted as shown in Figure 2. In addition, we selected signals in other time periods for processing for many times, and similar phenomenon occurred.

One can see from Figures 2A–C are HS images, its abscissa, ordinate represent time, frequency, respectively. To facilitate observation, we intercepted the effective frequency range of 0-40 Hz. By comparing Figures 2A–C, we found that the energy distribution of HS image in interictal phase was more dispersed and smaller energy value than that in ictal phase. At the same time, the HMS images corresponding to the above three signals were depicted in Figures 2D–F, in which the abscissa and the ordinate described the frequency and the energy amplitude, respectively. The HMS offers a measure of total HE contribution from each frequency value. The area below the HMS curves in Figures 2D–F represents the total HE over the entire frequency span. It can be observed from HMS that the energy of interictal EEG is contained mostly in δ band, while the δ band in the ictal EEG accounts for a small proportion of total energy.

To further study the feasibility of HS in automatic seizure identification, we converted the EEG signal segments into HS images and concatenated the images into an image stack (Figure 1B). The CNN classifier was used for automatic identification of the above concatenated images.

(1) To obtain more information of the same time segment of EEG, 1D signals were converted into 2D concatenated images.
(2) To overcome the imbalance issue of CNN, the same duration of interictal and ictal EEG signals were extracted, and interictal EEG signals from the large number of interictal phases were extracted randomly.
(3) To identify epileptic EEG signals accurately, two consecutive sets of convolutional/pooling layers were used. Convolutional layer could extract edges, shapes and textures of a spectrogram. The activation function of convolutional layers was ReLU. The convolution filter size was 3 × 3 and the number of convolutional units was 32 and 64, respectively. We adopted the maxpooling layer, set the pooling size to 2 × 2, and used Adam as the optimizer which solved the problem of large swing range in optimization and can speed up the convergence of function. Two layers of pooling layer and one layer of dropout layer were designed, which was to reduce the model complexity while retaining key information, prevented overfitting of the model

TABLE 1 Seizure identification results and comparison table of classification results (Sen, Sensitivity; Acc, Accuracy; Spe, Specificity).

Authors	Methods	EEG data source	Performance (%)
Acharya et al. (2018)	13-layer deep CNN structure	Bonn	Acc: 88.4
Mandhouj et al. (2021)	Using STFT Spectrogram with deep CNN	Bonn	Acc: 98.22
Yuan et al. (2019)	Spectrogram with STFT using multi-view deep learning framework	CHB-MIT	Acc: 94.3
			AUC: 95.7
Tsiouris et al. (2018a)	Discrete wavelet transform (DWT) + LSTM	CHB-MIT	Sen: 99.84
			Spe: 99.86
Fergus et al. (2015)	Power spectral density (PSD) + KNN	CHB-MIT	Sen: 95.1
Tsiouris et al. (2018b)	Spectral analysis, STFT+SSM	CHB-MIT	Sen: 88
Rashed-Al-Mahfuz et al. (2021)	VGG16+ frequency components	CHB-MIT	Acc: 99.2
Our paper	Spectrogram with HHT of multi-channel EEG using CNN	CHB-MIT	Sen: 99.8
			Spe: 97.4
			Acc:98.7
			AUC:99.9
			F1_score:98.7

and improved the generalization ability of the model. The cross-validation was leave-one-out cross validation(LOOCV). 80% data were selected for the training set, and the rest data were used for the test one.

(4) To verify generalizability of the model, external EEG signals of other subjects (except the 10 subjects) in CHB-MIT dataset were used to test.

Sensitivity, accuracy, AUC (area value under ROC curve), F1_ score and specificity were calculated to evaluate the performance of the classifier, as shown in Table 1. The identification effect of 96.5% was also achieved for the external images. We summarized the references of EEG detection and classification of epilepsy using time-frequency spectral analysis or machine learning. Our results and the comparative classification result are listed in Table 1.

From Table 1 one notice that some recent research methods could achieve a certain degree of classification effect. However, our proposed scheme using multi-channel scalp EEG automatic recognition could obtain better classification effect. Compared with the exiting studies, it was found that our model achieves comparable identification effect. It showed that it was feasible to identify seizures from the perspective of whole brain.

3.2. Building brain networks

The above method can expand the energy distribution of epileptic EEG signals and identify epileptic signals more accurately in time-frequency domain. However, in spatial domain, because the brain network constructed by 23 channels EEG can more truly reflect the information transmission and functional activities among the brain regions, it is also very important to further analyze the causality and connectivity among different parts of the brain. Next, EEG signals are used for further research the synchronous behavior of the brain networks.

We calculated the STE values among each signal segment, and built a brain function network of 23 nodes with STE as the edge weight. Then, using this method, a weighted adjacent network with 500 multi-channel signal segments in batch was built. The representative diagrams of network and adjacency matrix are shown in Figure 3. We set the threshold by traversal and found the appropriate threshold, and set the threshold of STE to 0.02 after verification in the subsequent experiment. For clearer image display, we set the threshold of STE to 0.08. Only edges larger than the threshold value could be drawn.

Figures 3A,C show brain functional networks of ictal and interictal phases. The different colors of the network connection edges represent the relative intensity of the STE, the network nodes correspond to the channels, and the arrows indicate the directions of "information flow." Therefore, this brain network is a weighted network with direction, which may provide some useful clues for the localization of epileptic focus. Figures 3B,D show adjacency matrices of ictal and interictal phases. The vertical and horizontal coordinates of the adjacency matrix heat map represent the number of the network node, and the color bar describes the value of the STE. We can see from this figure, under the same threshold conditions, the network has more connectors during ictal phase than during interictal phase in most cases.

3.3. Network analysis

To verify the feasibility and effectiveness of our methods, the following two schemes were adopted: one was to use network analysis toolbox, the other one was Kuramoto phase oscillator model. As the first test method, the analysis toolbox called GRETNA[2] (Wang et al., 2015) which was a graph theoretical network analysis toolbox for imaging connectomics was adopted. Network properties of the 500 networks constructed above was calculated.

---

[2] http://www.itrc.org/projects/gretna/

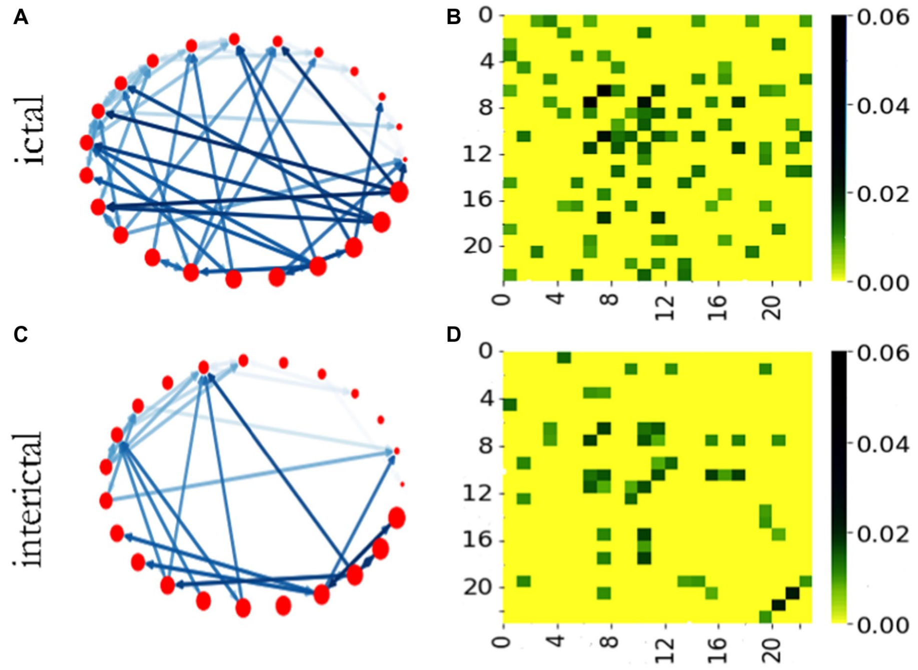

FIGURE 3
Brain networks and adjacency matrices of ictal and interictal phases. **(A)** The network in ictal stage. **(B)** Adjacency matrix of ictal network. **(C)** The network in interictal stage. **(D)** Adjacency matrix of interictal network.

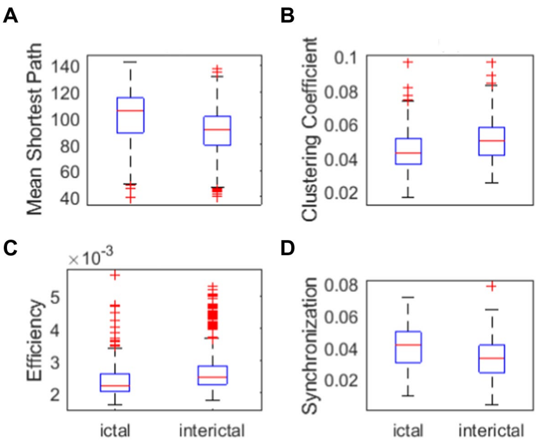

FIGURE 4
Network properties. **(A)** Mean shortest path of ictal and interictal networks. **(B)** Clustering coefficient of ictal and interictal networks. **(C)** Efficiency of ictal and interictal networks. **(D)** Synchronization of ictal and interictal networks.

Some network properties parameters, such as mean shortest path, clustering coefficient, efficiency and synchronization were used to distinguish the ictal and the interictal phases. The results are shown in Figure 4.

One can see from Figure 4A that, the mean shortest path in ictal phase is greater than that in interictal phase. Clustering coefficient in the ictal phase is lower than that in the interictal phase(Figure 4B). Efficiency of ictal networks is lower than efficiency of interictal networks (Figure 4C), which represents the work efficiency of the brain decline during the seizure. Clinical studies show that patients with intractable epilepsy often have cognitive impairment, including memory loss, language, expression problems, and intellectual decline. According to the graph theory, the brain efficiency of patients with refractory epilepsy is lower, suggesting that the efficiency of long-distance information transmission and the ability to integrate information of patients with refractory epilepsy are reduced within a certain range. Therefore, mean shortest path in ictal stage is higher. Clustering coefficient is lower in ictal stage due to shorter path length can promote clustering of network node. The efficiency in ictal stages is lower due to the impact on brain function during the seizures. These clinical conclusions are consistent with the experimental results.

As can be seen in Figure 4D, synchronization in ictal phase is greater than that in interictal phase, which represent the cerebral cortex during ictal phase is more susceptible to abnormal synchronous discharges. Next, the synchronization of the brain network is further verified. We performed some statistical analysis to determine the difference of parameters of network properties between ictal signal and interictal signal. This was confirmed by the lack of concordance between statistical analysis and main part of the paper. Therefore, we proposed not mentioning these analyzes.

The second verification method is to use Kuramoto phase oscillator model. As a simplified neural quality model, this model can be used to describe the average field of large-scale neural activities, so as to further verify the synchronization of multi-channel EEG brain network and explain the large-scale neuroelectrical behavior of a single neuron. In the network, STE was used as the weight of edges, the greater the STE, the stronger the information transfer intensity

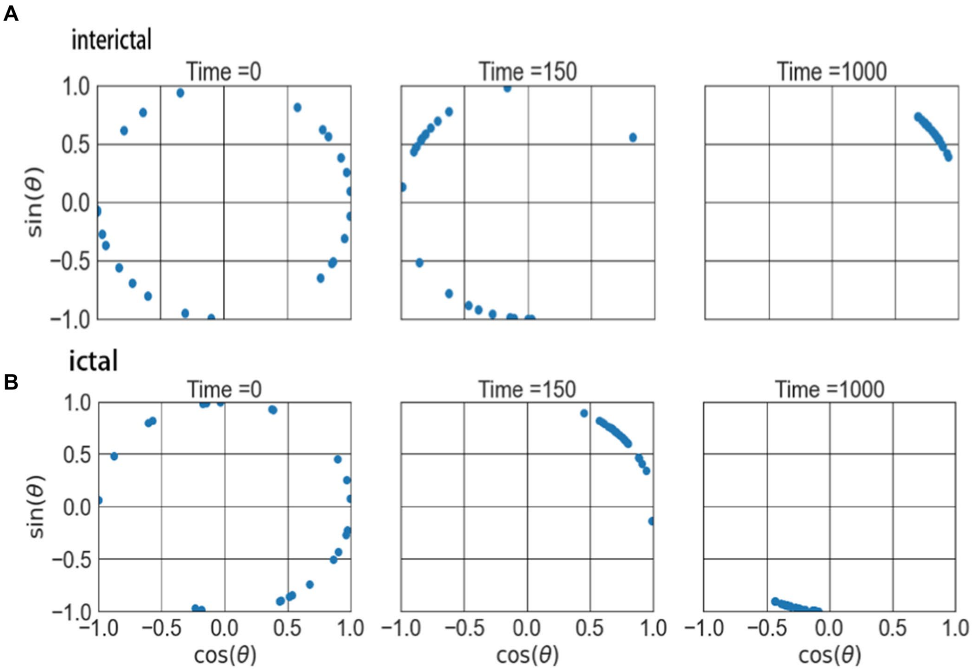

FIGURE 5
The attractors of two type of networks on the complex plane. **(A)** The attractors of interictal network. **(B)** The atttactors of ictal network.

between the two channels and the closer the connection between the two nodes.

In order to observe the attractor synchronous behavior in the process of time evolution better, networks of ictal and interictal phases with similar coordination coefficients are selected. In the model, the internal frequencies of 23 coupling oscillators are evenly distributed in the interval [0,1], the coupling strength $K = 3.5$. The results are shown in Figure 5.

Figure 5 shows the evolution result of the 23 oscillators over time. At the beginning, the phases of these oscillators are different and randomly distributed in different positions on a ring of the network, as shown in the first column of the figure. As time goes on, the oscillators begin to gather in one direction, and when $t = 150$, the oscillators have contracted and converged to a certain extent (as shown in the middle column). When the time evolution reaches $t = 1{,}000$, the oscillators further shrink and converge to form an attractor structure, as shown in the right column in the figure. This indicates that the signals during the ictal enter the synchronization state more quickly. These network properties can provide reference for exploring the non-invasive identification marks and dynamic mechanisms of epilepsy.

4. Conclusion

In the paper, we explored the characteristics of EEG signals in ictal and interictal phases in time-frequency and spatial domain. HS reflect time-frequency characteristics of multi-EEG in time frequency domain, and achieve good identification results. The sensitivity is 99.8%, accuracy is 98.7%, specificity is 97.4%, F1-score is 98.7%, and AUC-ROC is 99.9%. Brain function networks which reflect spatial characteristics of multi-EEG present different characteristics between ictal and interictal phase, which is verified by network properties and Kuramoto model. Experiments indicates that the network properties are different between interical stages and ictal stages, and the signals during the ictal enter the synchronization state more quickly. This part of work can also be improved from the following two aspects: (1) Due to the less number of scalp EEG channels in this data set, the function network could not describe the details of EEG signals. (2) Some networks did not support the experimental results with Kuramoto model. The next step is to further research the relationship between network hierarchy and remote synchronization or relay synchronization, which requires the construction of more complex brain networks, such as EEG with more channels, MEG, and fMRI networks as well.

Data availability statement

The original contributions presented in the study are included in the article/supplementary material, further inquiries can be directed to the corresponding author.

Author contributions

XL: investigation, methodology, methodology development or design of methodology, visualization writing–original draft, writing–review and editing, and data curation. JZ: conceptualization, methodology, funding acquisition, project administration, supervision, and writing-review and editing. SH: formal analysis, validation, and software. MY: data collection and validation. MW and TW: data analysis and processing. All authors contributed to the article and approved the submitted version.

Funding

This study was funded by the project of University Natural Science Research Project of Anhui Province (No. KJ2020A0618), the project of Academic and technical leaders candidate of Anhui Province (No. 2022H286), the Natural Science Foundation of Anhui Province, China (No. 1908085MA25), the Key Research and Development Plan of Anhui Province, China (No. 2022a05020011), the University Synergy Innovation Program of Anhui Province, China (No. GXXT-2022-044), the Excellent Scientific Research Innovation Team Project of Universities in Anhui Province, China (No. 2022AH010075), and the Academic Support Project for Top-notch Talents in Disciplines (Majors) of Universities in Anhui Province, China (No. gxbjZD2022042).

Conflict of interest

The authors declare that the research was conducted in the absence of any commercial or financial relationships that could be construed as a potential conflict of interest.

Publisher's note

References

Acharya, U. R., Oh, S. L., Hagiwara, Y., Tan, J. H., and Adeli, H. (2018). Deep convolutional neural network for the automated detection and diagnosis of seizure using EEG signals. *Comput. Biol. Med.* 100, 270–278. doi: 10.1016/j.compbiomed.2017.09.017

Ansari, A. H., Cherian, P. J., Caicedo, A., and Naulaers, G. (2019). Neonatal seizure detection using deep convolutional neural networks. *Int. J. Neural Syst.* 29:1850011. doi: 10.1142/S0129065718500119

Antony, M. J., Sankaralingam, B. P., Mahendran, R. K., Gardezi, A. A., Shafiq, M., Choi, J. G., et al. (2022). Classification of EEG using adaptive SVM classifier with CSP and online recursive independent component analysis. *Sensors* 22:7596. doi: 10.3390/s22197596

Bansal, K., Garcia, J. O., Tompson, S. H., Verstynen, T., Vettel, J. M., and Muldoon, S. F. (2019). Cognitive chimera states in human brain networks. Science. *Advances* 5:eaau8535. doi: 10.1126/sciadv.aau8535

Biju, K. S., Hakkim, H. A., and Jibukumar, M. G. (2017). Ictal EEG classification based on amplitude and frequency contours of IMFs. *Biocybern. Biomed. Eng.* 37, 172–183. doi: 10.1016/j.bbe.2016.12.005

Emami, A., Kunii, N., Matsuo, T., Shinozaki, T., Kawai, K., and Takahashi, H. (2019). Seizure detection by convolutional neural network-based analysis of scalp electroencephalography plot images. *Neuroimage Clin.* 22:101684. doi: 10.1016/j.nicl.2019.101684

Fergus, P., Hignett, D., Hussain, A., Al-Jumeily, D., and Abdel-Aziz, K. (2015). Automatic epileptic seizure detection using scalp EEG and advanced artificial intelligence techniques. *Biomed. Res. Int.* 2015:986736. doi: 10.1155/2015/986736

Fu, K., Qu, J. F., Chai, Y., and Zou, T. (2015). Hilbert marginal spectrum analysis for automatic seizure detection in EEG signals. *Biomed. Signal Process. Control* 18, 179–185. doi: 10.1016/j.bspc.2015.01.002

Gramfort, A., Luessi, M., Larson, E., Engemann, D. A., Strohmeier, D., Brodbeck, C., et al. (2013). MEG and EEG data analysis with MNE-Python. *Front. Neurosci.* 7:267. doi: 10.3389/fnins.2013.00267

Hopfengärtner, R., Kasper, B. S., Graf, W., Gollwitzer, S., Kreiselmeyer, G., Stefan, H., et al. (2014). Automatic seizure detection in long-term scalp EEG using an adaptive thresholding technique: a validation study for clinical routine. *Clin. Neurophysiol.* 125, 1346–1352. doi: 10.1016/j.clinph.2013.12.104

Huang, N. E., Shen, Z., Long, S. R., Wu, M. L. C., Shih, H. H., Zheng, Q., et al. (1998). The empirical mode decomposition and the Hilbert spectrum for nonlinear and non-stationary time series analysis. *Proc. Math. Phys. Eng. Sci.* 454, 903–995. doi: 10.1098/rspa.1998.0193

Li, Z. H., Li, S. F., Yu, T., and Li, X. (2020). Measuring the coupling direction between neural oscillations with weighted symbolic transfer entropy. *Entropy* 22:1442. doi: 10.3390/e22121442

Lu, X. J., Zhang, J. Q., Huang, S. F., Lu, J., Ye, M. Q., and Wang, M. S. (2021). Detection and classification of epileptic EEG signals by the methods of nonlinear dynamics. *Chaos, Solitons Fractals* 151:111032. doi: 10.1016/j.chaos.2021.111032

Lv, G., Zhang, N. Y., Ma, K. X., Weng, J., Zhu, P., Chen, F., et al. (2021). Functional brain network dynamics based on the Hindmarsh–rose model. *Nonlinear Dyn.* 104, 1475–1489. doi: 10.1007/s11071-021-06318-1

Lynn, C. W., and Bassett, D. S. (2019). The physics of brain network structure, function and control. *Nat. Rev. Phys.* 1, 318–332. doi: 10.1038/s42254-019-0040-8

Ma, J., and Tang, J. (2017). A review for dynamics in neuron and neuronal network. *Nonlinear Dyn.* 89, 1569–1578. doi: 10.1007/s11071-017-3565-3

Majhi, S., Bera, B. K., Ghosh, D., and Perc, M. (2018). Chimera states in neuronal networks a review. *Phys Life Rev* 28, 100–121. doi: 10.1016/j.plrev.2018.09.003

Mandhouj, B., Cherni, M. A., and Sayadi, M. (2021). An automated classification of EEG signals based on spectrogram and CNN for epilepsy diagnosis. *Analog Integr. Circ. Sig. Process* 108, 101–110. doi: 10.1007/s10470-021-01805-2

Proix, T., Jirs, V. K., Bartolomei, F., Guye, M., and Truccolo, W. (2018). Predicting the spatiotemporal diversity of seizure propagation and termination in human focal epilepsy. *Nat. Commun.* 9:1088. doi: 10.1038/s41467-018-02973-y

Raghu, S., Sriraam, N., Temel, Y., Rao, S. V., and Kubben, P. L. (2020). EEG based multi-class seizure type classification using convolutional neural network and transfer learning. *Neural Netw.* 124, 202–212. doi: 10.1016/j.neunet.2020.01.017

Rashed-Al-Mahfuz, M., Moni, M. A., Uddin, S., Alyami, S. A., Summers, M. A., and Eapen, V. (2021). A deep convolutional neural network method to detect seizures and characteristic frequencies using epileptic electroencephalogram (EEG) data. *IEEE J. Transl. Eng. Health Med.* 9:2000112. doi: 10.1109/JTEHM.2021.3050925

Rodrigues, F. A., Peron, T. K. D. M., Ji, P., and Kurths, J. (2016). The Kuramoto model in complex networks. *Phys. Rep.* 610, 1–98. doi: 10.1016/j.physrep.2015.10.008

San-Segundo, R., Gil-Martín, M., D'Haro-Enríquez, L. F., and Pardo, J. M. (2019). Classification of epileptic EEG recordings using signal transforms and convolutional neural networks. *Comput. Biol. Med.* 109, 148–158. doi: 10.1016/j.compbiomed.2019.04.031

Schreiber, T. (2000). Measuring information transfer. *Phys. Rev. Lett.* 85, 461–464. doi: 10.1103/PhysRevLett.85.461

Shimono, M., and Beggs, J. M. (2015). Functional clusters, hubs, and communities in the cortical micro-connectome. *Cereb. Cortex* 25, 3743–3757. doi: 10.1093/cercor/bhu252

Shoeb, A. H. (2009). *Application of machine learning to epileptic seizure onset detection and treatment. PhD Thesis*. Massachusetts Institute of Technology, pp. 157–162.

Shoeibi, A., Ghassemi, N., Khodatars, M., Jafari, M., and Acharya, U. R. (2021). Epileptic seizures detection using deep learning techniques: a review. *Int. J. Environ. Res. Public Health* 18:5780. doi: 10.3390/ijerph18115780

Staniek, M., and Lehnertz, K. (2008). Symbolic transfer entropy. *Phys. Rev. Lett.* 100, 3136–3140. doi: 10.1103/PhysRevLett.100.158101

Staniek, M., and Lehnertz, K. (2009). Symbolic transfer entropy inferring directionality in biosignals. *Biomed. Eng.* 54, 323–328. doi: 10.1515/BMT.2009.040

Supriya, S., Siuly, S., Wang, H., and Zhang, Y. C. (2020). Automated epilepsy detection techniques from electroencephalogram signals: a review study. *Health Inf. Sci. Syst.* 8:33. doi: 10.1007/s13755-020-00129-1

Tsai, F. F., Fan, S. Z., Lin, Y. S., Huang, N. E., and Yeh, J. R. (2016). Investigating power density and the degree of nonlinearity in intrinsic components of anesthesia EEG by the Hilbert-Huang transform. *PLoS One* 11:e0168108. doi: 10.1371/journal.pone.0168108

Tsiouris, K., Markoula, S., Konitsiotis, S., Koutsouris, D. D., and Fotiadis, D. I. (2018a). A robust unsupervised epileptic seizure detection methodology to accelerate large EEG database evaluation. *Biomed. Signal Process. Control* 40, 275–285. doi: 10.1016/j.bspc.2017.09.029

Tsiouris, K., Pezoulas, V. C., Zervakis, M., Konitsiotis, S., Koutsouris, D. D., and Fotiadis, D. I. (2018b). A long short-term memory deep learning network for the prediction of epileptic seizures using EEG signals. *Comput. Biol. Med.* 99, 24–37. doi: 10.1016/j.compbiomed.2018.05.019

Wang, J. J., Qiu, S. J., Xu, Y., Liu, Z. Y., Wen, X., Hu, X., et al. (2014). Graph theoretical analysis reveals disrupted topological properties of whole brain functional networks in temporal lobe epilepsy. *Clin. Neurophysiol.* 125, 1744–1756. doi: 10.1016/j.clinph.2013.12.120

Wang, J. H., Wang, X. D., Xia, M. R., Liao, X. H., Evans, A., et al. (2015). GRETNA a graph theoretical network analysis toolbox for imaging connectomics. *Front. Hum. Neurosci.* 9:386. doi: 10.3389/fnhum.2015.00386

Wu, M. C., and Huang, N. E. (2009). *Biomedical data processing using HHT: a review advanced biosignal processing*. Berlin: Springer, 335–352.

Yuan, Y., Xun, G., Jia, K., and Zhang, A. D. (2019). A multi-view deep learning framework for EEG seizure detection. *IEEE J. Biomed. Health Inform.* 23, 83–94. doi: 10.1109/JBHI.2018.2871678

Frontiers in Neuroscience

TYPE Original Research
PUBLISHED 18 May 2023
DOI 10.3389/fnins.2023.1174096

A data security scheme based on EEG characteristics for body area networks

Tong Bai[1†], Yuhao Jiang[1†], Jiazhang Yang[2], Jiasai Luo[1]* and Ya Du[3]*

[1]School of Optoelectronic Engineering, Chongqing University of Posts and Telecommunications, Chongqing, China, [2]The Women and Children Hospital of Yongchuan, Chongqing, China, [3]Department of Peripheral Vascular (Wound Repair), Chongqing Hospital of Traditional Chinese Medicine, Chongqing, China

OPEN ACCESS

EDITED BY
Xiaomin Yang,
Sichuan University, China

REVIEWED BY
Tianhan Li,
Xinxiang Medical University, China
Wuzhong Yin,
Southwest University of Science and Technology, China

*CORRESPONDENCE
Jiasai Luo
✉ luojs@cqupt.edu.cn
Ya Du
✉ 361974588@qq.com

[†]These authors have contributed equally to this work and share first authorship

RECEIVED 25 February 2023
ACCEPTED 21 March 2023
PUBLISHED 18 May 2023

CITATION
Bai T, Jiang Y, Yang J, Luo J and Du Y (2023) A data security scheme based on EEG characteristics for body area networks. *Front. Neurosci.* 17:1174096. doi: 10.3389/fnins.2023.1174096

Body area network (BAN) is a body-centered network of wireless wearable devices. As the basic technology of telemedicine service, BAN has aroused an immense interest in academia and the industry and provides a new technical method to solve the problems that exist in the field of medicine. However, guaranteeing full proof security of BAN during practical applications has become a technical issue that hinders the further development of BAN technology. In this article, we propose a data encryption method based on electroencephalogram (EEG) characteristic values and linear feedback shift register (LFSR) to solve the problem of data security in BAN. First, the characteristics of human EEG signals were extracted based on the wavelet packet transform method and as the MD5 input data to ensure its randomness. Then, an LFSR stream key generator was adopted. The 128-bit initial key obtained through the message-digest algorithm 5 (MD5) was used to generate the stream key for BAN data encryption. Finally, the effectiveness of the proposed security scheme was verified by various experimental evaluations. The experimental results showed that the correlation coefficient of data before and after encryption was very low, and it was difficult for the attacker to obtain the statistical features of the plaintext. Therefore, the EEG-based security scheme proposed in this article presents the advantages of high randomness and low computational complexity for BAN systems.

KEYWORDS

body area network, electroencephalogram, data security, wavelet packet transform, linear feedback shift register

1. Introduction

Body area network (BAN) is an important means to solve problems, such as insufficient medical resources, rising treatment costs, and poor medical conditions, which are caused by the growing population in the world (Hassan et al., 2017; Abidi et al., 2020; Liu et al., 2021). As an emerging technology, BAN has aroused an immense interest in academia and industry since its inception. In 2012, the Institute of Electrical and Electronics Engineers (IEEE) published an official standard, IEEE 802.15.6: Wireless Body Area Networks (Standard, 2012). As shown in Figure 1, the said standard defines a human-centered wireless communication network as consisting of sensor nodes and related devices placed on or inside the human body (Pandey et al., 2019). Due to the particularity of BAN, the network transmits users' privacy information, and consequently, any unauthorized access or illegal data tampering will cause major problems to users; therefore, BAN has set high requirements for security (Shen et al., 2018; Hajar et al., 2021). However, the BAN system is limited in resources

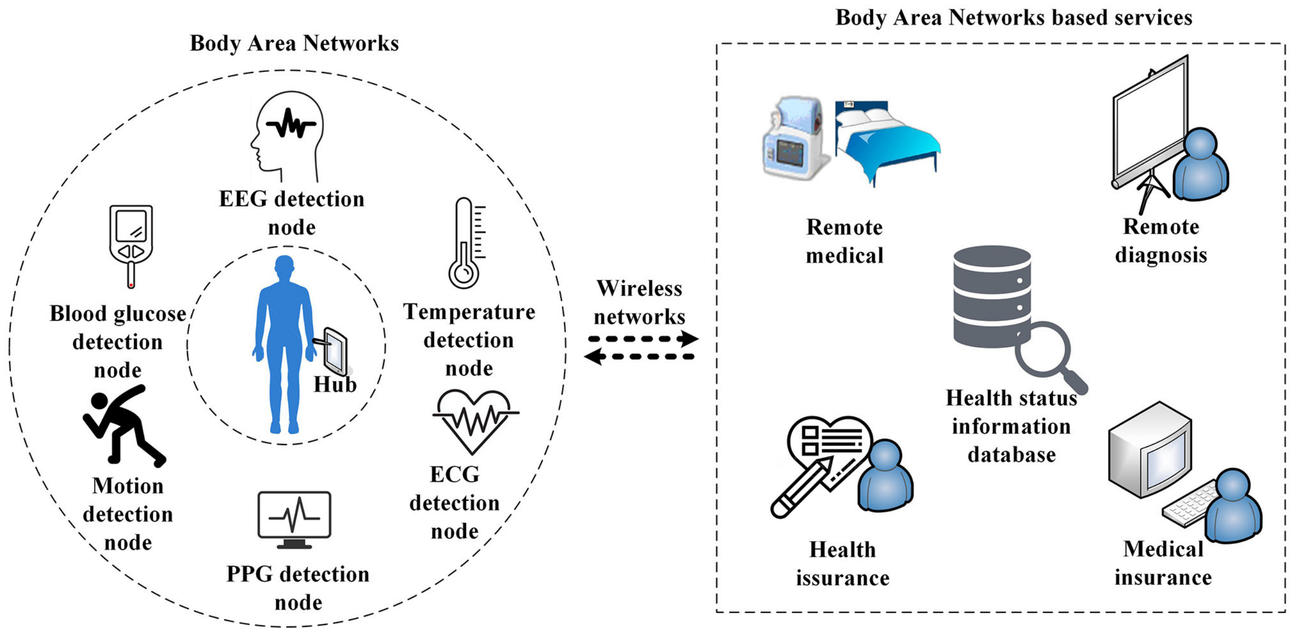

FIGURE 1
Body area network (BAN) system and its applications.

and is sensitive to the energy consumption of sensor nodes; therefore, most of the existing network security schemes are not applicable (Shi et al., 2012; Qadri et al., 2020). Therefore, designing a security solution with low power consumption and high-intensity security that meets the requirements of a BAN system to realize that data security has become a major challenge in the field of BAN research (Narwal and Mohapatra, 2021).

Researchers have proposed a variety of ways to improve the safety of BAN data. The first way for data encryption is the conventional symmetric encryption scheme. The advanced encryption standard (AES)-based encryption method for BAN data has been proposed in the study of Gangadari and Rafi Ahamed (2016). The second-order reversible one-dimensional cellular automata are used to replace the lookup tables in the AES algorithm to generate an S-box for the nonlinear substitution of data. The experimental results have shown that this scheme includes better security features than the conventional AES algorithm. However, generating the encryption key requires adequate amounts computation, and the BAN system uses more energy due to data encryption. Therefore, the conventional symmetric encryption scheme is not suitable for a BAN system (Bai et al., 2019; Wang et al., 2020). The second way for data encryption is based on the physiological sign information in a BAN system. Different from common sensor nodes, the sensor nodes in BAN collect human physiological sign parameters. These parameters will present different characteristics according to different individuals. Even for the same individual, the information on physiological signs is time-varying. Therefore, these parameters collected from the human body can be used for data security in a BAN system (Al-Janabi et al., 2017). Compared with traditional data encryption schemes, these key generation methods can effectively reduce energy consumption in the process of encryption (Liu et al., 2013; Mainanwal et al., 2015). In their study Wang et al. (2011) proposed a method to extract characteristic values of electrocardiogram (ECG) signals based on the implicit Markov model, and the encryption key for BAN data was generated by combining the hash function. This scheme does not require key distribution and strict time synchronization. Fast Fourier Transform (FFT) is performed on an ECG signal and photoplethysmogram (PPG) signal, respectively, as described in the study by Venkatasubramanian et al. (2008) and by Ramli et al. (2013), and the generated characteristic values and fuzzy algorithm are used to construct a security mechanism for BAN. In his study, Moosavi (2021) puts forward two different key generation methods based on the PPG signal to improve the security of BAN. The first method is realized using the Galois linear feedback shift register (LFSR) and a continuous interbeat interval (IBI) of the PPG signal. The second method is realized using the IBI as the seed generator for the AES algorithm. Compared with the existing methods that only rely on the IBI sequence, this method provides better random performance. In the study by Faragó et al. (2019), a time-domain technique based on the cross-correlation has been proposed to evaluate the characteristics of ECG, PPG, or electromyography (EMG) signals for the identification and authentication in BAN systems. This method can complete the security authentication of nodes without increasing the calculation amount of BAN nodes. In this article, we propose a security scheme based on the recognition of EEG characteristics and the LFSR method for BAN. The random EEG signal characteristics containing individual differences were calculated as the input data for MD5 to solve the security problem of the key. The simple structure of the LFSR was used to generate a random stream key, which improves the data encryption strength of a BAN system.

The remainder of this article is organized as follows: Section 2 puts forward the EEG signal and the characteristic value extraction method. Section 3 presents the initial key generation method based on MD5. Section 4 provides the generation method of keys based on the LFSR. Section 5 presents the experimental results of the encryption data and provides the analysis. Finally, the conclusion of the security scheme is given in Section 6.

2. EEG signal acquisition and characteristic value extraction method

2.1. EEG signal acquisition

Electroencephalogram (EEG) is a method for recording the effect of electrical activity on the nerve cells in the brain to reflect the brain activity in a human being. The human brain is made up of tens of thousands of neurons, and the EEG signals are the electrical signals that are generated by the activity between these neurons (Lotte et al., 2018). The single-lead EEG has poor determinacy and strong randomness, thus the nonlinear research is limited to some extent and the recognition results are poor. While the multi-lead EEG contains more information concerning the human brain, it can better re?ect the overall information on brain activity (Galderisi et al., 1996).

It is difficult to accurately characterize the electrical activity of the human brain because the EEG is characterized by a strong background noise, a weak signal amplitude, a strong non-stationarity, and randomness. The concept of frequency was first used to describe the electrical activity in the brain in 1929. The frequency of electrical activity in the human brain varies between 0.5 Hz and 30 Hz. At present, it is generally accepted that the range of EEG frequency variations is divided into four frequency bands, which are: (1) δ wave: frequency is 0.5–4 Hz and the amplitude is 20–200 μV. (2) θ wave: frequency is 4–7 Hz and the amplitude is 20–150 μV. (3) α wave: frequency is 8–13 Hz and the amplitude is 20$\sim$100 μV. (4) β wave: frequency is 13–30 Hz and the amplitude is 5–20 μV.

In this study, the EEG experimental dataset SEED-IV was used for experimental testing. In SEED-IV, 15 volunteers between 20 and 24 years of age were involved in the experiment, and 72 movie clips were selected as a library of four emotions (happiness, sadness, fear, and neutral). Each volunteer was required to undergo three sessions with an interval of one week or more, and each session contained 24 trials. Each trial usually lasted $\sim$3 min and is divided into three parts: 5 s hint of start, approximately 2 min movie clip, and 45 s emotion assessment. In the dataset, EEG signals were extracted from each volunteer at different times during the same scene and the same stimulus. As shown in Figure 2, the multi-channel original EEG signals were extracted by the 62-channel ESI NeuroScan system with the sampling frequency of 200 Hz. The other irrelevant bands were filtered with filters ranging from 0.5 Hz to 75 Hz to remove noise. Then, the time-domain and frequency-domain characteristics of EEG signals were obtained, and the EEG signals were expressed effectively (Zhang et al., 2013; Meng et al., 2014; Yang et al., 2014).

2.2. Extraction method of EEG characteristics

Electroencephalogram is a time-varying and non-stationary signal. Since the EEG signal was discovered, the usual method of analysis is to calculate the power spectrum of the EEG signal by Fourier transform; however, the Fourier transform is based on the premise of a stationary random process. However, the EEG signals detected in practical applications cannot satisfy the hypothesis of stationarity, such as the EEG signals in sleep, seizure, or other states; therefore only by combining time and frequency processing can better results be obtained.

The wavelet transform is equivalent to a digital microscope, including the functions of magnification, narrowing, and panning. The function of a wavelet transform is similar to that of a set of band-pass filters with an equal bandwidth and a variable center frequency. Compared with the traditional Fourier transform, the wavelet transform is a local transform of space/time and frequency, which can effectively extract information from signals, and carry out a multi-scale detailed analysis of functions or signals through operational functions such as scaling and shift, with good time-frequency characteristics. The wavelet transform can provide a frequency-varying "time-frequency" window, which automatically narrows when high-frequency information is detected, allowing for a fine analysis of the signal at higher frequencies. When a low-frequency signal is detected, the "time-frequency" window is automatically widened to allow for conducting a profile analysis of the signal at a lower frequency. The time-frequency characteristics of the wavelet transform are very suitable for analyzing the transient characteristics and time-varying characteristics of non-stationary signals.

The wavelet packet decomposition, also known as optimal subband tree structuring, is the further optimization of the wavelet transform. The concept behind wavelet packet decomposition is to use the analysis tree to represent the wavelet packet, that is, to analyze the details of the input signal using the wavelet transform with several iterations. The idea behind the main algorithm of wavelet packet decomposition is that, on the basis of the wavelet transform, in each level of signal decomposition, in addition to the further decomposition of the low-frequency subband, further decomposition of the the high-frequency subband also takes place. Finally, by minimizing the cost function, the optimal signal decomposition path is calculated, and the original signal is decomposed according to the decomposition path. Compared with the traditional wavelet analysis, the wavelet packet analysis can adaptively select the best basis function according to the characteristics of the analyzed signal after the multi-level division of the frequency band so as to make it match the signal and improve the analysis ability of the signal (Yin et al., 2008). In the wavelet packet analysis, $\varphi(t)$

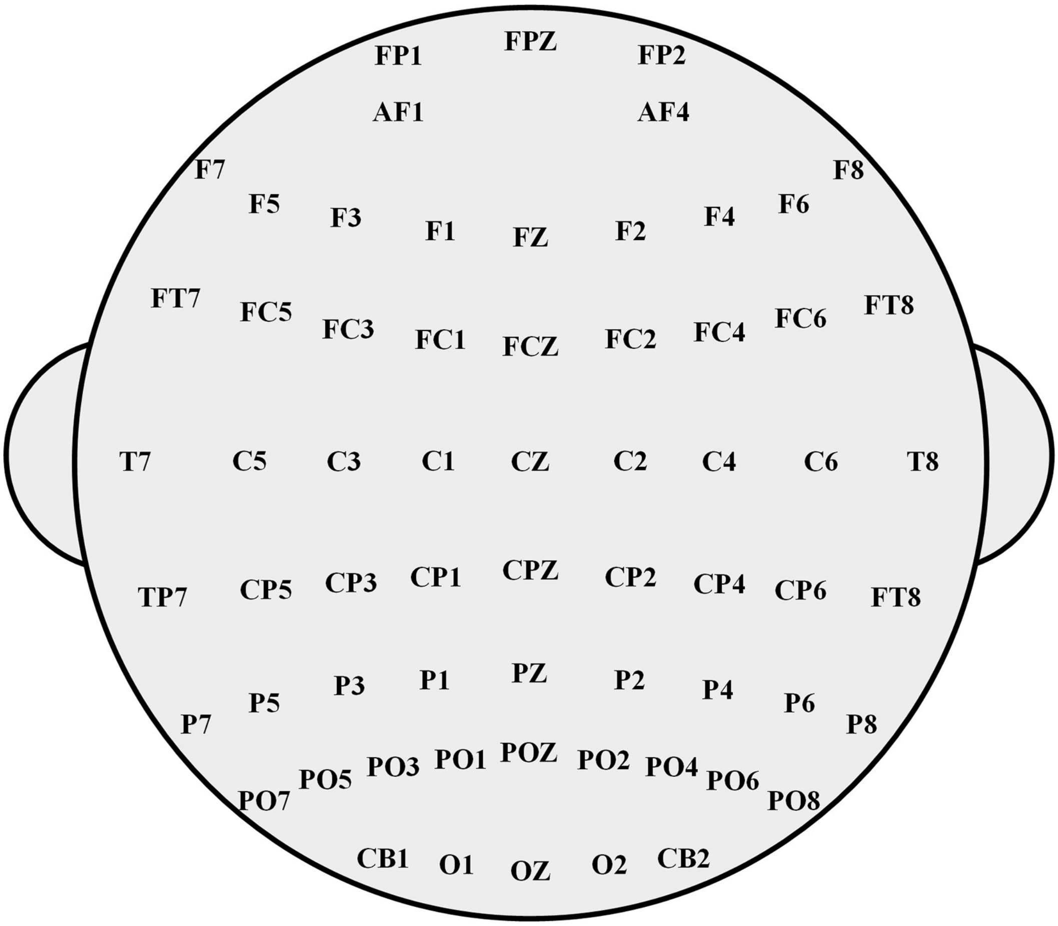

FIGURE 2
A 62-channel ESI NeuroScan system with the sampling frequency of 200 Hz.

represents the scale function and $\psi(t)$ represents the wavelet function, therefore:

$$\psi_0(t) = \varphi(t) \tag{1}$$

$$\psi_1(t) = \psi(t) \tag{2}$$

$$\psi_{2m}(t) = \sum_{k=-\infty}^{+\infty} h_k \psi_m(2t-k) \tag{3}$$

$$\psi_{2m+1}(t) = \sum_{k=-\infty}^{+\infty} g_k \psi_m(2t-k), \tag{4}$$

where h_k is the low-pass filter and g_k is the high-pass filter. Function $\{\psi_n\}$ is the wavelet packet of the scale function $\varphi(t)$.

In this article, the wavelet packet transform theory was used to process EEG signals, and the characteristics of different EEG frequency bands (α wave, β wave, δ wave, and θ wave) were calculated. Through a multi-resolution decomposition of the wavelet packet, the optimal wavelet packet tree was selected to reconstruct the specified EEG frequency bands. In this article, a discrete Meyer wavelet was used to decompose EEG signals. The Fourier transform of the Meyer wavelet scale function is:

$$\varphi(t)\begin{cases}(2\pi)^{\frac{1}{2}} & |t| < \frac{2\pi}{3}\\ (2\pi)^{-\frac{1}{2}}\cos\left[\frac{\pi}{2}\nu\left(\frac{3}{2\pi}|t|-1\right)\right] & \frac{2\pi}{3}\le|t|\le\frac{4\pi}{3}\\ 0 & \text{else}\end{cases} \tag{5}$$

$$\nu(t) = \begin{cases}0 & t\le 0\\ 1 & t\ge 1\end{cases} \tag{6}$$

$$\nu(t) + \nu(1-t) = 1 \tag{7}$$

The EEG signal was decomposed into eight layers, and the minimum frequency resolution can be estimated by formula (8).

$$f_{\min} = \frac{f_s}{2\cdot 2^8} = 0.3906\text{Hz}, \tag{8}$$

where f_s is the sampling frequency of the EEG signal and the value of f_s is 200 Hz.

The more the layers of wavelet packet decomposition, the higher the frequency resolution. The wavelet packet decomposition satisfies four kinds of EEG frequency band filtering requirements.

3. Initial key generation method

After performing the extraction method of EEG characteristics, MD5 and LFSR were used to generate keys for data encryption, as shown in Figure 3. The message-digest (MD) algorithm is a widely used password hash function, which has the following characteristics: first, the length of the output sequence calculated by the MD algorithm is fixed, regardless of the length of the input message. Second, the message digest appears randomly. In fact, different input data in the MD algorithm will result in different output sequences after calculation. Third, as the MD algorithm is a one-way function, it can only calculate the summary sequence from the input data bit can neither recover any input data from the output sequence nor find any information related to the input data from the output sequence. The MD5 algorithm generates a 128-bit (16-byte) hash sequence based on the input data. It can be used to verify the integrity and consistency of data transmission. The MD5 algorithm was announced in 1992 to replace the MD4 algorithm. MD5 treats the entire file as one large text message and generates a unique MD5 message digest through an irreversible string conversion algorithm. If anyone makes any changes to a file, its MD5 value will change.

The principle of the MD5 algorithm is that the input data was grouped into 512 bits. Each group was then divided into sixteen 32-bit subgroups, and the grouped data were processed through a series of calculations. Finally, the 128-bit hash output sequence is composed of four groups of 32-bit sequences in sequence. Figure 4 shows the process of the MD5 algorithm. Each operation was performed by the 128-bit result value of the previous round and the current 512-bit value. The MD5 process is as follows:

(1) In the MD5 algorithm, the input data need to be padded by bits first, and the bit number of the data modulo 512 is required to be 448. Even if the bit number of the input data modulo 512 yields exactly 448, it must be padded by bits. The first bit of the padding bits is 1 and the rest is 0.
(2) The MD5 algorithm uses four 32-bit registers, A, B, C, and D, to store intermediate variables and the final result. Registers A, B, C, and D are assigned initial values at the beginning of the MD5 calculation.
(3) MD5 algorithm defines four nonlinear functions, F, G, H, and I, to process the input data after grouping. Four different functions, F, G, H, and I, are used to process each 512-bit dataset. Each round takes the data in the updated register, A, B, C, and D, and the current 512-bit dataset as input and gets the new register values of A, B, C, and D after calculation.
(4) The final values of A, B, C, and D are spliced together in the order from low-bit data to high-bit data to form the output data.

4. Stream key generation based in LFSR

Taking some sequences existing in the shift register as the input of the linear feedback function, after making certain calculations in the function, the output results were filled to the leftmost end of the shift register so that such a shift register would have a continuous output. This shift register is called the linear feedback shift register (LFSR). In fact, the feedback function in the LFSR only performs an XOR on certain bits in the shift register and populates the result to the leftmost end of the shift register, as shown in Figure 5. The data of each bit in the LFSR may or may not participate in the XOR, and the bits that participate in the XOR are called taps. An *n*-order LFSR can only traverse 2^n-1 states at most, that is to say, the maximum period of an LFSR is 2^n-1. The sequence generated by an LFSR with a period of 2^n-1 is called the *m* sequence, and the *m* sequence has a higher encryption strength among the LFSR of the same level. The cipher text is calculated by the pseudorandom sequence XOR the plaintext.

The expression of the 128-order *m* sequence used for key generation is shown in formula (9).

$$f(N) = N^{127} + N^{126} + 1 \tag{9}$$

5. Experimental results and analysis

To verify the designed data security scheme based on EEG characteristics and LFSR, MATLAB software is used to simulate the encryption of image data. Using image data for verification of the designed data security scheme is important because the BAN system contains a large number of images such as electromyography images, endoscopic images, and medical images. Furthermore, image data are more intuitive for verification. In this article, the image Airplane and a medical endoscopic image were used to verify the encryption effect of the proposed data security scheme. Figure 6 shows the original images and the encrypted images.

Gray distribution refers to the distribution of gray value of gray images, which reflects the most basic statistical characteristics of an image and is generally represented by a gray histogram. The gray value distribution of the original image is usually uneven; therefore, there is a certain probability to crack the image data by calculating the statistical features. Figure 7 presents the gray histogram results of the image Airplane and the medical endoscopic image. As shown in Figure 7A, the left gray histogram is the gray value distribution of the original image, and it is relatively concentrated. However, after the encryption is completed, the result of the distribution of the images becomes more uniform, as shown in the right gray histogram of Figure 7A. Similar to Figures 7A, B yields the same result after encryption. Therefore, through the security scheme proposed in this article, the gray value distribution of the images is scrambled and became more uniform.

The two-dimensional correlation of images is used to verify the correlation degree of the original image data and the encrypted one,

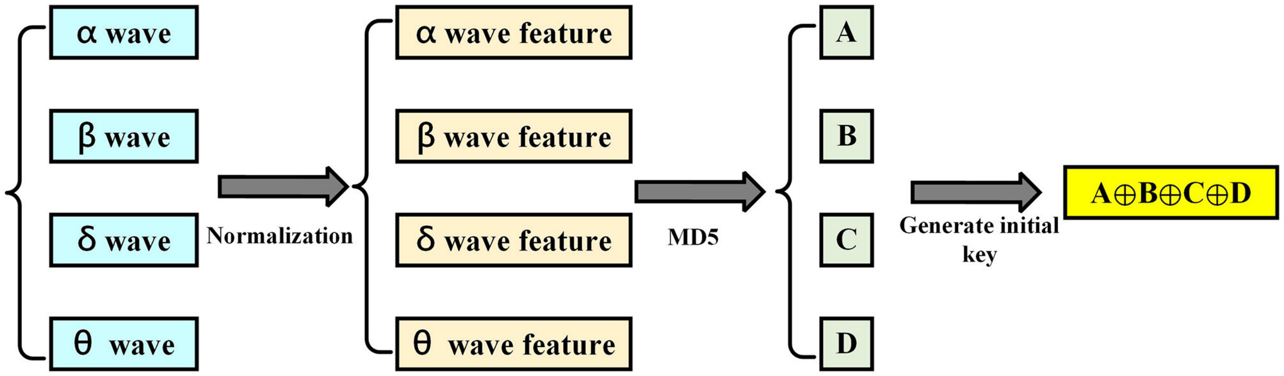

FIGURE 3
Flowchart of the key for BAN data security.

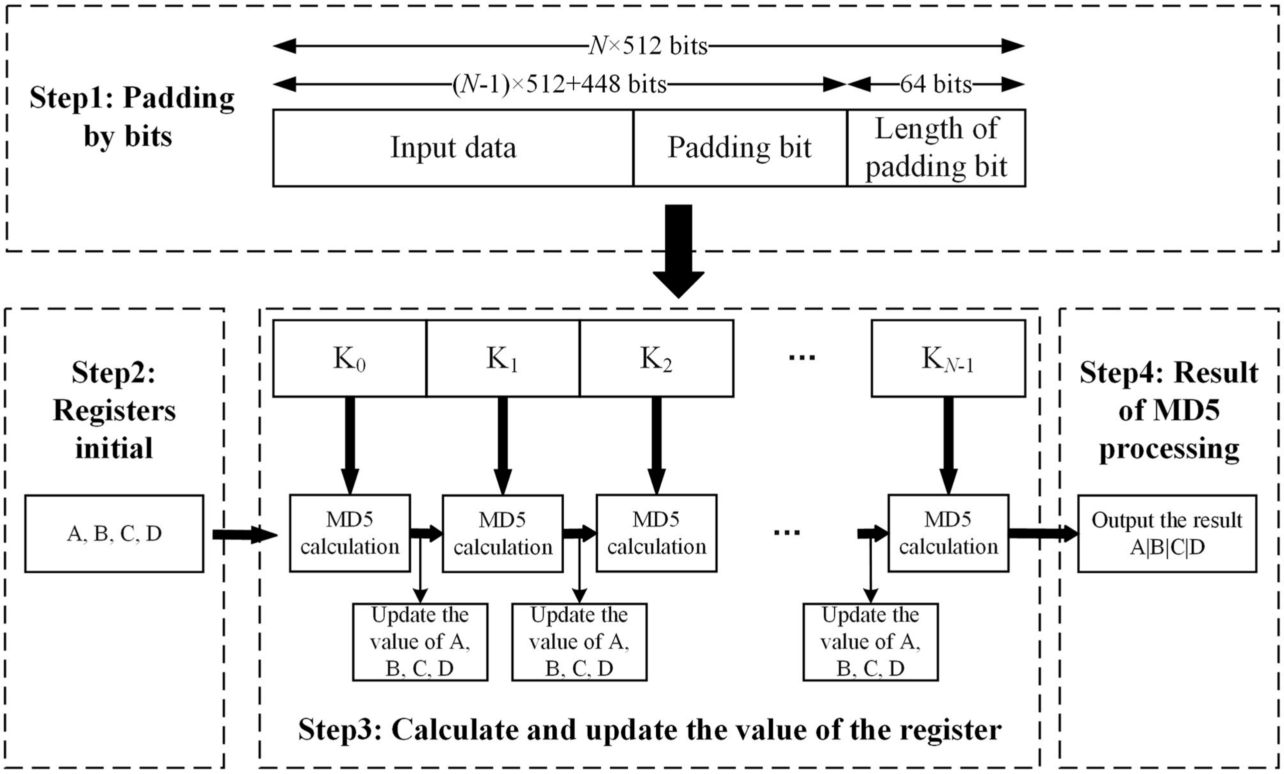

FIGURE 4
Flowchart of MD5 processing.

and K is the correlation coefficient. The calculation method of K is given as follows:

$$K=\sum_{a=1}^{M}\sum_{b=1}^{N}(O_{ab}-\overline{O})(E_{ab}-\overline{E})/\sqrt{\left(\sum_{a=1}^{M}\sum_{b=1}^{N}(O_{ab}-\overline{O})^2\right)\left(\sum_{a=1}^{M}\sum_{b=1}^{N}(E_{ab}-\overline{E})^2\right)} \quad (10)$$

where O_{ab} and E_{ab}, respectively, represent the gray values of the image Airplane and the medical endoscopic image at the point (a, b) before and after the encryption.

After the designed method in this article was used to encrypt the image Airplane and the medical endoscopic image, the two-dimensional correlation coefficients K_1 $=1.38\times10^{-8}$ and K_1 $=3.24\times10^{-9}$ of the two images before and after encryption were calculated by formula (9). It can be observed that the two-dimensional correlation coefficient approaches 0,

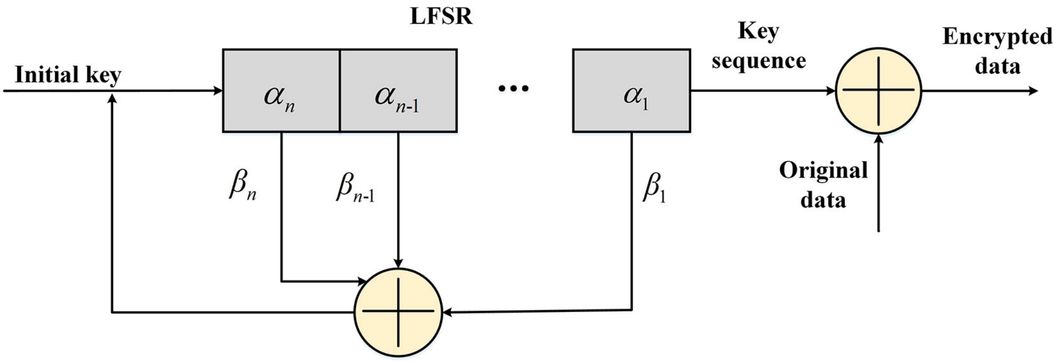

FIGURE 5
Linear feedback shift register (LFSR)-based encryption process.

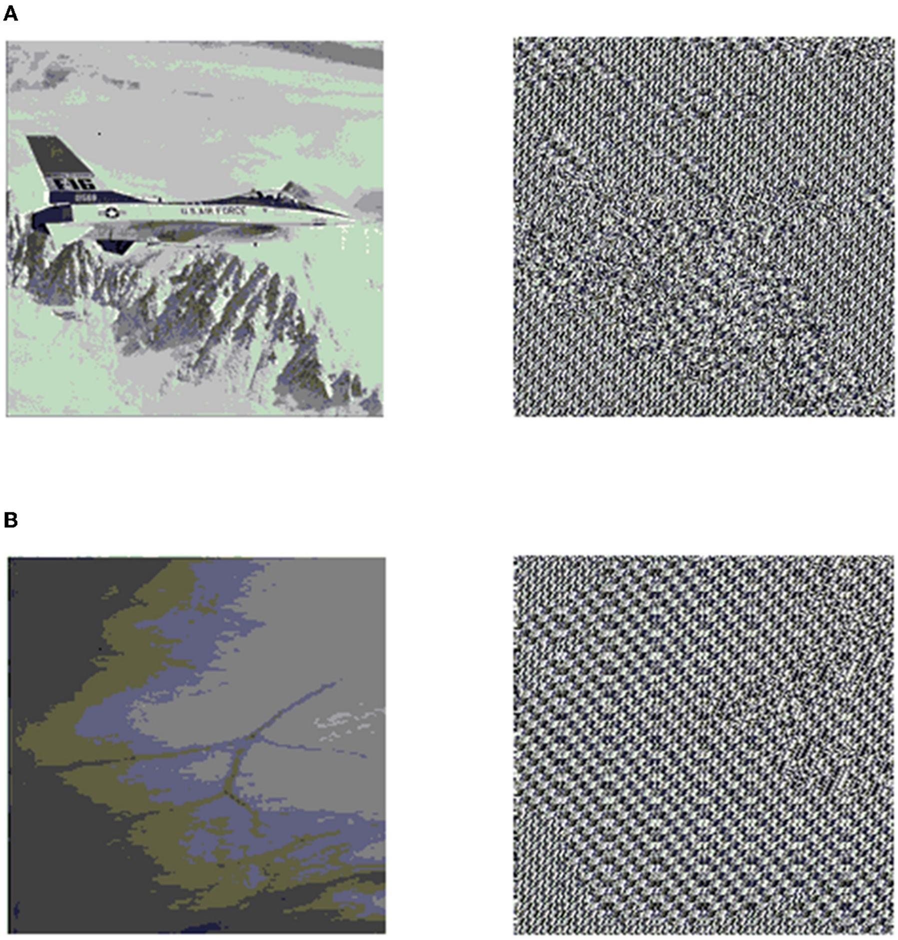

FIGURE 6
Original and encrypted images. **(A)** Airplane. **(B)** Medical endoscopic image.

indicating that the correlation of images before and after encryption is very low. This method can effectively encrypt image data.

To verify the correlation of adjacent pixels in the images, we select the adjacent pixel pairs in the original image and the encrypted one, and R is the correlation coefficient.

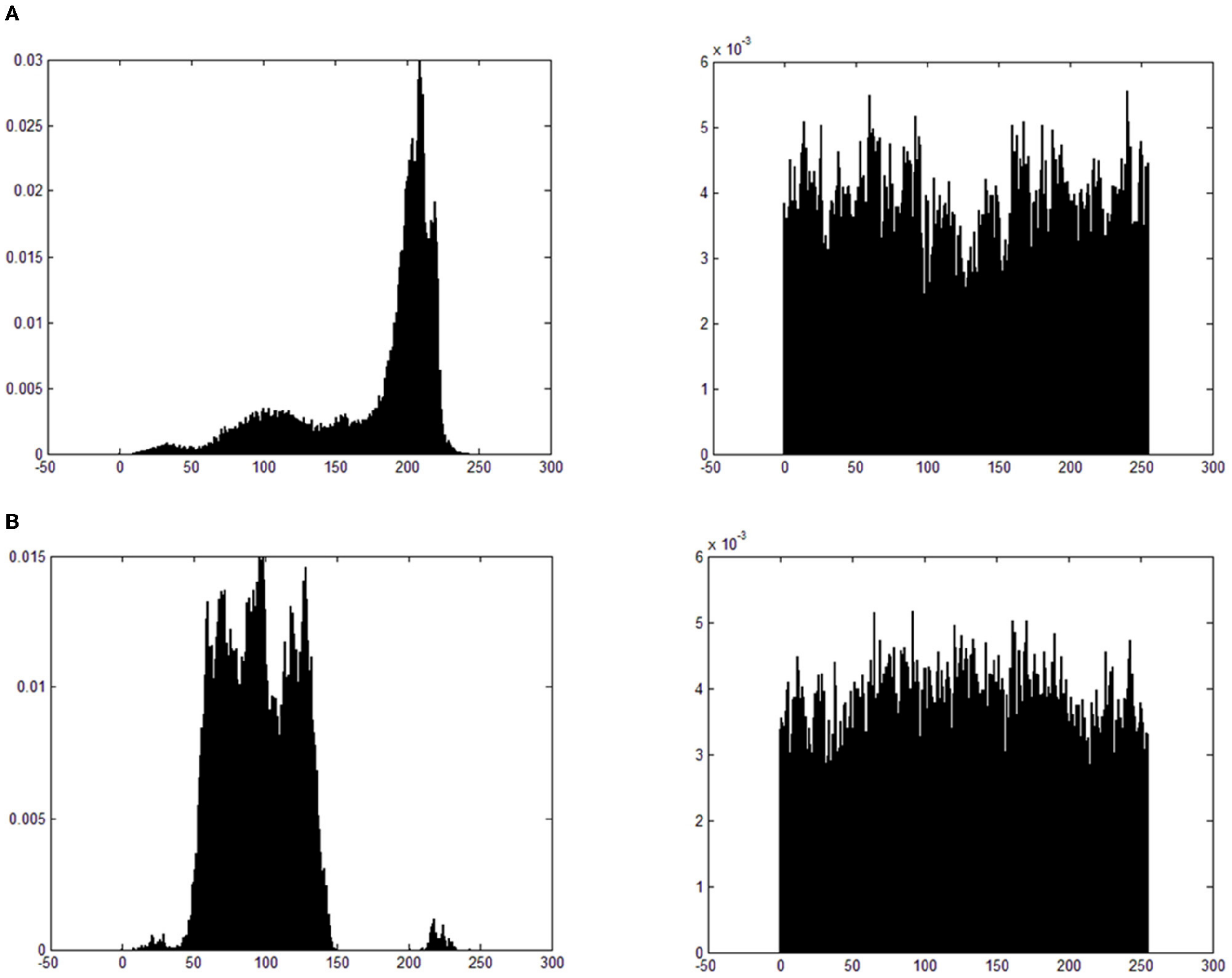

FIGURE 7
Gray histogram of the original and encrypted images. **(A)** Airplane. **(B)** Medical endoscopic image.

The calculation method of R is shown in formula (14). Furthermore, the correlation coefficients in the vertical, horizontal, and diagonal directions of the images are calculated, respectively,

$$E(x) = \sum_{i=1}^{N} x_i / N \tag{11}$$

$$D(x) = \sum_{i=1}^{N} [x_i - E(x)] / N \tag{12}$$

$$\operatorname{cov}(x, y) = \sum_{i=1}^{N} [x_i - E(x)] \left[y_i - E(y)\right] / N \tag{13}$$

$$R = \frac{\operatorname{cov}(x, y)}{\sqrt{D(x)\, D(y)}} \tag{14}$$

,

where x_i and y_i are the gray values of the ith adjacent pixel pairs, $E(x)$ and $E(y)$ are the averages of the image data, $D(x)$ and $D(y)$ are the variances, which measure the deviation between the image data and its average and N is the adjacent pair number of the image.

The calculated results of the correlation coefficient between the original image and the encrypted image are shown in Table 1. It is worth noting that, after data encryption of the image Airplane and the medical endoscopic image, the correlation of adjacent pixels in the three directions is effectively reduced, and it is difficult for the attacker to obtain the statistical features of the plaintext, thus improving the security of the system.

6. Conclusion

To meet the requirements of low power consumption and high-intensity security in a BAN system, this article proposes a data security scheme that is based on EEG characteristic values and LFSR construction. To be specific, the characteristics of EEG signals are mined by the wavelet packet transform, and α, β, δ, and θ waves are constructed to effectively characterize the features of EEG signals, which are input into the MD5 system through

TABLE 1 The correlation coefficient of the images in three directions.

Image name	*R*	Vertical direction	Horizontal direction	Diagonal direction
Airplane	Original	0.8834	0.9251	0.9118
	Encrypted	0.6247	0.2763	0.5570
Medical endoscopic image	Original	0.9251	0.9472	0.9346
	Encrypted	0.5896	0.3107	0.5713

normalization, and the initial key is calculated. Then, a 128-order *m* sequence is used to generate a stream key to encrypt privacy data in BAN. Finally, a variety of evaluation results prove that the proposed security scheme has enough ability to ensure data security in BAN. The BAN security scheme in this article only considers the method of data encryption; however, it does not consider the scheme of node authentication, which has certain limitations. In the future study, this project will invest more research in the following aspects. According to the relatively simple hardware structure of LFSR (m sequence), the advantages of the proposed method are further verified. Based on the characteristics of the BAN system, other types of feature extraction and calculation methods, such as ECG, PPG, and gait, will be studied to determine whether they are suitable for data security. There are still some important security problems in BAN that need to be solved. Therefore, the solutions for authentication with low power consumption and high reliability in BAN systems will be investigated by us.

Data availability statement

Publicly available datasets were analyzed in this study. This data can be found at: https://bcmi.sjtu.edu.cn/home/seed/seed-iv.html.

Author contributions

TB: conceptualization, methodology, writing—original draft, and writing—review and editing. JL: design of the methodology and validation of the experiments. YJ: validation and editing. JY: supervision. YD: validation. All authors contributed to the article and approved the submitted version.

Funding

The project was funded by the National Natural Science Foundation of China (62171073, 61971079, and U21A20447), the Department of Science and Technology of Sichuan Province (2020YFQ0025 and 2020YJ0151), the Project of Central Nervous System Drug Key Laboratory of Sichuan Province (210022-01SZ, 200020-01SZ, 200028-01SZ, and 200027-01SZ), the Nature Science Foundation of Chongqing (cstc2019jcyj-msxmX0275, cstc2020jcyj-cxttX0002, cstc2019jcyjmsxmX0666, cstc2021jscx-gksbx0051, and cstc2021jcyj-bsh0221), the Science and Technology Research Project of Chongqing Municipal Education Commission (KJZD-k202000604, KJQN202100602, KJQN202100602, and KJQN202000604), the Key Research Project of Southwest Medical University (2021ZKZD019), the special support for the Chongqing Postdoctoral Research Project (2021XM3010 and 2021XM2051), and the Project funded by the China Postdoctoral Science Foundation (2022MD713702, 2021MD703941, and 2021M693931).

Acknowledgments

We acknowledge the School of Optoelectronic Engineering of Chongqing University of Posts and Telecommunications for their assistance in the research.

Conflict of interest

The authors declare that the research was conducted in the absence of any commercial or financial relationships that could be construed as a potential conflict of interest.

Publisher's note

References

Abidi, B., Jilbab, A., and Mohamed, E. H. (2020). Wireless body area networks: a comprehensive survey. *J. Med. Engin. Technol.* 44, 97–107. doi: 10.1080/030920201729882

Al-Janabi, S., Al-Shourbaji, I., Shojafar, M., and Shamshirband, S. (2017). Survey of main challenges (security and privacy) in wireless body area networks for healthcare applications. *Egypt. Inform. J.* 18, 113–122. doi: 10.1016/j.eij.11001

Bai, T., Lin, J., Li, G., Wang, H., Ran, P., Li, Z., et al. (2019). A lightweight method of data encryption in BANs using electrocardiogram signal. *Fut. Gen. Comp. Sys.* 92, 800–811. doi: 10.1016/j.future.01031

Faragó, P., Groza, R., Ivanciu, L., and Hintea, S. (2019). A correlation-based biometric identification technique for ECG, PPG and EMG. In *2019 42nd international conference on telecommunications and signal processing (TSP)* (pp. 716–719). IEEE. doi: 10.1109./TSP.2019.8768810

Galderisi, S., Mucci, A., Bucci, P., Mignone, M. L., and Maj, M. (1996). Multilead quantitative EEG profile of clozapine in resting and vigilance-controlled conditions. *Psychiatry Res. Neuroimag.* 67, 113–122. doi: 10.1016./0925-4927(96)02883-1

Gangadari, B. R., and Rafi Ahamed, S. (2016). Design of cryptographically secure AES like S-Box using second-order reversible cellular automata for wireless body area network applications. *Healthcare Technol. Lett.* 3, 177–183. doi: 10.1049./htl.2016.0033

Hajar, M. S., Al-Kadri, M. O., and Kalutarage, H. K. (2021). A survey on wireless body area networks: architecture, security challenges and research opportunities. *Comp. Sec.* 104, 1–27. doi: 10.1016./j.cose.2021.102211

Hassan, M. M., Lin, K., Yue, X., and Wan, J. (2017). A multimedia healthcare data sharing approach through cloud-based body area network. *Future Gen. Comp. Sys.* 66, 48–58. doi: 10.1016/j.future.12016

Liu, J., Zhang, Z., Chen, X., and Kwak, K. S. (2013). Certificateless remote anonymous authentication schemes for wirelessbody area networks. *IEEE Transact. Parall. Distrib. Sys.* 25, 332–342. doi: 10.1109./TPDS.2013.145

Liu, Q., Mkongwa, K. G., and Zhang, C. (2021). Performance issues in wireless body area networks for the healthcare application: a survey and future prospects. *SN Appl. Sci.* 3, 1–19. doi: 10.1007./s42452-020-04058-2

Lotte, F., Bougrain, L., Cichocki, A., Clerc, M., Congedo, M., Rakotomamonjy, A., et al. (2018). A review of classification algorithms for EEG-based brain–computer interfaces: a 10 year update. *J. Neural Eng.* 15, 031005. doi: 10.1088./1741-2560/4/2/R01

Mainanwal, V., Gupta, M., and Upadhayay, S. K. (2015). A survey on wireless body area network: Security technology and its design methodology issue. In *2015 International Conference on Innovations in Information, Embedded and Communication Systems (ICIIECS)* (pp. 1-5). IEEE. doi: 10.1109./ICIIECS.2015.7193088

Meng, J., Yao, L., Sheng, X., Zhang, D., and Zhu, X. (2014). Simultaneously optimizing spatial spectral features based on mutual information for EEG classification. *IEEE Transact. Biomed. Engin.* 62, 227–240. doi: 10.1109./TBME.2014.2345458

Moosavi, S. R. (2021). PPG-KeyGen: using photoplethysmogram for key generation in wearable devices. *Procedia Comput. Sci.* 184, 291–298.doi: 10.1016/j.procs.03038

Narwal, B., and Mohapatra, A. K. (2021). A survey on security and authentication in wireless body area networks. *J. Sys. Architect.* 113, 101883. doi: 10.1016./j.sysarc.2020.101883

Pandey, I., Dutta, H. S., and Banerjee, J. S. (2019). WBAN: a smart approach to next generation e-healthcare system. In *2019 3rd International Conference on Computing Methodologies and Communication (ICCMC)* (pp. 344-349). IEEE. doi: 10.1109./ICCMC.2019.8819713

Qadri, Y. A., Nauman, A., Zikria, Y. B., Vasilakos, A. V., and Kim, S. W. (2020). The future of healthcare internet of things: a survey of emerging technologies. *IEEE Commun. Surv. Tutorials* 22, 1121–1167. doi: 10.1109./COMST.2020. 2973314

Ramli, S. N., Ahmad, R., and Abdollah, M. F. (2013). Electrocardiogram (ECG) signals as biometrics in securing wireless body area network. In *8th International Conference for Internet Technology and Secured Transactions (ICITST-2013)* (pp. 536-541). IEEE. doi: 10.1109./ICITST.2013.6750259

Shen, J., Gui, Z., Ji, S., Shen, J., Tan, H., Tang, Y., et al. (2018). Cloud-aided lightweight certificateless authentication protocol with anonymity for wireless body area networks. *J. Network Comp. Appl.* 106, 117–123. doi: 10.1016/j.jnca.01003

Shi, L., Li, M., Yu, S., and Yuan, J. (2012). *BANA: Body area network authentication exploiting channel characteristics. In Proceedings of the fifth ACM conference on Security and Privacy in Wireless and Mobile Networks* (pp. 27–38). doi: 10.1109./JSAC.2013.130913

Standard, I. E. E. E. for Local and metropolitan area networks part 15.6: Wireless Body Area Networks. *IEEE Std.* (2012) 802, 6. doi: 10.1109/IEEESTD.2012.6161600

Venkatasubramanian, K. K., Banerjee, A., and Gupta, S. K. (2008). "Plethysmogram-based secure inter-sensor communication in body area networks," in *MILCOM 2008-2008 IEEE Military Communications Conference* (pp. 1-7). IEEE. doi: 10.1109./MILCOM.2008.4753199

Wang, H., Fang, H., Xing, L., and Chen, M. (2011). An integrated biometric-based security framework using wavelet-domain HMM in wireless body area networks (WBAN). In *2011 IEEE international conference on communications (ICC)* (pp. 1-5). IEEE. doi: 10.1109./icc.2011.5962757

Wang, J., Han, K., Fan, S., Zhang, Y., Tan, H., Jeon, G., et al. (2020). A logistic mapping-based encryption scheme for Wireless Body Area Networks. *Future Gen. Comp. Sys.* 110, 57–67. doi: 10.1016/j.future.04002

Yang, C., Deng, Z., Choi, K. S., Jiang, Y., and Wang, S. (2014). Transductive domain adaptive learning for epileptic electroencephalogram recognition. *Artif. Intell. Med.* 62, 165–177. doi: 10.1016/j.artmed.10002

Yin, Y., Yu, H., and Zhang, H. (2008). A feature extraction method based on wavelet packet analysis for discrimination of Chinese vinegars using a gas sensors array. *Sens. Actuat. B Chem.* 134, 1005–1009. doi: 10.1016/j.snb.07018

Zhang, Y., Zhou, G., Jin, J., Wang, M., Wang, X., Cichocki, A., et al. (2013). L1-regularized multiway canonical correlation analysis for SSVEP-based BCI. *IEEE Transact. Neural Sys. Rehabilit. Engin.* 21, 887–896. doi: 10.1109/TNSRE.2013.2279680

Frontiers in Neuroscience

Provides a holistic understanding of brain function from genes to behavior

Part of the most cited neuroscience journal series which explores the brain - from the new eras of causation and anatomical neurosciences to neuroeconomics and neuroenergetics.

Discover the latest Research Topics

See more →

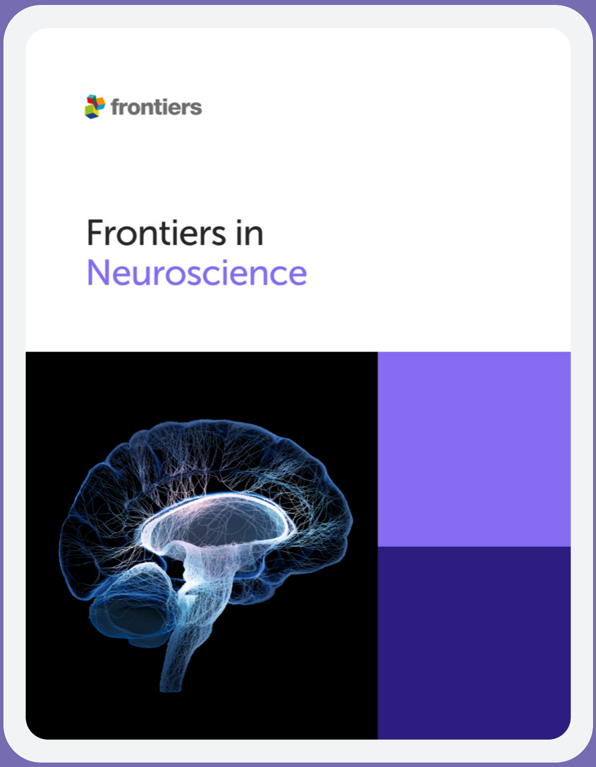

Frontiers

Avenue du Tribunal-Fédéral 34
1005 Lausanne, Switzerland
frontiersin.org

Contact us

+41 (0)21 510 17 00
frontiersin.org/about/contact